



Melissa Maria Cruz Torres

**Study of CP violation and amplitude analysis of
the decay $B^+ \rightarrow \pi^+ K^- K^+$ in the LHCb
experiment**

Tese de Doutorado

Thesis presented to the Programa de Pós-graduação em Física of PUC-Rio in partial fulfillment of the requirements for the degree of Doutor em Ciências - Física.

Advisor : Prof. Carla Göbel Burlamaqui de Mello
Co-advisor: Prof. Jussara Marques de Miranda

Rio de Janeiro
May 2017



Melissa Maria Cruz Torres

**Study of CP violation and amplitude analysis of the
decay $B^+ \rightarrow \pi^+ K^- K^+$ in the LHCb experiment**

Thesis presented to the Programa de Pós-Graduação em Física of PUC-Rio in partial fulfillment of the requirements for the degree of Doutor em Ciências – Física. Approved by the undersigned Examination Committee.

Profa. Carla Göbel Burlamaqui de Mello

Advisor

Departamento de Física – PUC-Rio

Profa. Jussara Marques de Miranda

Co-Advisor

CBPF

Prof. Gustavo Alberto Burdman

USP

Profa. Maria Clemencia Rosario Mora Herrera

UERJ

Prof. Bruno Souza de Paula

UFRJ

Prof. Arman Esmaili Taklimi

Departamento de Física – PUC-Rio

Prof. Márcio da Silveira Carvalho

Vice Dean of Graduate Studies

Centro Técnico Científico – PUC-Rio

Rio de Janeiro, May 22nd, 2017.

All rights reserved.

Melissa Maria Cruz Torres

Melissa Cruz is currently a PhD candidate of Physics Department at PUC-Rio. Her research focuses on CP violation measurements and Amplitude Analysis of charmless B decays. She also got her master degree in physics at PUC-Rio in 2013 working on branching ratio measurements in the Charm sector in the LHCb experiment. She undergraduated in Physics at the UNAH (Tegucigalpa, Honduras) in 2009 and in Electrical Engineer also at the UNAH in 2010.

Bibliographic data

Cruz Torres, Melissa Maria

Study of CP violation and amplitude analysis of the decay $B^+ \rightarrow \pi^+ K^- K^+$ in the LHCb experiment / Melissa Maria Cruz Torres; advisor: Carla Göbel Burlamaqui de Mello; co-advisor: Jussara Marques de Miranda. – Rio de Janeiro: PUC-Rio, Departamento de Física, 2017.

165 f. : il. color. ; 30 cm

Tese (doutorado) - Pontifícia Universidade Católica do Rio de Janeiro, Departamento de Física.

Inclui bibliografia.

1. Física – Teses. 2. Violação de CP. 3. Análise de Amplitudes. 4. Decaimentos de mésons B . I. Göbel Burlamaqui de Mello, Carla. II. Marques de Miranda, Jussara. III. Pontifícia Universidade Católica do Rio de Janeiro. Departamento de Física. IV. Título.

CDD: 510

To my beloved family.

Acknowledgement

In first place I want to thank God for giving me the gift of life. To my beloved family, my parents Andres Cruz and Candida Torres, because even in the distance they have always been fondly supporting me and encouraging me to always give the best. To my brother Cristian Cruz, that during his time also here in Rio, he always took care of me, making my life much easier far away from home. I want to lovingly thank my husband for all the love, support and company especially in the most tense moments in the elaboration of this thesis.

I want to give thanks trully especially to the person that has guided me in this path of knowledge, not only during these four year of doctorade but since my master times. To my advisor Carla Göbel, for always taking the time to teach me and patiently explain me everything from the most simple things to most complicated concepts. For all the enriching discussions in these six years. For all the advices that were not limited to the “classroom”.

To the CBPF group, for all the discussions, for the opportunity to work in such active enviroment and for all the teachings without which this work wouldn't be possible. To prof. Ignacio Bediga, Fernando, Juan, prof. Alberto, Valdir, Bruno, Laís, Ana, Alvaro, Patricia, Irina, Adlene, prof. Helder, prof. Massafferri. I want to especially thank my co-advisor prof. Jussara Miranda, for always be so kind in helping me, teaching me and guide me in the development of this work. For the meetings every day even if were for the most silly questions.

To all my friends at PUC and at CBPF. To my professors at UNAH.

To the CNPq for the financial support.

Abstract

Cruz Torres, Melissa Maria; Göbel Burlamaqui de Mello, Carla (Advisor); Marques de Miranda, Jussara (Co-Advisor). **Study of CP violation and amplitude analysis of the decay $B^+ \rightarrow \pi^+ K^- K^+$ in the LHCb experiment.** Rio de Janeiro, 2017. 165p. Tese de Doutorado — Departamento de Física, Pontifícia Universidade Católica do Rio de Janeiro.

In this thesis we present CP violation measurements and amplitude analysis of the decay $B^\pm \rightarrow \pi^\pm K^- K^+$. We use the data collected by the LHCb experiment in 2011 and 2012, corresponding to a total integrated luminosity of 3.0 fb^{-1} . The event selection is performed based on the exploitation of the topological features of $B^\pm \rightarrow \pi^\pm K^- K^+$ decay and an offline selection criteria is applied based on a multivariate analysis. The final sample has about 5000 events. A large integrated CP asymmetry is obtained: $\mathcal{A}_{CP}(B^\pm \rightarrow \pi^\pm K^- K^+) = -0.123 \pm 0.017 \pm 0.012 \pm 0.007$, where the first uncertainty is statistical, the second systematic, and the third due to CP asymmetry of the reference mode. Large CP asymmetries are also found in regions of the phase space. In order to understand the origin of these asymmetries, a model-dependent amplitude analysis is performed using the so-called Isobar Model formalism. It is the first time that an amplitude analysis is performed for this decay. The strategy adopted consists of the construction of models through a systematic procedure to consider all possible resonant contributions to the decay. We present results for three different models which describe the data well. The first model includes only well known resonant states. In the second model we use an alternative parametrization for the non-resonant component to account for specific regions that are not well described in the first model; and the third model is dedicated to the parametrization of the region with larger CP asymmetry found: the $\pi\pi \leftrightarrow KK$ rescattering region. All models give acceptable description of data, although their interpretation differ. In particular, the role of the $\pi\pi \leftrightarrow KK$ rescattering in this channel, regarding the CP violation effects, is still not totally clear and its understanding will benefit from studies with higher statistics, available from run II data at LHCb.

Keywords

CP violation; Amplitude Analysis; B -meson decays.

Resumo

Cruz Torres, Melissa Maria; Göbel Burlamaqui de Mello, Carla; Marques de Miranda, Jussara. **Estudo de violação de CP e análise de amplitudes do decaimento $B^+ \rightarrow \pi^+ K^- K^+$ no experimento LHCb**. Rio de Janeiro, 2017. 165p. Tese de Doutorado — Departamento de Física, Pontifícia Universidade Católica do Rio de Janeiro.

Nesta tese apresentamos a medida de violação CP e a análise de amplitudes do decaimento $B^\pm \rightarrow \pi^\pm K^- K^+$. São usados os dados do run I, coletados pelo experimento LHCb em 2011 and 2012, correspondendo a uma luminosidade integrada de 3.0 fb^{-1} de colisões próton-próton a 7 e 8 TeV no centro de massa. A seleção dos eventos é baseada na exploração das características topológicas do decaimento $B^\pm \rightarrow \pi^\pm K^- K^+$ e um critério de seleção subsequente é aplicado baseado em análise multivariada. A amostra final para análise tem cerca de 5000 eventos. Uma grande assimetria CP total é obtida: $\mathcal{A}_{CP}(B^\pm \rightarrow \pi^\pm K^- K^+) = -0.123 \pm 0.017 \pm 0.012 \pm 0.007$ (onde a primeira incerteza é estatística, a segunda sistemática, e a terceira devido à assimetria CP do canal de controle). Grandes assimetrias CP são também encontradas em regiões do espaço de fase do decaimento. Para poder entender a origem destas assimetrias, uma análise de amplitudes é realizada usando o chamado formalismo de Modelo Isobárico. A estratégia adotada consiste na construção de modelos através de um procedimento sistemático que considera todas as possíveis contribuições ressonantes ao decaimento. Apresentamos os resultados para três diferentes modelos que descrevem bem os dados. O primeiro modelo inclui somente estados ressonantes bem conhecidos. No segundo modelo, usamos parametrizações alternativas para a componente não ressonante para dar conta de regiões que não foram bem descritas no primeiro modelo; e o terceiro modelo é dedicado à parametrização da região com a maior assimetria CP encontrada: a região de re-espalhamento $\pi\pi \leftrightarrow KK$. Todos os modelos fornecem uma descrição aceitável dos dados, embora sua interpretação difira. Em particular, o papel do re-espalhamento $\pi\pi \leftrightarrow KK$ neste canal, a respeito dos efeitos de violação CP , ainda fica totalmente claro e seu entendimento será beneficiado por estudos com maior estatística, possíveis com os dados do Run II do LHCb.

Palavras-chave

Violação de CP ; Análise de Amplitudes ; Decaimentos de mésons B .

Contents

1	Introduction	18
2	Theoretical Fundamentals	20
2.1	Standard Model	20
2.2	CP Violation in the Standard Model	21
2.3	CP and CPT symmetry	23
2.4	The CKM matrix	23
2.5	CP violation mechanism	25
2.6	Three body B decays	26
2.7	The charmless three body decay $B^\pm \rightarrow \pi^\pm K^- K^+$	27
2.8	Dalitz Plot	29
2.9	The Square Dalitz plot	32
2.10	The phase space for $B^\pm \rightarrow \pi^\pm K^- K^+$	33
3	The LHCb Experiment	37
3.1	The Large Hadron Collider (LHC)	37
3.2	The LHCb detector	39
3.3	Operation conditions in 2011 and 2012	51
4	Data Selection	54
4.1	Dataset	54
4.2	Variables definition	54
4.3	Selection requirements	57
4.4	Offline Selection	60
4.5	Charm veto study	63
4.6	Simulated samples	64
4.7	Mass Fit	65
4.8	The $B^\pm \rightarrow \pi^\pm K^- K^+$ fit model	66
5	CP violation measurements	77
5.1	The charmless $B^\pm \rightarrow h^\pm h^- h^+$ decays	77
5.2	CP Asymmetry in regions of the phase space	81
6	The Dalitz plot formalism	85
6.1	The Isobar Model	85
6.2	The Dalitz plot Fit	97
6.3	Efficiency and background models for the Dalitz plot fit	98
6.4	Background Models	102
6.5	The probability density function	108
6.6	Fit Fractions and CP Asymmetry	112
7	Dalitz plot fit results	114
7.1	Families of fits	116
7.2	Classic Model (Model-2011)	117
7.3	Model 1	120

7.4	Model 2	121
8	Conclusions	130
	Bibliography	133
A	Mass Fit	140
B	Acceptances Maps	149
C	Exploring improvements of the L0 hadron trigger for Run II	153
C.1	Introduction	153
C.2	Strategy and tools	155
C.3	Summary	163

List of figures

Figure 2.1	CKM unitary triangle given by the Equation 2-15.	25
Figure 2.2	Penguin (top) and Tree-level (bottom) diagrams for $B^- \rightarrow \pi^- K^+ K^-$.	27
Figure 2.3	$B^+ \rightarrow \pi^+ K^- K^+$ decay for the case that K^+ is the bachelor particle. (left) $\cos \theta < 0$ ($\theta > 0$), (right) $\cos \theta > 0$ ($\theta < 0$).	28
Figure 2.4	A three body decay scheme. Figure extracted from PDG [1].	29
Figure 2.5	Example of the Dalitz plot boundaries for a decay. The sides of the Dalitz represent the variables minima and the corners their maxima. Figure extracted from PDG [1].	31
Figure 2.6	a) A cartoon of a DP showing the resonance structures with different spin. b) a Real Dalitz plot obtained in the Crystal Barrel experiment for the decay $p\bar{p} \rightarrow \pi^0 \pi^0 \pi^0$.	32
Figure 2.7	Jacobian determinant of transformations that would be obtained if the nominal Dalitz plot were evenly populated.	34
Figure 2.8	$B^\pm \rightarrow \pi^\pm K^- K^+$ Dalitz plot.	34
Figure 2.9	Dalitz Plot for $B^\pm \rightarrow \pi^\pm K^- K^+$ decay using the nominal variables $m_{\pi^\pm K^\mp}^2$ and $m_{K^- K^+}^2$ 2.9(a) and the square variables m' and θ' 2.9(b). The Dalitz plot distribution has been highlighted in different colors in order to show how the different regions transform into the SDP.	35
Figure 3.1	Pictorial view of the localization of the LHC experiments and their interaction points.	38
Figure 3.2	Simulation of the angular distribution for the pair $b\bar{b}$ as produced in the LHC ($\sqrt{s} = 8$ TeV)	39
Figure 3.3	Lateral view of the LHCb spectrometer. The subdetectors are explicitly indicated.	40
Figure 3.4	(left) Representation of the $R-$ sensor and $\phi-$ sensor. (right) A picture of the VELO modulus in the LHCb.	41
Figure 3.5	Schematic view of the LHCb experiment magnet.	42
Figure 3.6	Schematic view of the four layers of the Tracker Turicensis stations.	43
Figure 3.7	(a) View of the position of the four boxes of a IT station arranged around the beam pipe. (b) Frontal view where it can be seen the detector modules.	44
Figure 3.8	a) Cross section of a module. b) View of the OT straw-tube detector four layers in the $T_1 - T_3$ stations.	44
Figure 3.9	Representation of the five types of tracks reconstructed in the LHCb.	45
Figure 3.10	Schematic view of the RICH detectors.	47
Figure 3.11	Lateral view of the stations the form muon system M1-M5. The regions R1-R4 are also shown	49
Figure 3.12	Lateral view of the stations the form muon system M1-M5. The regions R1-R4 are also shown	50

Figure 3.13	Pile-up μ for the LHCb experiment during LHC Run I (Top) and Instantaneous luminosity reached per year (Bottom). Notice that for 2012 a stability for both was achieved.	52
Figure 3.14	Delivered (dark colour lines) and recorded luminosity (light colour line) per year by the LHCb during LHC Run I.	53
Figure 4.1	Topology for $B^\pm \rightarrow \pi^\pm K^- K^+$ decay.	55
Figure 4.2	Discriminating variable $BDTPCA$ output by the Boosted Decision Trees optimization common to all $B^\pm \rightarrow h^\pm h^- h^+$ channels. Signal: blue curve, background: red curve.	62
Figure 4.3	Background rejection as a function of signal efficiency for (a) $B^\pm \rightarrow \pi^\pm K^- K^+$, and (b) background rejection as a function of signal efficiency comparing 2011 and 2012 events.	62
Figure 4.4	$B^\pm \rightarrow \pi^\pm K^- K^+$ mass distributions for 2012 data before and after a cut on the BDT discriminating variable $BDTPCA > 0$.	63
Figure 4.5	(a) Distribution of events on the Daliz plot in the signal region without vetos applied (b) Distribution of events on the Daliz plot in the signal region with vetos are applied.	64
Figure 4.6	a) $m_{KK-\pi K}$ distribution with [1.834,1.894] GeV/c^2 m_{KK} veto window applied. b) $m_{KK-\pi K}$ distribution with [1.834,2.000] GeV/c^2 m_{KK} veto window applied	65
Figure 4.7	Invariant mass distribution $M_{\pi^+ K^- K^+}$ after all the selection criteria applied.	66
Figure 4.8	Result of the simultaneous fit to the 2011 data sample. Top row is the "Global_TIS or Hadron_TOS" trigger requirement, middle row the "Global_TIS and not Hadron_TOS" trigger requirement and the bottom plots the "Hadron_TOS" trigger selection. The plot of the right side is the same that of the left but in log scale with the pull distribution on the bottom pad. In each pair of distributions, the plot on the left is B^- and on the right is B^+ .	72
Figure 4.9	Result of the simultaneous fit to the 2012 data sample. Top row is the "Global_TIS or Hadron_TOS" trigger requirement, middle row the "Global_TIS and not Hadron_TOS" trigger requirement and the bottom plots the "Hadron_TOS" trigger selection. The plot of the right side is the same that of the left but in log scale with the pull distribution on the bottom pad. In each pair of distributions, the plot on the left is B^- and on the right is B^+ .	73
Figure 4.10	Result of the simultaneous fit to the combined 2011 and 2012 data samples. Top row is the "Global_TIS or Hadron_TOS" trigger requirement, middle row the "Global_TIS and not Hadron_TOS" trigger requirement and the bottom plots the "Hadron_TOS" trigger selection. The plot of the right side is the same that of the left but in log scale with the pull distribution on the bottom pad. In each pair of distributions, the plot on the left is B^- and on the right is B^+ .	74

- Figure 4.11 (a) Dalitz Plot for $B^+ \rightarrow \pi^+ K^- K^+$ and (b) for $B^- \rightarrow \pi^- K^+ K^-$ in the selected signal region. 76
- Figure 5.1 Tree and penguin diagrams for $B^\pm \rightarrow K^\pm \pi^+ \pi^-$ (top) and $B^\pm \rightarrow K^\pm K^+ K^-$ (bottom). 78
- Figure 5.2 Tree-level and penguin diagrams for $B^\pm \rightarrow \pi^\pm \pi^+ \pi^-$ (top) and $B^\pm \rightarrow \pi^\pm K^- K^+$ (bottom). 79
- Figure 5.3 A_{raw}^N measured in bins of Dalitz plot with background subtracted and acceptance corrected for (a) $B^\pm \rightarrow K^\pm K^+ K^-$, (b) $B^\pm \rightarrow K^\pm \pi^+ \pi^-$, (c) $B^\pm \rightarrow \pi^\pm \pi^+ \pi^-$ e (d) $B^\pm \rightarrow K^\pm K^+ \pi^-$. 82
- Figure 5.4 Invariant mass distribution in the rescattering region $m(\pi^+ \pi^-)$ and $m(K^+ K^-)$ between 1.0 a 1.5 GeV/c^2 for (a) $B^\pm \rightarrow K^\pm K^+ K^-$, (b) $B^\pm \rightarrow K^\pm \pi^+ \pi^-$, (c) $B^\pm \rightarrow \pi^\pm \pi^+ \pi^-$ and (d) $B^\pm \rightarrow K^\pm K^+ \pi^-$. The left side of each figure shows the B^- candidates and the right side the B^+ candidates. 83
- Figure 5.5 (a) Projection in the invariant mass $m_{\pi^+ K^-}$ and (b) $m_{K^- K^+}$ of $B^\pm \rightarrow \pi^\pm K^- K^+$. The solid black line represents B^+ events and the gray dashed line B^- event. 84
- Figure 6.1 Scheme of a three-body decay B through an intermediate resonant state R . 85
- Figure 6.2 (left) Phase shift δ_0^0 and (right) Inelasticity η_0^0 as a function of $m(K^- K^+)$. Figure extracted from [2] 92
- Figure 6.3 Possible resonance contributions in the $B^\pm \rightarrow \pi^\pm K^- K^+$ phase space. Resonances are parametrized using the Breit-Wigner lineshape. 94
- Figure 6.4 Possible resonance contributions in the $B^\pm \rightarrow \pi^\pm K^- K^+$ phase space. Resonances are parametrized using the Breit-Wigner lineshape. 95
- Figure 6.5 Possible resonance contributions in the $B^\pm \rightarrow \pi^\pm K^- K^+$ phase space. The non-resonant parametrization is used in the first row, the Flatté parametrization for the second and third row, The Tobias NR parametrization for the fourth and fifth row, and in the sixth row, the re-scattering parametrization. 96
- Figure 6.6 a), b) and c) show the histograms for the numerator, denominator and acceptance map, respectively for B^+ , TOS configuration-2012. d), e) and d) show the respective histograms for the TISnotTOS configuration. 100
- Figure 6.7 (a) Acceptance map 2012 TOS for B^+ without L0 correction (b) 2012 TOS L0 Hadron efficiency correction histogram (c) Total acceptance with TOS L0 Hadron efficiency correction applied. 102
- Figure 6.8 (a) Acceptance map 2012 TISnotTOS for B^+ without L0 correction (b) 2012 TISnotTOS L0 Hadron efficiency correction histogram (c) Total acceptance with TISnotTOS L0 Hadron efficiency correction applied. 103

Figure 6.9	a) 2011 acceptance for B^+ , b) 2012 acceptance for B^+ , c) 2011 and 2012 combined acceptance for B^+	104
Figure 6.10	a) 2011 acceptance for B^- , b) 2012 acceptance for B^- , c) 2011 and 2012 combined acceptance for B^-	104
Figure 6.11	Region a) from 5400 to 5450 MeV/c^2 , region b) from 5450 to 5500 MeV/c^2 , region c) greater than 5500 MeV/c^2	106
Figure 6.12	a) $m_{\pi K}^2$ vs B_m , b) $m_{K\pi}^2$ vs B_m , c) m_{KK}^2 vs B_m , a structure on c) can be seen for $B_m > 5500 \text{ MeV}/c^2$	107
Figure 6.13	a) Combinatorial events on the Dalitz plot using the complete right sideband $B_m > 5400 \text{ MeV}/c^2$ b) Combinatorial events on the Dalitz plot removing the events in the interval $5500 \text{ MeV}/c^2 < B_m < 5550 \text{ MeV}/c^2$.	107
Figure 6.14	a) Combinatorial background model in the square variables for the Dalitz plot fit b) smoothed version.	108
Figure 6.15	(a) Peaking background model in the square variables for the Dalitz plot fit. (b) smooth version.	109
Figure 7.1	1-D mass fit in the rescattering region $1 \text{ MeV}/c^2 < m_{K^-K^+}$ $1.5 \text{ MeV}/c^2$. B^- (left), B^+ (right).	114
Figure 7.2	(a) Dalitz Plot for $B^+ \rightarrow \pi^+ K^- K^+$ and (b) for $B^- \rightarrow$ $\pi^- K^+ K^-$ in the selected signal region.	115
Figure 7.3	Regions of the Dalitz plot that correspond for a $\cos \theta_{12} > 0$ (in blue) and $\cos \theta_{12} < 0$ (in red).	119
Figure 7.4	Classic model (fit 2011). For each plot B^- (top), B^+ (middle) and the difference ($B^- - B^+$, bottom). a) ($\cos \theta_{12} > 0$), b) ($\cos \theta_{12} < 0$) and c) show the projections on $m_{\pi^\pm K^\mp}^2$. d) ($\cos \theta_{23} > 0$), e) ($\cos \theta_{23} < 0$) and f) the projections on $m_{K^-K^+}^2$ and g) and h) the projections on $m_{\pi^\pm K^\pm}^2$. The line in blue represents the model, the black dots the data and the region in red the background estimation	124
Figure 7.5	Regions of the Dalitz plot that correspond for a $\cos \theta_{23} > 0$ (in blue) and $\cos \theta_{23} < 0$ (in red).	125
Figure 7.6	Classic model (fit 2011) χ^2 map. The global χ^2 value obtained is of 1.76	125
Figure 7.7	Model 1 (fit 2014) χ^2 map. The global χ^2 value obtained is of 1.45	126
Figure 7.8	Model 1 (fit 2014). For each plot B^- (top), B^+ (middle) and the difference ($B^- - B^+$, bottom). a) ($\cos \theta_{12} > 0$), b) ($\cos \theta_{12} < 0$) and c) show the projections on $m_{\pi^\pm K^\mp}^2$. d) ($\cos \theta_{23} > 0$), e) ($\cos \theta_{23} < 0$) and f) the projections on $m_{K^-K^+}^2$ and g) and h) the projections on $m_{\pi^\pm K^\pm}^2$. The line in blue represents the model, the black dots the data and the region in red the background estimation	127
Figure 7.9	Model 2 (fit 1201) χ^2 map. The global χ^2 value obtained is of 1.54	128

- Figure 7.10 Model 2 (fit1201). For each plot B^- (top), B^+ (middle) and the difference ($B^- - B^+$, bottom). a) ($\cos\text{Hel}12 > 0$), b) ($\cos\text{Hel}12 < 0$) and c) show the projections on $m_{\pi^\pm K^\mp}^2$. d) ($\cos\text{Hel}23 > 0$), e) ($\cos\text{Hel}23 < 0$) and f) the projections on $m_{K^- K^+}^2$ and g) and h) the projections on $m_{\pi^\pm K^\pm}^2$. The line in blue represents the model, the black dots the data and the region in red the background estimation. 129
- Figure A.1 Fits to the MC invariant mass distributions of the $B^\pm \rightarrow \pi^\pm K^- K^+$ of 2011 MC sample divided in the trigger configuration chosen for this analysis: "Global_TIS or Hadron_TOS" (first row), "Global_TIS and not Hadron_TOS" (second row) and "Hadron_TOS" (last row). The plot on the right side is the same as the left side, but in log scale and with the pull distribution on the bottom pad. In each pair of distributions, the plot on the left is B^- and on the right is B^+ . 141
- Figure A.2 Fits to the MC invariant mass distributions of the $B^\pm \rightarrow \pi^\pm K^- K^+$ of 2012 MC sample divided in the trigger configuration chosen for this analysis: "Global_TIS or Hadron_TOS" (first row), "Global_TIS and not Hadron_TOS" (second row) and "Hadron_TOS" (last row). The plot on the right side is the same as the left side, but in log scale and with the pull distribution on the bottom pad. In each pair of distributions, the plot on the left is B^- and on the right is B^+ . 142
- Figure A.3 Fits to the MC invariant mass distributions of the $B^\pm \rightarrow \pi^\pm K^- K^+$ of the combined 2011 and 2012 MC samples, divided in the trigger configuration chosen for this analysis: "Global_TIS or Hadron_TOS" (first row), "Global_TIS and not Hadron_TOS" (second row) and "Hadron_TOS" (last row). The plot on the right side is the same as the left side, but in log scale and with the pull distribution on the bottom pad. In each pair of distributions, the plot on the left is B^- and on the right is B^+ . 143
- Figure A.4 Peaking background of $B^\pm \rightarrow K^\pm K^+ K^-$ (left) and $B^\pm \rightarrow K^\pm \pi^+ \pi^-$ (right) with the result superimposed. 143
- Figure B.1 2011 Acceptance maps for $B^\pm \rightarrow \pi^\pm K^- K^+$. Acceptance map without correction (first column), L0 Hadron efficiency correction histogram (second column), total acceptance map with correction applied (third column). First row for TOS minus, second row for TISnotTOS minus, third row for TOS plus and fourth row for TISnotTOS plus. 151
- Figure B.2 2012 Acceptance maps for $B^\pm \rightarrow \pi^\pm K^- K^+$. Acceptance map without correction (first column), L0 Hadron efficiency correction histogram (second column), total acceptance map with correction applied (third column). First row for TOS minus, second row for TISnotTOS minus, third row for TOS plus and fourth row for TISnotTOS plus. 152

Figure C.1	Efficiency of the LHCb low-level trigger on representative simulated signals as a function of event accept rate at instantaneous luminosity $L = 1 \times 10^{33} \text{ cm}^{-2}\text{s}^{-1}$. Plot reproduced from Fig. 3.2 in Ref. [3]	154
Figure C.2	Distributions of relative gains associated with $\sum E_t$ using real data.	158
Figure C.3	Distributions of relative gains associated with $\sum E_{t2}$ using real data.	159
Figure C.4	Distributions of relative gains associated with various requirements on the logical "AND" between the energy of the leading jet and the sum of the energies in all calorimeter towers. Results using real Data	159
Figure C.5	Distributions of relative gains associated with various requirements on the logical "OR" between the energy of the leading jet and the sum of the energies in all calorimeter towers. Results using real Data.	160
Figure C.6	Distributions of relative gains associated with various requirements on the logical "AND" between the energy of the second leading jet and the sum of the energies in all calorimeter towers. Results using real Data	160
Figure C.7	Distributions of relative gains associated with various requirements on the logical "OR" between the energy of the second leading jet and the sum of the energies in all calorimeter towers. Results using real Data.	161
Figure C.8	Distributions of relative gains associated with various requirements on the logical "AND" between the energy of the leading jet and the second leading jet. Results using real Data.	161
Figure C.9	Distributions of relative gains associated with various requirements on the logical "OR" between the energy of the leading jet and the second leading jet. Results using real Data.	162
Figure C.10	Distributions of relative gains associated with the $E_{t1} + E_{t2}$ AND $E_{t1} + E_{t2} + E_{t3}$ configuration, using signal MC and min-bias sample.	164
Figure C.11	Distributions of relative gains associated with the E_{t1} OR $E_{t1} + E_{t2} + E_{t3}$ configuration, using signal MC and min-bias sample.	164
Figure C.12	Distributions of relative gains associated with the E_{t1} OR $E_{t1} \times E_{t2}$ configuration, using signal MC and min-bias sample.	165

List of tables

Table 2.1	Quarks families.	20
Table 2.2	Leptons families.	21
Table 2.3	Left-handed fields transforms as doublet and right-handed fields as singlets of the group $SU_L(2)$.	21
Table 3.1	Parameters values for the optimal running conditions for the LHCb.	51
Table 4.1	L0 thresholds in 2011 and 2012.	58
Table 4.2	StrippingBu2hhh_KKK_inclLine stripping 20 line for charmless B^\pm decays to three light hadrons.	60
Table 4.3	MC signal statistics used on the multivariate analysis training.	61
Table 4.4	PID selection criteria for $B^\pm \rightarrow \pi^\pm K^- K^+$ decay.	62
Table 4.5	Generation criteria for large MC samples.	64
Table 4.6	Large MC signal statistics.	64
Table 4.7	Branching fraction and fraction of the peaking background f_{bkg} with respect to the signal yield ($B^\pm \rightarrow \pi^\pm K^- K^+$) obtained from Eq. 4-15	70
Table 4.8	Floating parameters of the simultaneous fit to the 2011 data sample regarding to Figure 4.8.	71
Table 4.9	Floating parameters of the simultaneous fit to the 2012 data sample regarding to Figure 4.9.	74
Table 4.10	Floating parameters of the simultaneous fit to the 2011 and 2012 data sample regarding to Figure 4.10.	75
Table 4.11	Number of events of the different components per year in the signal region ($[5266, 5300]$ MeV/ c^2). Their relative percentage contribution is also shown.	75
Table 5.1	Number of signal candidates and charge asymmetries in the rescattering region $m(\pi^+\pi^-)$ or $m(K^+K^-)$ between 1.0 e 1.5 GeV/ c^2	83
Table 6.1	Angular distribution using Zemach tensor formalism.	87
Table 6.2	Blatt-Weisskopf barrier factor used to correct the amplitude for penetration effects where z_0 represents the value of z when the invariant mass is equal to the pole mass of the resonance.	89
Table 6.3	Signal and background events in the chosen signal region, for the 2011+2012 data sample.	105
Table 7.1	Signal and background events set on the Dalitz plot fit.	117
Table 7.2	Classic model: model components (1st column), fit fraction for each component for B^+ (B^-) on 2nd (3rd) column, magnitude and phase on 4th and 5th column for B^+ , 6th and 7th for B^- . CP asymmetry on 8th.	118

Table 7.3	Model 1: Model components (1st column), fit fraction for each component for B^+ (B^-) on 2nd (3rd) column, magnitude and phase on 4th and 5th column for B^+ , 6th and 7th for B^- . CP asymmetry on 8th.	121
Table 7.4	Model 2: Model components (1st column), fit fraction for each component for B^+ (B^-) on 2nd (3rd) column, magnitude and phase on 4th and 5th column for B^+ , 6th and 7th for B^- . CP asymmetry on 8th.	122
Table A.1	Parameters of the PDF signal shape extracted from the fit to the 2011 MC sample for the trigger lines “Global_TIS or Hadron_TOS” (second column), “Global_TIS and not Hadron_TOS” (third column)” and “Hadron_TOS” (fourth column). The parameters with F are those which are left to float during the fit to data.	144
Table A.2	Parameters of the PDF signal shape extracted from the fit to the 2012 MC sample for the trigger lines “Global_TIS or Hadron_TOS” (second column), “Global_TIS and not Hadron_TOS” (third column)” and “Hadron_TOS” (fourth column). The parameters with F are those which are left to float during the fit to data.	145
Table A.3	Parameters of the PDF signal shape extracted from the fit to the combined 2011 and 2012 MC sample for the trigger lines “Global_TIS or Hadron_TOS” (second column), “Global_TIS and not Hadron_TOS” (third column)” and “Hadron_TOS” (fourth column). The parameters with F are those which are left to float during the fit to data.	146
Table A.4	Parameters of the $B^\pm \rightarrow K^\pm K^+ K^-$ and $B^\pm \rightarrow K^\pm \pi^+ \pi^-$ reflection extracted from the unbinned extended maximum likelihood fit to the 2011 and 2012 MC samples.	147
Table A.5	Parameters of the partially reconstructed background of $B_s^0 \rightarrow 4$ -body and $B \rightarrow 4$ -body. The C aside the parameters indicates they are fixed during the fit to data but the fraction of its PDF is left to float.	148
Table C.1	Trigger scenarios tested only using the available information to the LODU. In the first column is presented the scenario being tested and in the following columns the relative efficiency gain for the different channels. This values correspond for a retention of 2.3%	162
Table C.2	Trigger scenarios tested only using the available information to the LODU. In the first column is presented the scenario being tested and in the following columns the relative efficiency gain for the different channels. This values correspond for a retention of 3.1%	163

1

Introduction

One of the most intriguing phenomenon in Physics is the preponderance of matter over antimatter in the Universe. The violation of the Charge-Parity (CP) symmetry is known to be one of the necessary ingredients for this [4]. The Standard Model (SM) of Particle Physics is a theory that successfully describes the fundamental building blocks of matter (and antimatter) and how they interact with each other. With three generations of quarks and leptons, it naturally brings possible sources of CP violation through flavour mixing matrices. In the quark sector, this is the so-called Cabibbo-Kobayashi-Maskawa matrix [5]. However, the level of matter-antimatter asymmetry observed in the Universe seems not to be due only to what is predicted from the SM. A comprehensive study of different processes where CP violation can be manifested is crucial for the understanding of this phenomenon.

A particular environment for CP violation studies is the decays of B^+ ($\bar{b}u$) mesons ¹ to final states with pions and kaons - these are called *charmless* decays. At quark level, two main diagrams can contribute with the same order of magnitude: the tree level transition $b \rightarrow u$ and the loop-induced (penguin) transition $b \rightarrow (u, c, t) \rightarrow d, s$. Besides, when there are three or more particles in the final state, resonances decaying through the strong interactions can be formed, enriching even more the dynamics of these processes.

The goal of this thesis is the study of the hadronic charmless B^+ decay into the final state $\pi^+ K^- K^+$. Resonances can appear in the two-body systems formed by $\pi^+ K^-$ and $K^- K^+$ which can interfere potentially producing sizeable CP violation effects. These effects can appear as a difference in the total number of B^+ and B^- decays observed (as an integrated CP asymmetry) as well as within the phase space of the decay - its *Dalitz plot*. The study of these signatures comprise our main interest in this decay.

Our dataset comes from the proton-proton collisions at 7 and 8 TeV collected by the LHCb experiment in 2011 and 2012, respectively. To pursue the CP violation studies in $B^\pm \rightarrow \pi^\pm K^- K^+$ decays a first strategy is to measure the integrated CP asymmetry and to look whether there are specific regions in the Dalitz plot where sizeable asymmetries appear. Then, and representing a more challenging approach, we explore the Dalitz plot through

¹In this work, the CP conjugate processes are implicit and will be explicitly indicated when necessary.

an amplitude analysis to try to identify the resonance substructures and how their interferences lead to potential CP effects. This is the first time such a study is performed.

This thesis has the following structure: In Chapter 2 we present a brief description of the theoretical aspects related to our analysis. In Chapter 3 the LHCb experiment is described. The strategy followed for the event selection of $B^\pm \rightarrow \pi^\pm K^- K^+$ decays is discussed in Chapter 4. In Chapter 5, the results of the model-independent CP violation measurements are presented. In Chapter 6 the formalism used in the amplitude analysis is discussed and the corresponding strategy of implementation is presented. Finally the results are given in Chapter 7 and our conclusions in Chapter 8. There are two Appendices (A and B) dedicated to technical details of the analysis. Additionally, Appendix C discusses the results of a project developed as part of the service work for the LHCb collaboration, which consists of the study of new strategies for the level-0 trigger in the selection of multi-body hadronic decays.

2 Theoretical Fundamentals

2.1 Standard Model

The Standard Model (SM) of particle physics is a gauge theory that describes the fundamental interactions among elementary particles [6] [7], e.g. strong, weak, and electromagnetic interactions¹. The symmetry group on which the Standard Model is based is:

$$SU_c(3) \times SU_L(2) \times U_Y(1). \quad (2-1)$$

$SU_c(3)$ is a non-abelian symmetry group associated to the strong interactions between particles with colour charge. Its corresponding field theory is the Quantum Chromodynamics (QCD). $SU_L(2) \times U_Y(1)$ is the symmetry group associated to the electroweak sector [8, 9, 10], where Y represents the hypercharge given by the Gell-Mann-Nishijima relation:

$$Q = T_3 + Y/2 \quad (2-2)$$

and where Q is the electric charge and T_3 is the third component of the weak isospin. This relation holds for all particles. The fundamental interactions are mediated through spin-1 gauge fields: 8 massless gluons for the strong interactions, 1 massless photon for the electromagnetic interaction and 3 massive bosons W^\pm, Z for the weak interaction.

Elementary particles are classified into two categories in the Standard Model: bosons and fermions. The first category is constituted by the spin 1 gauge bosons described above and by the spin-0 Higgs boson. The Higgs boson is the quantum of the Higgs field, through which, when particles interact with it, they acquire their masses [11, 12]. On the other hand, leptons and quarks are fermions, representing the matter fields. Fermions are classified by generations or families, as shown in Tables 2.1 and 2.2.

$$\begin{matrix} 1^{st} & 2^{nd} & 3^{rd} \\ \begin{pmatrix} u \\ d' \end{pmatrix} & \begin{pmatrix} c \\ s' \end{pmatrix} & \begin{pmatrix} t \\ b' \end{pmatrix} \end{matrix}$$

Table 2.1: Quarks families.

¹The gravitational interaction is not described in the Standard Model.

$$\begin{array}{ccc} 1^{st} & 2^{nd} & 3^{rd} \\ \begin{pmatrix} e \\ \nu_e \end{pmatrix} & \begin{pmatrix} \mu \\ \nu_\mu \end{pmatrix} & \begin{pmatrix} \tau \\ \nu_\tau \end{pmatrix} \end{array}$$

Table 2.2: Leptons families.

$$\begin{pmatrix} \nu_l & q_u \\ l & q_d \end{pmatrix} \equiv \begin{pmatrix} \nu_l \\ l \end{pmatrix}_L, \begin{pmatrix} q_u \\ q_d \end{pmatrix}_L, l_R, q_{uR}, q_{dR},$$

Table 2.3: Left-handed fields transforms as doublet and right-handed fields as singlets of the group $SU_L(2)$.

It is observed that the left-handed² fields transform like doublets of $SU(2)_L$ while their analogous right-handed fields transform like singlets of $SU(2)_L$, see Table 2.3. Notice that the SM does not have right-handed neutrinos. This is a consequence from the fact that the electroweak interaction is a chiral gauge theory that distinguish left and right handedness, as they transform in different representations of the gauge group. In chiral theories there are not mass terms as the gauge is maintained invariant and the coupling occurs only between fermionic fields with same chirality. To explain the “massive” world in which we live, where fermions³ and the gauge bosons, W^\pm, Z have mass, it is necessary to have the coupling between both chiralities (left-handed and right-handed fermionic fields) through a scalar field. This chirality mixing in the SM is described through the Yukawa interaction and where the scalar field corresponds to the Higgs field.

The Higgs field has non-zero vacuum expectation values, in which the vacuum is only invariant under the subgroup $U(1)_{QED}$ of $SU_L(2) \times U_Y(1)$. Thus the symmetry breaking of the gauge in the vacuum gives as a result the spontaneous symmetry breaking:

$$SU_c(3) \times SU_L(2) \times U_Y(1) \rightarrow SU_c(3) \times U_{QED}(1) \quad (2-3)$$

The spontaneous symmetry breaking is responsible for the mass generation of weak bosons, the Higgs boson, fermions and the mixing between families of quarks [13, 14].

2.2

CP Violation in the Standard Model

The differences between matter and antimatter observed in the universe has as one of their main ingredients the violation of the charge-parity (CP)

²Where left-handed or right-handed refers to the chirality of the field.

³Where neutrinos are considered to not have mass.

symmetry, known as CP -Violation [15] [16]. In the Standard Model, this phenomenon is introduced through the mass mixing matrix between the three families of quarks.

Within the framework of Quantum Field Theory the flavour symmetry is explicitly broken by the Yukawa interaction (\mathcal{L}_{Yukawa}). If we write down the Lagrangian for \mathcal{L}_{Yukawa} before the symmetry breaking and take only the hadronic part for the three generations of quarks, it will be given by:

$$\mathcal{L}_{Yukawa} = -Y^d \bar{Q}_L \phi d_R - Y^u \bar{Q}_L \phi^* u_R + h.c., \quad (2-4)$$

where $Y^{u,d}$ are the Yukawa couplings represented by 3×3 complex matrices, Q_L represents the left-handed doublets and u_R, d_R the right-handed singlets, ϕ (ϕ^*) is the field (charge conjugate field) of the Higgs doublet. Under spontaneous symmetry breaking, the mass matrices, which arises as a consequence of the Higgs field having non-zero vacuum expectation values, have the form:

$$M^{u,d} = \frac{v}{\sqrt{2}} Y^{u,d} \quad (2-5)$$

where the $\mathcal{R}e(\phi^0) \rightarrow \frac{v+h^0}{\sqrt{2}}$ (where “0” indicates the electric charge) is substituted in the Yukawa interaction, Equation 2-4, v is the vacuum expectation value and h^0 is the respective component of the real scalar Higgs field. The physical mass states arise when diagonalizing the mass matrices, Equation 2-5, also known as the mass basis. This is performed through the transformation:

$$M_{diag}^{u,d} = U_L^{\dagger(u,d)} Y^{u,d} U_R^{(u,d)} (v/\sqrt{2}), \quad (2-6)$$

where $U_L^{u,d}$ and $U_R^{u,d}$ are unitary matrices. The fermions mass eigenstates and eigenvalues are obtained through the transformation, using this unitary matrices, of the form: $u'_L = U_L^u u_L$, $d'_L = U_L^d d_L$ and $u'_R = U_R^u u_R$, $d'_R = U_R^d d_R$.

It is also obtained the charged current interactions for quarks, after the symmetry breaking, in terms of these eigenstates as:

$$\mathcal{L}_{W^\pm} = \frac{g}{\sqrt{2}} \bar{u}_L \gamma^\mu [(U_L^u)^\dagger (U_L^d)] d_L W_\mu^+ + h.c., \quad (2-7)$$

where the coupling only occurs for left-handed fermionic fields. The combination $V = U_L^{u\dagger} U_L^d$ is a 3×3 unitary matrix known as the Cabibbo-Kobayashi-Maskawa (CKM) matrix. As V is non diagonal, the W^\pm gauge bosons couple to quarks mass eigenstates of different families, and so it represents the mixing matrix for quarks. It is by means of this matrix that the CP -Violation phenomena is introduced in the Standard Model, more details about it will be given in the following sections.

2.3

CP and *CPT* symmetry

Before giving a more detailed explanation about the CKM matrix it would be desirable to have a better insight on the *CP* symmetry.

A symmetry is related to the invariance of a physics system under the influence of a set of transformations. Charge (*C*), Parity (*P*) and Time reversal (*T*) are classified as discrete symmetries as are their combinations *CP* and *CPT*. The parity symmetry represents the physics invariance under a discrete transformation that changes the sign of spatial coordinates. The charge conjugate, that does not have analogous in Classical Mechanics, is related to the existence of an anti-particle for every particle. This was a brilliant prediction within the framework of Relativistic Quantum Mechanics made by Paul Dirac and confirmed afterwards by the discovery of the positron. The time reversal transformation consists of the sign change of the time coordinate.

Individually, *C* and *P* symmetries are violated through weak interactions, but it was believed until 1964 that *CP*, the combined transformation of *C* and *P*, was a symmetry of nature. Cronin and Fitch [17] discovered that this was not the case, when they observed *CP* violation in neutral kaons decays.

The phenomenon of *CP* violation occurs when there is a difference between a decay and its *CP* conjugate process. The so-called direct *CP* violation is due to the difference of the magnitude of the decay amplitude between a particle decaying into a certain final state and the corresponding decay of its antiparticle. In the Standard Model this difference has its origins in the weak phases of the CKM matrix.

The *CPT* theorem [18] establishes that any physics theory must be invariant under the simultaneous transformation of *C*, *P* and *T*; this is a powerful statement with a solid theoretical base derived from the more general properties of Quantum Field Theory. As a result of the *CPT* theorem, the *CP*-violation is equivalent to violation of *T*. An immediate consequence of the *CPT* symmetry is the fact that the mass and the lifetime of a particle and its antiparticle are the same.

2.4

The CKM matrix

The introduction of *CP* violation in the Standard Model was possible through the mixing matrix among the three families of quarks. The physicists Kobayashi and Maskawa [5] proposed the so called CKM matrix, being the most general unitary matrix that describes this mixing:

$$\begin{pmatrix} d' \\ s' \\ b' \end{pmatrix} = \begin{pmatrix} V_{ud} & V_{us} & V_{ub} \\ V_{cd} & V_{cs} & V_{cb} \\ V_{td} & V_{ts} & V_{tb} \end{pmatrix} \begin{pmatrix} d \\ s \\ b \end{pmatrix}, \quad (2-8)$$

The transition probability amplitude between any up-type (u, c, t) and down-type (d, s, b) quarks is described in the CKM matrix as proportional to the matrix element $V_{qq'}$. As was mentioned in Section 2.1, the weak charged currents couple the rotated quark states which can be expressed as:

$$j^\mu = (\bar{u}, \bar{c}, \bar{t}) \gamma^\mu (1 - \gamma^5) V \begin{pmatrix} d \\ s \\ b \end{pmatrix},$$

where V is the CKM matrix. Being unitary, this matrix depends on three real parameters and one complex phase, associated to CP violation. There exist several parametrizations for the CKM matrix; the Wolfenstein parametrization [19] is the most used. It is based on experimental measurements and is expanded in terms of $\lambda = \sin \theta_c$ (≈ 0.225), where θ_c is the Cabibbo angle. It has the following form:

$$V = \begin{pmatrix} 1 - \lambda^2/2 & \lambda & A\lambda^3(\rho - i\eta) \\ -\lambda & 1 - \lambda^2/2 & A\lambda^2 \\ A\lambda^3(1 - \rho - i\eta) & -A\lambda^2 & 1 \end{pmatrix} + O(\lambda^4), \quad (2-9)$$

where η expresses the complex nature of V , responsible for CP violation.

From the condition of unitarity for V , the orthogonality between any two of its columns gives six equations:

$$V_{ud}V_{cd}^* + V_{us}V_{cs}^* + V_{ub}V_{cb}^* = 0, \quad (2-10)$$

$$V_{td}V_{cd}^* + V_{ts}V_{cs}^* + V_{tb}V_{cb}^* = 0, \quad (2-11)$$

$$V_{td}V_{ud}^* + V_{ts}V_{us}^* + V_{tb}V_{ub}^* = 0, \quad (2-12)$$

$$V_{ud}V_{us}^* + V_{cd}V_{cs}^* + V_{td}V_{ts}^* = 0, \quad (2-13)$$

$$V_{us}V_{ub}^* + V_{cs}V_{cb}^* + V_{ts}V_{tb}^* = 0, \quad (2-14)$$

$$V_{ud}V_{ub}^* + V_{cd}V_{cb}^* + V_{td}V_{tb}^* = 0, \quad (2-15)$$

These equations can be represented by triangles in the complex plane. Particularly Equation 2-15 represents a triangle in which its sides have the

same order of magnitude:

$$\begin{aligned} V_{ud}V_{ub}^* + V_{cd}V_{cb}^* + V_{td}V_{tb}^* &= 0 \\ O(\lambda^3) \quad O(\lambda^3) \quad O(\lambda^3) \end{aligned}$$

Normalizing with respect to the real term $V_{cd}V_{cb}^*$, the unitary triangle is shown in Figure 2.1.

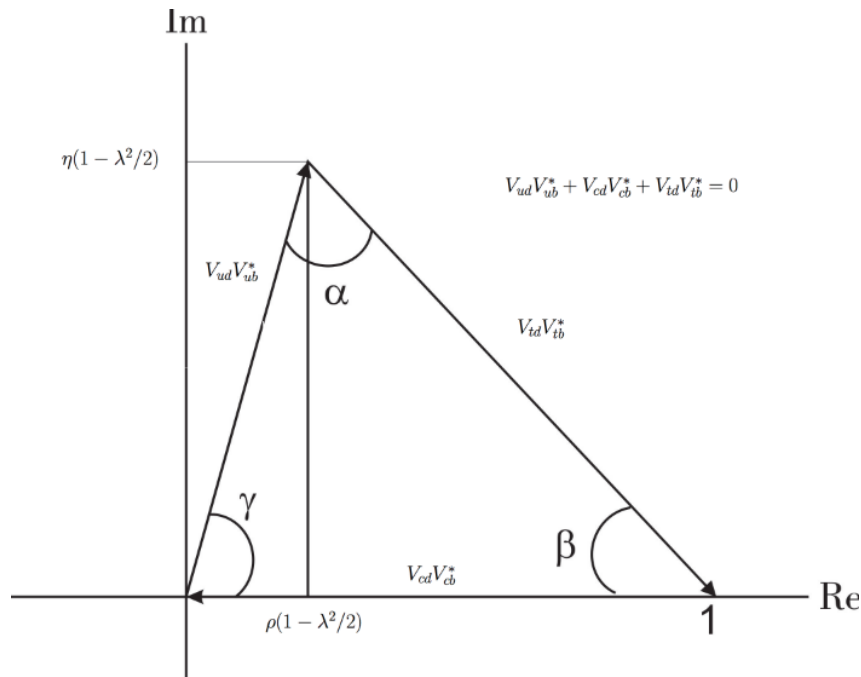


Figure 2.1: CKM unitary triangle given by the Equation 2-15.

The three angles of the unitary triangle, α , β and γ represent, up to $O(\lambda^3)$, the CP violation phenomena in the CKM matrix.

2.5

CP violation mechanism

The CP violation phenomenon occur when there is a difference between a decay and its CP conjugate, which in the SM is associated to the presence of a complex phase in the quark mixing matrix. There are three mechanisms through which CP violation can be observed:

1. Direct CP violation: For charged decays (as B^\pm) this is the only mechanism through which CP violation can happen. This is the case when the magnitude of the decay amplitude of a particle and antiparticle are different [20]:

$$|A| \neq |\bar{A}|$$

Experimentally the observable to which we can access is the square of decay amplitude. This is traduced in the number of events measured for a decay mode. This mean that if there is a difference between the number of events measured for a particle and its CP conjugate, $|A|^2 \neq |\bar{A}|^2$, it would be a clear indication of CP violation in the decay.

2. CP violation by mixing: This is related to the difference in the rate of oscillation between a neutral meson and its antiparticle. Neutral particles evolve in time oscillating between the particle and antiparticle states.
3. CP violation through the interference between decay amplitude and mixing: This is the result of the interference between a decay without mixing and one that has mixing.

In this work, we are concerned with direct CP violation appearing in $B^\pm \rightarrow \pi^\pm K^- K^+$, so emphasis is given on this.

2.6

Three body B decays

The $B^+(u\bar{b})$ meson and its CP conjugate $B^-(\bar{u}b)$, which have a lifetime of $\sim 1,638 \times 10^{-12} s$ and mass of $\sim 5279 \text{ MeV}/c^2$ [1] have gained a lot of attention in the last decades for being a good laboratory in the study of CP violation and for the search of new physics. The different modes through which a B meson can decay are related to the hadronization that occurs together with the weak decay process. A three-body final state can be obtained through two different mechanism; through resonant intermediate states, where a resonance is characterized for being an unstable particle that rapidly decays through strong interaction, or through the spontaneous disintegration into the three final state particles (non-resonant process). The total decay amplitude for a three-body decay can then be expressed as the sum of the partial contributing amplitudes:

$$A_f = \sum_n a_n e^{i(\phi_n + \delta_n)},$$

$$\bar{A}_f = \sum_m a_m e^{i(\phi_m - \delta_m)},$$

where ϕ represents the strong phases and δ the weak phases. Notice that the strong phase is invariant under CP transformation but the weak phase is not.

2.7

The charmless three body decay $B^\pm \rightarrow \pi^\pm K^- K^+$

The charmless B^\pm decay into $\pi^\pm K^- K^+$ is a suppressed decay [21] since it involves transitions of the type $b \rightarrow d$ (penguin amplitude) or $b \rightarrow u$ (tree-level amplitude), both of order λ^3 (see Eq. 2-9) as shown by the Feynman diagrams in Fig. 2.2. The branching fraction for this decay is $(5.0 \pm 0.5 \pm 0.5) \times 10^{-6}$ [1], which experimentally is reflected in the low statistics of events available. As it will be shown later, our analysis has about 5000 events, in contrast, for example, with the statistics available for other charmless B^\pm decays: $B^\pm \rightarrow \pi^\pm \pi^+ \pi^-$ ($\sim 25\text{K}$ events), $B^\pm \rightarrow K^\pm \pi^+ \pi^-$ ($\sim 181\text{K}$ events), $B^\pm \rightarrow K^\pm K^+ K^-$ ($\sim 109\text{K}$ events) [22], also collected by the LHCb experiment.

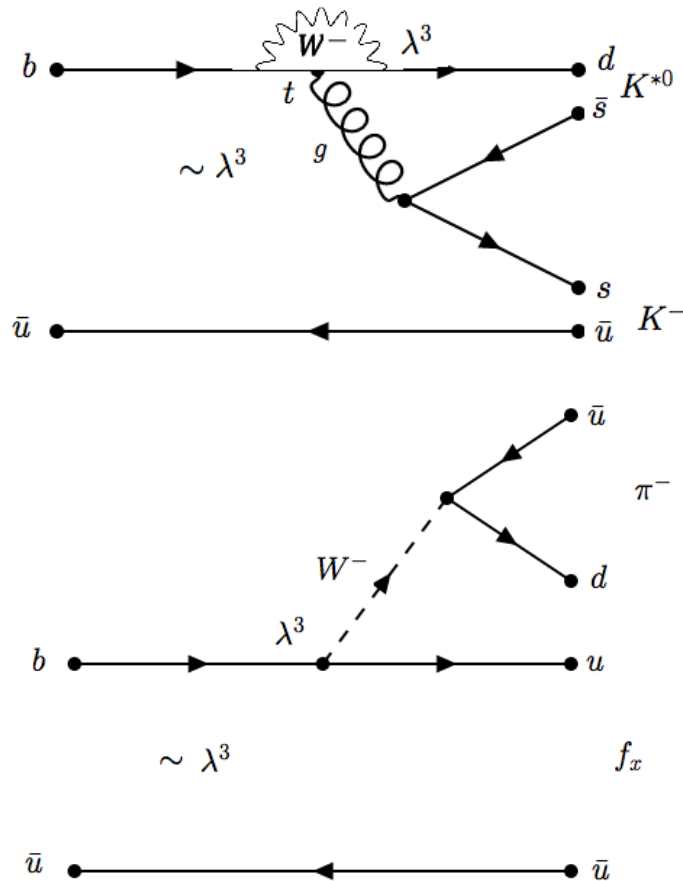


Figure 2.2: Penguin (top) and Tree-level (bottom) diagrams for $B^- \rightarrow \pi^- K^+ K^-$.

From Figure 2.2 (top) we observe that decays of the type $B \rightarrow K^{*0} K$ are dominated by the gluonic penguin diagrams with the transition of quarks $b \rightarrow d$, where K^{*0} is a resonance that rapidly decays into the final state πK . This means that $B^\pm \rightarrow \pi^\pm K^- K^+$ could have then, as resonance contributions, states like $K^{*0}(892)$, $K_0^{*0}(1430)$, $K_2^{*0}(892)$, κ, \dots etc. On the other hand, from

the tree-level diagram (transition $b \rightarrow u$), Figure 2.2 (bottom), we obtain resonant states of the type f_x , which holds for any resonance decaying into two kaons in the final state, such as $f_2(1270)$, $f_0(1370)$, $f_0(980)$,...etc. To know which resonance states are indeed contributing to the $B^\pm \rightarrow \pi^\pm K^- K^+$ decay is one of the main objectives of an amplitude analysis.

From now on the following particle ordering will be used, that for B^+ , will read as:

- π^+ will be referred as d_1 , the first daughter.
- K^- will be referred as d_2 , the second daughter.
- K^+ will be referred as d_3 , the third daughter.

and correspondingly, with opposite charge, for B^- .

Also, if a resonant state is composed by the first and second daughter $\pi^+ K^-$, then the third daughter will be referred as the bachelor. In the same way, if the resonance is composed by the daughter 2 and 3, that is, $K^- K^+$, then the bachelor will be d_1 .

A definition that will be used in the following sections is of the helicity angle (and the cosine of the helicity angle). This is defined as the angle between the bachelor particle and the resonance daughter with equal charge. For example, for the case that a resonance is composed by $\pi^+ K^-$, the helicity angle θ is defined as the angle between the particle d_1 (π^+) and the bachelor d_3 (K^+), measured in the rest frame of the resonance. This is shown in Figure 2.3. Similar reasoning can be followed for the case of a resonance in the $K^- K^+$ system.

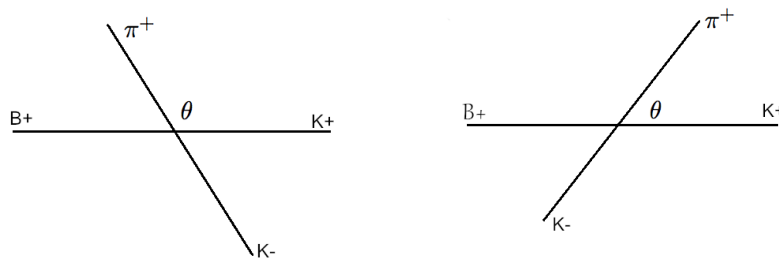


Figure 2.3: $B^+ \rightarrow \pi^+ K^- K^+$ decay for the case that K^+ is the bachelor particle. (left) $\cos \theta < 0$ ($\theta > 0$), (right) $\cos \theta > 0$ ($\theta < 0$).

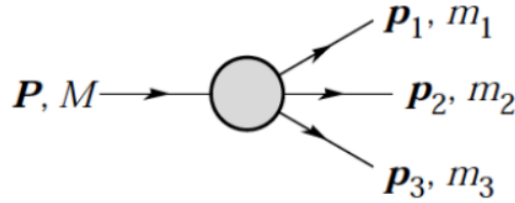


Figure 2.4: A three body decay scheme. Figure extracted from PDG [1].

2.8

Dalitz Plot

The Dalitz plot (DP) [23] is defined as the visual representation of a three-body decay phase space and is described in terms of two independent Lorentz invariant variables. If we consider a three-body decay as pictured in Figure 2.4, in which a particle of mass M and 4-momentum P decays into three spin-0 daughter particles of mass m_i and 4-momentum p_i , this can be easily derived in the following way: having three particles in the final state and so their corresponding 3-momentum vectors, we count $3 \times 3 = 9$ degrees of freedom, considering the 4-momentum conservation of the process (-4 degrees of freedom) and the three Euler's angles (-3 degrees of freedom) with respect to mother reference frame, it can be finally concluded that there are only two independent variables [24].

A set of invariant variables can be constructed using the 4-momentum vectors of the daughter particles, which can be expressed as:

$$\begin{aligned} s_{12}^2 &= (p_1 + p_2)^2 = m_{12}^2 \\ s_{23}^2 &= (p_2 + p_3)^2 = m_{23}^2 \\ s_{31}^2 &= (p_3 + p_1)^2 = m_{31}^2 \end{aligned} \quad (2-16)$$

The physical region of any three-body decay channel can be defined in terms of any two of the three invariant variables in Eq. 2-16, or by any related to these by a linear transformation with constant jacobian, for example any pair of energies E_i^*, E_j^* or any pair of kinetic energies ($T = E - m$) T_i, T_j [25]. For $B^\pm \rightarrow \pi^\pm K^- K^+$ Dalitz plot we use the invariant variables in Equation 2-16, thus the Dalitz plot features that will be discussed below are given using these type of variables.

The boundaries of a Dalitz plot are intrinsically determined by the kinematic of the decay. These are limited by a maximum and a minimum value of m_{ij}^2 , where i and j refers to any pair combination of the daughter particles in the final state, which can be expressed for each invariant axis as:

$$(m_i + m_j)^2 \leq m_{ij}^2 \leq (M - m_k)^2, \quad (2-17)$$

where the $m_{ij}^{min} = (m_i + m_j)^2$ is the square of the sum of the masses of the daughters i and j that are combined to make the system. In this limit the angle between i and j is zero ($\theta_{ij} = 0$) and the angles $\theta_{ik} = \theta_{jk} = \pi$. This results to the $\cos(\theta_{ij}) = 1$. This means that the momenta of the particles i and j are collinear and opposite to the particle k . On the other hand, the maximum limit is obtained when using the mother's mass and by extracting the k daughter's mass, that is when the all the momenta is devoted to the m_{ij} system. In this case the $\theta_{ij} = \pi$ and $\theta_{ik} = \theta_{jk} = 0$ and so the $\cos(\theta_{ij}) = -1$, i.e. the momenta of the particles i and j are collinear and are in opposite direction ($p_i = -p_j$) and the daughter k is at rest ($p_k = 0$).

The decay rate for the process is defined as:

$$d\Gamma = \frac{1}{(2\pi)^5 M^5} \int |\mathcal{A}|^2 \delta^4(p - \sum_{i=1}^3 p_i) \frac{d^4 p_1}{2E_1} \frac{d^4 p_2}{2E_2} d^4 p_3 \delta(p_3^2 - m_3^2), \quad (2-18)$$

where \mathcal{A} is the total decay amplitude and contains any dynamic information related to the process. The contour of the Dalitz plot for three body decays is constrained by the four-dimensional delta function. The one-dimensional delta function corresponds to real (on-shell) particles in the final state. Integrating in $d^3 p_3$ it can be obtained that:

$$d\Gamma = \frac{\pi^2}{2(2\pi)^5 M} \int |\mathcal{A}|^2 \delta_{\cos \theta_{12}} dE_1 dE_2 d\cos \theta_{12}, \quad (2-19)$$

where $\delta_{\cos \theta_{12}}$, determines the angle between the particle 1 and 2, and is defined as:

$$\delta_{\cos \theta_{12}} = \delta(\cos(\theta_{12}) - \frac{M^2 + m_1^2 + m_2^2 + m_3^2 - 2M(E_1 + E_2) + 2E_1 E_2}{2p_1 p_2}) \quad (2-20)$$

Using the energy relations and integrating in the cosine, the decay rate can be written in terms of the Dalitz variables as:

$$d\Gamma = \frac{1}{(2\pi)^3 32M^3} |\mathcal{A}|^2 dm_{12}^2 dm_{23}^2 \quad (2-21)$$

This expression offers a great insight on the potential of the Dalitz plot. The decay rate is directly related to the total decay amplitude \mathcal{A} , meaning that

the dynamic of the reaction is directly reflected by the point distribution in the Dalitz plot, where each point represents an event of the decay $P \rightarrow p_1 + p_2 + p_3$. If \mathcal{A} is constant then the DP will be uniformly populated.

An example of a Dalitz plot is presented on Figure 2.5 where the kinematic limits has been indicated.

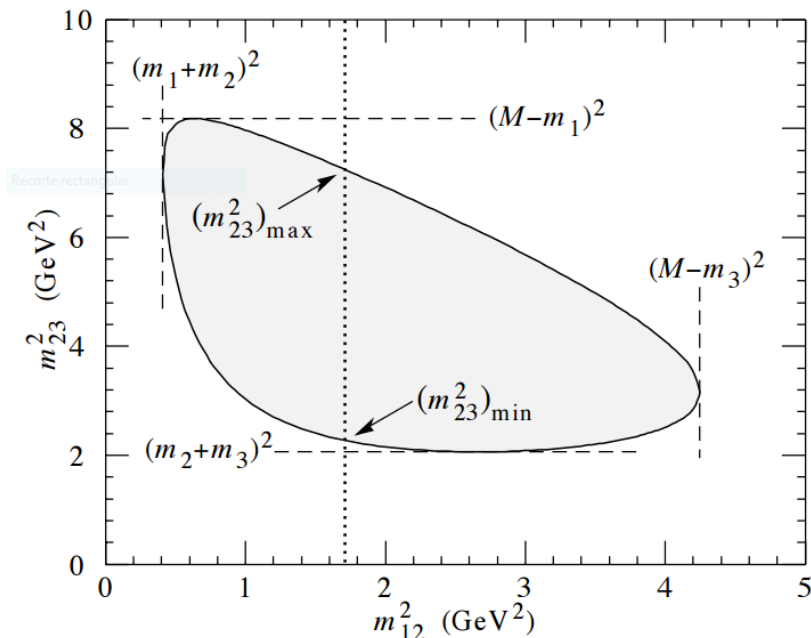


Figure 2.5: Example of the Dalitz plot boundaries for a decay. The sides of the Dalitz represent the variables minima and the corners their maxima. Figure extracted from PDG [1].

The Dalitz plot allows us to visually inspect the interference of the quantum mechanical amplitudes of the final state particles. For a decay that is mainly dominated by intermediate resonance states (see Section 2.6), its Dalitz plot will be populated by bands. Each band will have a certain width with its position determined around a certain value of the squared two-particles invariant mass (the two particles system that conforms the resonance). Then, the band will be perpendicular to the axis that makes the invariant mass of the resonance.

A resonance state can also be identified by the spin signature left in the Dalitz plot. Scalar resonances (spin 0) will appear as broad bands, vector resonance (spin 1) will have two “peaks” and one “valley”, resonances of spin 2 will have three “peaks” and two “valleys” and so on.

The interferences of neighbor resonances, that is, resonances that share the same physical region in the phase space, can be identified by the density of points in the Dalitz. If two bands overlap they can interfere in a constructive or destructive way. If there is constructive interference a high density of

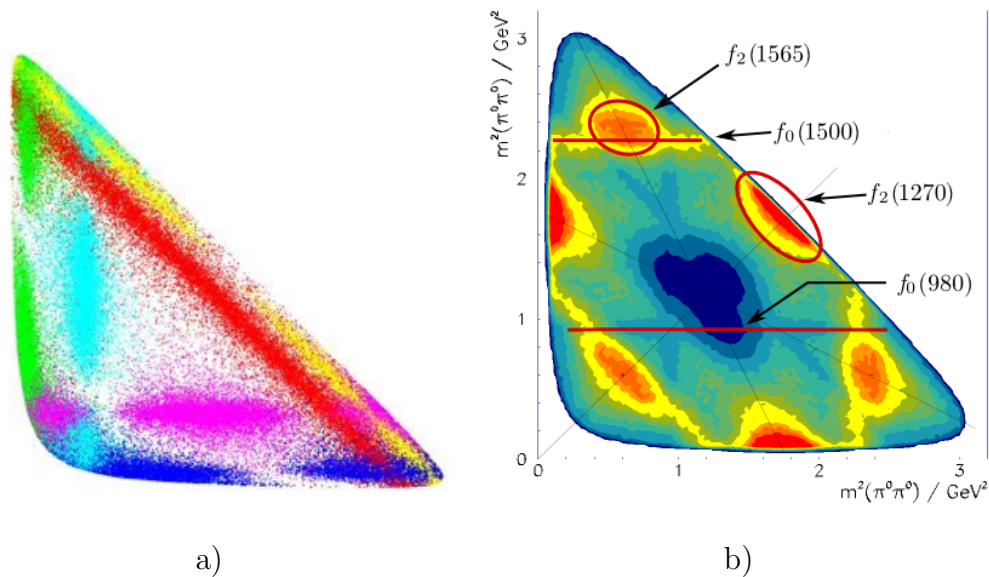


Figure 2.6: a) A cartoon of a DP showing the resonance structures with different spin. b) a Real Dalitz plot obtained in the Crystal Barrel experiment for the decay $p\bar{p} \rightarrow \pi^0\pi^0\pi^0$.

points will be evident as the two square amplitude involved will be added. If there is a destructive interference, the region will be observed with almost no density of points at all. Figure 2.6(a) shows a cartoon of a Dalitz plot where different resonance states with different spins have been depicted. For example the band in blue represents a scalar resonance as it clearly doesn't have an angular distribution. The dark blue resonance at the bottom part of the Dalitz is a resonance of spin 1, and the light blue resonance perpendicular to the horizontal axis has spin 2. Figure 2.6 (b) shows a real Dalitz plot from the Crystal Barrel [26] experiment, where the annihilation of a proton with a antiproton resulted in the production of three π^0 . The different resonance contributions are indicated in the plot. As there are three identical particles in the final state, the dalitz plot is symmetrical with respect to any axis.

2.9

The Square Dalitz plot

As it was just indicated, the resonant sub-structure of a decay can be revealed through their signatures in the Dalitz plot. The interference among the resonant states are responsible for rich structures, being these of great interest in order to understand the dynamic involved in a decay mode and the scope for an amplitude analysis. Some phenomena, like CP violation, are fully understood only when the dynamic of the decay mode is well known.

B^\pm mesons decaying into charmless three body final states are characterised for having a Dalitz plot that is dominated by resonant states near its

kinematic boundaries. These intermediate states decay into two light mesons. These are regions with high sensitivity, in which high variations occur in a very small area. In order to avoid losing information, one can alternatively apply a variable transformation to the standard Dalitz plot variables:

$$dm_{12}^2 dm_{23}^2 \rightarrow |det J| dm' d\theta', \quad (2-22)$$

where m_{12}^2 and m_{23}^2 are the Dalitz plot variables, J is the jacobian of the transformation. The new variables are defined as [27]:

$$\begin{aligned} m' &\equiv \frac{1}{\pi} \arccos \left(2 \frac{m_{12} - m_{12}^{min}}{m_{12}^{max} + m_{12}^{min}} - 1 \right) \\ \theta' &\equiv \frac{1}{\pi} \theta_{12} \end{aligned} \quad (2-23)$$

θ_{12} is the helicity angle of the “12” system (angle between the bachelor particle “3” and one of the resonance particles in the rest frame of R) and m_{12}^{min} and m_{12}^{max} are the kinematics limits of m_{12} .

The general form for the Jacobian of transformation is given by:

$$|det J| = 4 |P_2^*| |P_3^*| m_{12} \frac{\partial m_{12}}{\partial m'} \frac{\partial \cos \theta_{12}}{\partial \theta'} \quad (2-24)$$

These transformations translate the Dalitz plot into a rectangle plane denoted as the square Dalitz Plot (SDP) [27] and the variables defined in Eq. 2-23 are called the square Dalitz variables. By such transformation the curved edges of the boundaries are avoided, which is one of the advantages when constructing the efficiency model for the amplitude analysis. The square variables put more emphasize to regions where the events density is higher and so allowing a more easy parametrization. Figure 2.7 shows the Jacobian determinant of transformations that would be obtained if the nominal Dalitz plot were evenly populated.

2.10

The phase space for $B^\pm \rightarrow \pi^\pm K^- K^+$

The two Dalitz plot variables that were chosen for $B^\pm \rightarrow \pi^\pm K^- K^+$ are those where the resonance contributions are expected. The particle ordering on this decays is as indicated in Section 2.7, the first daughter corresponds to π^\pm , the second to K^\mp , and the third one to K^\pm . Since it is not expected any resonant contribution in the $K^+ \pi^+$ (and $K^- \pi^-$) pair, the two independent variables used⁴ are $m_{\pi^\pm K^\mp}^2$ and $m_{K^- K^+}^2$. Using the $B^\pm \rightarrow \pi^\pm K^- K^+$ data

⁴ $m_{K^\mp K^\pm}^2$ will be expressed as $m_{K^- K^+}^2$ indistinctly for B^+ and B^- .

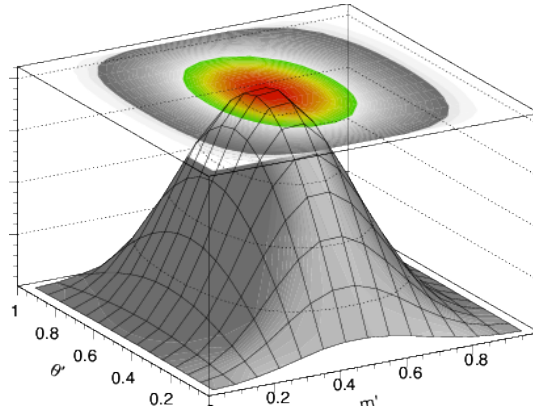


Figure 2.7: Jacobian determinant of transformations that would be obtained if the nominal Dalitz plot were evenly populated.

sample, after all the selection criteria applied (which will be explained in Section 4.3), the Dalitz plot for $B^\pm \rightarrow \pi^\pm K^- K^+$ is shown in Figure 2.8, where the horizontal axis corresponds to the $\pi^\pm K^\mp$ system and the vertical axis to the $K^- K^+$ system. It can be seen, as anticipated, that the resonance contributions are mainly located at low mass, occupying a relatively small region if compared to the large central region of the Dalitz where non resonant structures are observed. As will be explained in Section 6.4 this large region is mostly populated by random events that happened to be triggered as $B^\pm \rightarrow \pi^\pm K^- K^+$ candidate but in fact are source of the combinatorial background and from the non-resonant contribution.

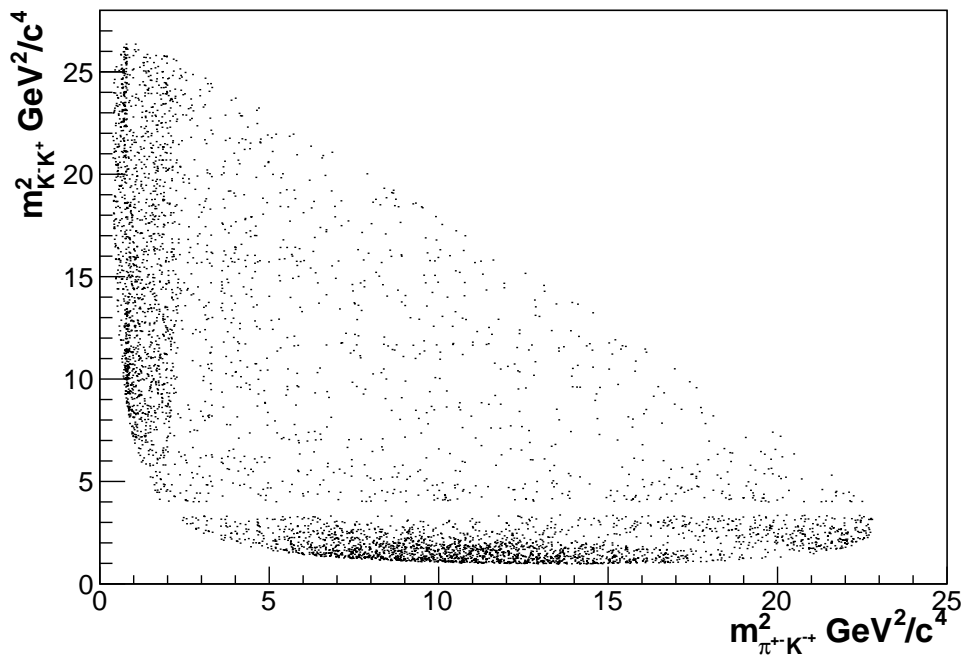


Figure 2.8: $B^\pm \rightarrow \pi^\pm K^- K^+$ Dalitz plot.

Also two straight bands with no events can be notice on each axis. These correspond to the veto of the charm contributions $\bar{D}^0 \rightarrow \pi^\pm K^\mp$ and $\bar{D}^0 \rightarrow K^- K^+$. More details will be given in Section 4.3.

The $B^\pm \rightarrow \pi^\pm K^- K^+$ Dalitz plot shows strong patterns of interferences. The most prominent pattern is the slice with almost no event located at high mass in the horizontal axis $\sim 13 \text{ GeV}^2/c^4 < m_{\pi^\pm K^\mp}^2 < 20 \text{ GeV}^2/c^4$. Which resonances are contributing in both $K^- K^+$ and $\pi^\pm K^\mp$ systems, how are they interfering with each other, and how CP violation emerges in this scenario, are questions to be answered. This calls for the necessity of an amplitude analysis of this decay. By qualitative inspection of the Dalitz plots, at low mass, in the pair $\pi^\pm K^\mp$, the signature of the resonance $K^{*0}(892)$ seems to be appearing very close to the border. Its mass resonance is located by the $K^{*0}(892)$ mass central value ($m_{K^{*0}(892)}^2 \sim 0.801 [\text{GeV}/c^2]^2$) and also has two lobes revealing a spin 1 distribution. Another contribution for the $\pi^\pm K^\mp$ system is a broad resonance that is interfering with $K^{*0}(892)$, it has spin 0 and its mass is consistent with the resonance $K_0^{*0}(1430)$.

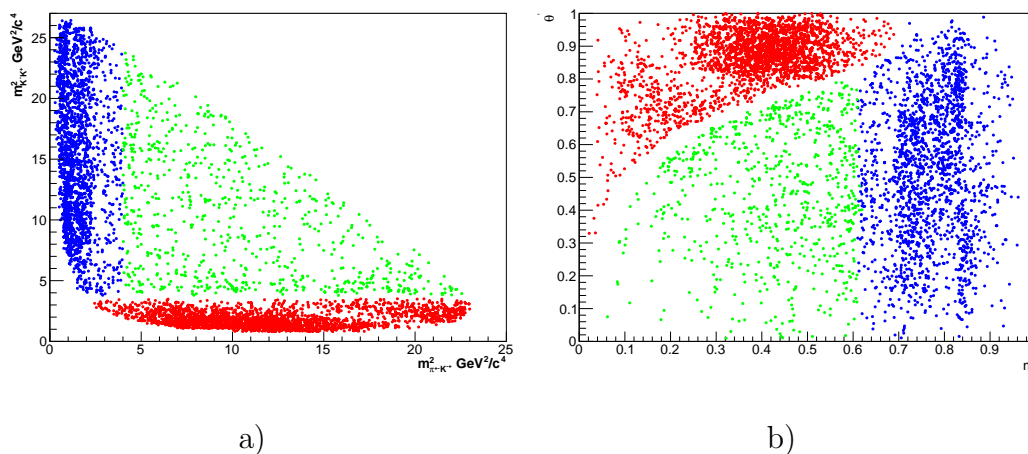


Figure 2.9: Dalitz Plot for $B^\pm \rightarrow \pi^\pm K^- K^+$ decay using the nominal variables $m_{\pi^\pm K^\mp}^2$ and $m_{K^- K^+}^2$ 2.9(a) and the square variables m' and θ' 2.9(b). The Dalitz plot distribution has been highlighted in different colors in order to show how the different regions transform into the SDP.

The square Dalitz plot variables for $B^\pm \rightarrow \pi^\pm K^- K^+$ are constructed taking m_{12}^2 as $m_{\pi^\pm K^\mp}^2$. The resonance locations in the Square Dalitz is not so intuitive as in the nominal Dalitz. Small regions can be enlarged and the curved borders no longer exist, resulting that some regions usually appear like a ‘‘S’’ shape in the SDP. For this reason, on this analysis the SDP only will be used to compute the efficiency and background models that will be used later in the Dalitz plot fit. In Figure 2.9(a) the nominal Dalitz plot has been projected

with some regions being highlighted in different colors, while in Figure 2.9(b) the corresponding Square Dalitz plot is shown, so we can see how the mapping of the distribution occurs.

3

The LHCb Experiment

3.1

The Large Hadron Collider (LHC)

The Large Hadron Collider (LHC) [28] is the largest accelerator and particle collider ever built. It is located at CERN, in the border between France and Switzerland, near Geneva. It was constructed with the objective to collide high-energy particle beams that travel close to the speed of light in opposite directions, in two 27 kilometers superconducting rings at an underground depth between 45 to 170 meters.

The beams travel in the LHC in ultrahigh vacuum, at a temperature of -271°C . These are guided, around the rings, by a strong magnetic field produced by superconducting magnets; 1232 dipole magnets are used to direct the beams and 392 quadrupole magnets are used to focus.

The LHC was projected, in their nominal configuration, to collide beams of protons at $\sqrt{s} = 14$ TeV in the center-of-mass energy, with a luminosity of $\mathcal{L} = 10^{34} \text{ cm}^{-2} \text{ s}^{-1}$. To met this objective, the accelerator was projected to be filled with 2802 bunch of protons, with 1.1×10^{11} protons per bunch in each beam, and with a beam crossing every 25 ns.

The detectors of the four main experiments, each one designed with different purposes, are located in different interaction points. When the desired energy is met and the beams collide, the detectors of these experiments, that works simultaneously, start their data recording. An schematic view is presented on Figure 3.1

These experiment are:

ALICE (A Large Ion Collider Experiment) [29]. The detector of the ALICE experiment was designed to study collision of heavy-ions (Pb–Pb or p –Pb). These collisions recreates conditions very similar to those just after the big bang, in which matter passes to a quark-gluon plasma state and where quarks are not in confinement. The study of the quark-gluon plasma is of great interest in Quantum Chromodynamics (QCD) theory, in order to understand the confinement phenomena and the the chiral-symmetry restoration.

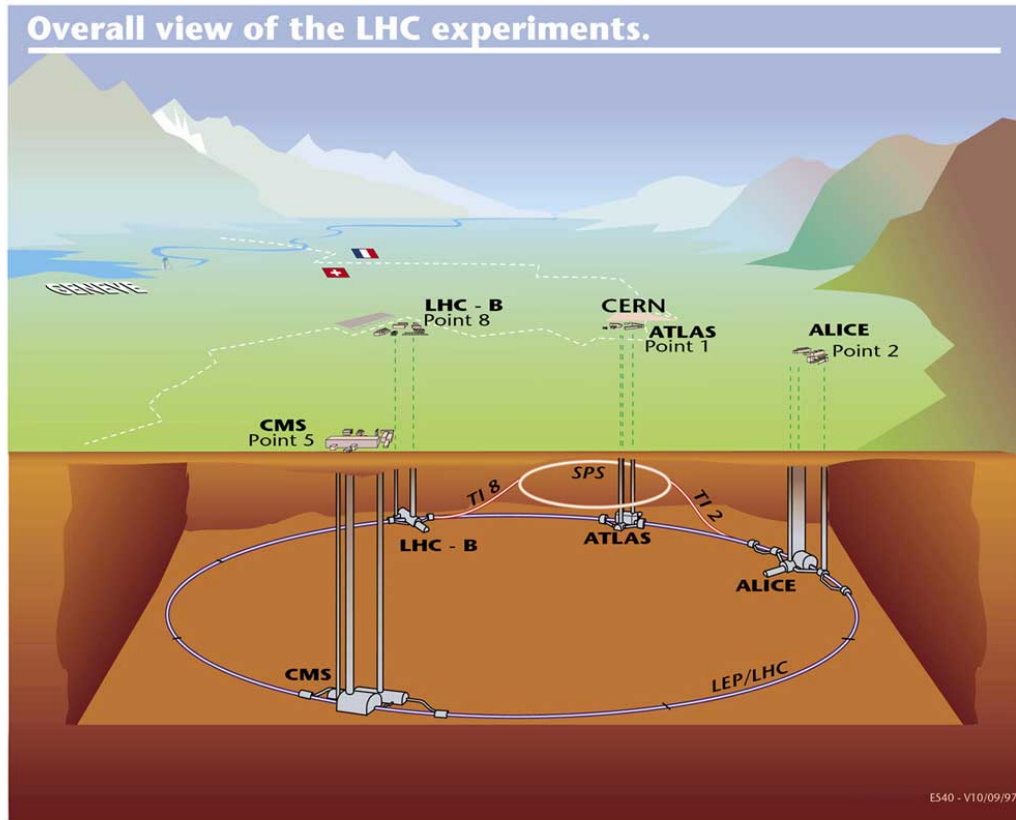


Figure 3.1: Pictorial view of the localization of the LHC experiments and their interaction points.

ATLAS (A toroidal LHC apparatus)[30]. This is one of the two experiments at LHC that have as an objective the study of a wide range of physics. One of these was the search for the Higgs boson, which represents the most important discovery of the last decades.

CMS (Compact Muon Solenoid) [31]. This experiment has also general purposes, like ATLAS, but uses a different operating strategy. Uses complementary detection, especially related to the magnet and muon system.

LHCb (Large Hadron Collider Beauty) [32]. The LHCb experiment has as an objective the study of CP violation phenomena and rare decays in heavy hadrons, that is, mesons and baryons with b and c in their quark content. The study of CP violation will allow us to investigate the difference between matter and antimatter observed in the universe.

3.2 The LHCb detector

The LHCb detector [33] is a single-arm forward spectrometer projected to highly efficiently detect beauty and charm hadrons, in order to perform precision measurements of CP violation and rare decays. In high energies, the production of b and \bar{b} (or c and \bar{c})—quarks have an angular distribution close to the beam pipe, see Fig. 3.2, and with the feature that both tracks are predominantly produced in the same forward or backward direction. As a consequence, the resulting pair of B or D hadrons appears in the same hemisphere. The detector has an angular acceptance that spans polar angles from 15 mrad to 300 mrad in the horizontal bending plane, and from 10 mrad to 250 mrad in the vertical non-bending plane, equivalent to a pseudorapidity of $1.9 < \eta < 4.9$. Thus, the geometry of the detector was chosen with the objective of optimize the quantity of particles reconstructed in this angular acceptance. The reference system adopted is such that the z axis is in the beam direction, the x axis in the horizontal plane and the y axis in the vertical plane. The LHCb detector is shown on Fig. 3.3

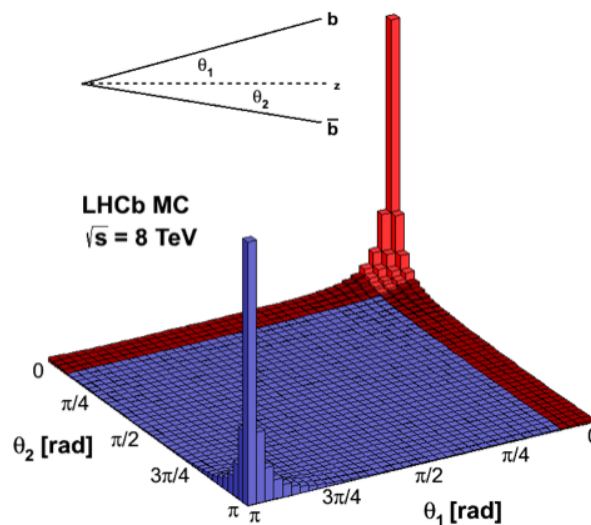


Figure 3.2: Simulation of the angular distribution for the pair $b\bar{b}$ as produced in the LHC ($\sqrt{s} = 8$ TeV)

In order to fully explore B and D decays, the LHCb uses a series of subdetectors each one with different purposes. The first subdetector is located at the interaction point, and the others subsequently located up to an extension of 20 m. In order to perform precision measurements, these subdetectors must be able to provide the following information: a good precision in the track and vertex reconstruction of mesons B and D , where the point in which the particles are created is called the primary vertex and the point where they

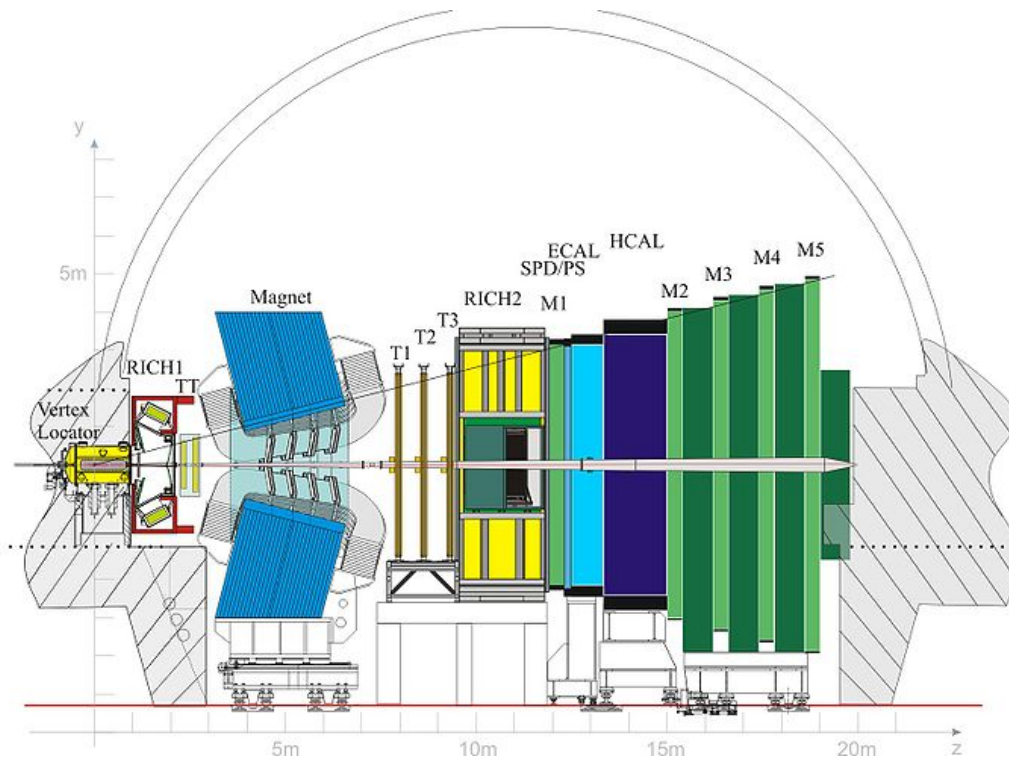


Figure 3.3: Lateral view of the LHCb spectrometer. The subdetectors are explicitly indicated.

decay the secondary vertex; an extremely good identification of the particle in the final states, which is fundamental for the study of specific decay channels; an excellent mass resolution and high precision momentum measurements. A trigger system, fast and flexible, but with a high efficiency in separating the events of interest for a large variety of final states.

The LHCb projected nominal luminosity is of $\mathcal{L} = 2 \times 10^{32} \text{ cm}^{-2} \text{ s}^{-1}$, which is lower than for the other experiments. This luminosity was envisioned in order to maintain the good performance of the detectors, more details will be given in Section 3.3.

In the following each subdetector will be described.

3.2.1 The VERtex LOcator (VELO)]

The VELO [34] is located surrounding the pp interaction region and provides precise information about the coordinates of tracks, that are left by the particles produced in the primary vertex. These coordinates are used in the reconstruction and localization of the secondary vertex. The distance between the primary and secondary vertices is an important characteristic that allows to distinguish beauty and charm hadrons, as their lifetime are long compared to

the decays driven by strong or electromagnetic interactions. This characteristic form the basis of many trigger decisions

The VELO consists of 21 half-moon silicon strip modulus, with two identical sides, disposed perpendicularly to beam around the LHCb interaction point. Each modulus has a R - sensor and a ϕ - sensor as shown in Fig. 3.4.

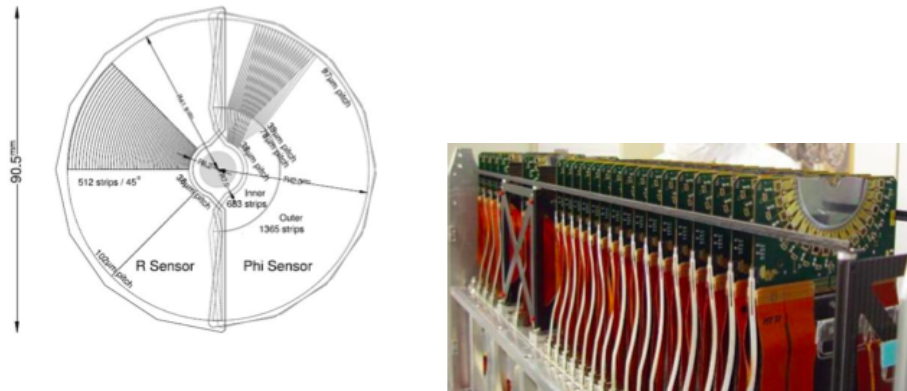


Figure 3.4: (left) Representation of the R - sensor and ϕ - sensor. (right) A picture of the VELO modulus in the LHCb.

Each modulus was designed to provide 3D spatial information for the reconstruction of tracks and vertices. The ϕ -sensor gives information about the azimuthal coordinate in the beam direction and the R - sensor gives information about the radial coordinate. The z coordinate is obtained through the position of each modulus in the experiment. The spatial resolution for the reconstruction of the primary vertex is of $40\mu\text{m}$ in the z axis and $10\mu\text{m}$ in the ϕ direction and of $150\mu\text{m}$ and $300\mu\text{m}$, respectively for the secondary vertex. The geometry of the VELO is such that the modulus are separated by few centimeters of distance in the z axis, this with the finality of their superposition and thus to avoid idle detection regions.

3.2.2 The Magnet

The magnet [35], together with the tracking system used in the experiment, consists of a dipole magnet that allows measurements of charge and momentum of charged particles. Covers an angular distance of ± 250 mrad in the vertical acceptance and of ± 300 mrad in the horizontal acceptance. The two coils have a trapezoidal shape and are bent at 45° , they produce an integrated field of 4 Tm for trajectory of particles with 10 m in length.

The polarity of the magnet can be inverted, allowing the data taking either when the field is pointing up (“MagUp”) or pointing down (“MagDown”).

This allows the study and lower values of the systematics errors in a variety measurements. An schematic view of the magnet is shown in Figure 3.5.

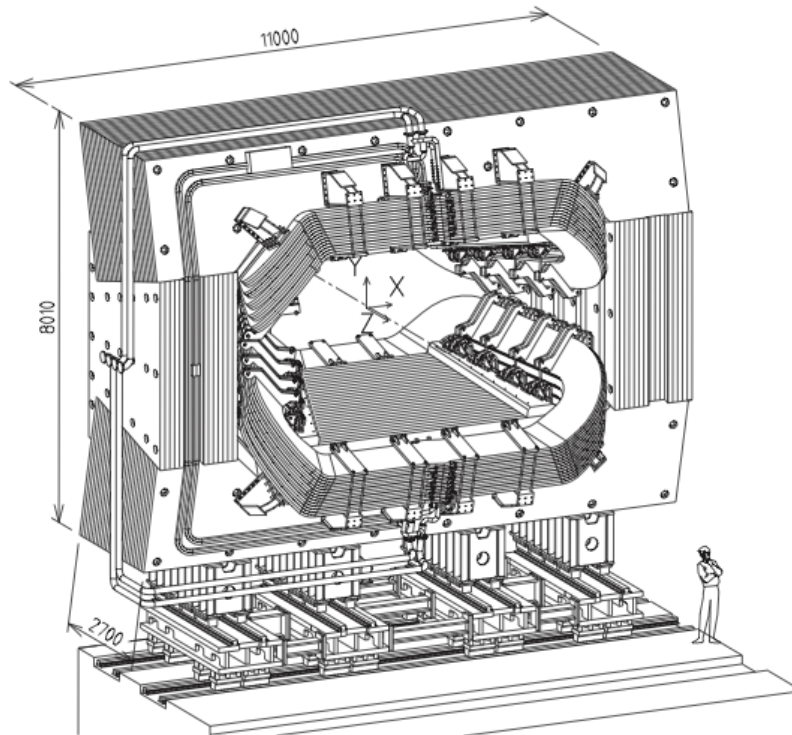


Figure 3.5: Schematic view of the LHCb experiment magnet.

3.2.3 Tracking System

The tracking system [36] which is composed by the VELO and four tracking stations, provides information about the trajectories of charged particles, and thus allowing their reconstruction and of the displaced vertices. As mentioned before, the VELO is located around the interaction point. The tracking stations can be divided into two groups: the Tracker Turicensis (TT) stations located before the magnet; and a three stations $T_1 - T_3$ located downstream the magnet, which are divided into two regions: an inner region (IT) [37] and outer one (OT) [38]. The description of these stations is presented in the following.

Tracker Turicensis (TT)

The Tracker Turicensis is located between the RICH1 detector and the LHCb magnet and is constituted by two stations. Its main objective is to provide information about tracks with low momentum. The TT stations covers a rectangular area of about 120 cm in height and 150 cm in width. Each station is composed of four layers of silicon sensors, where each sensor has dimensions

of 9.64 cm wide, 9.44 cm long and $500 \mu\text{m}$ thick. In total there are 512 silicon microstrips. The four layers are arranged in a geometry “ $x-u-v-x'$ ”, that is, the x layer aligned vertically with the y axis, while the layer u has a rotation of -5° and the v layer of 5° respect to y axis. Each sensor has a precision of $50 \mu\text{m}$ in the position measurement. An schematic view is shown in Fig. 3.6.

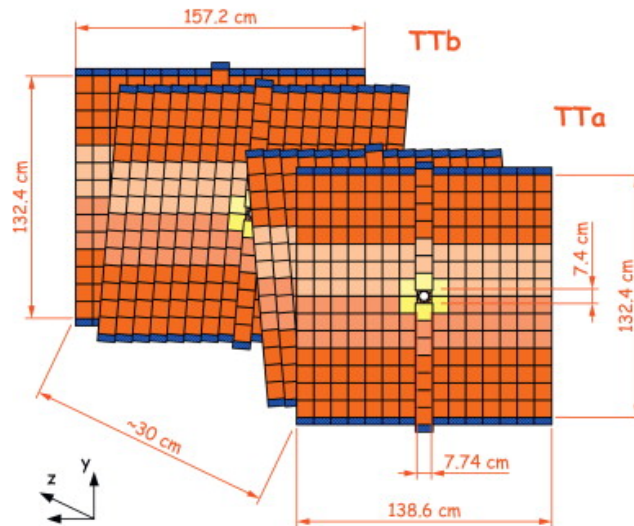


Figure 3.6: Schematic view of the four layers of the Tracker Turicensis stations.

Inner Tracker (IT)

The Inner Tracker sensors are located in the tracking stations $T_1 - T_3$ and covers a cross-shaped area around the beam pipe. Each of the three IT stations have four individual boxes arranged around the beam axis, and each box has four silicon layers, with the same geometry as the TT, $x-u-v-x$. The upper and lower boxes have seven modules, and in each module a single sensor. This is shown in Figs. 3.7(a) and 3.7(b). The lateral boxes also contain seven modules, each one with two sensors. These sensors are 7.6 cm wide, 11 cm long and with $320 \mu\text{m}$ thick for the upper and lower modules, $420 \mu\text{m}$ thick for the laterals ones. In total is composed by 384 silicon microstrip. The resolution on the position is a little greater than $50 \mu\text{m}$.

Outer Tracker

The outer regions of the tracking stations $T_1 - T_3$ are composed by a straw-tube detector (OT) [39]. In these regions, the flux of particles is lower than in the IT stations and so do have lower occupancy. They are also responsible in the determination of the trajectories of charged particles, and together with the magnet information is possible to determine their

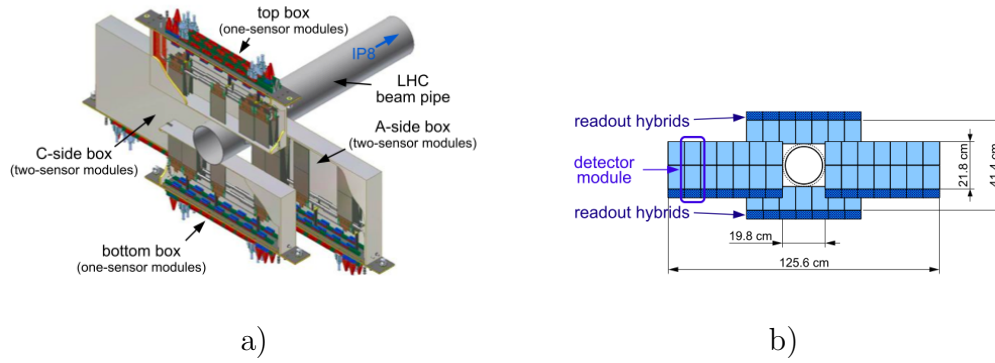


Figure 3.7: (a) View of the position of the four boxes of a IT station arranged around the beam pipe. (b) Frontal view where it can be seen the detector modules.

momentum. The OT stations consists of four layers with 4608 of cylindrical straw-tube. These layers also have a geometry $x-u-v-x$ as in the IT and TT stations. The tubes are filled with a gas mixture of Ar (70%), CO_2 (28.5%) and O_2 (1.5 %) and do have an inner diameter of 4.9 mm. When charged particles pass through the straw tubes ionise the gas along their trajectory. These chambers provides a drift-time below that 50 ns and a resolution of 200 μm . Schematics view of the OT detector is shown in Fig. 3.8

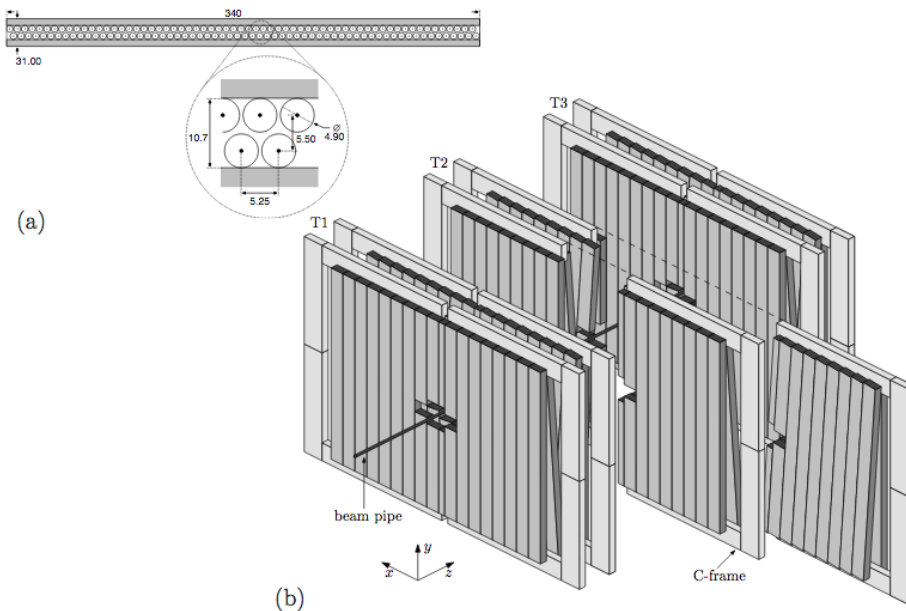


Figure 3.8: a) Cross section of a module. b) View of the OT straw-tube detector four layers in the $T_1 - T_3$ stations.

Tracks reconstruction

The reconstruction of the trajectories left by the particles in their path through the detectors, is performed through a software that combines all the information just described. A typical event in the LHCb contains about 100 tracks.

The fit algorithm used by the LHCb is based on the method of “Kalman-Filter”. This algorithm updates progressively the information of the fit, thus increasing the knowledge of the trajectory, without the necessity of performing the whole fit all over again. This is one of the advantages of the “Kalman-Filter” method. The quality of the tracks is monitored by the fit χ^2 .

There exists five types of reconstructed tracks in LHCb, which can be classified in:

1. VELO tracks: These are tracks the only pass through the VELO and then exit the detector acceptance.
2. Upstream track: These are reconstructed tracks that only pass through the VELO and TT.
3. Downstream tracks: These are reconstructed tracks that only pass through the TT and T_1-T_3 stations, in general this tracks correspond to particle that decays outside the VELO.
4. Long tracks: Are tracks that were reconstructed using the information of all the detectors (VELO, TT, T_1-T_3), and thus have a good resolution.
5. T tracks: these are the products of secondary interactions, reconstructed only using the information os the T_1-T_3 stations.

The five types of tracks are shown in Fig. 3.9

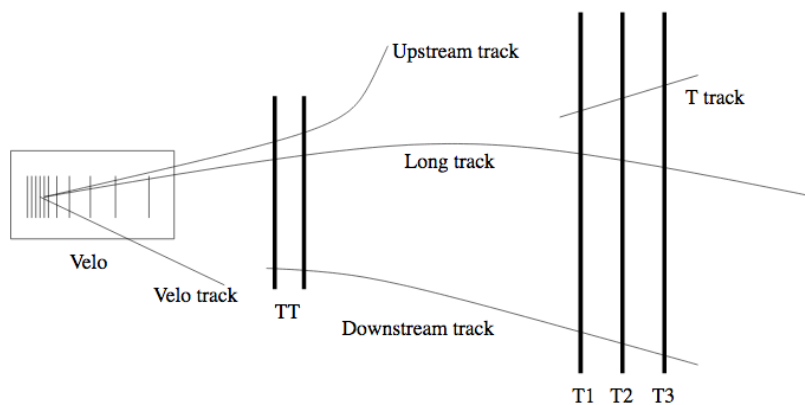


Figure 3.9: Representation of the five types of tracks reconstructed in the LHCb.

3.2.4 Ring-Imaging Cherenkov (RICH) system

The identification of particles like, pions, kaons, protons, electrons and muons is one the fundamental characteristics of the LHCb. The correct separation between pions and kaons is of particular importance in the study of beauty and charm hadrons. The LHCb have three subdetectors dedicated to the particle identification: two RICH stations [40] [41] in association with the tracking system, have as objective the particle identification; the muon stations that identifies muons; and the calorimeters that provide measurements of the energy deposited by the particles and identifies neutral particles.

For the particle identification, the RICH uses the Cherenkov radiation. When a charged particle propagates in a dielectric medium, with a velocity greater than the speed of light in that medium, it emits radiation. The emission of these Cherenkov photons form a cone with an angle θ_c with respect to the trajectory. This angle is given by:

$$\cos \theta_c = \frac{1}{vn}, \quad (3-1)$$

where v is the velocity of the particle, n is the refraction index in that medium and θ_c is the Cherenkov angle. The particle identification is performed with the combination of the momentum measurement associated to the track and the velocity of the particle. In order to cover the whole range of the momentum spectra of the charged particles, the first station, the RICH1, is located between the VELO and the TT. The second station, the RICH2, is located between the T₃ station and the muons stations.

The RICH1 was projected for the detection of particles with low momenta (2-60 GeV), that have the characteristics to emerge with large polar angles. It is composed by air gel radiators SiO₂ with $n = 1.03$ and C₄F₁₀ with $n = 1.0014$. The RICH2 was projected on the other hand to the detection of particles with high momentum (15-100 GeV), that emerges with small angles; it has only one radiator gas CF₄ with $n = 1.005$. For both detectors RICH, the Cherenkov light is focussed in the detectors of hybrid photons (FPD), using a combination of spherical (RICH1) and flat (RICH2) mirrors. A lateral view if the RICH1 and RICH2 is shown in Fig. 3.10.

3.2.5 Calorimeters

The calorimeters system of the LHCb [42] [43] has the following functionalities: provides the identification of electrons, photons and hadrons as of measurements in their position and energy; they make the selection of the trans-

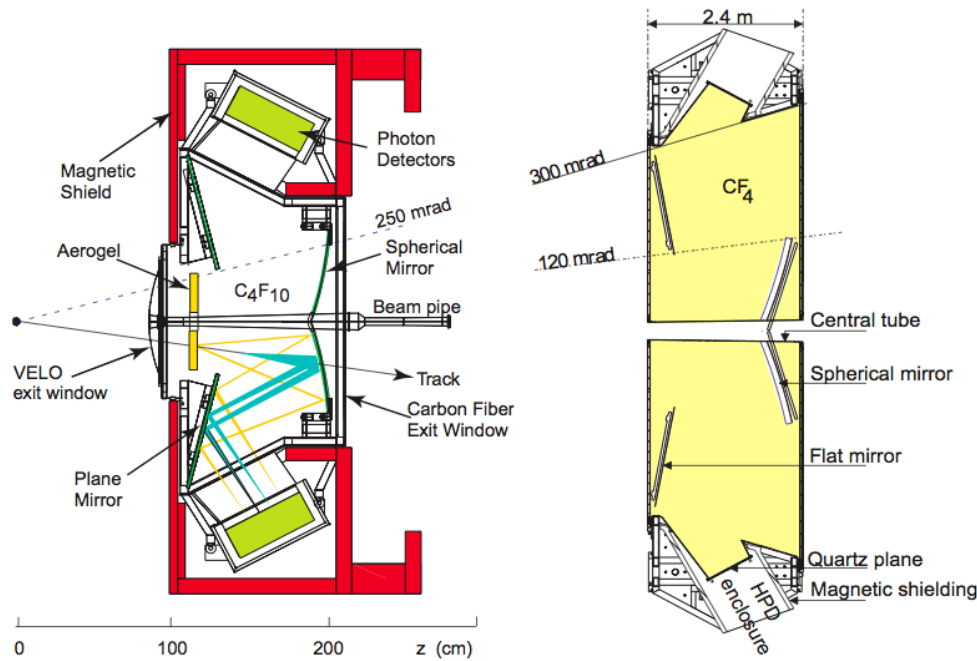


Figure 3.10: Schematic view of the RICH detectors.

verse energy of hadrons and of electrons and photons candidates that is used in the first trigger level (L0), which make a decision $4 \mu\text{m}$ after the interaction event. The system is constituted by an electromagnetic calorimeter (ECAL), a hadronic calorimeter (HCAL) and of two stations SPD/PD.

The calorimeters perform the measurements of the total energy deposited in the medium when this is transversed by a particle. The particle, after a certain distance X_0 (radiation wave length), produce new particles with lower energy. This effect is called shower. With the calorimeters well calibrated, it is possible to determine the energy of the particle responsible for the shower. The passage of the produced particles through the scintillators generates photons that can be collected by the photomultiplier tubes.

The SPD and PS detectors help in the identification of particles. The SPD (Scintillator Pad Detector) helps in the rejection of electrons with high transverse momentum in neutral pions decays, being its principal function the discrimination of the resulting e^- and γ shower. The PD (Preshower Detector), on the other hand rejects the background due to charge pions. The detectors SPD and PS are localized before the ECAL, separated by a lead sheet of 15 mm, both systems consist of two scintillator plates.

The ECAL has as objective the measurement of the energy of electrons and photons and to perform the reconstruction of π^0 . It is composed by a sheet of lead of 2 mm, a scintillator plate of 4mm and of a white layer to avoid

reflection in the scintillator. The energy resolution is a function of the particle energy and it is given by $10\%/\sqrt{E} \otimes 1\%$

The HCAL has as objective the measurement of the energy of protons, neutrons, pions and kaons. Its operating principle is the same as of the ECAL, with the difference that the hadronic showers are determined by λ (the interaction nuclear length) which is greater than the radiation length. For that reason, the HCAL is more dense than the ECAL, intercalating scintillator plates of 4 mm and iron plates of 16 mm. The energy resolution is of $80\%/\sqrt{E} \otimes 10\%$

3.2.6

The muons system

The muon system [44, 45] [46] has as objective the offline identification of muons and to provide information to muon trigger. It is composed of five stations (M1-M5). The station M1 is located before the calorimeter, to increase the precision in the measurement of the linear momentum of the muons identified in the trigger; the stations M2-M5 are positioned at the end of the spectrometer, where only muons are able to reach. To avoid any background from hadrons, the four stations M2-M5 are intercalated with iron filters. Due to different pile-up, the muon chambers are divided into four regions: R1-R4. A lateral schematic view of the muon system is shown in Fig. 3.11. Two technologies are used in the detector: Multi Wire Proportional Chamber (MWPC), predominantly used in all the stations and, in the region R1 of the station M1, the Gas Electron Multiplier (GEM).

The MWPC is constituted by a gas mixture of Ar, CO₂ and CF₄. This chamber when is transversed by a muon, will produce an electron shower. These electrons are taken to the anode, producing an electric signal. The ions are taken to the cathode. The GEM is composed also by a gas mixture of Ar, CO₂ and CF₄ and has three metal layers with a high density of holes, intercalated between the cathode and anode, submitted to high voltage. The ionized electrons are multiplied and collected by the holes.

Trigger

The bunch crossing frequency of the LHC is of 40 MHz. This is translated to a frequency of visible interaction per bunch crossing of 10 MHz in the LHCb spectrometer. This high rate cannot all be written to storage, given the limited capacity of the computer farm. In this sense, the trigger system [47], must be able to reduce this rate to a value of the order of few KHz while, in the

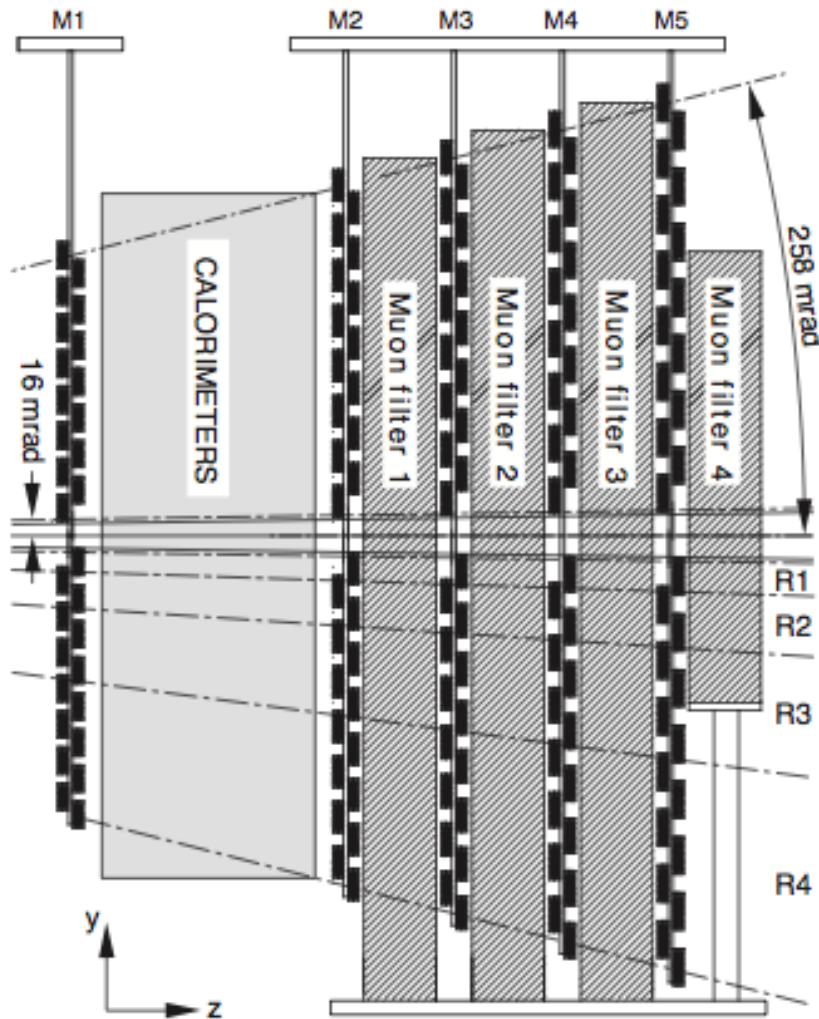


Figure 3.11: Lateral view of the stations the form muon system M1-M5. The regions R1-R4 are also shown

other hand, selecting only interesting events. To this end, the trigger is divided into two levels: the *L0-level* (L0) and the *High level trigger* (HLT) [3] [48].

The L0 level trigger is implemented in hardware and reduces the event rate to 1.1 MHz. At this rate the whole LHCb detector can be read out. The L0 trigger selects electrons, photons and hadrons with high transverse energy and high transverse momentum muons. It uses the informations provided by the electromagnetic and hadronic calorimeters and from the muon chambers. These information are processed by a L0 decision center, L0DU (L0 Decision Unit), where an event is approved or not. The L0 decision is made $4 \mu\text{s}$ after beam crossing, also called as the trigger latency.

After the L0 selection, the events are processed by a second stage, the HLT trigger level. The data is sent to an *Event Filter Farm* (EFF), where

thousands of Personal Computers (PCs) run the algorithms of the HLT, which are written in C++, due to its good performance and speed. The HLT is in turn divided into two stages: the HLT1 and HLT2.

The first stage, the HLT1, has as objective to reduce the event rate, this has a value of 40 KHz (80 KHz) in 2011 (2012). On this stage a partial event reconstruction and an inclusive selection of the signal candidates is performed, using the informations from the VELO and from the tracking system. Cuts on this reconstructed events, like in the impact parameter or momentum, are applied.

In the HLT2 stage, algorithms of fast reconstruction are used and more rigorous criteria to the events selected in the HLT1 stage are applied. In this stage the rate of accepted events was reduced to ~ 3 kHz in 2011 and to 5 kHz in 2012. A total reconstruction of the events is performed and an inclusive and exclusive data selection is made mainly for b and c hadrons. These selections are separated by “lines”, where each line represent an specific decay channel. The representation of each of these stages is shown on Figure 3.12.

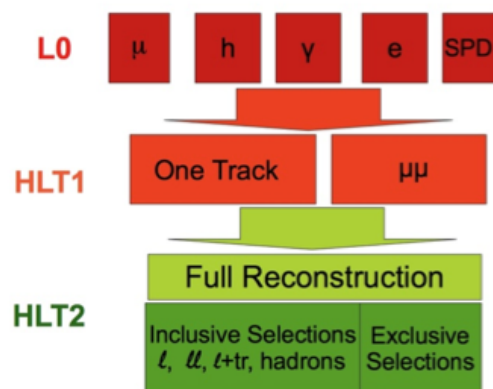


Figure 3.12: Lateral view of the stations the form muon system M1-M5. The regions R1-R4 are also shown

In the following a brief description about operating conditions in 2011 and 2012 is given, being that the analyses presented in this thesis, were performed with the run I data collected by the LHCb.

3.3 Operation conditions in 2011 and 2012

The design and capabilities of each subdetector conforming the LHCb detector were projected to efficiently collect events containing b and c hadrons. Since the first data taking period in 2010, the LHCb operation conditions have been evolving, responding to the higher luminosity being delivered [49].

In optimal running conditions, the LHCb designed luminosity was projected to be:

$$L = \sum_{i=1}^{N_b} \frac{f_{rev} N_i^1 N_i^2 S}{4\pi\epsilon\beta^*} = 2 \times 10^{32} \text{ cm}^{-2} \text{ s}^{-1}, \quad (3-2)$$

where N_b represents the number of colliding bunches per beam, f_{rev} is the bunch revolution frequency. N_i^1 and N_i^2 is the number of protons per bunch, S is the beam crossing angle at LHCb, ϵ is the normalized emittance to the beam, and β^* is the beta function, referring to as the focus of the beam in the collision point. The expected average number of visible interactions per beam crossing is defined as μ . This is a critical parameter in the LHCb performance also known as pile-up. Table 3.3 summarize the values for each parameter in this nominal conditions.

The designed projected luminosity is two order of magnitude lower than the LHC design value. The reason of this choice is that high occupancy (or event pile-up) leads to complications in the b-decay vertex reconstruction, flavour tagging and to excessive reconstruction times in HLT. Also the combinatorial backgrounds levels are increased.

Parameter	Nominal Value
$N_i^{1,2}$	$\sim 10^{11}$
N_b	2622
f_{rev} [kHz]	11,245
ϵ [$\mu\text{m rad}$]	3.75
β^* [m]	10
L [$\text{cm}^{-2} \text{s}^{-1}$]	2×10^{32}

Table 3.1: Parameters values for the optimal running conditions for the LHCb.

The evolution of the LHCb operation conditions can be seen in Fig. 3.13 for the LHC Run I [50]. This includes the years 2010, 2011 and 2012. In the top figure, a graph of the pile-up (μ) for each year is shown in contrast with design value (purple dashed line); in the bottom, the instantaneous luminosity is presented. It can be noticed that since the first year of data taking (2010), the reference values of μ and L were exceeded. This was possible due to fundamental system developments which led to the extension of the physics

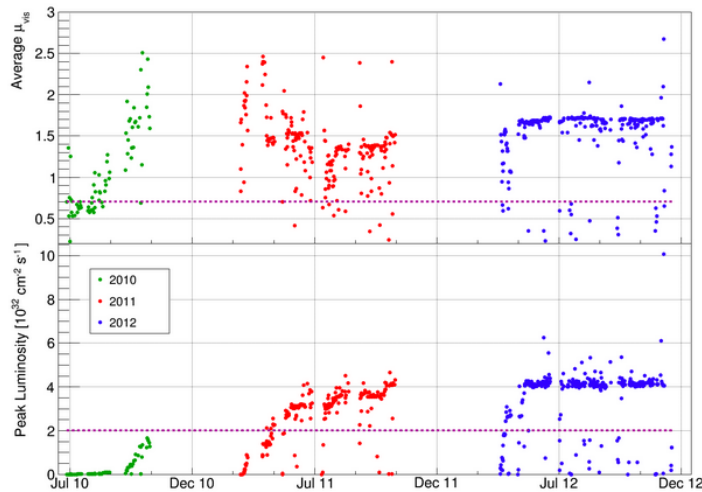


Figure 3.13: Pile-up μ for the LHCb experiment during LHC Run I (Top) and Instantaneous luminosity reached per year (Bottom). Notice that for 2012 a stability for both was achieved.

program. The LHC beam energy was 3.5 TeV for 2010 and 2011 and 4 TeV for 2012.

In 2010 the highest luminosity achieved was of 75% of the LHCb design value. The number of bunches was low and with a pile-up much larger than $\mu = 0.4$, which quickly reached as high as three. Even though with the no favorable conditions of increased detector occupancy, it was demonstrated the efficient performance of the sub-detectors, readout system and reconstruction system as the physics was not compromised.

In 2011, with a fast re-commissioning, a reduced pile-up was possible with a larger number of bunch crossing (1300). The LHC collided bunches of protons to every 50 ns (being 25 ns the nominal value). Most part of the data collected by LHCb in 2011 was at a luminosity of $3.5 \times 10^{32} \text{cm}^{-2} \text{s}^{-1}$ greater than the design value of $2 \times 10^{32} \text{cm}^{-2} \text{s}^{-1}$. For this purpose the LHCb implemented a procedure, at interaction point, so the instantaneous luminosity could be kept stable within 5% of the fill, by adjusting the overlap of the beams. This procedure allowed to minimise the effects of luminosity decrease and to tune the same trigger configuration during a fill.

In 2012 the LHCb took data at a luminosity of $4 \times 10^{32} \text{cm}^{-2} \text{s}^{-1}$, twice the design value, and it was achieved after only one month with the bunch crossing at 50 ns. The beam energy was increased to 4 TeV. An important mechanism was implemented: a strategy consisting on deferring a fraction of the HLT processing to a inter-fill time, between the LHC collision periods allowed to increase the data sample available for physics analysis. During the data taking about 20% of the L0 accepted events were temporarily saved to

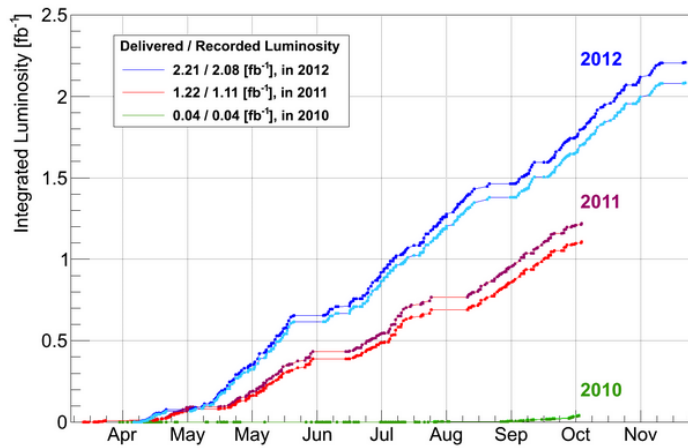


Figure 3.14: Delivered (dark colour lines) and recorded luminosity (light colour line) per year by the LHCb during LHC Run I.

local disks of the Event-Filter-Farm nodes, to then be processed after the end of stable beams. This year was also characterized by a stable trigger configuration.

For 2011 and 2012, the integrated luminosity recorded by the LHCb was of 1.11 fb^{-1} and 2.08 fb^{-1} , respectively. The evolution of the integrated luminosity recorded by the LHCb can be seen in Fig. 3.14, where the dark coloured lines represents the delivered luminosity and light coloured lines the recorded ones.

The ratio of recorded over delivered luminosity is defined as the average operational efficiency. This efficiency was of 93% for the LHC Run I [51].

4

Data Selection

4.1

Dataset

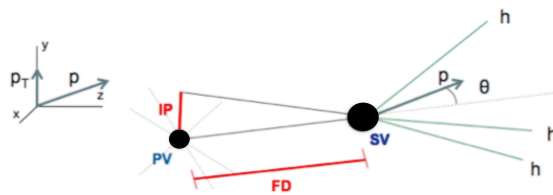
The dataset used in the analysis consists of the data sample collected by the LHCb in 2011 and 2012. This corresponds to an integrated luminosity of 3.0 fb^{-1} . The total luminosity achieved per year is the sum of the recorded ones for each magnet condition. For 2011, the sample recorded for the magnet down polarity was $571 \pm 20 \text{ pb}^{-1}$ and it was $433 \pm 15 \text{ pb}^{-1}$ for the magnet up, comprising a total integrated luminosity of $1005 \pm 25 \text{ pb}^{-1}$. For 2012, the sample consists of $1016 \pm 50 \text{ pb}^{-1}$ of magnet down data and $1016 \pm 50 \text{ pb}^{-1}$ of magnet up data, adding up to a total integrated luminosity of $2032 \pm 71 \text{ pb}^{-1}$. The whole process regarding to the selection of $B^\pm \rightarrow \pi^\pm K^- K^+$ events, which starts at the very moment of the data taking (thanks to the trigger system) until it is saved on disk and delivered for the analysis, will be explained below in the next sections.

4.2

Variables definition

B -meson decays can be identified through their topological characteristics. This is achieved by analyzing and reconstructing their decay products by the signatures they leave in their path through the detector. The selection of signal events (B^\pm candidates) is then mainly based on the exploration of these topological features. To this end, it is useful to define a set of variables that are associated to the physical quantities that characterize a decay and which are measured with good precision by the LHCb sub-detectors. The separation of signal from background events in a sample is a crucial point in the analysis, and this is achieved by imposing requirements in the most discriminating variables.

The typical topology for a $B^\pm \rightarrow \pi^\pm K^- K^+$ decay is shown in Fig. 4.1. The B meson is produced in the interaction point referred as to the primary vertex (PV), and can be characterized by a flight distance (FD) before decaying into the daughter particles. The point where it decays is known as the secondary vertex (SV). Other features like high transverse momentum (P_T), high impact parameter (IP) for the tracks, as well a requirement to come from a

Figure 4.1: Topology for $B^\pm \rightarrow \pi^\pm K^- K^+$ decay.

common secondary vertex, are some of the most used variables to discriminate signal from background events.

For the $B^\pm \rightarrow \pi^\pm K^- K^+$ sample, three dominant sources of background can be identified:

1. Combinatorial background. This type of background comes from the random combination of three not related tracks that fakes to form a B^+ vertex.
2. Peaking background. This kind of background comes from the contamination of other beauty decays, where there has been a mis-identification of pions and kaons with the particles in the final state.
3. 4-body partially reconstructed decays. This kind of background occurs when a particle is not reconstructed in a 4-body decay that shares same final state particles as our signal decay, leading to a fake $B^\pm \rightarrow \pi^\pm K^- K^+$.

To reduce the background levels, the variables that are more intrinsically related to the topology of the signal are the most desired to use. Their definition, using the B^+ decay, are shown here:

Mass (M) : M represents the invariant mass of a candidate B^+ . It is reconstructed using the 4-momentum conservation $P^\mu = p_1^\mu + p_2^\mu + p_3^\mu$, where P^μ is the 4-momentum for the mother particle (B^+) and $p_{1,2,3}^\mu$ are the 4-momentum for the particle daughters (d_1, d_2, d_3), respectively. The invariant mass is then defined as:

$$M = \sqrt{E^2 - \vec{p} \cdot \vec{p}}, \quad (4-1)$$

where $\vec{p} = \vec{p}_1 + \vec{p}_2 + \vec{p}_3$, is the sum of the daughters 3-momenta and $E = E_1 + E_2 + E_3$ is the sum of their respective energies.

B^+ Impact parameter (IP) : The B **IP** is the minimum distance of a B candidate track to the primary vertex.

B^+ **IP** χ^2 : The **IP** χ^2 is defined as the difference in the vertex-fit χ^2 of the PV reconstructed with and without the B^+ candidate track.

Track impact parameters IP : The daughters **IP** is defined as the minimum distance of a track (d_1, d_2, d_3) to the primary vertice.

Track IP χ^2 : Is defined as the difference in the vertex-fit χ^2 of the PV reconstructed with and without the inclusion of the track being considered.

B^+ **momentum (P)** : The momentum P of the mother particle B^+ is defined as the sum of the daughters momenta.

B^+ **momentum (P_T)** : Is the measurement of the momentum P in the transverse direction to the beam.

Track P_T : Is the component of the momentum transverse to the beam for each daughter particle.

Sum of P_T of tracks : Is the scalar sum of the daughters P_T .

Distance from SV to any PV (FD) : The distance that the particle travels before decaying, distance from the PV to SV, is known as the flight distance (**FD**). This information is provided by the VELO with high precision.

B^+ **flight distance FD** χ^2 : is defined as the ratio between the squared value of the FD and the squared value of the combined uncertainties of the PV and SV fits.

Secondary vertex χ^2 : A good quality of the secondary vertex is required by imposing that the three daughter tracks form a good vertex.

B^+ **cos(θ)** : θ is defined as the angle between the momentum vector of B^+ and the vector that goes from the PV to SV. Is expected that θ is small so the $\cos(\theta)$ is approximately 1.

B^+ M^{COR} : Used in the case of partial reconstruction, the corrected mass is defined as:

$$M^{COR} = \sqrt{m^2 + |P_T^{miss}|^2 + |P_T^{miss}|}, \quad (4-2)$$

where P_T^{miss} is the transverse momentum of the missing particle in relation to the B^+ momenta (P). This allows to recover the original flight direction of the B^+ meson.

DOCA : It is defined as the distance of closest approach between any two tracks. For a decay with three particles in the final state there exist

three possibilities of DOCA: combination of the tracks d_1d_2 , d_1d_3 , and d_2d_3 .

Maximum DOCA : Refers to higher DOCA among the three possibilities mentioned above.

ProbNN : Is a variable used for the identification of particles. It uses Neural Networks in order to assign an ID to each particle under study. It is especially useful to reduce the background due to $K - \pi$ and $\pi - K$ mis-identification. The information provided by the RICH detectors, calorimeters and muon system is used.

4.3

Selection requirements

As mentioned before, the selection of hadronic B decays is based in the exploitation of their topological characteristics. All the stages through which the B candidates are refined have been optimised to select events with the physical features expected for these decays. The whole process can be divided in the following steps: trigger, stripping and offline selection criteria. All of them will be discussed in the following.

4.3.1

Trigger selection

As mentioned in Section 3.2.6, the LHCb trigger consists of two levels: a L0 level trigger implemented in hardware and a High-level trigger implemented in software. The main purpose of the trigger system is to select interesting events, rejecting large amount of background in a very efficient and fast way. The selection of B candidates starts in the very moment of the data taking process.

L0 Level Trigger

The first level, the L0 trigger, is synchronous with the 40 MHz bunch crossing signal of the LHC. This rate is reduced to 1 MHz at which all the detector is read-out. The L0 trigger selection relies on the information provided by the calorimeters to trigger high transverse energy (E_T) electrons, photons, hadrons and neutral pions and, by the muons chambers, muons with high transverse momentum. It also uses the pile-up sub-trigger information to reject very busy or null events. All of these information are collected in a Decision Unit (L0DU) which give a response with a maximum latency of $4\mu s$. The distinction between photons, electrons or hadrons candidates is possible due to

Candidate	2011	2012
Hadron	3.5 GeV	3.7 GeV
Electron	2.5 GeV	3 GeV
Photon	2.5 GeV	3 GeV
Single muon	1.48 GeV	1.76 GeV
Dimuon muon $p_{T1} \times p_{T2}$	$(1.296 \text{ GeV})^2$	$(1.6 \text{ GeV})^2$

Table 4.1: L0 thresholds in 2011 and 2012.

the signatures left on their path through the detectors. The L0-calorimeter trigger computes the transverse energy deposited in cluster of 2×2 cells. The highest E_T candidate of each type is selected and send to the L0DU, where different thresholds, specific to each type of candidate, are applied to eventually trigger a positive decision.

The three types candidates are defined as:

- Hadron candidate (L0Hadron): Candidates that have a transverse energy (E_T) deposited in the HCAL cells above a given threshold. If there exit a high E_T cluster in the ECAL that is located in front of the HCAL cluster, then the total transverse energy will be the sum of both.
- Photon Candidate: Have a E_T above threshold deposited in the ECAL with 1 or 2 hits in the PS cell in front of the ECAL cluster but with no hits in the SPD cells corresponding to the PS cells.
- Electron candidate: In addition to the photon requirements, at least one SPD cell hit in front of the PS cells must be observed.

The L0-Muon trigger selects muons with high transverse momentum. For this purpose the five stations of the muon detector are divided in four quadrants, where each quadrant is connected to a L0 muon processor. The identification of hits that form a straight line through the five muon station is performed. The two muon tracks with the highest and second highest P_T are selected on each quadrant resulting up to eight candidates. Then, a single muon selection or a Dimuon selection can be done. The threshold imposes in the L0 trigger for 2011 and 2012 are shown in Table 4.1.

In this level our candidates are required to be L0Hadron TOS or TIS in any of the other physical channels (electrons, photons and muons), where **TOS** (Triggered On Signal) means that our candidates fired the trigger precisely by the association of the detectors information with the signal of the candidates, while **TIS** (Triggered Independent of Signal), means that the events that fire the trigger are not necessarily related with signal of the candidate.

High Level Trigger

The high level trigger is implemented in software and runs in a CPU farm of about 29 000 logical cores. This is separated into two levels HLT1 and HLT2. The HLT1 performs a partial reconstruction of events and an inclusive selection of signal candidates. Our candidates are selected through the inclusive Hlt1TrackAllL0 trigger line, that searches for good quality tracks candidates based on the P_T and by well defined flight distance. At this stage the rate is reduced to 80 kHz. The HLT2 performs a full event reconstruction for all tracks. A set of inclusive or exclusive selections are applied, most of them based on topological features [52]. Our candidates are selected by the Hlt2Topo(2, 3, or 4-Body) TOS inclusive trigger lines which are characterized by the use of a multivariate selection for B^+ decays. The output rate of the topological trigger was of 3 KHz for 2011 and of 5 KHz for 2012 [53].

4.3.2 Stripping Selection

After the trigger selection, the data saved to storage is further processed to separate the events by the physics of interest. The raw data is processed for reconstruction and attribution of the physical quantities in the event. In this way, the energy measured by the calorimeters HCAL and ECAL, the hits associated to the track position and their momentum as well as the information related to the particle identification are reconstructed. These events are saved in a format called data Summary Tape (DST). Then in the next step, the *rDST*, pre-selection algorithms are applied. The *rDST* is analysed and a sequence of selections is used to create candidates and select events by the physics of interest. The whole process is known as *stripping*.

The $B^\pm \rightarrow \pi^\pm K^- K^+$ decay mode is selected as part of the inclusive stripping line `StrippingBu2hhh_KKK_inclLine`¹ of `stripping20`, in which all particles are reconstructed as kaons². As a result, a large three-body invariant mass window is required in order to include all hhh final states. In the offline analysis stage, the $B^\pm \rightarrow \pi^\pm K^- K^+$ invariant mass is recalculated assigning the correct mass hypothesis.

Loose initial restrictions are imposed on track variables like the IP χ^2 , momenta P and transverse momenta P_T . Also, loose requirements are set for the maximum distance of closest approach DOCA between any two tracks. The three tracks are required to form a common secondary vertex with a

¹This stripping line uses `StdAllNoPIDKaons`.

²The stripping selection was intended to include the four charmless B^\pm decays, $B^\pm \rightarrow \pi^\pm \pi^+ \pi^-$, $B^\pm \rightarrow K^\pm \pi^+ \pi^-$, $B^\pm \rightarrow \pi^\pm K^- K^+$ and $B^\pm \rightarrow K^\pm K^+ K^-$ because of their topological similarities. Whenever necessary, we will refer to these channels as $h^\pm h^- h^+$

Variables	Selection cuts
Tracks P_T	$> 0.1 \text{ GeV}/c$
Tracks P	$> 1.5 \text{ GeV}/c$
Tracks $IP\chi^2$	> 1
Tracks $\chi^2/n.d.f.$	< 3
Tracks GhostProb	< 0.5
Sum of P_T of tracks	$> 4.5 \text{ GeV}/c$
Sum of P of tracks	$> 20. \text{ GeV}/c$
Sum of $IP\chi^2$ of tracks	> 500
P_T of the highest- P_T track	$> 1.5 \text{ GeV}/c$
Maximum DOCA	$< 0.2 \text{ mm}$
B^\pm candidate M_{KKK}	$5.05 - 6.30 \text{ GeV}/c^2$
B^\pm candidate M_{KKK}^{COR}	$4 - 7 \text{ GeV}/c^2$
B^\pm candidate $IP \chi^2$	< 10
B^\pm candidate P_T	$> 1. \text{ GeV}/c$
Distance from SV to any PV	$> 3 \text{ mm}$
Secondary Vertex χ^2	< 12
B^\pm candidate $\cos(\theta)$	> 0.99998
B^\pm Flight Distance χ^2	> 500

Table 4.2: StrippingBu2hhh_KKK_inclLine stripping 20 line for charmless B^\pm decays to three light hadrons.

good χ^2 . The SV has to be displaced from the primary vertex due to the large flight distance FD of the B^\pm meson before decaying. The reconstructed B^\pm momentum vector points to the PV, resulting typically in a small impact parameter and angle θ between the momentum and the flight direction. The B^\pm candidates are further required to have a corrected mass M^{COR} range, calculated when all daughters are assigned kaon masses (M_{KKK}^{COR})³. A summary of the stripping criteria is given in Table 4.2.

4.4 Offline Selection

To separate signal $B^\pm \rightarrow \pi^\pm K^- K^+$ events from background events in order to obtain a more pure sample, an offline selection is also applied. We use a multivariate selection (Boosted Decision Trees) [54, 55] to reduce the combinatorial background and particle identification to handle contamination from other b -hadron decays (cross-feed). We apply D^0 veto to reject charm contributions to the final state. We also discard events with more than one

³ M_{KKK}^{COR} stands for the cases where a genuine decay, e.g. $B^\pm \rightarrow \pi^\pm K^- K^+$, is reconstructed as a $B^\pm \rightarrow K^\pm K^+ K^-$, as required in the stripping. For these cases the B mass will not be around $5279 \text{ MeV}/c^2$ due to the $K - \pi$ mis-ID and we need to re-evaluate the B mass in order to not exclude the $B^\pm \rightarrow \pi^\pm K^- K^+$ signal. The mass window in the stripping is defined as $4-7 \text{ GeV}/c^2$ to include all signal channels taken into consideration in the strip line.

Decay		2011	2012
$B^+ \rightarrow \pi^+ \pi^- \pi^+$	MagUp	500998	1015498
	MagDown	428626	1013996
$B^+ \rightarrow \pi^+ K^- K^+$	MagUp	256750	509797
	MagDown	262250	511198
$B^+ \rightarrow K^+ K^- K^+$	MagUp	516749	1020497
	MagDown	518749	1019496
$B^+ \rightarrow \pi^+ K^- K^+$	MagUp	257250	513000
	MagDown	252748	511197

Table 4.3: MC signal statistics used on the multivariate analysis training.

candidate that passed the final selection, since we do not expect more than one signal B candidate per event due to the low branching ratios of the decay channels. For $B^\pm \rightarrow \pi^\pm K^- K^+$, about 1% of the candidates in the data and simulated samples have been excluded.

The boosted decision trees (BDT) multivariate analysis uses the tools from the TMVA package [56]. For this purpose a set of input variables are provided to be pre-processed with the Principal Component Analysis (PCA) method. A linear transformations of the variables that aims to maximize their variability, before BDT training. At this stage no particle identification criteria is used. For the optimization the Monte Carlo samples (MC) of all four $B^\pm \rightarrow h^\pm h^- h^+$ channels are used as signal (these MC samples will be explained below) and the 2012's data collected in the region $5.40 \text{ GeV}/c^2 < m_B < 5.58 \text{ GeV}/c^2$ (high side-band mass) from the $B^\pm \rightarrow \pi^\pm \pi^+ \pi^-$ decay, is used as background. The reason for using $B^\pm \rightarrow \pi^\pm \pi^+ \pi^-$ right-side band as background is that all of its cross-feed modes lie below the B mass which is not the case for $B^\pm \rightarrow \pi^\pm K^- K^+$. In Table 4.3 the MC statistics used for each channel is summarized.

The optimization is focused on rejecting combinatorial background. The cut on the BDT output variable is chosen as the one that maximizes the significance⁴ $S/\sqrt{S+B}$. The common cut chosen was of $BDT > 0$.

In Fig. 4.2, the BDT output for signal (blue) and background events (red) are shown. In Fig. 4.3(a), we show the background rejection as a function of the signal efficiency for $B^\pm \rightarrow \pi^\pm K^- K^+$ 2012, comparing the performance of the separate (red) to the common (cyan) optimizations. In Fig. 4.3(b) it is shown the background rejection against the signal efficiency curves comparing 2011 and 2012 events. The $B^\pm \rightarrow \pi^\pm K^- K^+$ mass distributions for 2012 data is shown in Fig. 4.4, before (black) and after (blue) the cut on the BDT output variable, without particle identification requirements.

⁴S and B are obtained from fits to data for a given BDT cut and applying PID requirements.

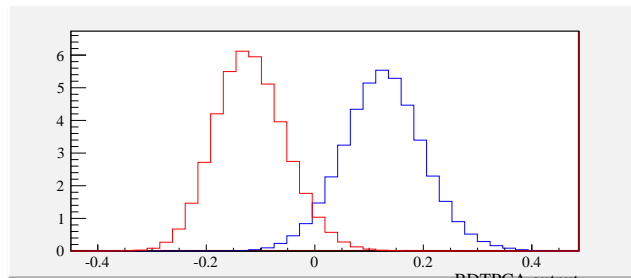


Figure 4.2: Discriminating variable $BDTPCA$ output by the Boosted Decision Trees optimization common to all $B^\pm \rightarrow h^\pm h^- h^+$ channels. Signal: blue curve, background: red curve.

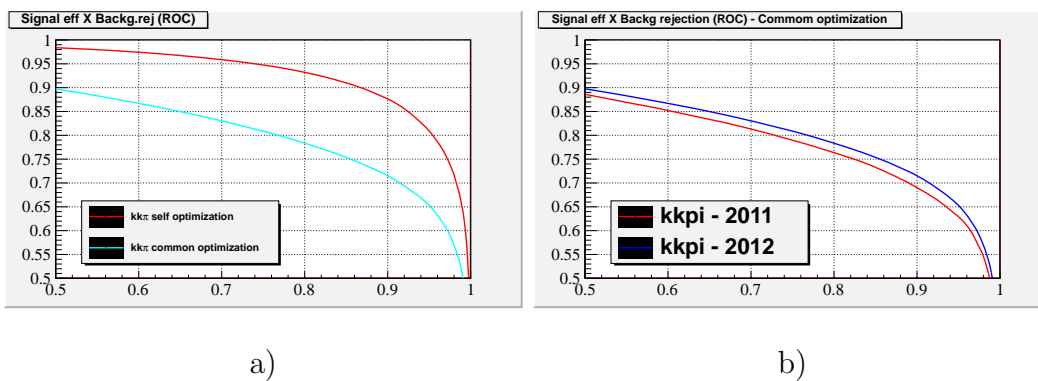


Figure 4.3: Background rejection as a function of signal efficiency for (a) $B^\pm \rightarrow \pi^\pm K^- K^+$, and (b) background rejection as a function of signal efficiency comparing 2011 and 2012 events.

Decay	Daughter	PID selection cuts
$B^+ \rightarrow \pi^+ K^- K^+$	Kaons	$\text{ProbNNk} > 0.45$ & $\text{ProbNNpi} < 0.5$
	Pion	$\text{ProbNNpi} > 0.5$ & $\text{ProbNNk} < 0.05$

Table 4.4: PID selection criteria for $B^\pm \rightarrow \pi^\pm K^- K^+$ decay.

PID selection

Particle identification (PID) [57] is a crucial variable in reducing the background levels in the $B^\pm \rightarrow \pi^\pm K^- K^+$ mass spectrum. The feed-through of the other beauty modes can appear due to the mis-identification (mis-ID) of pions or kaons forming peaking backgrounds. In addition, partially reconstructed B decays are also present in our spectra. After the trigger requirements, stripping and the TMVA selection, which is aimed at the combinatorial background, the remaining background is rich in decays of beauty hadrons, either fully or partially reconstructed decays. Particle identification (PID) is the only way to handle this type of background. Generally speaking, the PID selection should minimize the cross-feed from other $h^\pm h^- h^+$ decays with mis-ID hadrons, while keeping most of the signal. In the determination of the PID cuts, we take both aspects into consideration, searching for a compromise between the efficiency

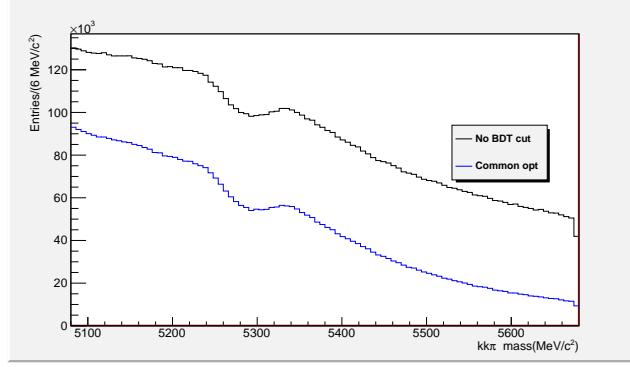


Figure 4.4: $B^\pm \rightarrow \pi^\pm K^- K^+$ mass distributions for 2012 data before and after a cut on the BDT discriminating variable $BDTPCA > 0$.

for the signal and the rejection of the background.

The basic source of contamination is the $K - \pi$ and $\pi - K$ mis-ID. The $p - K$ mis-ID is negligible, while muons are rejected by a muon veto applied to each track. The PID selection criteria for $B^\pm \rightarrow \pi^\pm K^- K^+$ decay channel are shown in Table 4.4.

4.5 Charm veto study

The major contamination from the charm sector comes from the decay chains of the type, $B^+ \rightarrow \bar{D}^0 \pi^+$ and $B^+ \rightarrow \bar{D}^0 K^+$, where $\bar{D}^0 \rightarrow K^- K^+$ or $\bar{D}^0 \rightarrow \pi^- K^+$, see Fig. 4.5(a). The exclusion of its contribution on each axis of the Dalitz plot is done through the veto of events around the D^0 mass. For that purpose we cut off events in the region $(1.834 < m_{\pi^\pm K^\mp}^2 < 1.894)$ GeV/c^2 for the πK system and $(1.834 < m_{K^- K^+} < 2.000)$ GeV/c^2 for the KK combination. The latter has a wider window to account for possible contamination of $\bar{D}^0 \rightarrow \pi^- K^+$ ($D^0 \rightarrow \pi^+ K^-$) where the pion is mis-identified as kaon. To better illustrate the need of the wider mass cut, in Fig. 4.6(a) we project the $m_{KK-\pi K}$ variable using $(1.834 < m_{K^- K^+} < 1.894)$ GeV/c^2 window. As can be seen there are a excess of events corresponding to $\bar{D}^0 \rightarrow \pi^- K^+$ ($D^0 \rightarrow \pi^+ K^-$). In Fig. 4.6(b) it is shown the same distribution after increasing the $m_{K^- K^+}$ veto window, showing that the remnants of $\bar{D}^0 \rightarrow \pi K$ events are negligible. The Dalitz plot after the vetos are applied is shown on Fig. 4.5(b).

4.5.1 Fiducial cut

Particle identification does not perform so well for tracks with momentum higher than 100 GeV/c and pseudorapidity (η) outside the window of 1.5 to 5.5. Hence, B^\pm candidates for which the tracks do not satisfy the momentum

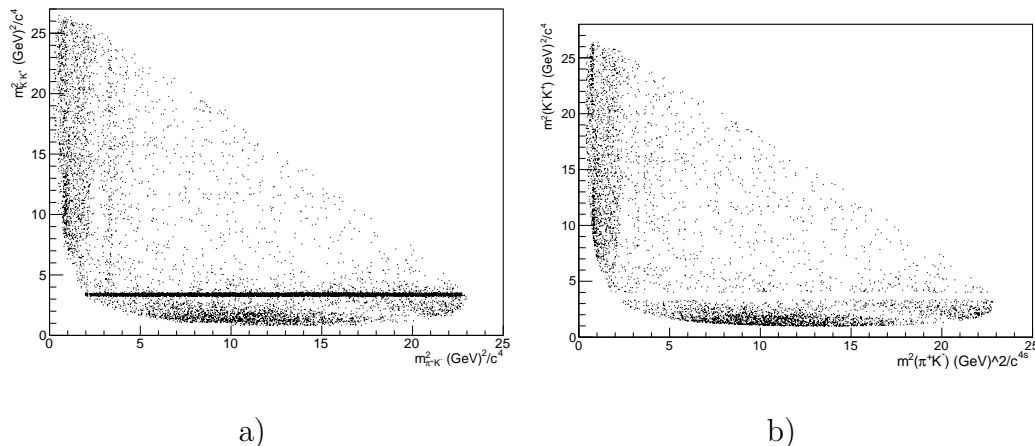


Figure 4.5: (a) Distribution of events on the Daliz plot in the signal region without vetos applied (b) Distribution of events on the Daliz plot in the signal region with vetoes are applied.

Variables	Selection cuts
Tracks P_T	$> 90 \text{ MeV}/c$
Tracks P	$> 1400 \text{ MeV}/c$
B^\pm candidate P_T	$> 1000 \text{ MeV}/c$
B^\pm candidate P	$> 17000 \text{ MeV}/c$

Table 4.5: Generation criteria for large MC samples.

Decay		2011 after gencuts	2012 after gencuts
$B^+ \rightarrow \pi^+ K^- K^+$	MagUp	2161036	2110799
	MagDown	2176803	2087890

Table 4.6: Large MC signal statistics.

and pseudorapidity requirements ($P < 100 \text{ GeV}/c$ AND $1.5 < \eta < 5.5$) are excluded. This requirement also shows improvement in the rejection of peaking background.

4.6 Simulated samples

Simulation data necessary for signal efficiency and background studies are obtained from the full LHCb simulation process: Monte Carlo (MC) events are generated using Pythia 8 [58, 59], the simulation of the passage through the detector is made by GEANT [60] [61], and then passed through the reconstruction software as the data events. In order to obtain a very large statistics, loose cuts were applied at the generation level: loose restriction on the tracks and B candidates momenta (P) and transverse momenta (P_T). The generation criteria for the large MC samples are listed in Table 4.5 and have been found to be highly efficient as can be seen in Table 4.6.

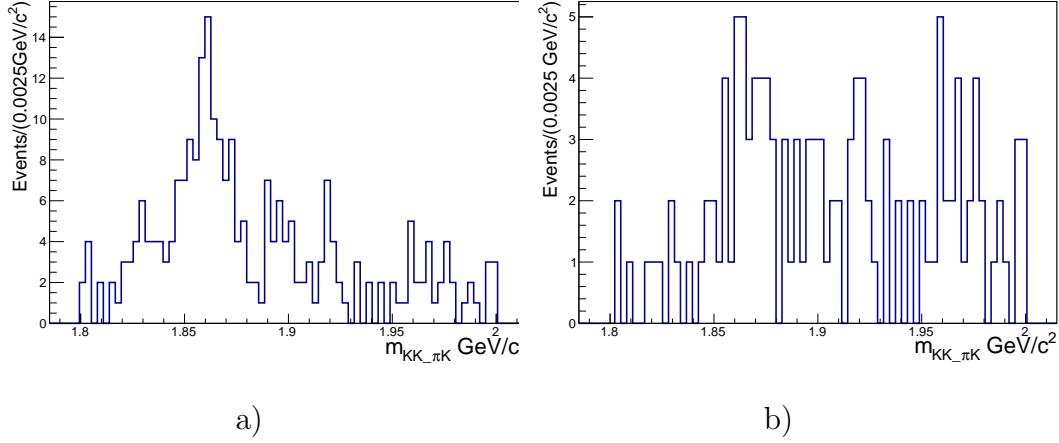


Figure 4.6: a) $m_{KK-\pi K}$ distribution with $[1.834, 1.894]$ GeV/c^2 m_{KK} veto window applied. b) $m_{KK-\pi K}$ distribution with $[1.834, 2.000]$ GeV/c^2 m_{KK} veto window applied

4.6.1 Selection for the simulated samples

The $B^\pm \rightarrow \pi^\pm K^- K^+$ MC samples pass through the same selection as for the data (stripping, trigger and offline selection). A match between the reconstructed tracks and the simulated tracks is made to guarantee that the MC candidates are true $B^\pm \rightarrow \pi^\pm K^- K^+$.

The other $B^\pm \rightarrow h^\pm h^- h^+$ MC samples are also studied as they can potentially appear in the $B^\pm \rightarrow \pi^\pm K^- K^+$ spectrum as cross-feeds, as explained in the following sections.

4.7 Mass Fit

After applying all selection criteria described in the previous section, the $B^\pm \rightarrow \pi^\pm K^- K^+$ mass spectrum obtained is shown in Fig. 4.7. To obtain the yield of $B^\pm \rightarrow \pi^\pm K^- K^+$ candidates, we need to parametrize each one of the components contributing in the mass spectrum in the range $5080 - 5580$ MeV/c^2 . The fit is made simultaneously for B^+ and B^- , allowing us to obtain the raw asymmetry and the contribution of each type of background. These will serve as input for the Dalitz plot fit later in section 6.2. For this purpose we construct a total probability density function (PDF) that takes into account the signal and background individual parametrizations and then perform a likelihood fit. The background sources are classified as combinatorial background, partially reconstructed backgrounds (mostly from four-body decays with a missing particle) and peaking backgrounds that have

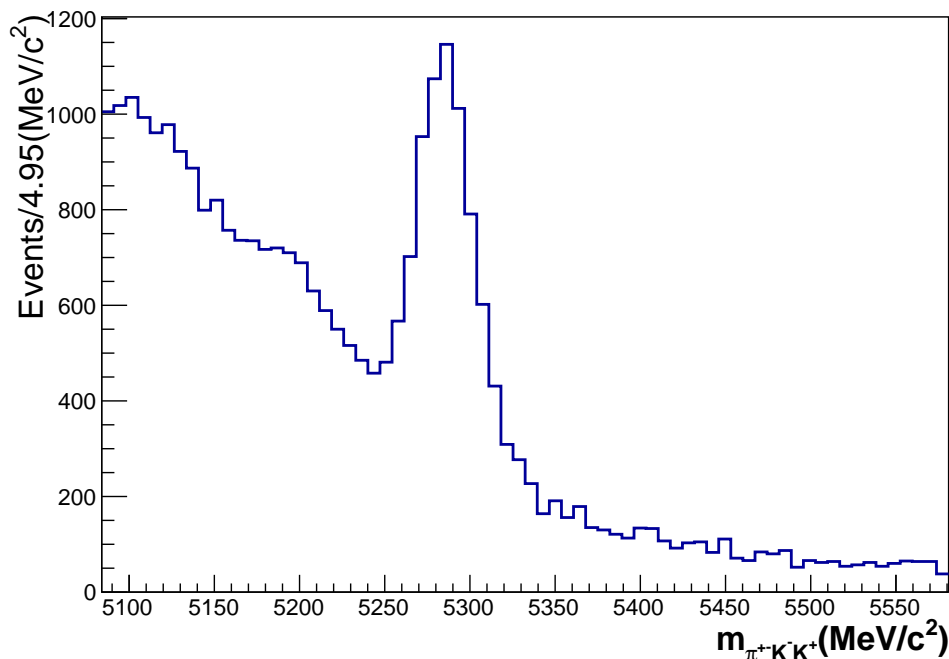


Figure 4.7: Invariant mass distribution $M_{\pi^+K^-K^+}$ after all the selection criteria applied.

one or more particles misidentified. As will be discussed, studies are carried out in the simulated samples to obtain the shapes of each component, then we use these shapes in the mass fit to real data, with some of them (mostly the associated to the background) totally fixed.

The PDF functions that are used to parametrize the mass spectrum differ for each one of the analyses that are discussed in this work. Nevertheless the procedure of implementation is the same. We will explicitly indicate which PDF functions are used for the CP violation measurements analysis and which ones are used for the amplitude analysis.

4.8

The $B^\pm \rightarrow \pi^\pm K^- K^+$ fit model

To obtain the signal yield and the background estimation, we perform a simultaneous unbinned maximum likelihood fit to data. The fit procedure, using PDFs that account for each type of contribution, is implemented using the tools provided by the *RooFit* data modeling package [62]. For signal, we calculate the charge raw asymmetry A_{raw}^S , which includes CP violation as well as detection and production effects, defined as:

$$A_{\text{raw}}^S = \frac{N_S^- - N_S^+}{N_S^- + N_S^+}, \quad (4-3)$$

where N_S^- and N_S^+ are the number of B^- and B^+ decays, respectively. We can express N_S^- and N_S^+ as functions of A_{raw}^S and $N_S \equiv N_S^- + N_S^+$ in the following way:

$$A_{\text{raw}}^S = \frac{N_S^- - (N_S - N_S^-)}{[N_S^- + (N_S - N_S^-)]} \Rightarrow N_S^- = \frac{N_S}{2} (1 + A_{\text{raw}}^S) \quad (4-4)$$

$$A_{\text{raw}}^S = \frac{(N_S - N_S^+) - N_S^+}{[(N_S - N_S^+) + N_S^+]} \Rightarrow N_S^+ = \frac{N_S}{2} (1 - A_{\text{raw}}^S). \quad (4-5)$$

The total mass fit model function, F^\pm , for B^\pm signal is then written as

$$\begin{aligned} F^\pm &= \left[\frac{N_S}{2} (1 \mp A_{\text{raw}}^S) \right] F_S^\pm + \left[\frac{N_{\text{comb}}}{2} (1 \mp A^{\text{comb}}) \right] F_{\text{comb}}^\pm + \\ &+ \sum_{i=1} \left[\frac{(f_{\text{bkg}_i} N_S)}{2} (1 \mp A_{CP}^{\text{bkg}_i}) \right] F_{\text{bkg}_i}^\pm, \end{aligned} \quad (4-6)$$

where N_{comb} is the total number of combinatorial background events. A^{comb} and $A_{CP}^{\text{bkg}_i}$ allows for charge asymmetries in the combinatorial and peaking background sources, respectively. The sum in i indicates the different components for peaking/partial backgrounds, with $(f_{\text{bkg}_i} N_S)$ the respective number of events. F_S^\pm , F_{comb}^\pm and $F_{\text{bkg}_i}^\pm$ are the functions describing the signal, combinatorial background, and peaking/partial backgrounds, respectively. Each of these functions are detailed in the following subsections.

4.8.1

The signal fit model

The signal PDF for $B^\pm \rightarrow \pi^\pm K^- K^+$, represented by $F_S^\pm(m)$ for B^+ and B^- respectively in Eq. 4-6, is composed by the sum of a Gaussian plus two Crystal-Ball [63] functions. This parametrization is derived from MC studies as showed a better description of the signal shape and at the same time provided the best stability to data. Other choices were tested like the sum of a Gaussian plus a single Crystal-Ball, but the former showed a better fit on the simulated signal events. The two Crystal-Balls are needed to account for the non Gaussian asymmetric tails of the signal, including final state radiation (FSR). We use common parameters for both $F_S^+(m)$ and $F_S^-(m)$, and they can be expressed as (omitting \pm):

$$F_S(m) = G(m) + F_{CB1}(m) + F_{CB2}(m), \quad (4-7)$$

where $G(m)$ stands for the Gaussian function and $F_{CB1}(m)$ and $F_{CB2}(m)$ for the two Crystal Ball. The function $G(m)$ is defined as:

$$G(m) = \frac{1}{\sqrt{2\pi}} e^{-\frac{1}{2}\left(\frac{m-\mu_G}{\sigma_G}\right)^2}$$

where μ_G and σ_G are the mass and width, respectively and are let free to float in the fit.

The function $F_{CBi}(m)$, $i = 1, 2$ are the Crystal Ball functions, which is piecewise-defined, consisting of a Gaussian peak and a power-law tail to account for the asymmetric Gaussian behaviour of the signal. It is defined as:

$$F_{CBi} = \begin{cases} e^{-\frac{1}{2}\left(\frac{m-\mu_{CBi}}{\sigma_{CBi}}\right)^2} & \text{if } \frac{m-\mu_{CBi}}{\sigma_{CBi}} > -\alpha^{sig} \\ \left(\frac{n_i^{sig}}{|\alpha_i^{sig}|}\right)^{n_i} e^{-\frac{|\alpha_i^{sig}|^2}{2}} \left(\frac{n_i^{sig}}{|\alpha_i^{sig}|} - |\alpha_i^{sig}| - \frac{m-\mu_{CBi}}{\sigma_{CBi}}\right) & \text{if } \frac{m-\mu_{CBi}}{\sigma_{CBi}} \leq -\alpha^{sig} \end{cases} \quad (4-8)$$

where the parameters are μ_{CBi} , σ_{CBi} , α_i^{sig} and the power n_i^{sig} , $i = (1, 2)$. Only the mean and width, μ_{CBi} and σ_{CBi} , are let free to float in the fit.

Differences between simulated and data distributions of the signal are expected since the simulation cannot describe the detector perfectly. In order to account for these differences, coefficients are introduced to model the variation of the mean and width of the Gaussian and Crystal-Ball functions. For the Gaussian parametrization the mean and width are expressed as:

$$\begin{aligned} \mu_G &= C^\mu \mu_{MC}^{sig} \\ \sigma_G &= C^\sigma \sigma_{MC}^{sig}, \end{aligned} \quad (4-9)$$

where μ_{MC}^{sig} and σ_{MC}^{sig} are the initial values obtained from the MC, and C^μ and C^σ are two coefficients introduced to model, respectively, the variation of μ_G and σ_G . These coefficients are let to float within values close to one

The variation of the mean and width of the Crystal-Ball functions are also driven by the coefficients C^μ and C^σ in the following way:

$$\begin{aligned} \mu_{CBi} &= A_{CBi}^\mu (C^\mu \mu_{MC}^{sig}) = A_{CBi}^{\mu_i} \mu_G \\ \sigma_{CBi} &= A_{CBi}^\sigma (C^\sigma \sigma_{MC}^{sig}) = A_{CBi}^{\sigma_i} \sigma_G, \end{aligned} \quad (4-10)$$

where the two factors $A_{CBi}^{\mu_i}$ and $A_{CBi}^{\sigma_i}$, obtained from the fit to the MC samples, are fixed in the fit to data. They are introduced to perform a shift in the values of μ_{CBi} and σ_{CBi} with respect to those of the Gaussian function and thus to maintain their correlation during the fit.

More details about the MC studies performed to obtain the signal PDF

will be given in the appendix A in Section A.0.2.

4.8.2

Background fit models

Different PDF functions are used to model the background sources. The combinatorial background is parametrized with an exponential PDF with one free parameter: its slope b . This is defined as:

$$F_{comb}(m) = \exp [b \cdot (m - 5080)] , \quad (4-11)$$

For the peaking backgrounds $B^\pm \rightarrow K^\pm \pi^+ \pi^-$ and $B^\pm \rightarrow K^\pm K^+ K^-$, we perform MC studies to obtain the shape of these contributions in the $B^\pm \rightarrow \pi^\pm K^- K^+$ mass spectrum. These shapes are then fixed in the fit.

For the peaking $B^\pm \rightarrow K^\pm \pi^+ \pi^-$ we perform a single mis-id of the π^\mp by a K^\mp , which is the only possible scenario that will result in a reflection into $B^\pm \rightarrow \pi^\pm K^- K^+$. This reflection is parametrized by a Gaussian plus two Crystal-Balls functions, as the signal, and is defined as:

$$F_{bkg}^{K\pi\pi}(m) = G^{K\pi\pi}(m) + F_{CB1}^{K\pi\pi}(m) + F_{CB2}^{K\pi\pi}(m), \quad (4-12)$$

where we explicitly indicate that it refers to the $B^\pm \rightarrow K^\pm \pi^+ \pi^-$ reflection. The two parameters for the Gaussian, the mean and width, and the corresponding parameters for the Crystal-Ball functions, are all fixed in the fit. Their respective values are shown in Table A.4 in appendix A.

The peaking $B^\pm \rightarrow K^\pm K^+ K^-$ is the result of a K^\pm mis-identified as π^\pm , its contribution is parametrized by the sum of a Gaussian plus two Crystal-Balls plus one exponential. Its total PDF is then expressed as:

$$F_{bkg}^{KKK}(m) = G^{KKK}(m) + F_{CB1}^{KKK}(m) + F_{CB2}^{KKK}(m) + E^{KKK}(m), \quad (4-13)$$

where the exponential E^{KKK} have the form:

$$E_{KKK}(m) = \exp [b^{KKK} \cdot (m - s^{KKK})] , \quad (4-14)$$

where b^{KKK} is the slope and s^{KKK} the shift of the exponential. All parameters values obtained for the $B^\pm \rightarrow K^\pm K^+ K^-$ reflection were also fixed in the fit and these are also shown on appendix A in Table A.4. The $B^\pm \rightarrow \pi^\pm \pi^+ \pi^-$ decay is also a possible peaking background contamination, that requires a double mis-ID. Two pions have to be misidentified as kaons. It is found that this contribution is negligible and it is not considered.

The event yields of the two peaking background are estimated as $N_{bkgi} = f_{bkgi} N_S$, where f_{bkgi} is the fraction of the background component with respect

Table 4.7: Branching fraction and fraction of the peaking background f_{bkg} with respect to the signal yield ($B^\pm \rightarrow \pi^\pm K^- K^+$) obtained from Eq. 4-15

(a) 2011 sample only.		
Mode	Branching fraction	Fraction from MC
$B^\pm \rightarrow K^\pm \pi^+ \pi^-$	$(5.10 \pm 0.29) \times 10^{-5}$	(0.067 ± 0.010)
$B^\pm \rightarrow K^\pm K^+ K^-$	$(3.40 \pm 0.14) \times 10^{-5}$	(0.067 ± 0.010)
(b) 2012 sample only.		
Mode	Branching fraction	Fraction from MC
$B^\pm \rightarrow K^\pm \pi^+ \pi^-$	$(5.10 \pm 0.29) \times 10^{-5}$	(0.066 ± 0.010)
$B^\pm \rightarrow K^\pm K^+ K^-$	$(3.40 \pm 0.14) \times 10^{-5}$	(0.052 ± 0.008)

to the signal yield, see Eq. 4-6. This fraction is calculated as:

$$f_{bkgi} \equiv \frac{N_{bkgi}}{N_S} = \frac{\mathcal{B}_{bkgi}}{\mathcal{B}_{S_i}} \times \frac{\epsilon_{bkgi}}{\epsilon_{S_i}}, \quad (4-15)$$

where \mathcal{B}_{bkgi} and \mathcal{B}_{S_i} are the branching ratios taken from the PDG, and ϵ_{bkgi} and ϵ_{S_i} are the efficiencies from the MC selection. The branching fraction and fraction for each peaking contribution, separated by year, is shown in Table 4.7.

The partially reconstructed background contaminations are the result of 4-body B decays with a missing charged or neutral particle, or from 4-body B_s^0 decays with a missing charged particle. We have two possible partially reconstructed backgrounds: B_s^0 with a missed charged pion, like $B_s^0 \rightarrow D_s^-(\pi^+ K^- K^+) \pi^+$ or $B_s^0 \rightarrow \bar{K}^{*0} K^{*0}$ and possible other modes; and B decays with a missed charged or neutral pion, like $B^0 \rightarrow D_s^-(\pi^+ K^- K^+) \pi^+$, $B^\pm \rightarrow D_s^-(\pi^+ K^- K^+) \pi^\pm$, $B^\pm \rightarrow K^{*\pm}(K^\pm \pi^0) \pi^\pm K^\mp$ and $B^0 \rightarrow K^+ K^- \pi^+ \pi^-$.

Both components, B_s^0 or B (B^\pm , B^0), are parametrized by an Argus function [64] convoluted with a Gaussian resolution, which is given by:

$$\mathcal{A}(m; m_t, c, p) = \frac{2^{-p} c^{2(p+1)}}{\Gamma(p+1) - \Gamma(p+1, c^2/2)} \cdot \frac{m}{m_t^2} \left(1 - \frac{m^2}{m_t^2}\right)^p \exp\left[-\frac{1}{2} c^2 \left(1 - \frac{m^2}{m_t^2}\right)\right] \quad (4-16)$$

with three parameters: the mass threshold m_t upper limit, the curvature c and the power p which controls the falling of its slope. All of these parameters are fixed in fit with same values for both components, except for the mass threshold which is fixed in different values. The fractions of both components, B_s^0 and B , are left to float. In Table A.5 in appendix A are shown these parameters values. The f_{bkgi} is also free in the fit, opposed to the corresponding fraction contributions of the peaking backgrounds which are fixed.

Table 4.8: Floating parameters of the simultaneous fit to the 2011 data sample regarding to Figure 4.8.

Parameters	TOS or TIS	TIS not TOS	TOS
signal			
C^μ	1.0007 ± 0.0001	1.0002 ± 0.0002	1.0005 ± 0.0001
C^σ	1.03 ± 0.04	1.12 ± 0.07	1.04 ± 0.05
A_{RAW}	$-0.1272^{+0.0299}_{-0.0300}$	$-0.1303^{+0.0478}_{-0.0479}$	$-0.1245^{+0.0375}_{-0.0377}$
N_S	$1968.7^{+87.7}_{-83.3}$	$844.5^{+47.8}_{-45.2}$	$1142.1^{+47.2}_{-47.3}$
combinatorial			
b	-0.0054 ± 0.0005	-0.0056 ± 0.0005	-0.0050 ± 0.0002
N_{comb}	4688.3 ± 414.4	2657.0 ± 119.7	1936.6 ± 97.8
A_{asym}	-0.0049 ± 0.0198	0.0135 ± 0.0255	-0.0297 ± 0.0326
$B_s^0 \rightarrow 4\text{-body}$ (partially rec. component)			
Fraction [%]	1.899 ± 0.200	1.977 ± 0.200	1.904 ± 0.146
$B \rightarrow 4\text{-body}$ (partially rec. component)			
Fraction [%]	0.267 ± 0.129	0.257 ± 0.117	0.312 ± 0.083

4.8.3

$B^\pm \rightarrow \pi^\pm K^- K^+$ mass spectrum fit results

Using the signal and background parametrization described in the previous subsection, we perform a simultaneous B^+ and B^- extended unbinned maximum likelihood fit to data. We let to float the mean and width coefficients C^μ and C^σ for the signal PDF. For the combinatorial background one parameter: the slope b . The shape for the peaking and 4-body partially reconstructed decays backgrounds are all fixed in the fit.

We are interested in obtaining the number of signal events and the asymmetry of the signal. Also we want the number of each type of background events and the asymmetry associated to combinatorial background (the asymmetry for the peaking/partially reconstructed backgrounds is fixed to zero) and the signal and background PDF parameters values that are let free in the fit.

The mass fit plots for B^- (left) and B^+ (right) are shown in Figs. 4.8, 4.9 and 4.10 for 2011, 2012 and the combined 2011 and 2012 data samples, respectively. Each row in the figures corresponds to different trigger configurations: TIS or TOS (top), TIS not TOS (middle) and TOS (bottom). The parameters extracted from the fit to the 2011, 2012 and the combined samples are listed in the Tables 4.8, 4.9 and 4.10, respectively.

Signal mass window for the Amplitude Analysis

As can be seen in Figs. 4.8, 4.9 and 4.10, the region around the mass peak is highly populated by the contamination of several background sources. At the left side we have high levels of a background which has structure as it comes from 4-body partially reconstructed decays. Besides, underneath the signal, more to the right, there is a contribution from $B^\pm \rightarrow K^\pm \pi^+ \pi^-$.

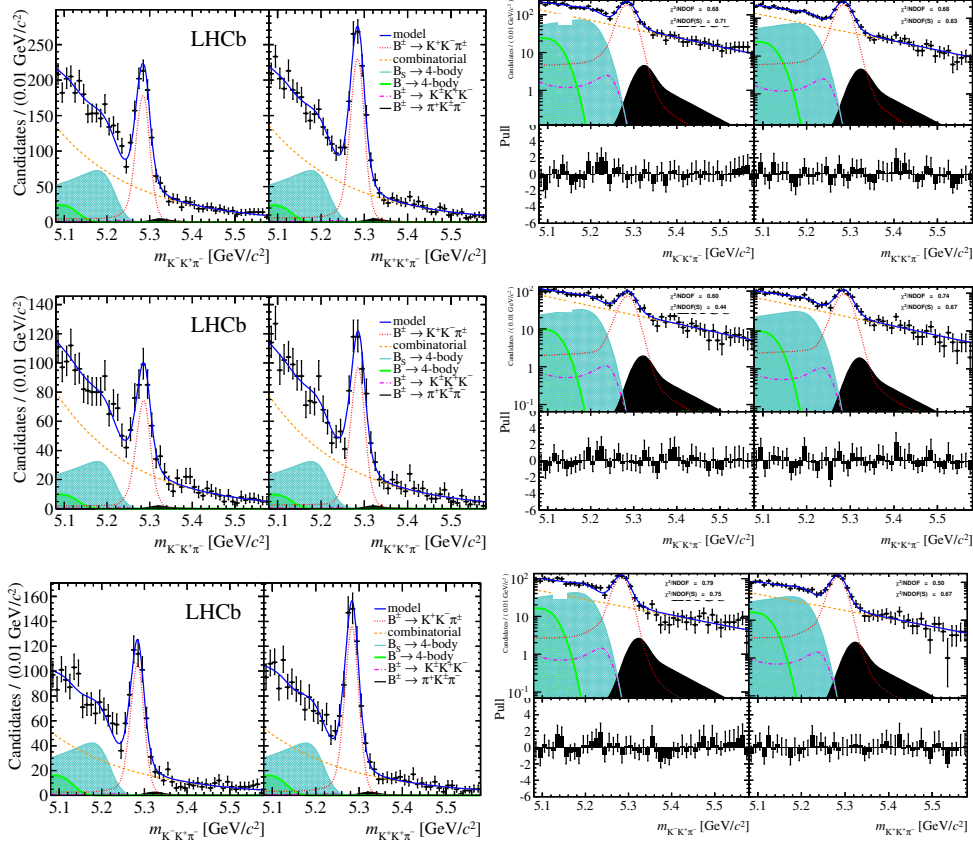


Figure 4.8: Result of the simultaneous fit to the 2011 data sample. Top row is the “Global_TIS or Hadron_TOS” trigger requirement, middle row the “Global_TIS and not Hadron_TOS” trigger requirement and the bottom plots the “Hadron_TOS” trigger selection. The plot of the right side is the same that of the left but in log scale with the pull distribution on the bottom pad. In each pair of distributions, the plot on the left is B^- and on the right is B^+ .

In order to obtain a high purity sample for the amplitude analysis, a mass window of ± 17 MeV (from 5266 to 5300 MeV/c^2) around the peak of the signal PDF is chosen as the signal region. Table 4.11 shows the integral of each fit model component at this region. From these results we observe that the more prominent background contributions come from the combinatorial background and from the peaking background $B^\pm \rightarrow K^\pm \pi^+ \pi^-$. As we will see in Section 6.4, these contributions are properly considered as we need to model their distribution in the Dalitz plot when doing the Dalitz plot fit.

The projection of the events in the $B^+ \rightarrow \pi^+ K^- K^+$ and $B^- \rightarrow \pi^- K^+ K^-$ Dalitz plot, for the selected signal window, are shown in Figs. 4.11 and 4.11(b).

For the measurements of CP violation asymmetries in a model-independent analysis, described in the following chapter and performed much earlier than the amplitude analysis, the samples are slightly different. There are some differences related to chosen PDF functions, for example a Cruijff

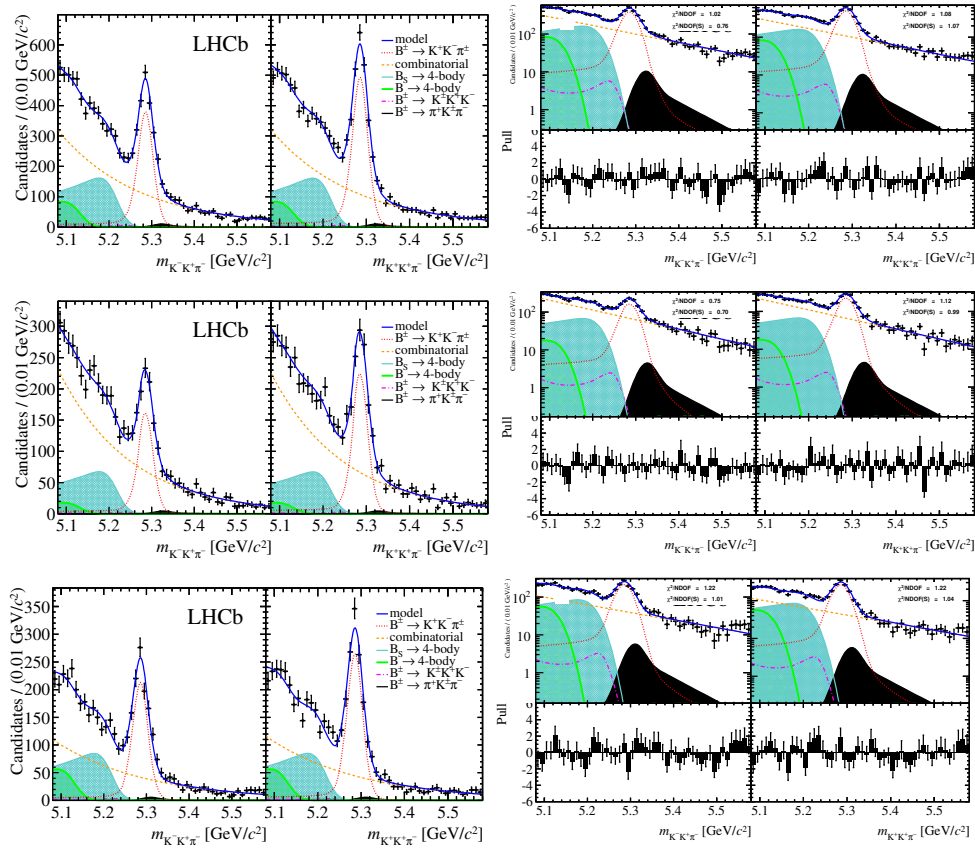


Figure 4.9: Result of the simultaneous fit to the 2012 data sample. Top row is the “Global_TIS or Hadron_TOS” trigger requirement, middle row the “Global_TIS and not Hadron_TOS” trigger requirement and the bottom plots the “Hadron_TOS” trigger selection. The plot of the right side is the same that of the left but in log scale with the pull distribution on the bottom pad. In each pair of distributions, the plot on the left is B^- and on the right is B^+ .

function [65] was used for the signal and for the peaking backgrounds. The fiducial cuts were still not introduced, and the charm veto in the KK system was from 1.834 to 1.894 GeV/c^2 .

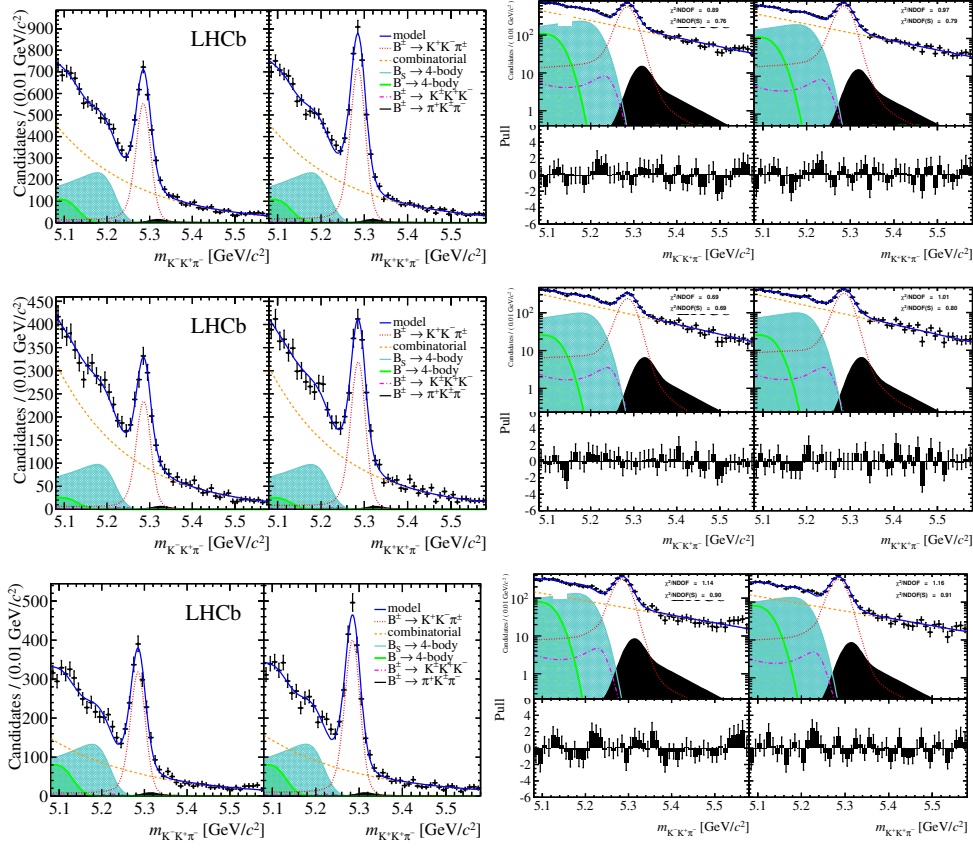


Figure 4.10: Result of the simultaneous fit to the combined 2011 and 2012 data samples. Top row is the “Global_TIS or Hadron_TOS” trigger requirement, middle row the “Global_TIS and not Hadron_TOS” trigger requirement and the bottom plots the “Hadron_TOS” trigger selection. The plot of the right side is the same that of the left but in log scale with the pull distribution on the bottom pad. In each pair of distributions, the plot on the left is B^- and on the right is B^+ .

Table 4.9: Floating parameters of the simultaneous fit to the 2012 data sample regarding to Figure 4.9.

Parameters	TOS or TIS	TIS not TOS	TOS
signal			
C^μ	1.0006 ± 0.0001	1.0012 ± 0.0001	0.9982 ± 0.0001
C^σ	1.14 ± 0.04	1.15 ± 0.04	1.15 ± 0.04
A_{RAW}	$-0.1307^{+0.0202}_{-0.0197}$	$-0.1649^{+0.0321}_{-0.0321}$	$-0.1059^{+0.0259}_{-0.0259}$
N_S	$4552.8^{+115.8}_{-152.1}$	$1968.7^{+80.8}_{-79.4}$	$2510.1(-69.460, 71.072)^{+71.1}_{-69.5}$
combinatorial			
b	-0.0053 ± 0.0007	-0.0059 ± 0.0001	$-0.0049 + / - 0.00016265$
N_{comb}	11222.0 ± 736.5	7282.2 ± 265.4	4359.9 ± 147.5
A_{asym}	-0.0035 ± 0.0129	0.0127 ± 0.0149	-0.0273 ± 0.0218
$B_s^0 \rightarrow 4\text{-body}$ (partially rec. component)			
Fraction [%]	1.827 ± 0.144	1.762 ± 0.186	1.742 ± 0.095
$B \rightarrow 4\text{-body}$ (partially rec. component)			
Fraction [%]	0.404 ± 0.091	0.199 ± 0.080	0.494 ± 0.057

Table 4.10: Floating parameters of the simultaneous fit to the 2011 and 2012 data sample regarding to Figure 4.10.

Parameters	TOS or TIS	TIS not TOS	TOS
signal			
C^μ	0.9997 ± 0.0001	1.0002 ± 0.0002	1.0005 ± 0.0001
C^σ	1.21 ± 0.04	1.12 ± 0.07	1.04 ± 0.05
A_{RAW}	$-0.1307^{+0.0168}_{-0.0169}$	$-0.1303^{+0.0478}_{-0.0479}$	$-0.1245^{+0.0375}_{-0.0377}$
N_S	$6516.4^{+175.6}_{-174.4}$	$844.5^{+47.8}_{-45.2}$	$1142.1^{+47.2}_{-47.3}$
combinatorial			
b	-0.0053 ± 0.0002	-0.0056 ± 0.0005	-0.0050 ± 0.0002
N_{comb}	15966.0 ± 845.5	2657.0 ± 119.7	1936.6 ± 97.8
A_{asym}	-0.0033 ± 0.0108	0.0135 ± 0.0255	-0.0297 ± 0.0326
$B_s^0 \rightarrow 4\text{-body}$ (partially rec. component)			
Fraction [%]	1.833 ± 0.118	1.977 ± 0.200	1.904 ± 0.146
$B \rightarrow 4\text{-body}$ (partially rec. component)			
Fraction [%]	0.364 ± 0.075	0.257 ± 0.117	0.312 ± 0.083

Table 4.11: Number of events of the different components per year in the signal region ($[5266, 5300]$ MeV/ c^2). Their relative percentage contribution is also shown.

Channels	TIS or TOS		TIS not TOS		TOS	
2011						
$B^\pm \rightarrow \pi^\pm K^- K^+$	1180	(78.20%)	490	(72.70%)	690	(82.93%)
Combinatorial	309	(20.48%)	174	(25.81%)	130	(15.63%)
$B^\pm \rightarrow K^\pm K^+ K^-$	4	(0.26%)	2	(0.30%)	2	(0.24%)
$B^\pm \rightarrow K^\pm \pi^+ \pi^-$	12	(0.80%)	6	(0.89%)	8	(0.96%)
$B_s^0 \rightarrow 4\text{-body}$	4	(0.26%)	2	(0.30%)	2	(0.24%)
$B \rightarrow 4\text{-body}$	0	(0.00%)	0	(0.00%)	0	(0.00%)
Total Yield	1509	(100.00%)	674	(100.00%)	832	(100.00%)
Data	1503		677		826	
2012						
$B^\pm \rightarrow \pi^\pm K^- K^+$	2542	(76.31%)	1120	(69.91%)	1400	(80.55%)
Combinatorial	743	(22.31%)	464	(28.96%)	298	(17.15%)
$B^\pm \rightarrow K^\pm K^+ K^-$	8	(0.24%)	4	(0.25%)	2	(0.11%)
$B^\pm \rightarrow K^\pm \pi^+ \pi^-$	30	(0.90%)	10	(0.63%)	34	(1.96%)
$B_s^0 \rightarrow 4\text{-body}$	8	(0.24%)	4	(0.25%)	4	(0.23%)
$B \rightarrow 4\text{-body}$	0	(0.00%)	0	(0.00%)	0	(0.00%)
Total Yield	3331	(100.00%)	1602	(100.00%)	1738	(100.00%)
Data	3345		1605		1740	
2011 + 2012						
$B^\pm \rightarrow \pi^\pm K^- K^+$	3706	(76.63%)	1608	(70.59%)	2103	(81.89%)
Combinatorial	1056	(21.84%)	642	(28.18%)	413	(16.08%)
$B^\pm \rightarrow K^\pm K^+ K^-$	6	(0.12%)	6	(0.26%)	2	(0.08%)
$B^\pm \rightarrow K^\pm \pi^+ \pi^-$	56	(1.16%)	16	(0.71%)	42	(1.64%)
$B_s^0 \rightarrow 4\text{-body}$	12	(0.25%)	6	(0.26%)	8	(0.31%)
$B \rightarrow 4\text{-body}$	0	(0.00%)	0	(0.00%)	0	(0.00%)
Total Yield	4836	(100.00%)	2278	(100.00%)	2568	(100.00%)
Data	4848		2282		2566	

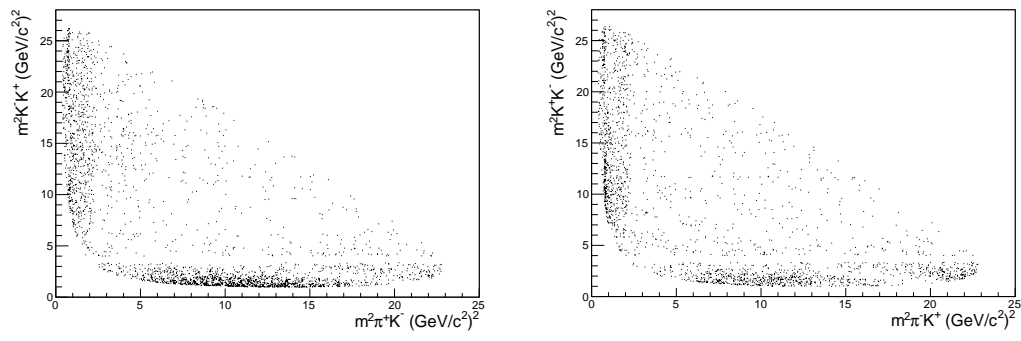


Figure 4.11: (a) Dalitz Plot for $B^+ \rightarrow \pi^+K^-K^+$ and (b) for $B^- \rightarrow \pi^-K^+K^-$ in the selected signal region.

5

CP violation measurements

One of the motivations for doing the amplitude analysis of $B^\pm \rightarrow \pi^\pm K^- K^+$ is driven by the results obtained in the work: “*CP* violation measurements in the phase space of charmless three body $B^\pm \rightarrow h^\pm h^- h^+$ decays” [22]. These *CP* violation studies are the result of a joined effort between researchers and students of the LHCb-Rio group (from CBPF, UFRJ and PUC-Rio). For the first part of my PhD, I have actively participated in this analysis. My main task was the construction of the signal efficiency model for all the $B^\pm \rightarrow h^\pm h^- h^+$ channels, needed in the computation of the *CP* asymmetry, as we will see in this chapter.

The results are very interesting and can be separated in two parts. The first part is related to the non-zero global inclusive *CP* asymmetry found in the phase space of all the $B^\pm \rightarrow h^\pm h^- h^+$ decays. Besides this, and as second part of the results, very interesting and unexpected large *CP* asymmetries in regions of the phase space were also observed. In this chapter the discussion of these results are presented with special emphasis to the $B^\pm \rightarrow \pi^\pm K^- K^+$ decay. We also discuss how these results call for an amplitude analysis for a better understanding of the origin of these asymmetries.

5.1

The charmless $B^\pm \rightarrow h^\pm h^- h^+$ decays

Charmless three-body B decays constitute an interesting scenario for the search of the possible sources of *CP* violation [66, 67, 68, 69], through the signatures left in the Dalitz plot. The four channels analyzed are very sensitive to *CP* violation effects [70, 71, 72] as their main contributing diagrams proceed through transitions of the type $b \rightarrow s(d)$ (penguin diagram) and $b \rightarrow u$ (tree diagram) and thus potentially leading to the interference of resonant intermediate states with different weak and strong phases [20] [73]. The four channels analyzed are $B^\pm \rightarrow \pi^\pm \pi^+ \pi^-$, $B^\pm \rightarrow K^\pm K^+ K^-$, $B^\pm \rightarrow K^\pm \pi^+ \pi^-$ and $B^\pm \rightarrow \pi^\pm K^- K^+$. The tree and penguin diagrams for these decays are shown in Figs. 5.1 and 5.2. The weak phase appearing in the tree-level contribution is the CKM angle. The strong phases can be due to different reasons. One possibility is attributed to the strong interaction between intermediate states of the decay, inducing local *CP* asymmetries in the presence of weak phases [74, 75]. Another possibility is *CP* violation induced

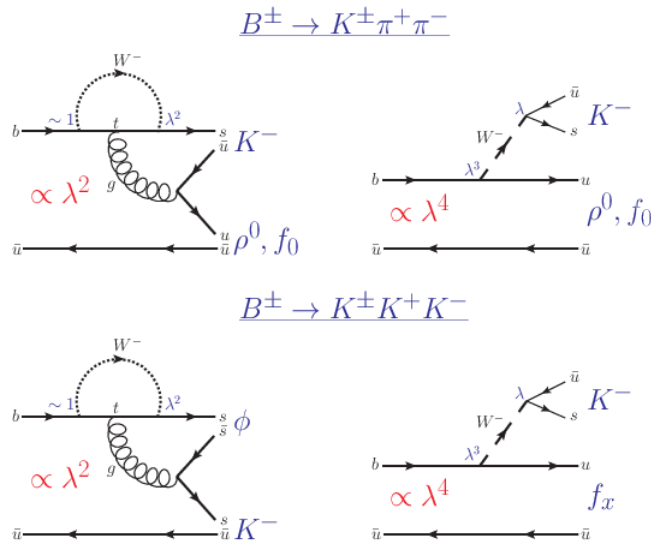


Figure 5.1: Tree and penguin diagrams for $B^\pm \rightarrow K^\pm \pi^+ \pi^-$ (top) and $B^\pm \rightarrow K^\pm K^+ K^-$ (bottom).

by the rescattering process $\pi\pi \leftrightarrow KK$ which manifests between coupled channels [76, 75, 77] like $B^\pm \rightarrow \pi^\pm K^- K^+$ and $B^\pm \rightarrow \pi^\pm \pi^+ \pi^-$.

5.1.1

The prelude for the CP asymmetry computation

The CPV measurements are performed with the Run I data collected by LHCb, which consists of a integrated luminosity of 3.0 fb^{-1} of pp collisions. Since the topology of the four channels is similar, the event selection for the four decay modes follow the same strategy and a full description can be found in [22] and on chapter 4.3 of this thesis.

The mode, $B^\pm \rightarrow J/\psi K^\pm$, used as a control sample [78] for the computation of the CP asymmetry, undergoes the same selection criteria as the applied to the four channels, except for the PID imposition, which is only applied to the kaon, and with the selection of the $m_{\pi\pi}$ phase space that contains the J/ψ decaying into $\mu\mu$.

5.1.2

The CP asymmetry

Once the final selection of the candidates has been made, the next step is to parameterize the mass spectra to obtain the signal yield and calculate the raw asymmetry. To this purpose a simultaneous unbinned extended maximum likelihood fit is performed for the mass region $5080\text{-}5580 \text{ MeV}/c^2$, where the signal and the background components (combinatorial, peaking and partially reconstructed backgrounds) are parameterized with probability density func-

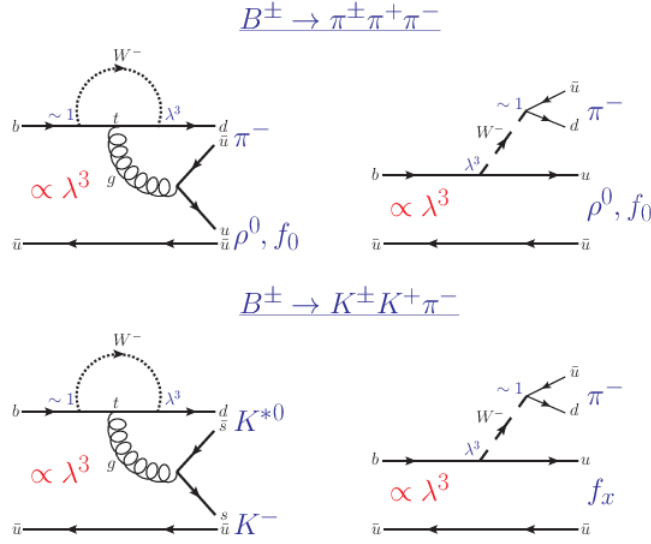


Figure 5.2: Tree-level and penguin diagrams for $B^\pm \rightarrow \pi^\pm \pi^+ \pi^-$ (top) and $B^\pm \rightarrow \pi^\pm K^- K^+$ (bottom).

tions (PDF), pretty much in the same way described in the previous chapter.

The raw asymmetry is defined as:

$$A'_{\text{raw}} = \frac{N_{B^-} - N_{B^+}}{N_{B^-} + N_{B^+}}, \quad (5-1)$$

where N_{B^-} and N_{B^+} are the number of events for B^- and B^+ respectively, which are obtained from the mass spectra fit. The A'_{raw} is due not only to CP violation. An acceptance correction has to be applied and other considerations like the B -meson production asymmetry and the interaction of the final state particles with matter, have to be taken into account in order to compute the CP asymmetry. The acceptance correction is applied through a factor R which is calculated from the signal efficiency models constructed for the decays modes. It is defined as $R = \frac{\langle \epsilon^- \rangle}{\langle \epsilon^+ \rangle}$, where ϵ^\pm is a data-weighted harmonic average efficiency. The raw asymmetry corrected by the acceptance is thus given by:

$$A_{\text{raw}} = \frac{N_{B^-}/R - N_{B^+}}{N_{B^-}/R + N_{B^+}}. \quad (5-2)$$

Writing down the explicitly form for number of events N_{B^-} and N_{B^+} we get:

$$N_{B^+} = (1 - A_{CP})(1 - A_D)(1 - A_P) \frac{N_S}{2}, \quad (5-3)$$

$$N_{B^-} = (1 + A_{CP})(1 + A_D)(1 + A_P) \frac{N_S}{2} R, \quad (5-4)$$

where A_{CP} is the asymmetry due to CP violation, A_P is the production

asymmetry, R is the correction factor as indicated above and considers the differences in the detection efficiency for B^+ and B^- , A_D is the detection asymmetry and takes into account the differences between negative and positive particle interaction with matter which cannot be properly represented using simulation samples and N_S represents the total number of events from the fit.

If we replace N_{B^-} and N_{B^+} in the Equation 5-2, A_{raw} can be written as:

$$A_{\text{raw}} = \frac{A_{CP} + A_P + A_D^{h'} + A_{CP}A_PA_D^{h'}}{1 + A_{CP}A_P + A_{CP}A_D^{h'} + A_PA_D^{h'}}. \quad (5-5)$$

For small asymmetries this expression can be simplified by neglecting the terms composed by the multiplication of two or three asymmetries. This lead thus to the following approximation:

$$A_{\text{raw}} \approx A_{CP} + A_P + A_D^{h'}, \quad (5-6)$$

where $A_D^{h'}$ denotes here the detection asymmetry according to the decay final state. The four decay modes can be separated into two categories. One that considers the decay modes that have the two charge-conjugate hadrons $h^+h^- = \pi^+\pi^-$ or K^+K^- in their final state with an unpaired kaon, namely, $B^\pm \rightarrow K^\pm K^+ K^-$ and $B^\pm \rightarrow K^\pm \pi^+ \pi^-$, then $A_D^{h'} = A_D^K$, and the other one that accounts for the decay modes that have the two charge-conjugate hadrons h^+h^- with a pion as the unpaired hadron, leading thus to $A_D^{h'} = A_D^\pi$. The decay modes that fall into the last category are $B^\pm \rightarrow \pi^\pm \pi^+ \pi^-$ and $B^\pm \rightarrow \pi^\pm K^- K^+$.

Following this separation, the A_{CP} can be calculated as:

$$A_{CP}(Khh) = A_{\text{raw}}(Khh) - A_P - A_D^K = A_{\text{raw}}(Khh) - A_\Delta, \quad (5-7)$$

$$A_{CP}(\pi hh) = A_{\text{raw}}(\pi hh) - A_P - A_D^\pi = A_{\text{raw}}(\pi hh) - A_\Delta + A_D^K - A_D^\pi, \quad (5-8)$$

where A_Δ was measured using the control sample with about 2.65×10^5 of $B^\pm \rightarrow J/\psi(\mu^+\mu^-)K^\pm$ decays. This correction is calculated from the raw asymmetry of $B^\pm \rightarrow J/\psi K^\pm$, as:

$$A_\Delta = A_{\text{raw}}(J/\psi K) - A_{CP}(J/\psi K), \quad (5-9)$$

where the world average for $A_{CP}(J/\psi K)$ is equal to $(0.1 \pm 0.7)\%$ [1]. The pion detection asymmetry was previously measured by the LHCb with a value of $A_D^\pi = (0.00 \pm 0.25)\%$ [79]. On the other hand, the kaon detection asymmetry was obtained using a sample of D^0 decays [80], resulting in $A_D^K = (-1.26 \pm 0.18)\%$.

Finally, the production asymmetry is calculated from the same sample of the control channel $B^\pm \rightarrow J/\psi K^\pm$, expressed as $A_P = A_\Delta - A_D^K$.

It is important to remark that the data was separated by trigger configuration, TIS and TOS, to take into consideration any asymmetry induced by the hadronic trigger (hardware level). The CP asymmetry is then calculated by trigger configuration using the expressions on Equations 5-7, 5-8 and 5-9, applied to the acceptance corrected raw asymmetry. The CP asymmetry for each decay mode is obtained as the weighted average of the asymmetries per trigger configuration and year, taking into account the possible correlations between the trigger samples.

The total integrated CP asymmetry found for the four channels are:

$$\begin{aligned} A_{CP}(B^\pm \rightarrow K^\pm \pi^+ \pi^-) &= +0.025 \pm 0.004 \pm 0.004 \pm 0.007, \\ A_{CP}(B^\pm \rightarrow K^\pm K^+ K^-) &= -0.036 \pm 0.004 \pm 0.002 \pm 0.007, \\ A_{CP}(B^\pm \rightarrow \pi^\pm \pi^+ \pi^-) &= +0.058 \pm 0.008 \pm 0.009 \pm 0.007, \\ A_{CP}(B^\pm \rightarrow \pi^\pm K^+ K^-) &= -0.123 \pm 0.017 \pm 0.012 \pm 0.007, \end{aligned}$$

where the first uncertainty is statistical, the second uncertainty is due to systematic effects, and the third is because of our limited knowledge of the CP asymmetry of $B^\pm \rightarrow J/\psi K^\pm$.

Notice that the largest asymmetry found corresponds to our signal $B^\pm \rightarrow \pi^\pm K^- K^+$ with about -12% and with a significance¹ of 5.6σ .

5.2 CP Asymmetry in regions of the phase space

One of the advantages of three body decays is that also allow the study of CP asymmetries in regions of the phase space. This provides more information about the possible sources of this phenomenon. From previous results obtained by the LHCb collaboration [69] [69], some theories have been discussed about these possible sources, one of these is the probability of asymmetry effects due to the rescattering process $\pi\pi \leftrightarrow KK$ [81].

In Fig. 5.3 it is shown the distribution of the raw asymmetry, A_{raw}^N , in bins of Dalitz plot, where A_{raw}^N is calculated as indicated in the expression 5-2, but with N^\pm being the number of events per bin [82, 83]. These asymmetries are calculated from the samples with background subtracted and acceptance corrected and the binning of the Dalitz plot is chosen to be adaptive in order to have the same number of events in each bin. These plots reveal rich structures, whose details lay in the origin of their dynamics. Notice that if there was no

¹The significance of this measurement is calculated as the ratio of the central value to the squared sum of the statistical and systematic uncertainties.

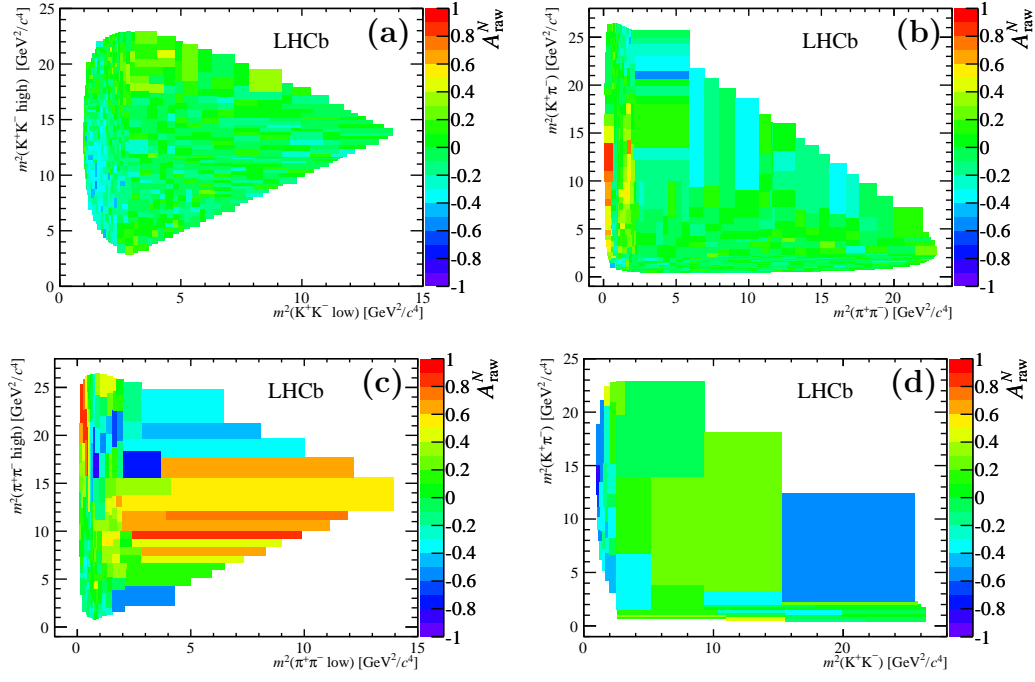


Figure 5.3: A_{raw}^N measured in bins of Dalitz plot with background subtracted and acceptance corrected for (a) $B^\pm \rightarrow K^\pm K^+ K^-$, (b) $B^\pm \rightarrow K^\pm \pi^+ \pi^-$, (c) $B^\pm \rightarrow \pi^\pm \pi^+ \pi^-$ e (d) $B^\pm \rightarrow K^\pm K^+ \pi^-$.

CP violation at all, what we should see is the Dalitz plots in a green color, A_{raw}^N fluctuating around zero. Nevertheless what it is found is that there are regions highlighted in red (or hot colors) meaning that there are more events of B^- than B^+ , and others regions in blue (or cold colors) meaning that there are more events of B^+ than B^- .

Exploring in more detail the distribution of these asymmetries in the $B^\pm \rightarrow \pi^\pm K^- K^+$ phase space, one region can be especially highlighted: the so-called rescattering region, which is defined from 1.0 to $(1.5)^2 \text{ GeV}^2/c^4$ in $m_{K^- K^+}^2$. The rescattering process $\pi\pi \leftrightarrow KK$, in the context of three body decays, means that a pair of mesons produced in the final state of a channel can appear in the final state of a related coupled channel by means of strong rescattering. A large CP asymmetry is observed for this region for $B^\pm \rightarrow \pi^\pm K^- K^+$ and this seems to have an intrinsic relation with this phenomenon. Large asymmetries were also found for this region for the others channels. Table 5.1 summarizes these results, where it is shown that the largest CP asymmetry found corresponds to $B^\pm \rightarrow \pi^\pm K^- K^+$ with about -33% .

From Table 5.1 it is observed that decays having two kaons in their final state, like $B^\pm \rightarrow \pi^\pm K^- K^+$, exhibits a negative CP asymmetry while those

Table 5.1: Number of signal candidates and charge asymmetries in the rescattering region $m(\pi^+\pi^-)$ or $m(K^+K^-)$ between 1.0 e 1.5 GeV/c^2

Decay	N_S	$A_{CP} \pm \sigma_{stat} \pm \sigma_{sist} \pm \sigma_{(J/\psi K^\pm)}$
$B^\pm \rightarrow K^\pm \pi^+ \pi^-$	$15\,562 \pm 165$	$+0.121 \pm 0.012 \pm 0.017 \pm 0.007$
$B^\pm \rightarrow K^\pm K^+ K^-$	$16\,992 \pm 142$	$-0.211 \pm 0.011 \pm 0.004 \pm 0.007$
$B^\pm \rightarrow \pi^\pm \pi^+ \pi^-$	4329 ± 76	$+0.172 \pm 0.021 \pm 0.015 \pm 0.007$
$B^\pm \rightarrow K^\pm K^+ \pi^-$	2500 ± 57	$-0.328 \pm 0.028 \pm 0.029 \pm 0.007$

with two pions in their final state, like its coupled channel² $B^\pm \rightarrow \pi^\pm \pi^+ \pi^-$, have a positive CP asymmetry. Even more, it was also observed that the amount of events gained by $B^+ \rightarrow \pi^+ K^- K^+$ with respect that to $B^- \rightarrow \pi^- K^+ K^-$ is in the same order of magnitude that the number of events lost by $B^+ \rightarrow \pi^+ \pi^- \pi^+$ in comparison with $B^- \rightarrow \pi^- \pi^+ \pi^-$.

Figure 5.4 shows the mass fit for the rescattering region for all channels, using the combined data 2011 and 2012. It is visually evident from these fits the difference between the number of events for B^+ (right) and B^- (left), and how the asymmetry is opposite in sign for a) $B^\pm \rightarrow K^\pm K^+ K^-$ and b) $B^\pm \rightarrow K^\pm \pi^+ \pi^-$ and for c) $B^\pm \rightarrow \pi^\pm \pi^+ \pi^-$ and d) $B^\pm \rightarrow \pi^\pm K^- K^+$.

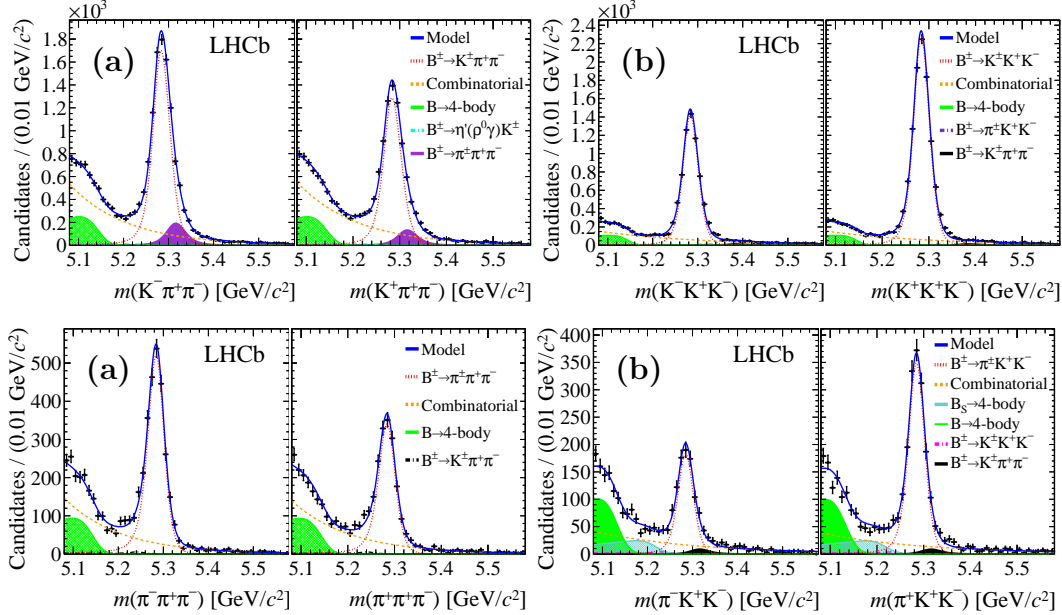


Figure 5.4: Invariant mass distribution in the rescattering region $m(\pi^+\pi^-)$ and $m(K^+K^-)$ between 1.0 a 1.5 GeV/c^2 for (a) $B^\pm \rightarrow K^\pm K^+ K^-$, (b) $B^\pm \rightarrow K^\pm \pi^+ \pi^-$, (c) $B^\pm \rightarrow \pi^\pm \pi^+ \pi^-$ and (d) $B^\pm \rightarrow \pi^\pm K^- K^+$. The left side of each figure shows the B^- candidates and the right side the B^+ candidates.

²Same behaviour was observed with the coupled channels $B^\pm \rightarrow K^\pm K^+ K^-$ and $B^\pm \rightarrow K^\pm \pi^+ \pi^-$.

The projection of data separated for B^+ and B^- in the two invariant masses $m_{\pi^+K^-}$ and $m_{K^+K^-}$ helps to put in evidence other regions of high asymmetries. Fig. 5.5 shows these projections in which the gray dashed lines represent the B^- events while the solid black lines the B^+ events. For $m_{\pi^+K^-}$ a clear asymmetry appears. For low values of $m_{\pi^+K^-}$ a peak of B^- events can be seen around $1 \text{ GeV}/c^2$, for high mass values where the angular projection of the of the resonant contributions of the KK system are present, the asymmetry is also evident. In $m_{K^+K^-}$ the prominent region of asymmetry is precisely that related to the rescattering process.

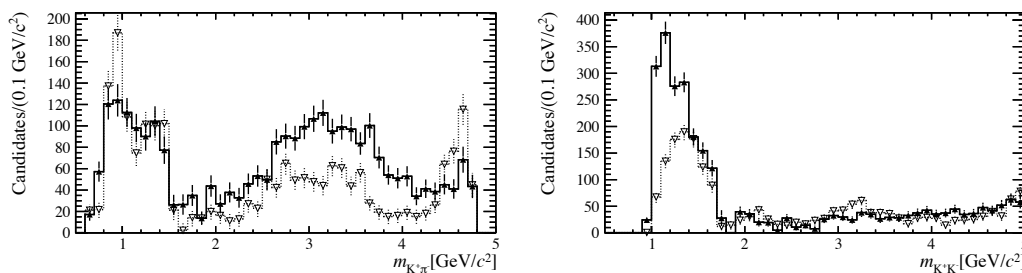


Figure 5.5: (a) Projection in the invariant mass $m_{\pi^+K^-}$ and (b) $m_{K^+K^-}$ of $B^\pm \rightarrow \pi^\pm K^- K^+$. The solid black line represents B^+ events and the gray dashed line B^- event.

In order to understand the origin of these large CP asymmetries, an amplitude analysis is required for all channels. The study of the resonant substructures that contribute to these decay modes and how they interfere with each other will shed light to understand the dynamic origin of the CP violation observed. The local CP asymmetry observed in the rescattering region for all channels is apparently related with the rescattering phenomena. This is of special interest for $B^\pm \rightarrow \pi^\pm K^- K^+$, since a large CP asymmetry is measured here and also, as this region is near the KK threshold, which is not expected to be populated by resonant contributions ($s\bar{s}$ resonances are not expected) thus the $B^\pm \rightarrow \pi^\pm K^- K^+$ mode can represent a great laboratory for the test of rescattering amplitudes. An interesting feature is related to the positive CP asymmetry observed for some channels and so, the negative asymmetry observed for their rescattering related channels. This seems to be a consequence of the CPT theorem, that requires that the sum of the partial widths of a family of decays that are related to each other by strong rescattering should be the same for particle and antiparticle [18].

6

The Dalitz plot formalism

The Dalitz plot analysis for a decay process is performed in order to reveal the dynamics and rich structures involved in the reaction. Different formalisms exist to this end, for instance: the Isobar Model Formalism, the Partial Wave analysis and the K-matrix theory.

The formalism used in the Dalitz plot analysis for $B^\pm \rightarrow \pi^\pm K^- K^+$ is the Isobar model and a more detailed description is presented in the following

6.1

The Isobar Model

The isobar model [84, 85] is the formalism conventionally used for the study of the resonant sub-structures of hadronic decays. It is a phenomenological approach that aims to describe the transition amplitude of decays proceeding through intermediate resonant states. In the case of a 3-body final state, a resonance plus a stable particle form a quasi two-body system that rapidly decays through strong interaction to the 3-body final state. A pictorial representation of this cascade process is shown in Fig. 6.1. The B meson decays into a resonant state R and to a stable pseudoscalar meson d_3 , usually referred as the bachelor. R then decays into two pseudoscalar mesons d_1 and d_2 .

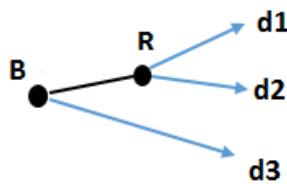


Figure 6.1: Scheme of a three-body decay B through an intermediate resonant state R .

6.1.1

The Decay Amplitude Construction

In general, the total decay amplitude can be represented as a sequence of independent amplitudes. Its construction takes into account the following considerations:

- Each two body process is associated to a Lorentz invariant amplitude that is consistent with momentum and angular momentum conservation in the interaction. It is constructed from the contraction of the available momentum and polarization 4-vectors.
- It includes a term that describes the resonance dynamics in the decay.
- Form Factors are also included to account for current limitations in describing low-energy strong interactions.

Altogether, the total decay amplitude for a 3-body decay is then represented in a general form as:

$$\mathcal{M}_R(B \rightarrow R(R \rightarrow d_1 d_2) d_3) = \langle d_1 d_2 | R_\lambda \rangle T_R \langle R_\lambda d_3 | B \rangle, \quad (6-1)$$

where λ is the helicity of the meson R , T_R is a function that represents the propagator of the resonance, usually taken as relativistic Breit-Wigner (more details will be given below), $\langle d_1 d_2 | R_\lambda \rangle$ represents the amplitude from the resonance state to the final state $d_1 d_2$ and $\langle R_\lambda d_3 | B \rangle$ from $B \rightarrow R d_3$.

If we first consider the special case of a vector meson intermediate state, and taking into account that the decay amplitude has to be Lorentz invariant and linear in the spin function, its construction can be derived from the scalar product of the available polarization vectors ϵ_λ^μ and the 4-momenta vectors p^μ . This leads to the expression of the transition amplitudes as:

$$\langle d_1 d_2 | R_\lambda \rangle = F_{R, d_1 d_2} (p_1 - p_2)_\nu \epsilon_\lambda^\nu, \quad (6-2)$$

$$\langle R_\lambda d_3 | B \rangle = F_{B, R d_3} (p_3)_\mu \epsilon_\lambda^\mu, \quad (6-3)$$

where $F_{R, d_1 d_2}$ and $F_{B, R d_3}$ are strong interaction form factors, p_1 , p_2 and p_3 are the 3-momenta of the daughter particles d_1 , d_2 and d_3 respectively. Putting all together and performing the sum over all the possible values of λ , which for a spin-1 resonance can take the values of ± 1 and 0, the total decay amplitude is expressed by:

$$\mathcal{M}_R(B \rightarrow R d_3 (R \rightarrow d_1 d_2)) = F_{R, d_1 d_2} F_{B, R d_3} \sum_\lambda \epsilon_\lambda^\mu \epsilon_\lambda^\nu (p_1 - p_2)_\nu (p_3)_\mu \times T_R, \quad (6-4)$$

From the completeness relation, the sum over the possible polarizations of the intermediate state, is given by:

$$\sum_{\lambda} \epsilon_{\lambda}^{*\mu} \epsilon_{\lambda}^{\nu} = -g^{\mu\nu} + \frac{p_R^{\mu} p_R^{\nu}}{p_R^2}, \quad (6-5)$$

where $g_{\mu\nu}$ is the Minkowski metric tensor. Eq. 6-5 can be reduced, in the reference frame of R , to the projection operator $P_1^{\mu\nu} = \delta^{ij}$. By using Eq. 6-5 in Eq. 6-4 in the resonance reference frame, where also $\vec{p}_1 = -\vec{p}_2$, the total amplitude can be rewritten as:

$$\mathcal{M}_R(B \rightarrow R d_3 (R \rightarrow d_1 d_2)) = F_{R,d_1 d_2} F_{B,R d_3} (-2\vec{p}_3 \cdot \vec{p}_1) \times T_R \quad (6-6)$$

The formalism above is for the particular case of a spin-1 resonance. It is desirable to have a general expression for the total decay amplitude regardless the resonance spin. Such formulation was developed by Charles Zemach using a tensor formalism [86, 87, 88]. In this sense the general form of \mathcal{M} is given by:

$$\mathcal{M}_R(B \rightarrow R d_3 (R \rightarrow d_1 d_2)) = F_{R,d_1 d_2} F_{B,R d_3} (-2|\vec{p}_3||\vec{p}_1|)^J P_J(\cos \theta_{13}) \times T_R, \quad (6-7)$$

where $P_J(\cos \theta_{13})$ is the Legendre polynomial of order J , and J is the spin of the resonance. θ_{13} is the angle between the particle d_1 and d_3 measured in the reference frame of R . The product $(-2|\vec{p}_3||\vec{p}_1|)^J P_J(\cos \theta_{13})$ represents the angular part of the decay amplitude. In Table 6.1 we show its expression for $J=0,1$ and 2.

It is important to remark that the resonant decay amplitude is a function of the squared invariant masses where the resonances contributions are expected. For our decay of analysis $B^{\pm} \rightarrow \pi^{\pm} K^{-} K^{+}$ this dependence will be explicitly indicated in the next section.

Resonance Spin	Angular distribution
0	1
1	$-2\vec{p}_3 \cdot \vec{p}_1$
2	$\frac{4}{3} [3(\vec{p}_3 \cdot \vec{p}_1) - (\vec{p}_3 \vec{p}_1)]$

Table 6.1: Angular distribution using Zemach tensor formalism.

6.1.2

Total decay amplitude for $B^\pm \rightarrow \pi^\pm K^- K^+$

The case mentioned above involves the situation in which a single resonant intermediate state is participating in the reaction. If we now consider the more general case in which the final state of a decay mode can be achieved through several different resonant states, the total decay amplitude can be written within the formalism of the Isobar Model as the coherent sum of the individual amplitudes of resonant and non-resonant contributing states.

For the particular case of $B^\pm \rightarrow \pi^\pm K^- K^+$ in which we expect resonant contributions in the $\pi^\pm K^\mp$ and $K^- K^+$ systems, the total decay amplitude \mathcal{A} and for its CP conjugate process $\bar{\mathcal{A}}$ can be expressed as:

$$\mathcal{A}(m_{\pi^+ K^-}^2, m_{K^- K^+}^2) = \sum_{i=1}^N c_i \mathcal{M}_{Ri}(m_{\pi^+ K^-}^2, m_{K^- K^+}^2), \quad (6-8)$$

$$\bar{\mathcal{A}}(m_{\pi^- K^+}^2, m_{K^+ K^-}^2) = \sum_{i=1}^N \bar{c}_i \bar{\mathcal{M}}_{Ri}(m_{\pi^- K^+}^2, m_{K^+ K^-}^2), \quad (6-9)$$

where $\mathcal{M}_{Ri}(m_{\pi^+ K^-}^2, m_{K^- K^+}^2)$ and $\bar{\mathcal{M}}_{Ri}(m_{\pi^- K^+}^2, m_{K^+ K^-}^2)$ are the resonant amplitudes for resonance i from a total of N , for B^+ and B^- respectively, given by Equation 6-6. c_i are complex coefficients that allow for different magnitudes and phases for the resonances involved in the decay. Notice that $c_i \neq \bar{c}_i$ to explicitly allow for CP violation.

In the following a more detailed discussion about the form factors and the resonance propagator present in the resonant decay amplitude, Equations 6-6, 6-9, will be presented.

6.1.3

Blatt-Weisskopf barrier factor

The introduction of form factors in the description of the hadronic decay amplitude accounts for penetration effects due to finite extend of the particles involved in the reaction.

The Blatt-Weisskopf barrier form factors [89] are taken to parametrize $F_{R,d_1 d_2}$ and F_{B,Rd_3} . Table 6.2 shows these factor for different spin values, and as a function of a variable z defined as: $z = |\vec{p}_1|d$ or $z = |\vec{p}_3|d$. Recall that $|\vec{p}_1|$ and $|\vec{p}_3|$ are the 3-momenta modulus of one of the particles that form resonance and of the bachelor, respectively, both measured in the rest frame of R . Finally d is the radius of penetration taken to be $4.0 \text{ GeV}^{-1} \approx 1 \text{ fm}$.

Spin value J	Barrier Factors ($F(z)$)
$J = 0$	1
$J = 1$	$\sqrt{\frac{(1+z_0^2)}{1+z^2}}$
$J = 2$	$\sqrt{\frac{(z_0^4+3z_0^2+9)}{z^4+3z^2+9}}$

Table 6.2: Blatt-Weisskopf barrier factor used to correct the amplitude for penetration effects where z_0 represents the value of z when the invariant mass is equal to the pole mass of the resonance.

6.1.4

Dynamical functions for resonances

As mentioned before, T_R in Eqs. 6-1, 6-6 and 6-7 represents the dynamical function or line shape used to describe the resonance's propagator. The possible parametrizations are not unique, the most interesting for this analysis are described below.

Breit-Wigner function The Breit-Wigner [90] is the lineshape more commonly used to describe resonances. It is an approximate model that offers a good description for narrow resonances e.g $K^*(892)$. Its expression is given by:

$$T_R(m_{ij}) = \frac{1}{m_R^2 - m_{ij}^2 - im_R \Gamma_{ij}(m_{ij})} \quad (6-10)$$

where m_{ij} is the two-body invariant mass corresponding to the two particles to which the resonance decays. For $B^\pm \rightarrow \pi^\pm K^- K^+$

it can correspond to $\pi^+ K^-$ or $K^- K^+$ systems. m_R is the nominal mass of the resonance R and $\Gamma_{ij}(m_{ij})$ is the mass dependent width. In the general case for a resonance decaying to spin-0 particles the latter can be expressed as:

$$\Gamma_{ij}(m_{ij}) = \Gamma_R \left(\frac{|\vec{p}_i|}{|\vec{p}_R|} \right)^{2J+1} \frac{m_R}{m_{ij}} (F^2(|\vec{p}_i|/d)). \quad (6-11)$$

where $|\vec{p}_i|$ denotes the resonance's daughter momentum and $|\vec{p}_R|$ is $|\vec{p}_i|$ for $m_{ij} = m_R$. The symbol Γ_R denotes the nominal width of the resonance. The values of m_R and Γ_R are obtained from PDG when they are well known.

Flatté parametrization The Flatté function [1] is commonly used for the description of resonances which invariant mass distribution is near to a

two-particle threshold. For example the light scalar mesons $f_0(980)$ and $a_0(980)$ are described by this function. Since their mass lie just below the K^-K^+ threshold, the parametrization is a modification of the relativistic Breit-Wigner distribution. The explicit form for $f_0(980)$ is given by:

$$T_{f_0(980)}(m_{K^-K^+}) = \frac{1}{m_{f_0}^2 - m_{K^-K^+}^2 - i[g_{f_0\pi^+\pi^-}^2 \rho_{\pi^+\pi^-}(m_{K^-K^+}) + g_{f_0K^-K^+}^2 \rho_{K^-K^+}(m_{K^-K^+})]}, \quad (6-12)$$

where $g_{f_0\pi^+\pi^-}^2$ and $g_{f_0K^-K^+}^2$ are respectively the $f_0(980)$ coupling constants to the $\pi^+\pi^-$ and K^-K^+ final states. $\rho_{ab}(m_{K^-K^+})$ and $\rho_{ab}(m_{\pi^+\pi^-})$ are phase space factors.

Flat non-resonant parametrization For a non-resonant decay, that is, when occurs the direct disintegration of the particle mother into three daughter particles, the most simple way to parametrize is using a flat function that populates equally the whole Dalitz Plot. This approach, however, totally ignores any dynamics involved in the decay.

Tobias non-resonant parametrization An alternative non-resonant parametrization uses a line shape involving a form factor of the type $(1 + \frac{s}{\Lambda^2})^{-1}$ as proposed in [77]. This form factor is a phenomenological description to parametrize the non-resonant amplitude emphasizing the region of low-energy production of the final state particles. In this sense this amplitude is more prominent in the pair threshold and suppressed for high energy regions. The parametrization is given by:

$$T_{nr}(m_{ij}^2) = \frac{1}{1 + \frac{m_{ij}^2}{\Lambda^2}}, \quad (6-13)$$

where Λ^2 is a free parameter. It can be used for both $m_{\pi^+K^-}^2$ and $m_{K^-K^+}^2$.

Parametrization for re-scattering process To parametrize a re-scattering amplitude in the context of three-body decays, it is important to take into account several features to its description. One of these is the function that describes its origin or source and the other one is the functional form of the elements of the transition amplitude. The concept of the rescattering $\pi\pi \rightarrow KK$ was developed within the context of two-body interactions. For three-body decays, it means that a pair of mesons produced in one channel will appear in the final state of a coupled channel. The phenomenological form factor that accounts for the source term is proposed in [77]. If we are interested in parameterizing

the rescattering amplitude for the process $\pi\pi \rightarrow KK$, the source term will read as:

$$\mathcal{A}_{source}(m_{K^-K^+}^2) = \frac{1}{1 + \frac{m_{K^-K^+}^2}{\Delta_{\pi\pi}^2}}, \quad (6-14)$$

where $\Delta_{\pi\pi}^2$ is a free parameter. In similar sense, the parametrization of the source term for the rescattering process $KK \rightarrow \pi\pi$ will be described by Equation 6-14 with Δ_{KK}^2 instead of $\Delta_{\pi\pi}^2$. The idea is to describe the partonic interaction (quark level tree and penguin diagrams) that produces the three mesons, which in principle should be different for the mesons pair $\pi\pi$ and KK . The total rescattering amplitude in B three-body decay is then expressed as:

$$\mathcal{A}_{scatt} = \mathcal{A}_{source} f_{rescattering}, \quad (6-15)$$

where $f_{rescattering}$ represents the rescattering amplitude of the S-wave in $I(isospin) = 0$ and $J = 0$, where the coupling between $\pi\pi \rightarrow KK$ was known to be important especially above the KK threshold. For others waves the KK channel was found to be weakly coupled [2].

The couple channel description includes elastic terms, i.e. $\pi\pi \rightarrow \pi\pi$ and $KK \rightarrow KK$, and the inelastic one $\pi\pi \rightarrow KK$, which in the two-body context should be symmetric by time reversal. The transition amplitude (T) is intrinsically related to the unitary S matrix by $S = 1 + iT$. The S matrix for the $\pi\pi$ and KK couple channel can be written as:

$$S = \begin{bmatrix} \eta e^{2i\delta_{\pi\pi}} & i\sqrt{1-\eta^2} e^{i(\delta_{\pi\pi}+\delta_{KK})} \\ i\sqrt{1-\eta^2} e^{i(\delta_{\pi\pi}+\delta_{KK})} & \eta e^{2i\delta_{KK}} \end{bmatrix} \quad (6-16)$$

where $\delta_{\pi\pi}$ and δ_{KK} are phase-shifts and η is the inelasticity, assumed to be unity for $\pi\pi$ while the KK channel is not open and smaller than 1 if the KK channel contributes. For the purpose of our amplitude analysis we need the non-diagonal rescattering amplitude that can be directly extracted from the full S-matrix above. However, the problem is how to described the phase-shifts and the inelasticity, which requires a model. For that purpose, we use in this analysis the parametrizations for the inelasticity and phase-shifts defined by Pelaez and Ynduráin [2] in 2005, as these phenomenological functions has been successfully tested to satisfy the important properties of unitarity and analyticity.

Their functional form for $I = 0$ S wave for the energy range 950 MeV

and 1420 MeV is defined as:

$$\cot \delta_0^{(0)}(s) = c_0 \frac{(s - M_s^2)(M_f^2 - s)}{M_f^2 s^{1/2}} \frac{|k_2|}{k_2^2}, \quad k_2 = \frac{\sqrt{s - 4m_K^2}}{2}; \quad (6-17)$$

$$\eta_0^{(0)} = 1 - \left(\epsilon_1 \frac{k_2}{s^{1/2}} + \epsilon_2 \frac{k_2^2}{s} \right) \frac{M'^2 - s}{s}. \quad (6-18)$$

where

$$\begin{aligned} c_0 &= 1.3 \pm 0.5, & M_f &= 1.320 \pm 50 \text{ GeV}; & M_s &= 0.920 \text{ GeV} \\ \epsilon_1 &= 2.4, & \epsilon_2 &= -5.5; & M' &= 1.5 \text{ GeV}. \end{aligned} \quad (6-19)$$

In Figure 6.2 the inelasticity η_0^0 and phase shift δ_0^0 is shown, evaluated with the parameters values given by Equation 6-19. As it can be observed the inelastic regimen goes for values of $m(K^- K^+)$ that are between ~ 1 GeV to 1.5 GeV where η_0^0 is positive and lower than one.

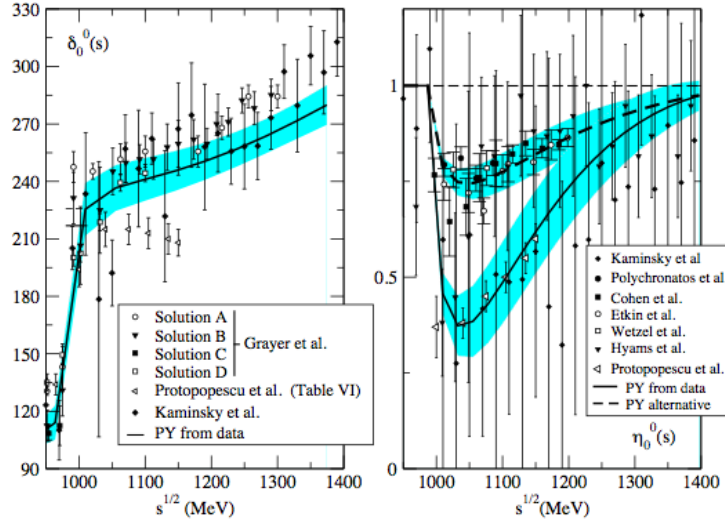


Figure 6.2: (left) Phase shift δ_0^0 and (right) Inelasticity η_0^0 as a function of $m(K^- K^+)$. Figure extracted from [2]

The parameters regarding to the description of the line shapes are all fixed in the Dalitz plot fit unless otherwise is stated. In Figures 6.3, 6.4 and 6.5 we show simulations of the Dalitz plot distributions for some of the possible resonances through which $B^\pm \rightarrow \pi^\pm K^- K^+$

may proceed, as was explained on section 2.7. They are parametrized with the various lineshapes described before and are obtained by taking $|\mathcal{M}_{Ri}|^2$ the probability density function. In the first column it is presented the Dalitz plot distribution, in the second column the projection onto $m_{\pi^+K^-}^2$ and in the third column projection onto $m_{K^-K^+}^2$. For Figure 6.3 and 6.4 all the resonances are parametrized using the Breit-Wigner lineshape. In Figure 6.5 other parametrization corresponding to non-resonant, flatté, Tobias non-resonant and rescattering lineshape are presented, respectively, from top to bottom.

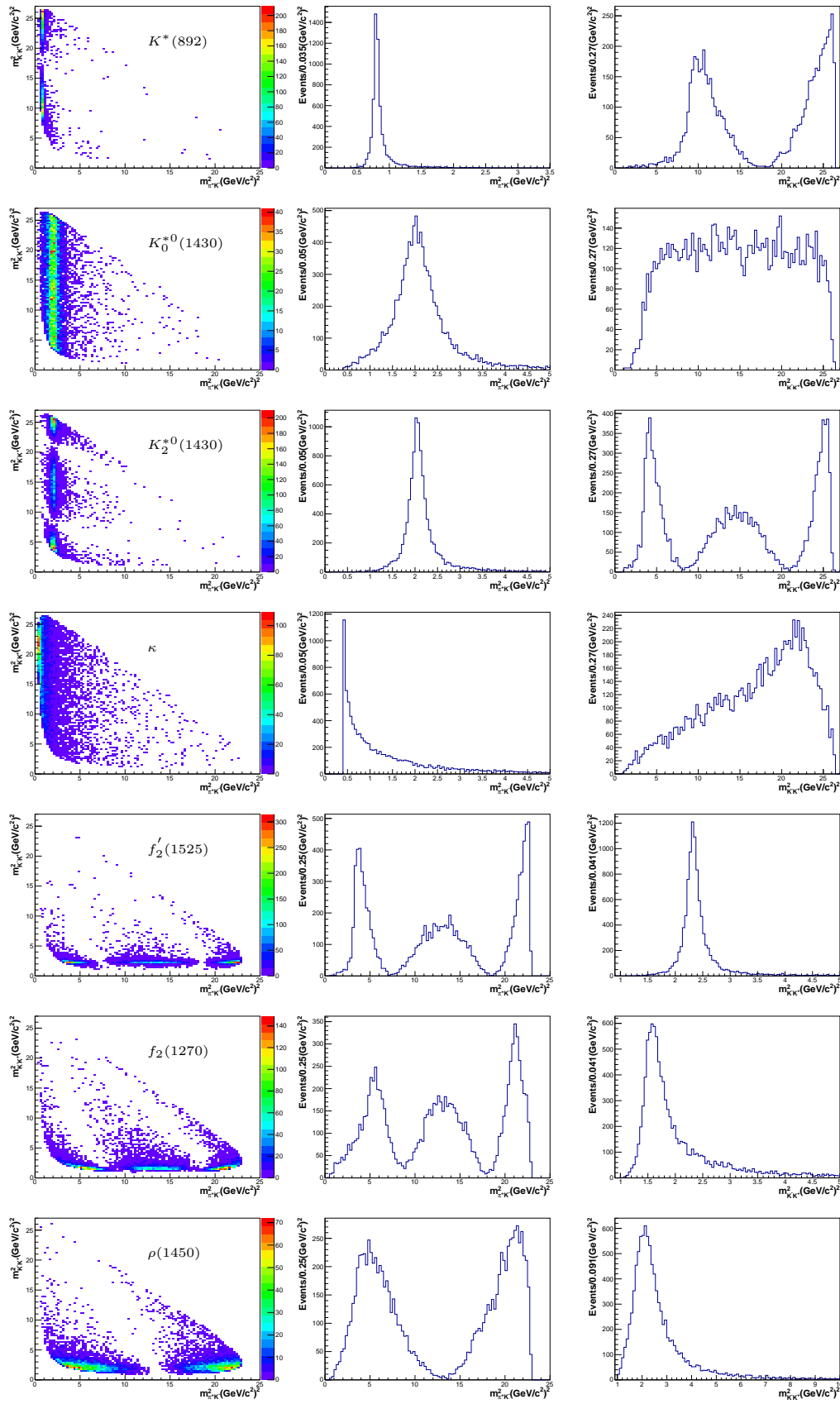


Figure 6.3: Possible resonance contributions in the $B^\pm \rightarrow \pi^\pm K^- K^+$ phase space. Resonances are parametrized using the Breit-Wigner lineshape.

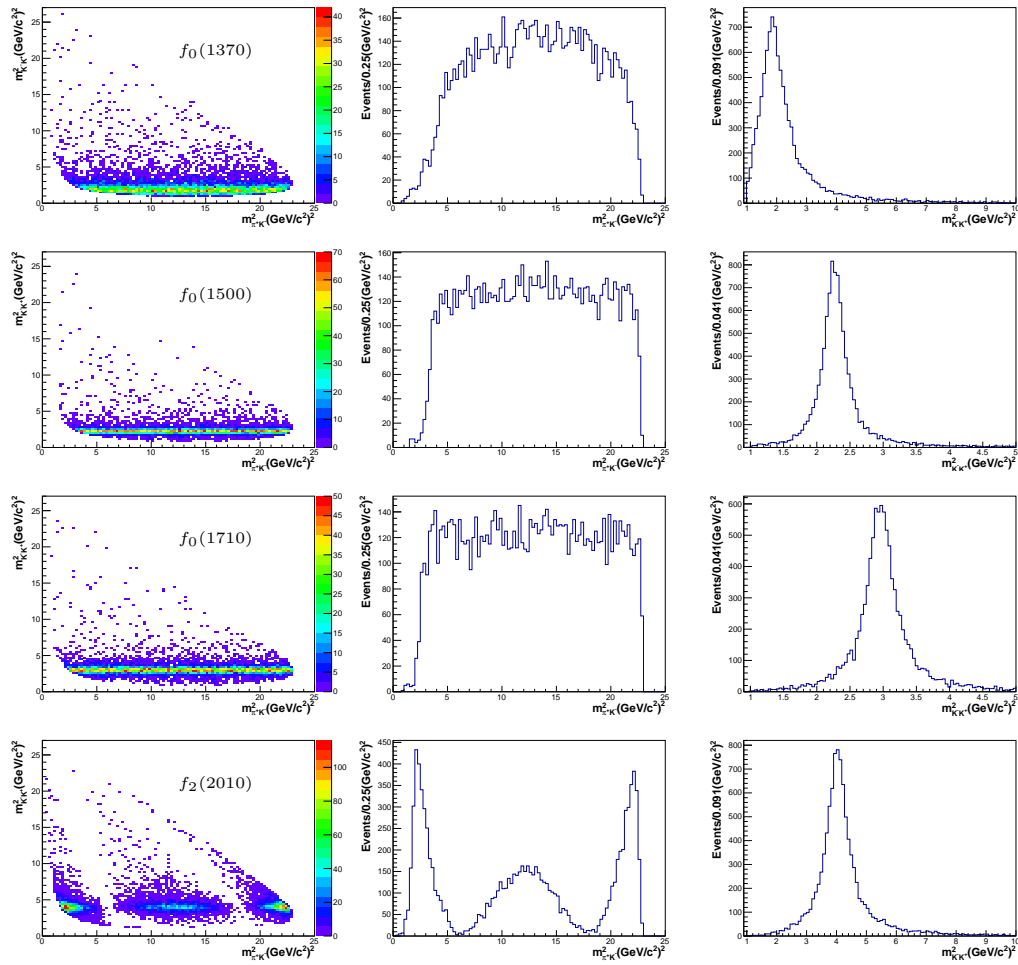


Figure 6.4: Possible resonance contributions in the $B^\pm \rightarrow \pi^\pm K^- K^+$ phase space. Resonances are parametrized using the Breit-Wigner lineshape.

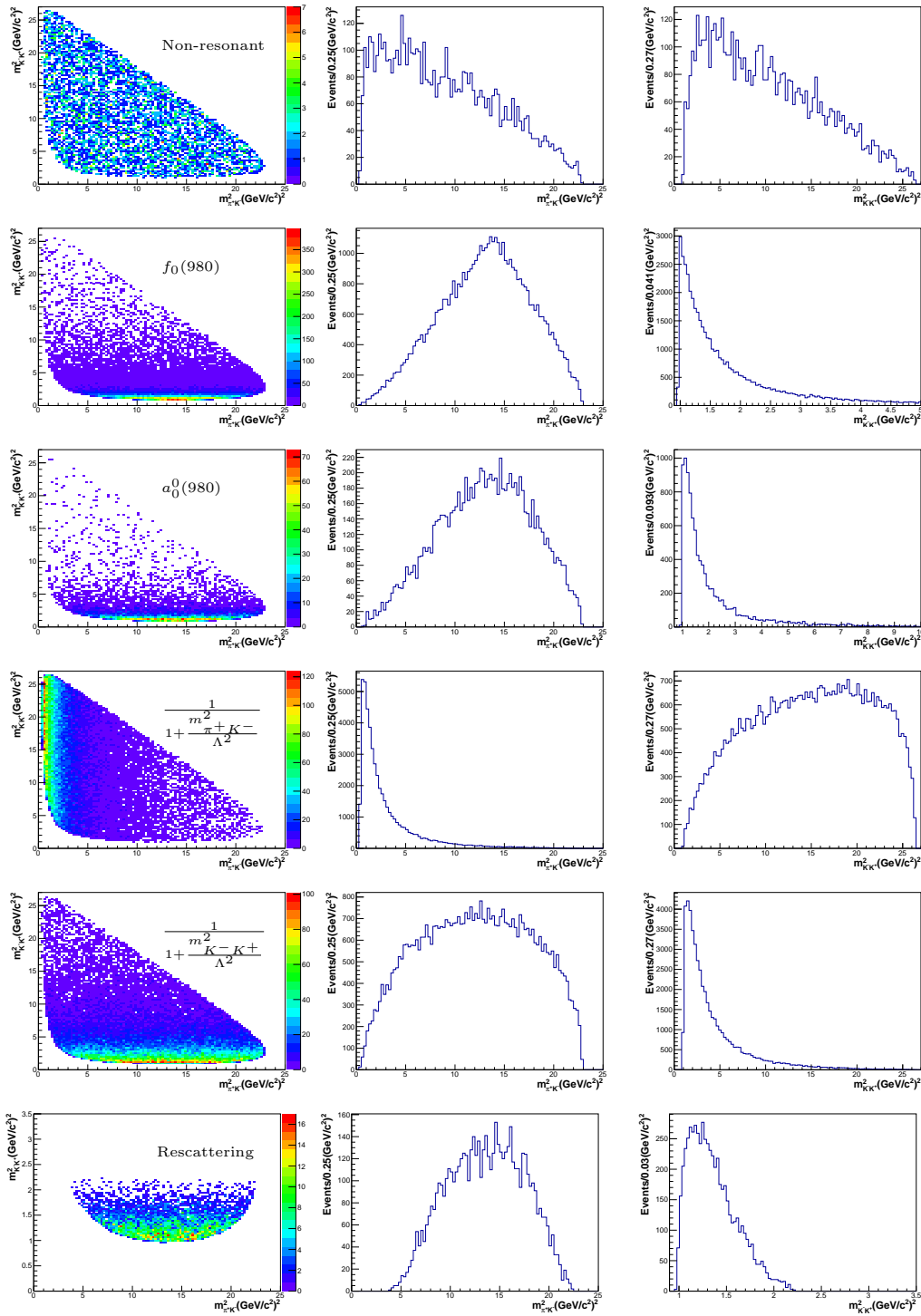


Figure 6.5: Possible resonance contributions in the $B^\pm \rightarrow \pi^\pm K^- K^+$ phase space. The non-resonant parametrization is used in the first row, the Flatté parametrization for the second and third row, The Tobias NR parametrization for the fourth and fifth row, and in the sixth row, the re-scattering parametrization.

6.2

The Dalitz plot Fit

As mentioned in Section 2.8 the main feature of the Dalitz plot of a three-body decay is that the decay rate is proportional to the square of its total decay amplitude with no extra phase space factors, and so, the dynamics involved in the reaction are reflected directly in the distribution of the events in the Dalitz plot. The possible resonant contributions appear as bands in the Dalitz plot, with characteristic angular distributions led by their spin, as explained in the previous chapter. These resonant states can interfere with each other resulting in rich structures, not always easy to interpret.

Experimentally we are interested to construct a probability density function using the information provided by the total decay amplitude for $B^\pm \rightarrow \pi^\pm K^- K^+$, see Eq. 6-9, relying on models that parametrize the signal efficiency and background components, to perform a Dalitz plot fit event by event and separated by charge. The aim is to extract the amplitudes and phases, and the relative contribution of each resonant state for B^+ and B^- respectively. The strategy for the Dalitz plot fit is presented in the following.

6.2.1

The strategy for the fit

In order to perform the Dalitz plots fit a few steps are followed:

- Define a window for the B^+ signal peak from the $\pi^+ K^- K^+$ mass spectrum fit, enhancing the signal to background ratio. This was chosen to be $\pm 17 \text{ MeV}/c^2$ following the considerations presented in Section 4.7
- Model the signal efficiency variation over the Dalitz plot, to account for the detector acceptance, sub-detector efficiencies and effects introduced in each stage of the event selection. This is constructed from the full LHCb simulation samples and is described in Section 6.3.
- Obtain the models for the background sources and their relative contribution in the signal region. See Section 6.4.
- Finally, perform the amplitude analysis fit to the Dalitz plot, including many possible states to find a good representation of the data. This is presented in the following chapter.
- The software of analysis used is LAURA++ [91].

6.3

Efficiency and background models for the Dalitz plot fit

Before performing any Dalitz plot fit, it is necessary to construct a signal efficiency model to account for acceptance effects introduced by the detector. Also in the signal region there exists the contamination from background events so the corresponding distribution of these events in the Dalitz plot needs to be parametrized.

First, it will be presented the construction of the efficiency model for B^+ and B^- used in the Dalitz plot fits. Then, the construction of models for background sources will be explained in detail.

6.3.1

The signal efficiency model

For the construction of the signal efficiency model or phase space acceptance correction, large full LHCb simulated samples generated flat in the Square Dalitz plot representation are used.

As indicated on section 2.9, in the SDP representation, the borders and corners of the standard Dalitz plot representation are enlarged relative to the less populated central region. The generation of events in this way increase the statistics in the more populated regions, which are also the regions where the acceptance has more pronounced variations. This also simplifies the histogram representation of the acceptance. The large statistics MC samples, which were described in Section 4.6, have the feature that their statistical error can be neglected if compared to the data fluctuation. Indeed for the $B^\pm \rightarrow \pi^\pm K^- K^+$ channel, after final cuts, our MC sample size is ~ 200 larger than our signal sample.

To construct the acceptance maps, the MC events are restricted to lie in the same mass window than the signal data, $5266\text{--}5300 \text{ MeV}/c^2$, and with the same selection requirements (with the exception of PID cuts). The PID efficiency weights are obtained from the **PidCalib** package [92] and are applied event by event. The PIDCalib implementation is explained in Appendix B. Due to the fact that the MC generation is not perfectly flat in the squared Dalitz plot, we also use an unbiased generated simulated sample, projected on a histogram in the square variables. The proper acceptance is then obtained as the division of both histograms with same binning: the one that has all the selection cuts divided by the one with the distribution of the unbiased generated events.

The efficiency maps are obtained by year and by subsamples of trigger configuration, as a L0 Hadron efficiency correction is further applied, then they

are added up properly. The main acceptance map for B^+ and B^- is a weighted average of the 2011 and 2012 acceptances, respectively.

Finally it is important to remark that the Dalitz plot fit is not sensitive to the efficiency scale but to its distribution shape in the phase space.

6.3.2

The acceptance maps

As was just indicated, the acceptance maps are generated separated by year, charge and also by trigger configuration, TOS and TISnotTOS, in order to later apply the L0 hadron efficiency correction. The baseline binning applied to the acceptance histograms consist of 18×18 bands in θ' and m' . This division was chosen with respect to the total statistics of the MC samples, with selection requirements, to have a least an event population of order $O(10^2)$ per bin, and taking care to not introduce fluctuation in the acceptance but rather be smoothly modelled.

The large MC statistics with selection cuts is comparable to that one of the standard sample generated with no cuts at the generator level, which is the denominator of the acceptance maps, both much larger than the data sample. Thus the acceptance statistical error can be neglected to first order. The generated sample distributions are scaled to the large production of the numerator samples. The scaling factors applied were found to be 67 and 36, respectively for 2011 and 2012.

In Figure 6.6(a) it is shown the projection of the MC events with selection requirements and PID efficiency weights applied for 2012, B^+ and TOS configuration. In Figure 6.6(b) it is shown the distribution of the generated sample and in Figure 6.6(c) the correspondent acceptance maps obtained as the division of histograms 6.6(a) and 6.6(b). Figures 6.6(d), 6.6(e) and 6.6(f) show the respective histograms for the TISnotTOS configuration. For 2012 B^- and 2011 similar histograms were produced.

6.3.3

Trigger Correction

A correction on the acceptance is performed to take into account the differences between data and MC with respect to the L0Hadron_TOS trigger efficiency. The correction is applied to the mutually exclusive subsamples TOS and TISnotTOS MC [93]. The correction to the acceptance consists in evaluating the ratio of the L0_Hadron efficiencies for data and MC (data/MC) in the square Dalitz plot variables. These correction histograms are then applied to the respective acceptance on each category.

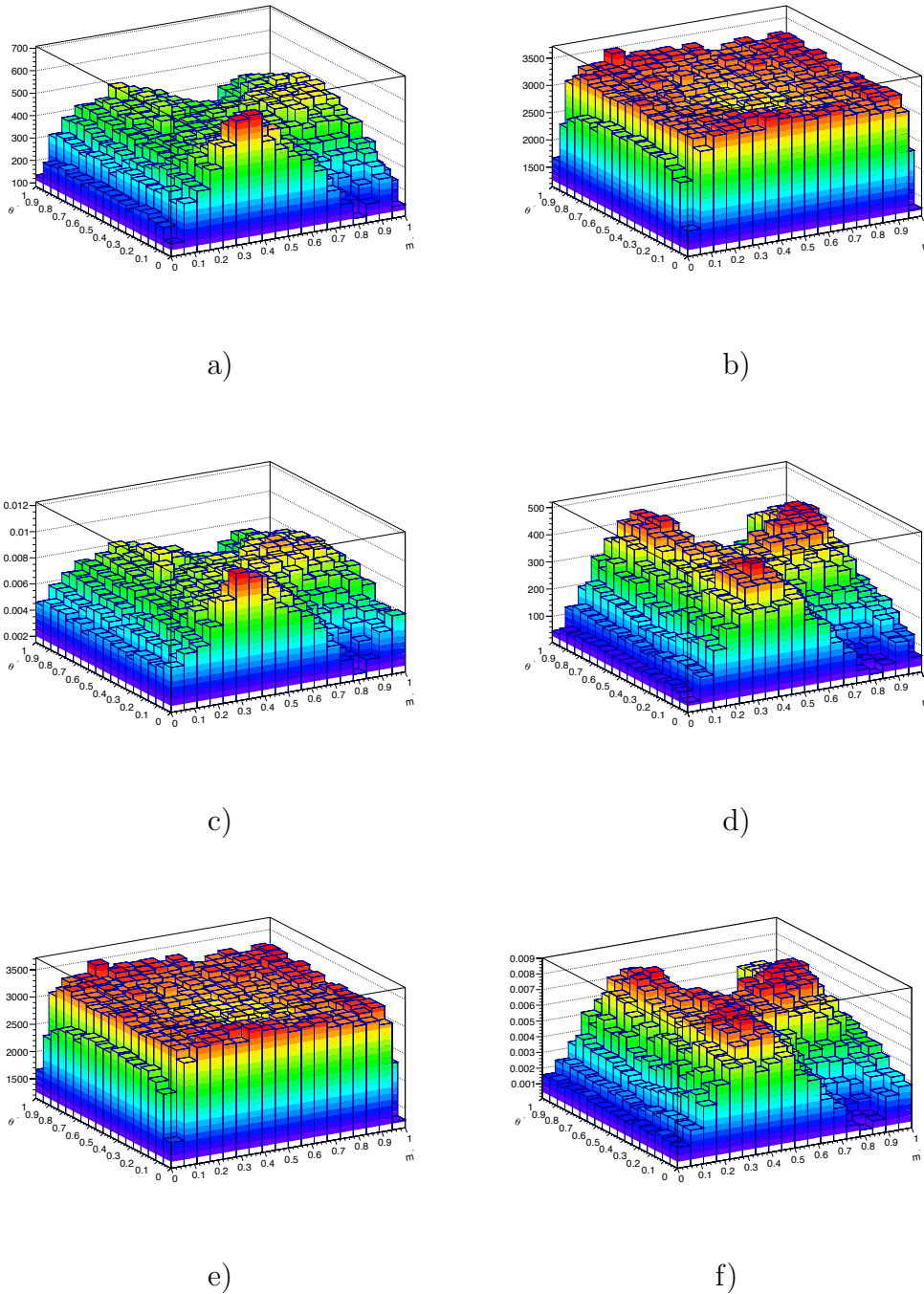


Figure 6.6: a), b) and c) show the histograms for the numerator, denominator and acceptance map, respectively for B^+ , TOS configuration-2012. d), e) and f) show the respective histograms for the TISnotTOS configuration.

The absolute efficiencies for data are obtained from calibration samples [94]. This is based on the track ID, magnet polarity, calorimeter location and deposited energy. It is also considered the probability of tracks causing clusters overlapping in the calorimeter. The efficiency for the candidate is calculated as the probability that at least one track or cluster fires the calorimeter

for the TOS case, none firing in the TISnotTOS case. The corresponding MC efficiency is simply the associated to events that fired the trigger (or not for the TISnotTOS case).

In Figure 6.7(a) is shown the acceptance map for TOS configuration 2012 for B^+ without the L0 correction, Figure 6.7(b) shows the corresponding L0 TOS correction histogram and Figure 6.7(c) the total acceptance with the correction applied. Figures 6.8(a), 6.8(b) and 6.8(c) shows the respective histograms for the TISnotTOS configuration. As can be seen there exists a variation in the trigger efficiency in the phase space up to $\sim 15\text{-}20\%$ evidencing the importance of its correction. The corresponding histograms for B^- 2012 and for B^+ and B^- 2011 can be found in Appendix B.

6.3.4

Combining acceptances

Finally, as a last step in the construction of the efficiency model, the acceptance histograms of each category are combined. At this point we have two histograms for each charge and by year: a TOS acceptance and a TISnotTOS acceptance for B^+ for 2011 and a TOS and TISnotTOS acceptance for B^+ for 2012. Similarly we have in total four acceptance histograms for B^- . It is necessary to combine, by charge, the four sub sample acceptances in a single map that will be smoothed via a 2D cubic spline fit. For each year the TOS and TISnotTOS histograms are added in the same proportion as data while keeping the overall normalisation. It is defined a weight factor, by year and by trigger subsample, given by:

$$w_{x_i} = R_{Total_i} * \frac{N_{x_i} data}{N_{x_i} mc}, \quad (6-20)$$

where x represents the trigger subsample TOS or TISnotTOS, i represents the year 2011 or 2012, R_{Total} is the ratio of the total number of events for the MC sample to the signal data sample. $N_{x_i} data$ is the number of events from the 1D mass fit, for the signal data, considering only x events. $N_{x_i} mc$ represents the respective x events from the MC sample. In general the combination of the acceptance histograms by year and by charge have the following form:

$$Acc_{total} = w_{TOS} \times Acc_{TOS} + w_{TISnotTOS} \times Acc_{TISnotTOS}, \quad (6-21)$$

where Acc_{TOS} and $Acc_{TISnotTOS}$ refers to the Acceptance histograms. To reach the overall final acceptance map, the average for 2011 and 2012 with $\sim 1:2$ weights is performed.

Figures 6.9(a) and 6.9(b) show the total acceptance for 2011 and 2012,

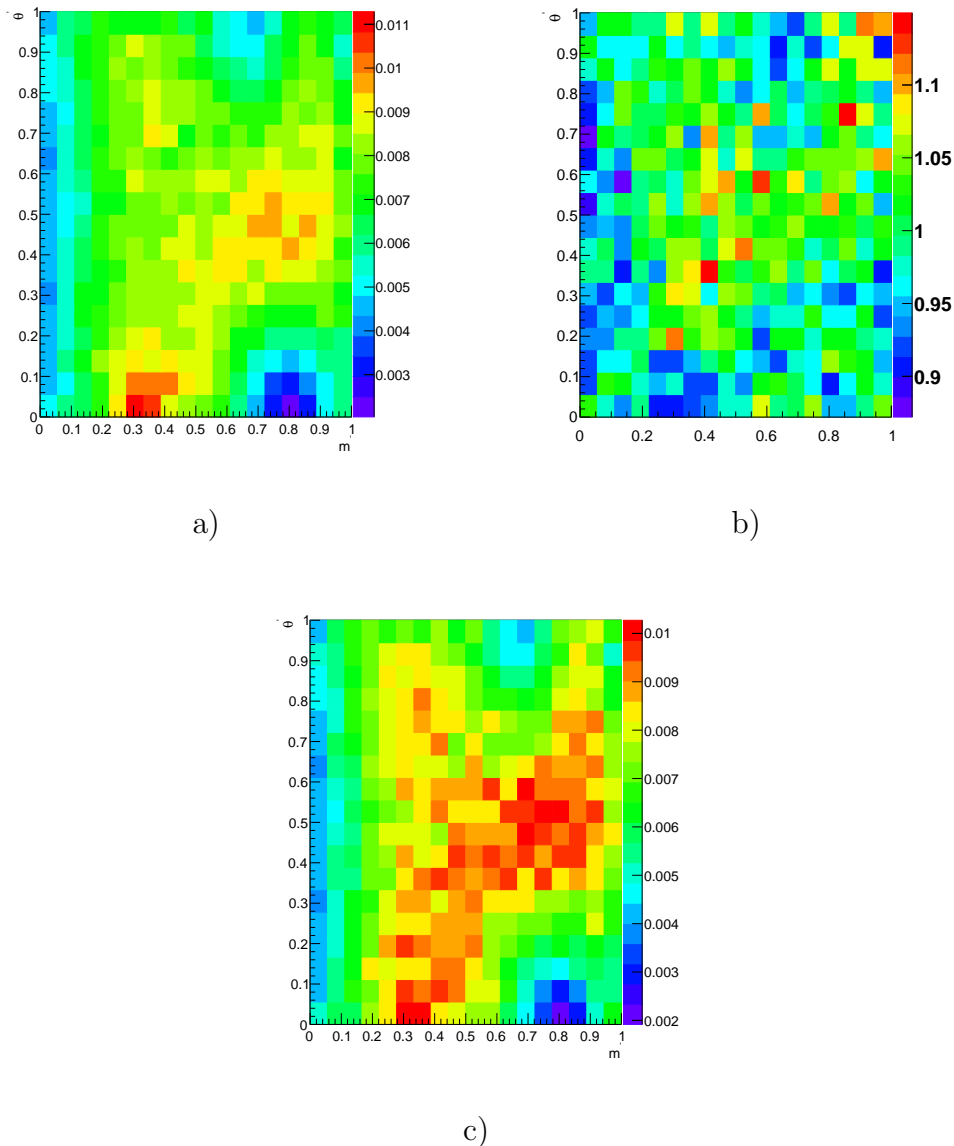


Figure 6.7: (a) Acceptance map 2012 TOS for B^+ without L0 correction (b) 2012 TOS L0 Hadron efficiency correction histogram (c) Total acceptance with TOS L0 Hadron efficiency correction applied.

respectively for B^+ . Figure 6.9(c) shows the final model for the B^+ efficiency, obtained by the combination of the 2011 and 2012 correspondent histograms. Figures 6.10(a), 6.10(b) and 6.10(c) show the respective total acceptance 2011+2012 and separated by year for B^- .

6.4 Background Models

The background parametrization is another important element that has to be included in the Dalitz plot fit. In the chosen signal region, as explained in Section 4.7, there are a few sources of background contamination which can

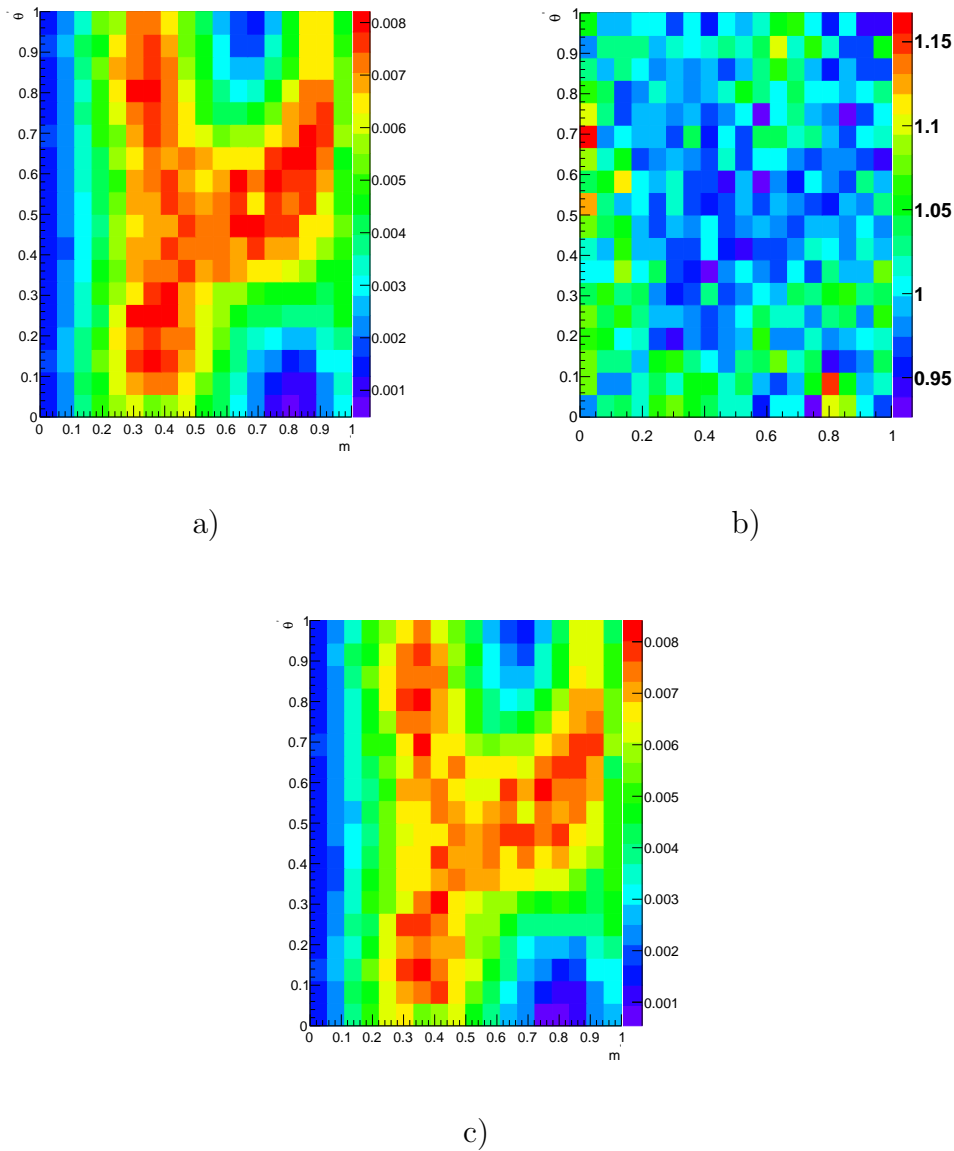


Figure 6.8: (a) Acceptance map 2012 TISnotTOS for B^+ without L0 correction (b) 2012 TISnotTOS L0 Hadron efficiency correction histogram (c) Total acceptance with TISnotTOS L0 Hadron efficiency correction applied.

be enumerated as:

1. Combinatorial background
2. Peaking background
3. Events from 4-body partially reconstructed decays.

The contribution of each type of background was obtained from the one-dimensional mass fit and summarized in Table 6.3. From these values it can be seen that the most prominent contribution comes from the combinatorial

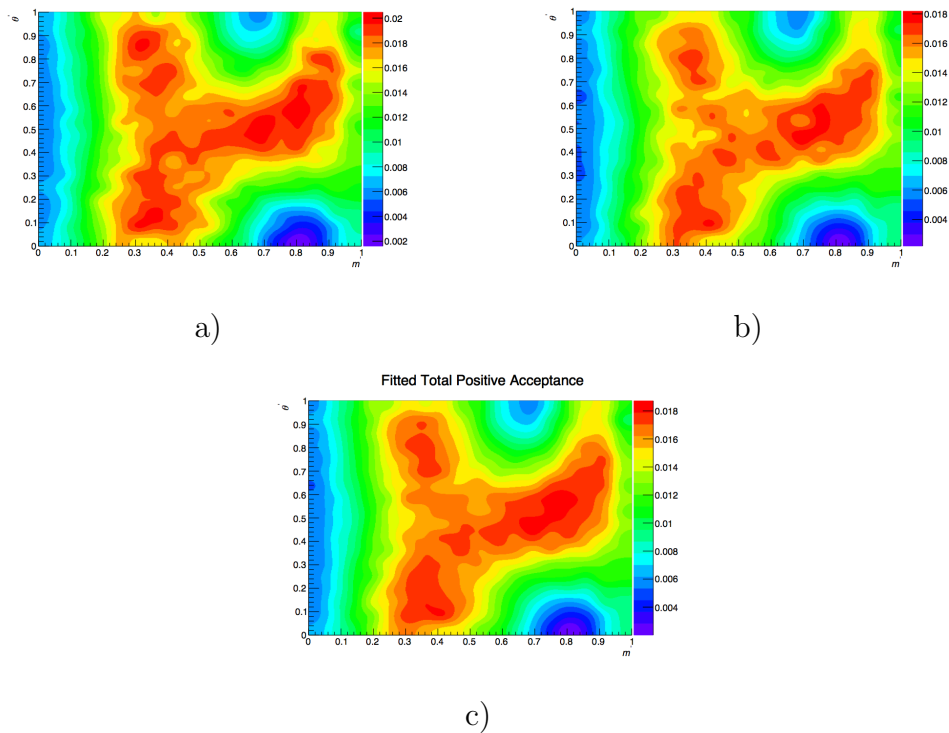


Figure 6.9: a) 2011 acceptance for B^+ , b) 2012 acceptance for B^+ , c) 2011 and 2012 combined acceptance for B^+

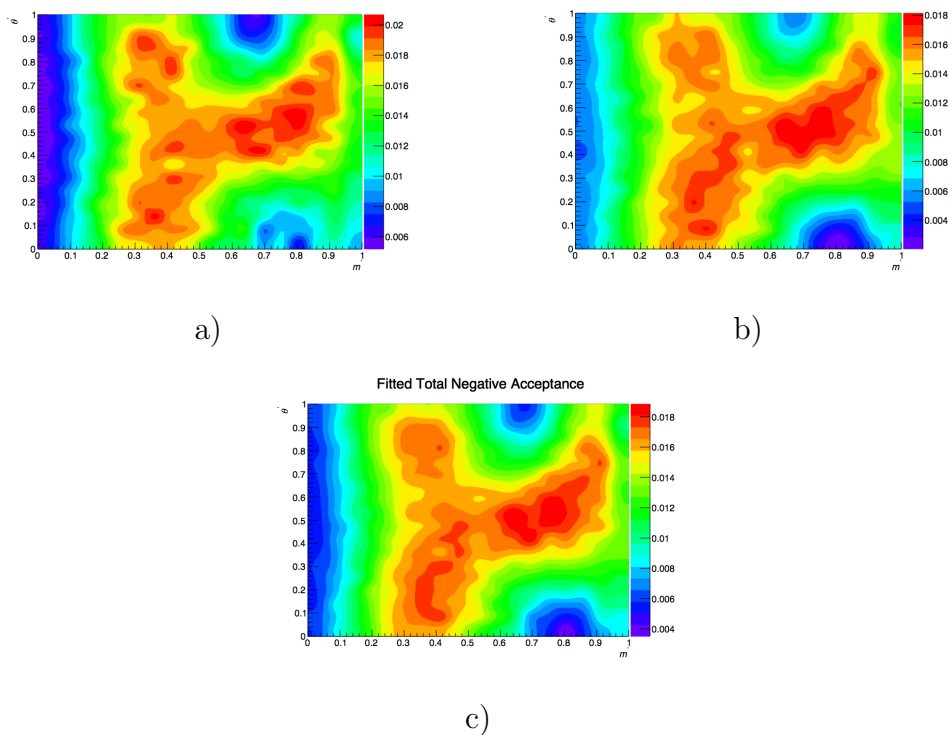


Figure 6.10: a) 2011 acceptance for B^- , b) 2012 acceptance for B^- , c) 2011 and 2012 combined acceptance for B^-

Category	Number of events
Signal	3706 (76.6%)
Combinatorial bkg.	1056 (21.8%)
$B^+ \rightarrow \pi^+\pi^-K^+$ peaking bkg.	56 (1.16%)
$B^+ \rightarrow K^+K^-K^+$ peaking bkg.	6 (0.12 %)
$B_s^0 \rightarrow 4$ -body	12 (0.25%)
$B \rightarrow 4$ -body	0 (0%)

Table 6.3: Signal and background events in the chosen signal region, for the 2011+2012 data sample.

background with $\sim 21\%$. Then, the contamination coming from the misidentification of a pion or a kaon, that is, the peaking backgrounds $B^\pm \rightarrow K^\pm K^+ K^-$ and $B^\pm \rightarrow K^\pm \pi^+ \pi^-$, is of about 0.12% and 1.2%, respectively. Due to the low statistics of our signal sample, we consider the modelling for the reflection of $B^\pm \rightarrow K^\pm \pi^+ \pi^-$ into $B^\pm \rightarrow \pi^\pm K^- K^+$, while the $B^\pm \rightarrow K^\pm K^+ K^-$ component is neglected. The contamination due to 4-body partially decays, with 0.25%, is also neglected.

6.4.1 Combinatorial background

In order to parametrize this kind of background the right sideband events from the mass spectra, starting from $B_M > 5400 \text{ MeV}/c^2$ is used. The left-side is highly populated with structures like 4-body partially reconstructed decays and so is not representative of the combinatorial background.

To ensure that we have a good model and that indeed is a reliable representation of the combinatorial events in the signal region we separate the right sideband into three intervals defined as:

- From 5400 to 5450 MeV/c^2 , region a)
- From 5450 to 5500 MeV/c^2 , region b)
- Greater than 5500 MeV/c^2 , region c)

The distribution of events for each region in the Dalitz plot can be found on Figure 6.11(a), 6.11(b) and 6.11(c), respectively. By inspecting these plots, a clear difference arises if we compare the Figure 6.11(c) with Figures 6.11(a) and 6.11(b). The presence of a structure that lives only in the high mass region c) is evident. To have a better insight of this structure, the projection of the Dalitz plot variables $m_{\pi^\pm K^\mp}^2$, $m_{K^\pm \pi^\pm}^2$, $m_{K^- K^+}^2$ against the B invariant mass was made. Exploring each of this plot on Figure 6.12(a), 6.12(b) and 6.12(c) it can be seen that there is a density of points for B_m in the interval of $B_m > 5500 \text{ MeV}/c^2$ and $m_{K^- K^+}^2 \sim 25\text{--}27 \text{ MeV}/c^2$, on Figure 6.12(c). This evidently

shows the existence of a structure that is not present in the signal region. On Figure 6.13(a) we have the combinatorial Dalitz plot distribution including all the right sideband events, and on Figure 6.13(b) when we exclude the events from 5500 to 5550 MeV/c^2 , where the structure is present.

Based on the just described study, the combinatorial background model is then obtained only using the right sideband events from the mass spectra in the interval $[5400, 5500] \text{ MeV}/c^2$. Figure 6.14(a) shows the model in the Square Dalitz plot and 6.14(b) the smooth version obtained from the fit to the combinatorial histogram with a 2D Cubic spline function.

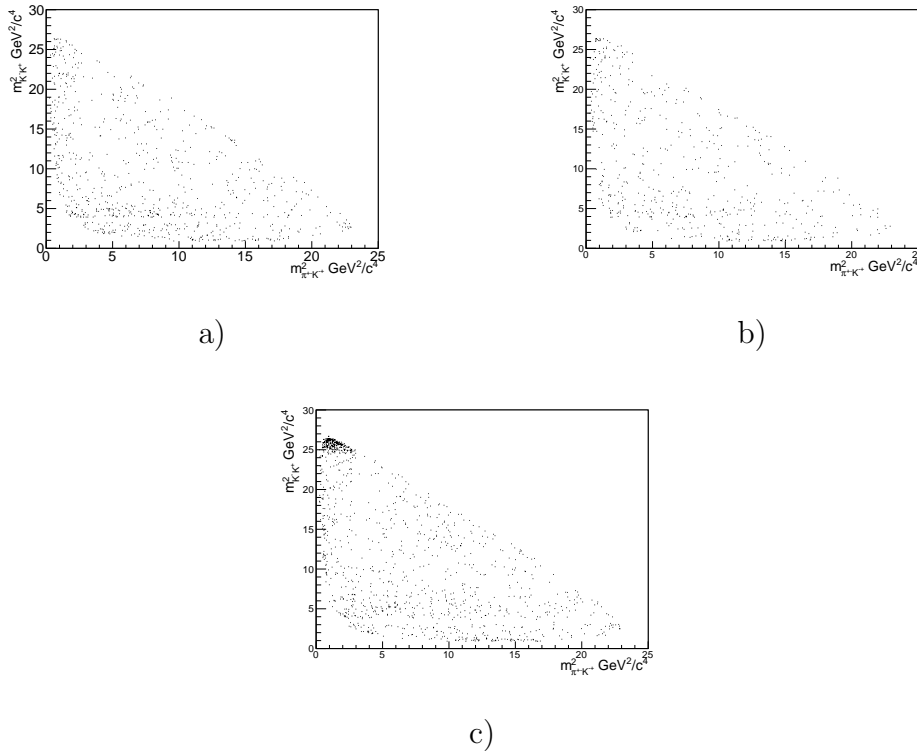


Figure 6.11: Region a) from 5400 to 5450 MeV/c^2 , region b) from 5450 to 5500 MeV/c^2 , region c) greater than 5500 MeV/c^2

6.4.2

Peaking background from $B^\pm \rightarrow K^\pm \pi^+ \pi^-$

To construct the model for the $B^\pm \rightarrow K^\pm \pi^+ \pi^-$ reflection, we generate a toy MC for the $B^\pm \rightarrow K^\pm \pi^+ \pi^-$ decay based in the amplitude analysis performed by the BaBar collaboration for this decay, by considering the resonance substructures shown in Table I of reference [95]. We generate 100K $B^\pm \rightarrow K^\pm \pi^+ \pi^-$ decays. Then, the incorrect assignment of a pion as a kaon is set, and the Dalitz variables are recalculated as if they are the $B^\pm \rightarrow \pi^\pm K^- K^+$ Dalitz plot variables. Finally the projection in the

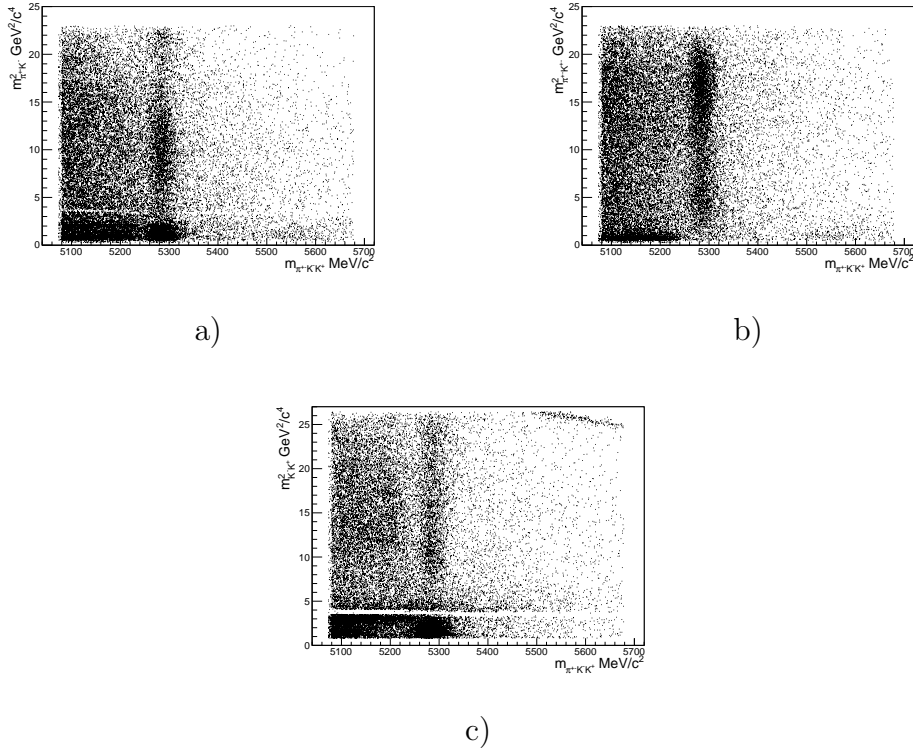


Figure 6.12: a) $m_{\pi^+K^+}^2$ vs B_m , b) $m_{K^+K^0}^2$ vs B_m , c) $m_{K^+K^0}^2$ vs B_m , a structure on c) can be seen for $B_m > 5500 \text{ MeV}/c^2$

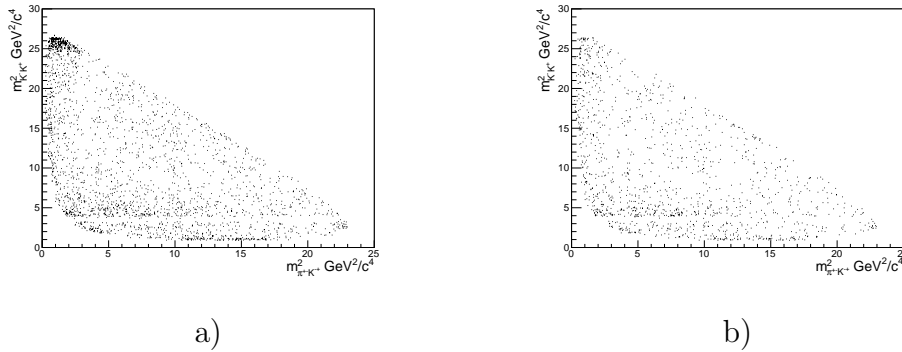
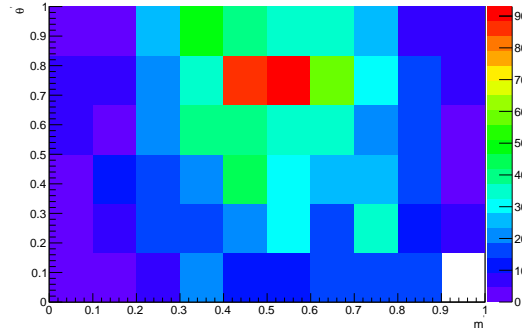
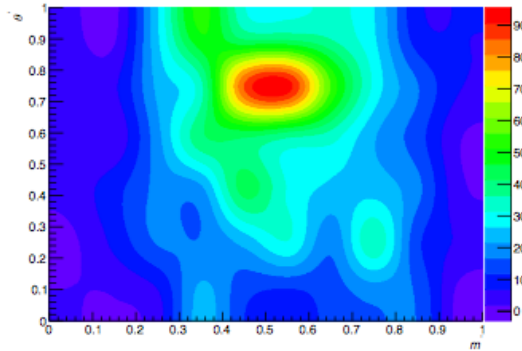


Figure 6.13: a) Combinatorial events on the Dalitz plot using the complete right sideband $B_m > 5400 \text{ MeV}/c^2$ b) Combinatorial events on the Dalitz plot removing the events in the interval $5500 \text{ MeV}/c^2 < B_m < 5550 \text{ MeV}/c^2$.

$B^\pm \rightarrow K^\pm \pi^+ \pi^-$ Square Dalitz plot is made and this is used as the model for the $B^\pm \rightarrow K^\pm \pi^+ \pi^-$ peaking background. Figure 6.15(a) shows the final model and 6.15(b) smooth version.



a)



b)

Figure 6.14: a) Combinatorial background model in the square variables for the Dalitz plot fit b) smoothed version.

6.5 The probability density function

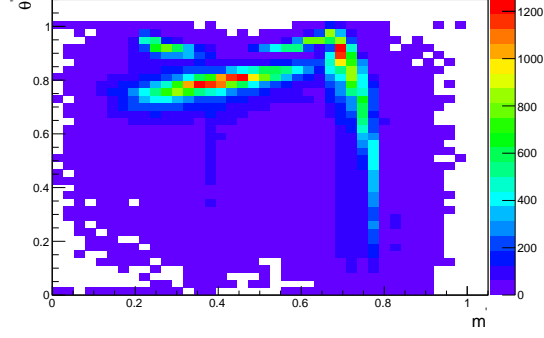
To perform the fit to the event distribution observed in the Dalitz plot, some considerations have to be taken into account. One of these is that each event in the phase space has associated a probability to be a signal event or a background event, and the other one is how the complex coefficient c_i are parametrized.

If it wasn't for the efficiency effects the signal probability density distribution would be simply given by the square of total decay amplitude \mathcal{A} , see Equation 6-9, this is expressed as¹:

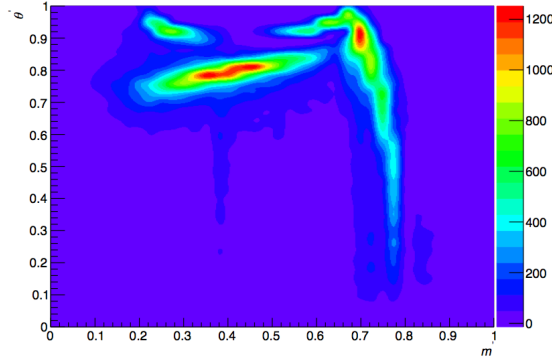
$$\mathcal{P}'_{sig}(m_{\pi^+K^-}^2, m_{K^-K^+}^2 | c_i) = |\mathcal{A}(m_{\pi^+K^-}^2, m_{K^-K^+}^2 | c_i)|^2, \quad (6-22)$$

where we have put the explicit dependence of c_i in the equation.

¹In a similar way $\bar{\mathcal{P}}'_{sig}(m_{\pi^-K^+}^2, m_{K^+K^-}^2 | \bar{c}_i) = |\bar{\mathcal{A}}(m_{\pi^-K^+}^2, m_{K^+K^-}^2, \bar{c}_i)|^2$ for the CP-conjugate process.



a)



b)

Figure 6.15: (a) Peaking background model in the square variables for the Dalitz plot fit. (b) smooth version.

Corrections due to the efficiency variations across the Dalitz plot must be considered and need to be included to correct the probability density function for each event. The expression for the signal PDF, correcting by the efficiency over the phase space has the form

$$\mathcal{P}_{sig}(m_{\pi^+K^-}^2, m_{K^-K^+}^2 | c_i) \propto \epsilon(m_{\pi^+K^-}^2, m_{K^-K^+}^2) \mathcal{P}'_{sig}(m_{\pi^+K^-}^2, m_{K^-K^+}^2 | c_i). \quad (6-23)$$

The total signal probability density function considering B^- and its process CP -conjugate B^+ is:

$$\mathcal{P}_{sig}(m_{\pi^\pm K^\mp}^2, m_{K^-K^+}^2 | c_i) = \frac{\frac{1+q_B}{2} \epsilon(m_{\pi^+K^-}^2, m_{K^-K^+}^2) |A(m_{\pi^+K^-}^2, m_{K^-K^+}^2)|^2 + \frac{1-q_B}{2} \bar{\epsilon}(m_{\pi^-K^+}^2, m_{K^+K^-}^2) |\bar{A}(m_{\pi^-K^+}^2, m_{K^+K^-}^2)|^2}{\mathcal{N}_s} \quad (6-24)$$

where q_B is the charge of the B -meson candidate. The denominator represents

the normalization factor and is given by:

$$\mathcal{N}_s = \iint_{DP} (\epsilon(m_{\pi^+K^-}^2, m_{K^-K^+}^2) |\mathcal{A}(m_{\pi^+K^-}^2, m_{K^-K^+}^2)|^2 + \bar{\epsilon}(m_{\pi^-K^+}^2, m_{K^+K^-}^2) |\bar{\mathcal{A}}(m_{\pi^-K^+}^2, m_{K^+K^-}^2)|^2) d^2 m_{\pi^\pm K^\mp} d^2 m_{K^\mp K^\pm} \quad (6-25)$$

Notice that the integral is performed over the whole Dalitz plot. The total probability density function also has to take into account the background sources, with shapes given by the histograms presented in Section 6.4 and with relative contribution given by the mass fit.

The total PDF is then:

$$\begin{aligned} \mathcal{P}(m_{\pi^\pm K^\mp}^2, m_{K^\mp K^\pm}^2 | c_i) &= N_{sig} \mathcal{P}_{sig}(m_{\pi^\pm K^\mp}^2, m_{K^\mp K^\pm}^2 | c_i) + N_{comb} \mathcal{P}_{comb}(m_{\pi^\pm K^\mp}^2, m_{K^\mp K^\pm}^2) \\ &+ N_{k\pi\pi} \mathcal{P}_{k\pi\pi}(m_{\pi^\pm K^\mp}^2, m_{K^\mp K^\pm}^2), \end{aligned} \quad (6-26)$$

where \mathcal{P}_{sig} represents the signal PDF, \mathcal{P}_{comb} the combinatorial background PDF and $\mathcal{P}_{k\pi\pi}$ the PDF for the reflection of $B^\pm \rightarrow K^\pm \pi^+ \pi^-$. N_{sig} , N_{comb} and $N_{k\pi\pi}$ represents the relative contribution of each type to the total number of candidates. They were obtained through 1D mass fit integrated in the signal region. Their values are presented on Table 6.3. The dependence of the complex coefficients is only carried in the signal PDF. The background modelling is totally fixed in the Dalitz plot fit.

6.5.1

The maximum likelihood estimator

The maximum likelihood estimator [96] is a technique widely used in high energy physics. It consists on estimating unknown parameters values given a data sample.

The probability density function $\mathcal{P}(x|\alpha)$, where x represents the observable data and α the unobservable parameters, is a function that parameterizes the distribution of the random variables x (the events) given α . On the other hand, the likelihood $\mathcal{L}(\alpha) = \mathcal{P}(x|\alpha)$ is a function of parameters α given the data, that is, it expresses the probability for observing data x for different choices of the values of parameters α . Mathematically both expressions are very similar but their concepts are different. The PDF is a probability density function of data and so must be normalized to one, while the likelihood is not a probability density function for α and so do not have the property to be normalized to unity.

If we repeat n independent observations of x , we can express the likelihood function as:

$$\mathcal{L}(\alpha) = \prod_i^n \mathcal{P}(x_i|\alpha) \quad (6-27)$$

The maximum likelihood estimators for the parameters are those that maximize the likelihood function. This means for example, in the context of some physical measurement, that for these parameters values, nature is more likely to generate the observed data.

Usually a more common way to work is taking the log or the -log of the likelihood function rather than the proper likelihood function. This is due to computational reasons. It is easier to the algorithm of optimisation to handle the log-likelihood function as multiplications become sums and also because it is numerically more stable. In this analysis we work with the negative log-likelihood function $-\ln\mathcal{L}$ (NLL) as the optimizer used *MINUIT* is constructed to minimize the results of a function. Thus minimizing this function is equivalent in maximizing the log-likelihood or the likelihood itself. The relation that $-\ln\mathcal{L}$ has to satisfy is:

$$-\frac{\partial}{\partial\alpha} \ln \mathcal{L} = -\frac{\partial}{\partial\alpha} \sum_i^n \ln \mathcal{P}(x_i|\alpha) = 0 \quad (6-28)$$

6.5.2

The likelihood function for $B^\pm \rightarrow \pi^\pm K^- K^+$

The likelihood function for $B^\pm \rightarrow \pi^\pm K^- K^+$ is constructed using the total probability function referred in Equation 6-26 and is expressed as:

$$\mathcal{L} = \prod_i^N \left(\sum_k N_k \mathcal{P}_k^i(m_{\pi^\pm K^\mp}^2, m_{K^- K^+}^2) \right) \quad (6-29)$$

where N_k is the yield for the event category k (signal or background), N is the total number of candidates and \mathcal{P}_k^i is the PDF for the category k for event i . The function $-2\ln\mathcal{L}$ is the one to be minimized in the unbinned fit to data.

6.5.3

The χ^2

The χ^2 is a statistical tool used to measure the goodness-of-fit. It is defined as

$$\chi^2 = \sum_{i=1}^{n_b} \frac{(y_i - f(x_i))^2}{f(x_i)} \quad (6-30)$$

where y_i is the number of events in the bin i and $f(x_i)$ is the number of events in the same bin² predicted by the fit. The total number of degrees of freedom is calculated to be $n_b - h - 1$, where n_b is total number of bins used and h is total number of free parameters in the fit.

6.5.4

The coefficient c_i

The isobar coefficients c_i are parametrized using Cartesian coordinates. This removes the problem of positive definite values that is present when using polar coordinates but, in the counter part, leads to fitted parameters that are less intuitive to interpret. Their expression are given by:

$$\begin{aligned} c_i &= (x_i + \Delta x_i) + i(y_i + \Delta y_i) \\ \bar{c}_i &= (x_i - \Delta x_i) + i(y_i - \Delta y_i), \end{aligned} \quad (6-31)$$

where x_i and y_i (Δx_i and Δy_i) are the CP-conserving (-violating) components of the decay amplitude. Their expression in polar coordinates will be used just in the presentation of the results of the Dalitz plot fit. These are given by:

$$\begin{aligned} a_i &= \sqrt{(x_i + \Delta x_i)^2 + (y_i + \Delta y_i)^2} \\ \delta_i &= \tan^{-1}\left(\frac{y_i + \Delta y_i}{x_i + \Delta x_i}\right) \end{aligned} \quad (6-32)$$

and for its CP conjugate particle as:

$$\begin{aligned} \bar{a}_i &= \sqrt{(x_i - \Delta x_i)^2 + (y_i - \Delta y_i)^2} \\ \bar{\delta}_i &= \tan^{-1}\left(\frac{y_i - \Delta y_i}{x_i - \Delta x_i}\right), \end{aligned} \quad (6-33)$$

6.6

Fit Fractions and CP Asymmetry

In order to allow the comparison of the results from different experiments and analyses, a standard definition has been set, namely the fit fraction (FF_i) contribution from each resonant state. This gives us a sense of the respective contribution that each component has in the model. The fit fraction for a given resonant decay mode is defined as the integral of its decay amplitude squared divided by the total matrix element squared for the complete Dalitz plot [27]:

²The intervals in which the data is split in a histogram is defined as “bin”.

$$FF_i = \frac{\iint (|c_i \mathcal{M}_i|^2 + |\bar{c}_i \bar{\mathcal{M}}_i|^2) dm_{\pi^+ K^-}^2 dm_{K^- K^+}^2}{\iint (|\mathcal{A}|^2 + |\bar{\mathcal{A}}|^2) dm_{\pi^+ K^-}^2 dm_{K^- K^+}^2} \quad (6-34)$$

It is also useful to define the fit fraction separated by CP -conjugate process (FF_i^\pm). This provides another tool to analyse the differences between the B^+ and B^- decays:

$$FF_i^+ = \frac{\iint (|c_i \mathcal{M}_i|^2) dm_{\pi^+ K^-}^2 dm_{K^- K^+}^2}{\iint (|\mathcal{A}|^2) dm_{\pi^+ K^-}^2 dm_{K^- K^+}^2} \quad (6-35)$$

and

$$FF_i^- = \frac{\iint (|\bar{c}_i \bar{\mathcal{M}}_i|^2) dm_{\pi^+ K^-}^2 dm_{K^- K^+}^2}{\iint (|\bar{\mathcal{A}}|^2) dm_{\pi^+ K^-}^2 dm_{K^- K^+}^2} \quad (6-36)$$

Since the denominator comes from the coherent sum of all contributions, taking into account any constructive or destructive effects, the total fit fraction will normally deviate from unity.

The CP asymmetry associated to each resonant state in the model is calculated using its corresponding magnitudes and phases found in the fit, which depend on x , Δx , y and Δy , this is expressed as [27]:

$$A_{cp,i} = \frac{|\bar{c}_i|^2 - |c_i|^2}{|\bar{c}_i|^2 + |c_i|^2} = \frac{-2(x_i \Delta x_i + y_i \Delta y_i)}{(x_i)^2 + (\Delta x_i)^2 + (y_i)^2 + (\Delta y_i)^2}. \quad (6-37)$$

In the next chapter we present the fit results for the $B^\pm \rightarrow \pi^\pm K^- K^+$ decays using the definitions presented here.

7

Dalitz plot fit results

To perform the Dalitz plot fit several preparatory stages were required, as explained in detail in the preceding chapter. Once we have all of these “ingredients” we are ready to perform the model dependent Dalitz plot fit using the Isobar Model formalism. Being this the first time that an amplitude analysis is performed for this channel, we have to be very careful in choosing the best strategy to build a reliable Isobar Model to genuinely represent the data and therefore the physics involved. Several challenges are foreseen in the analysis. First of all, we don’t count with a baseline model or a precedent model, which we could use as starting point. Secondly, there are special features of the decay itself. We recall here the large integrated CP asymmetry found for this channel, and even more the asymmetries in regions of the phase space found (shown in Chapter 5).

We repeat here the most clear example, which is shown in Figure 8.1. The $\pi^\pm K^- K^+$ mass fit is performed only in the expected rescattering region ($\sim 1 \text{ GeV}/c^2 < m_{K^- K^+} < 1.5 \text{ GeV}/c^2$) and a remarkable difference between B^- and B^+ arises. As explained in section 5.2, the CP asymmetry reported for this region is of about 32% with the interesting feature that, for this same region, a large amount of CP asymmetry was found on its coupled channel $B^\pm \rightarrow \pi^\pm \pi^+ \pi^-$ with opposite sign. This marks a motivation for the inclusion of a rescattering amplitude $\pi\pi \leftrightarrow KK$ in the Isobar Model.

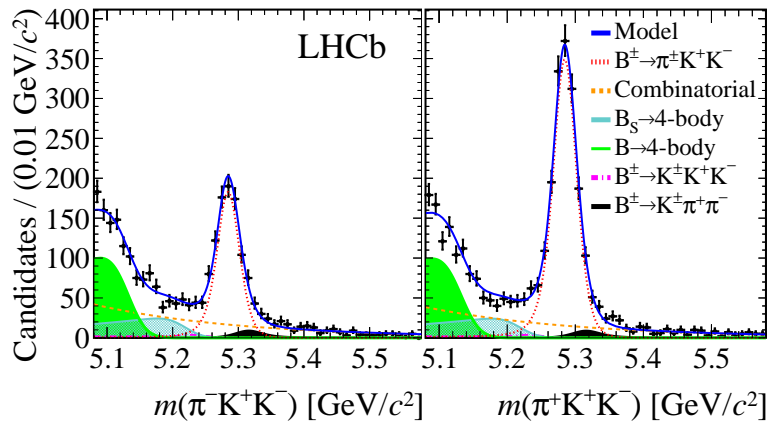
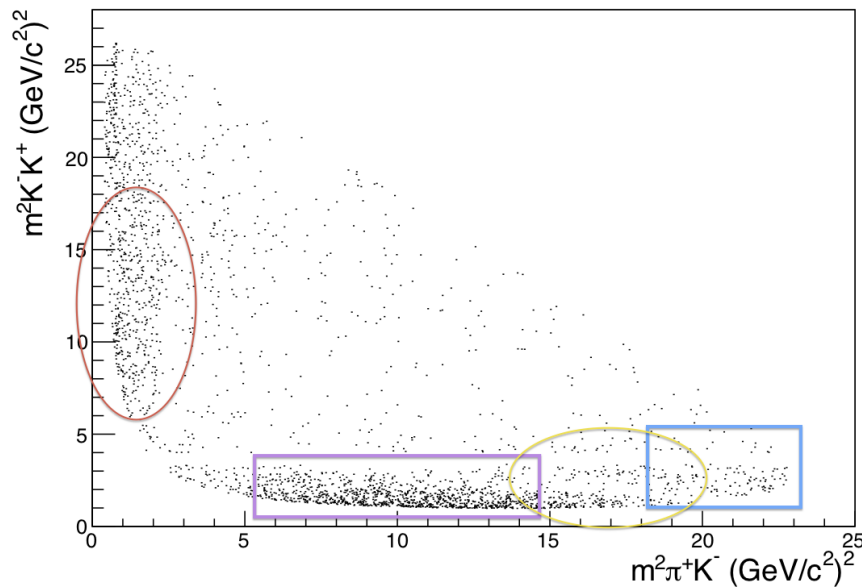


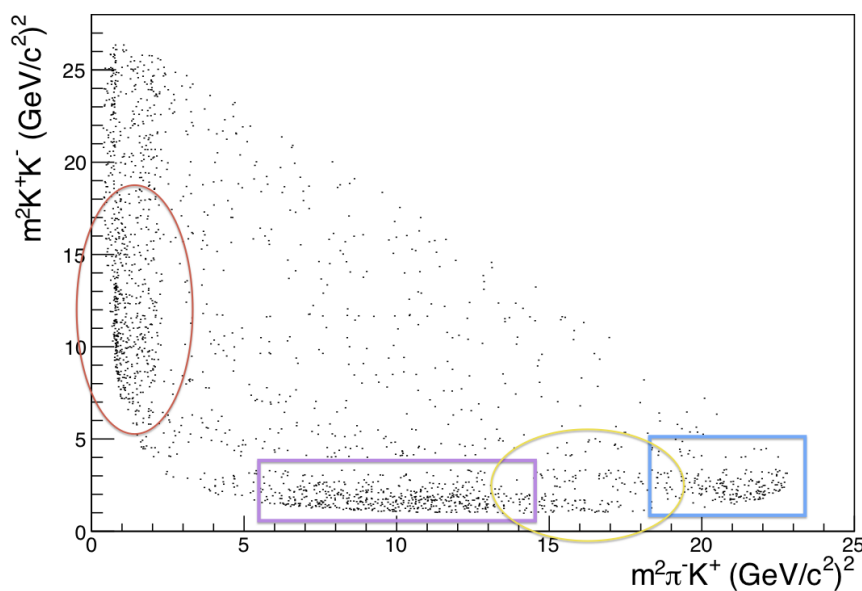
Figure 7.1: 1-D mass fit in the rescattering region $1 \text{ MeV}/c^2 < m_{K^- K^+} < 1.5 \text{ MeV}/c^2$. B^- (left), B^+ (right).

The rich dynamics involved in the decay and the evident CP asym-

metry present for B^+ and B^- are shown in their respective Dalitz plot in Figures 7.2(a) and 7.2(b), respectively. This makes evident the need of a separate Dalitz plot for B^+ and B^- . Some regions of high asymmetry have been highlighted on both Dalitz plots.



a)



b)

Figure 7.2: (a) Dalitz Plot for $B^+ \rightarrow \pi^+ K^- K^+$ and (b) for $B^- \rightarrow \pi^- K^+ K^-$ in the selected signal region.

From the leading diagrams contributions shown in Fig. 2.2, we can get some hints of what resonances could be contributing as intermediate states.

Having a penguin transition of the type $b \rightarrow d$, we expect to have in the $\pi^\pm K^\mp$ resonances, for example, $K^*(892)^0$ and a $K^*(1430)^0$. Their region in the Dalitz plot, $m_{\pi^\pm K^\mp}^2 < 1.5 \text{ (GeV)}^2/c^2$, $m_{\pi^\pm K^\mp}^2$ in the horizontal axis, shows a more pronounced density of points for B^- than for B^+ in the lower section where the bottom lobe of $K^*(892)^0$ would be located. The possibility of a non-resonant component being involved here is also considered.

On the other hand, the tree-level transition forms of a $u\bar{u}$ pair, which can lead to resonances of the type f_x contributing in the $K^- K^+$ system (the vertical axis). Resonances with almost pure $s\bar{s}$ composition, as $\phi(1020)$, are not expected and, for the same reason, $f_0(980)$ should be suppressed. By inspecting the $K^- K^+$ axis in the Dalitz plot, we cannot identify clear components but the rich structures observed are remarkable evidence of the dynamics being involved. One of these is the rescattering region as already mentioned. Another signature to highlight is the strong pattern of destructive interference, which is like a diagonal slice with almost no events, located in the high mass region of $m_{\pi^\pm K^\mp}^2$ around $13 \text{ (GeV)}^2/c^2$ and $20 \text{ (GeV)}^2/c^2$ and for $m^2(K^- K^+) < 3.5 \text{ (GeV)}^2/c^2$. It can also be observed that the surrounded areas, left and right, to this region exhibit evident CP asymmetries, see Figure 7.2.

In the strategy for the Dalitz plot fit, difficulties are encountered in the scalar sector where there are many possible contributions and which signatures are not very clear due to the absence of an angular distribution and broad structures. We need to be very cautious in the inclusion of scalar components because it is often possible to obtain better fit results by allowing many contributions interplaying. Nevertheless, this approach frequently produces unrealistic interference scenarios, with difficult interpretation. This is especially the case of the $K^- K^+$ system, where no a clear resonance signature is set and from where very strong patterns of interference are present, as was just described.

7.1

Families of fits

Three approaches are followed to fit the data. The first approach is a family of fits that only include known resonances. Taking the best one as a baseline, the most problematic regions are identified, where a poor description is obtained. The second approach is focussed in improving the fit in the $m_{\pi^\pm K^\mp}^2$ axis by including alternative parametrizations, like the Tobias NR [77]. Finally, a third approach is followed which consists of family focussing in the $K^- K^+$ system around the rescattering region, by allowing the presence of a dedicated amplitude like the Pelaez 2005 [2] function, explained in section 6.1.4. The best

Category	Number of events
Signal	3706
Combinatorial bkg.	1056
$B^+ \rightarrow \pi^+\pi^-K^+$ peaking bkg.	56

Table 7.1: Signal and background events set on the Dalitz plot fit.

fit of each family are presented below.

The criteria to establish whether a fit is “good” or “not”, is based in the likelihood found for the fit (looking for the best minimum global variance) and the χ^2 .

The results are presented through a table that summarizes the fit fraction contribution for each resonance in the model, their relative magnitudes and phases, for both B^+ and B^- . The CP asymmetry associated to each component is presented, calculated as explained in Section 6.6.

The square invariant mass of each system (K^-K^+ , $\pi^\pm K^\mp$, $\pi^\pm K^\pm$) is projected against the model and the background estimation. For each model, the χ^2 is calculated in adaptive bins in the Dalitz plot. For all models in this analysis, the reference channel is the $K^{*0}(892)K^+$, which phase is set to zero and magnitude is let free to float in the following way, translated in Cartesian coordinates: x is fixed in one, y is fixed in zero, Δx is let to be free and Δy is fixed in zero (the CP asymmetry was let to float, recalling that Δx and Δy are the CP-violating parameters in the fit, see Eq. 6-31). The number of signal and background events to which the Dalitz plot fit normalizes is summarized in Table 7.1, according to the results of the $\pi^\pm K^- K^+$ mass fit.

7.2

Classic Model (Model-2011)

We start our strategy by constructing a model that only includes well known resonances and parametrizations (mainly Breit-wigner and the flatté lineshapes were used). Looking into the $B^\pm \rightarrow \pi^\pm K^- K^+$ phase space, the presence $K^{*0}(892)$ is evident in the $\pi^\pm K^\mp$ axis. The $K_0^{*0}(1430)$ also seems to be present interfering with $K^{*0}(892)$. Using only these two components in the model, however is not enough to account for a good data description in the squared mass of the pair $\pi^\pm K^\mp$. Other components need to be added.

To include further states we adopt a procedure that consists in including one by one all the possible resonances in the model, and the one that provided the best likelihood is retained. The procedure is repeated again to test for further states. For the $K^- K^+$ axis, where not clear resonance signatures are

evident, the selection of the contributing components are mainly driven by this systematic procedure.

Our best result for the classic model is composed by 7 components, as detailed in Table 8.2. We find three components for $m_{\pi^\pm K^\mp}^2$: $K^{*0}(892)$, $K_0^{*0}(1430)$ and kappa (κ); and four components for $m_{K^- K^+}^2$: $\rho(1450)$, $f_2(1270)$, $f_0(1370)$ and $f_0(980)$. Lets discuss these results with further detail.

[NLL -9571] Component	Fit fraction (%)		Magnitude and phase coefficients				A_{CP} (%)
	B^+	B^-	a_i^+	$\delta_i^+ [^\circ]$	a_i^-	$\delta_i^- [^\circ]$	
$K^{*0}(892)$	5.6 ± 0.8	10.7 ± 1.0	0.92 ± 0.04	0 ± 0	1.08 ± 0.04	0 ± 0	16.5 ± 8.4
$K_0^{*0}(1430)$	13.0 ± 1.7	18.5 ± 2.8	1.39 ± 0.11	-147 ± 10	1.42 ± 0.12	175 ± 11	2.2 ± 10.1
κ	9.4 ± 1.4	9.1 ± 1.5	1.19 ± 0.11	107 ± 10	1.00 ± 0.10	49 ± 9	-17.2 ± 11.3
$\rho^0(1450)$	27.1 ± 1.5	34.9 ± 1.8	2.01 ± 0.11	-53 ± 26	1.96 ± 0.10	-91 ± 95	-2.9 ± 4.3
$f_2(1270)$	3.5 ± 0.9	10.0 ± 1.4	0.72 ± 0.10	24 ± 26	1.05 ± 0.09	-4 ± 17	35.5 ± 12.6
$f_0(1370)$	6.6 ± 2.1	0.1 ± 0.3	0.99 ± 0.16	-30 ± 28	0.12 ± 0.07	-77 ± 64	-97.3 ± 6.5
$f_0(980)$	35.1 ± 2.4	13.0 ± 2.0	2.29 ± 0.13	167 ± 29	1.19 ± 0.11	144 ± 20	-57.3 ± 6.0
Fit Fraction Sum	100.4	96.2					

Table 7.2: Classic model: model components (1st column), fit fraction for each component for B^+ (B^-) on 2nd (3rd) column, magnitude and phase on 4th and 5th column for B^+ , 6th and 7th for B^- . CP asymmetry on 8th.

By inspecting the results in Table 8.2, we observe that the largest fit fraction contribution in the $\pi^\pm K^\mp$ system is attributed to $K_0^{*0}(1430)$ ($\sim 13\%$ (B^+) and $\sim 18\%$ (B^-)), and it is mainly interfering with $K^{*0}(892)$. This can be easily derived if we see their position in the mass spectrum (Figure 6.3), $K^{*0}(892)$ and $K_0^{*0}(1430)$ are neighbor resonances while only the reminiscent of the κ tail is interacting with $K_0^{*0}(1430)$. For these three components it is also observed that $K^{*0}(892)$ and $K_0^{*0}(1430)$ have positive CP asymmetry, unlike the κ contribution appears with negative CP asymmetry.

The κ contribution, within the Classic Model, makes a better performance than other possibilities like a constant NR amplitude, which also generates a large sum of fit fractions and so reflecting a strong interference pattern in Dalitz plot fit¹. Yet, from the projections in the square invariant mass $m_{\pi^\pm K^\mp}^2$, for the region $0 \text{ GeV}/c^2 < m_{\pi K}^2 < 3.5 \text{ GeV}/c^2$ shown in Figures 7.4 a) ($\cos\theta_{12} > 0$) and b) ($\cos\theta_{12} < 0$), can be noticed that the presence of κ produce a little bump around its mass region and so, an excess in the model, not parametrizing very well the data (black points) in this region. The separation by the cosine of helicity angle, see Section 2.7, ($\cos\theta_{12}$) was made in order to observe the projections for different sections of the Dalitz plot. This is more

¹Remembering that even when we do not necessarily expect a sum of fit fractions equal to 1 because of the interference phenomena, we also do not expecte values so higher than one, like 1.50 or even 2.0!

meaningful if there exists the presence of vector resonances (like $K^{*0}(892)$), because provides information about how each lobe is interfering and thus their effects. The region that corresponds in the Dalitz plot for $\cos \theta_{12} > 0$ is shown in blue in Figure 7.3, and in red for $\cos \theta_{12} < 0$.

Overall on this axis a fair job is obtained using these three components but still a fine tuning is needed, this will be exploited in Model 1 below.

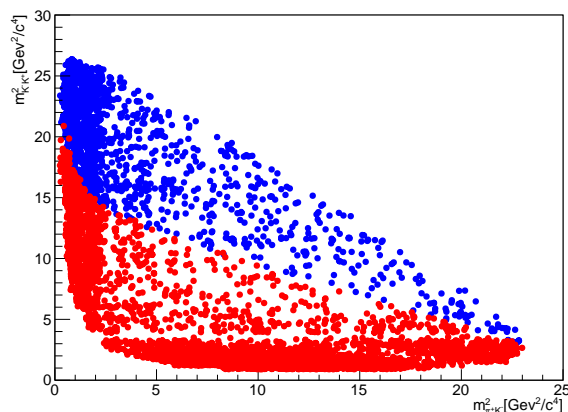


Figure 7.3: Regions of the Dalitz plot that correspond for a $\cos \theta_{12} > 0$ (in blue) and $\cos \theta_{12} < 0$ (in red).

The high mass region of $m_{\pi^{\pm}K^{\mp}}^2$, from $3.5 \text{ GeV}^2/c^2$ to $27 \text{ GeV}^2/c^2$, is shown in Fig. 7.4 c). It reflects the angular projection of the activities in the $m_{K^-K^+}^2$ sector. This shows a very strong pattern of interference with a slice with almost no events. See Figure 7.2. This represents a challenge since it is not clear in principle what possible contributions could create this effect. From the systematic procedure described, we find that the combination of a vector resonance, $\rho(1450)$, with $f_2(1270)$, a resonance of spin 2, do a very good description of this region.

For the expected rescattering region on $m_{K^-K^+}^2$ we are required to include two pseudo scalar resonances $f_0(980)$ and $f_0(1370)$ which offered the best description. It can be observed from Table 7.2 that a large amount of fit fraction is attributed to $f_0(980)$ which is a resonance believed to be mainly composed of $s\bar{s}$. It lies below than the K^-K^+ threshold, so the part that enters in play in the Dalitz plot fit is the tail of a modified Breit-Wigner (the Flatté parametrization). Yet a large contribution to it is attributed, which is an odd result. Besides if $f_0(980)\pi$ appears prominently in the $\pi^{\pm}K^-K^+$ final state, it should be more expressive in the $\pi^{\pm}\pi^-\pi^+$ final state, and this is not observed. It is also observed that in the model $f_0(980)$ and $f_0(1370)$ have large negatives CP asymmetries. The results are not conclusive. It is possible that $f_0(980)$ and $f_0(1370)$ could be mistakenly doing somebody else's job (this

will be discussed in Model 2). In Figures 7.4 d) and e) there are shown the projections in the $m_{K^-K^+}^2$ axis, for the region from 1 to 3.5 GeV/ c^2 (which includes the rescattering region) and separated by the cosine of the helicity angle ($\cos\theta_{23} > 0$ and $\cos\theta_{23} < 0$, see Figure 7.5). In Figure 7.4 f) is shown the projection in the high mass region, 3.5 to 27 GeV/ c^2 . Figures 7.4 g) and h) show the projection of model against data for $m_{\pi^\pm K^\mp}^2$.

The value of $-2\log\mathcal{L}$ obtained for the model is -9571 and a global $\chi^2/d.o.f$ equal to 1.76. Figure 7.6 shows χ^2 map constructed from an adaptive binning algorithm that ensures equal number of events on each bin. From the map it can be seen the regions with higher χ^2 values and so, where the Dalitz is poorly described. These correspond precisely to the rescattering region and in the lower $m_{\pi^\pm K^\mp}^2$ region near the threshold.

The next model that we are going to discuss concentrates the efforts to improve the overall $m_{\pi^\pm K^\mp}^2$ sector. In the same way the Model 2 show the results for the dedicated study in the low mass region in $m_{K^-K^+}^2$.

7.3

Model 1

Although in the Classic Isobar Model we obtain an overall good description of data, there are some regions that still need a more refined study. In this second family of fits we test some alternative lineshapes in order to improve the parametrization in the $\pi^\pm K^\mp$ system. For this purpose the Tobias NR [77] parametrization was added to the model² (with Λ set to 1 GeV/ c^2) and the kappa component is taken out. The inclusion of this contribution shows a better result than obtained with κ : the excess in the model for the low region in $m_{\pi^\pm K^\mp}^2$ disappears and in general the whole fit improves.

Some features can be highlighted from Table 8.3; by the inclusion of Tobias NR, a large interference with $K_0^{*0}(1430)$ is present, this can be seen as its fit fractions went from $\sim 13\%$ and $\sim 18\%$ to $\sim 1.7\%$ and $\sim 6.4\%$, respectively, and a high fit fraction is being attributed to Tobias NR. The signal of the asymmetries are conserved, positive for $K^{*0}(892)$ and $K_0^{*0}(1430)$, negative for Tobias NR (before for κ), but now the CP asymmetry due to $K_0^{*0}(1430)$ is larger. On the other hand, $K^{*0}(892)$ does not seem to be strongly affected as its solution is compatible with the obtained in the Classic Model. The projections in the $m_{\pi^\pm K^\mp}^2$ can be found on Figs. 7.8 a), b) and c). The model satisfactorily account for the data, but we must remind the that Tobias NR is an empirical parametrization used as an alternative to the non-resonant flat

²This value was obtained from the fit to the $B^\pm \rightarrow \pi^\pm \pi^+ \pi^-$ data.

parametrization, that gives more importance to low mass regions of the phase space opposed to the latter that populates equally the whole phase space.

In the $m_{K^-K^+}^2$ sector the results are compatible with the one obtained in the Classic Model. The mass projections in this axis are slightly better but with no specifically region preferred. The tendency is that $f_0(980)$ and $f_0(1370)$ continue to have a large negative CP asymmetry, and with $f_0(980)$ with a large fit fraction. Their projection are shown in Figure 7.8 d), e) and f).

[NLL -9656] Component	Fit fraction (%)		Magnitude and phase coefficients				A_{CP} (%)
	B^+	B^-	a_i^+	$\delta_i^+ [^\circ]$	a_i^-	$\delta_i^- [^\circ]$	
$K^{*0}(892)$	4.5 ± 0.9	9.3 ± 0.9	0.89 ± 0.06	0 ± 0	1.11 ± 0.06	0 ± 0	21.5 ± 10.6
$K_0^{*0}(1430)$	1.7 ± 0.5	6.3 ± 1.3	0.55 ± 0.09	177 ± 12	0.91 ± 0.11	137 ± 11	46.8 ± 14.9
<i>TobiasNR_Kpi</i>	34.0 ± 2.5	31.6 ± 2.8	2.46 ± 0.18	-128 ± 9	2.04 ± 0.15	167 ± 7	-18.4 ± 5.7
$\rho^0(1450)$	29.8 ± 1.9	32.6 ± 2.6	2.30 ± 0.15	-34 ± 11	2.07 ± 0.15	179 ± 18	-10.5 ± 4.6
$f_2(1270)$	2.0 ± 0.7	9.4 ± 1.4	0.60 ± 0.11	48 ± 16	1.12 ± 0.10	-91 ± 143	55.4 ± 13.3
$f_0(1370)$	2.3 ± 1.1	0.6 ± 0.7	0.63 ± 0.16	-37 ± 17	0.28 ± 0.16	-158 ± 25	-67.7 ± 33.0
$f_0(980)$	36.0 ± 3.2	9.7 ± 1.7	2.53 ± 0.17	-154 ± 12	1.13 ± 0.12	52 ± 24	-66.7 ± 5.5
Fit Fraction Sum	110.2	99.6					

Table 7.3: Model 1: Model components (1st column), fit fraction for each component for B^+ (B^-) on 2nd (3rd) column, magnitude and phase on 4th and 5th column for B^+ , 6th and 7th for B^- . CP asymmetry on 8th.

The $-2\log\mathcal{L}$ found for this model is -9656 which represents an improvement 85 units with respect to the Classic Model. The χ^2 map is depicted in Fig. 7.7 with a global value per d.o.f obtained equal to 1.45, showing indeed an improvement.

7.4 Model 2

The model 2 is a representation of the third approach in which we study in more detail the rescattering region. So far, considering Model 1 and the Classic Model, we can enumerate three resonant states contributing in the $\pi^\pm K^\mp$ system; $K^*(892)^0$, $K^*(1430)^0$ and Tobias NR. For the K^-K^+ system we have 4 components being two of them attributed mainly to the rescattering region: $f_0(980)$ and $f_0(1370)$. These two components do a reasonable description of data but their fit fraction contribution are not consistent with what is seen on the $B^\pm \rightarrow \pi^\pm \pi^+ \pi^-$ analysis.

Following this picture, we test the rescattering function Pelaez 2005 [2] as an alternative to replace both components ($f_0(980)$ and $f_0(1370)$). As explained in Section 6.1.4, this rescattering amplitude has been tested to work well in the region that goes from $\sim 0.950 \text{ GeV}/c^2$ to $1.5 \text{ GeV}/c^2$. We perform the Dalitz

plot fit with the established parameters values (with $\Delta_{\pi\pi}$ set³ to 1 GeV/ c^2) that are shown in Equation 6-19 following the reference [2]. We also test the scenario in which these parameters are let free to float, comments about this will be given below.

As can be seen in Figs. 7.10 d) and e) we obtain a qualitatively similar description of data as in the Classic Model and Model 1, now mainly using the rescattering component for the low $m_{K^-K^+}$ mass region. The substitution of the two pseudo-scalars by this rescattering parametrization brings some changes that need a mention. First, the large negative CP asymmetry before related to $f_0(980)$ and $f_0(1370)$, are now due to the rescattering component. Also the rescattering component has a large fit fraction but not as large as was observed before for $f_0(980)$. Nevertheless, the $-2\log\mathcal{L}$ is worse to -9606 (compared with Model 1 -9656). We observe that the sign of the asymmetries are maintained, and that the fit fraction of the other components remain in similar values. In Table 8.4 these results are summarized. The χ^2 map is shown in Figure 7.9, the global $\chi^2/d.o.f$ obtained is of 1.54.

[NLL -9606] Component	Fit fraction (%)		Magnitude and phase coefficients				A_{CP} (%)
	B^+	B^-	a_i^+	$\delta_i^+ [^\circ]$	a_i^-	$\delta_i^- [^\circ]$	
$K^{*0}(892)$	5.1 ± 0.9	9.5 ± 1.0	0.92 ± 0.05	0 ± 0	1.08 ± 0.05	0 ± 0	16.2 ± 9.1
$K_0^{*0}(1430)$	3.5 ± 0.8	5.6 ± 1.1	0.76 ± 0.09	-177 ± 11	0.83 ± 0.09	135 ± 10	8.4 ± 14.5
<i>TobiasNR_Kpi</i>	31.3 ± 4.0	36.0 ± 3.5	2.29 ± 0.25	-141 ± 7	2.10 ± 0.15	165 ± 6	-8.3 ± 7.6
$\rho^0(1450)$	27.9 ± 2.6	32.4 ± 1.8	2.16 ± 0.12	-175 ± 10	2.00 ± 0.11	149 ± 12	-7.9 ± 4.3
$f_2(1270)$	4.5 ± 0.9	11.3 ± 1.3	0.87 ± 0.09	-102 ± 11	1.18 ± 0.09	-121 ± 12	29.5 ± 10.1
Re-scattering	25.5 ± 2.2	7.4 ± 0.8	2.07 ± 0.10	-49 ± 12	0.95 ± 0.07	-74 ± 14	-64.9 ± 3.6
Fit Fraction Sum	97.8	102.1					

Table 7.4: Model 2: Model components (1st column), fit fraction for each component for B^+ (B^-) on 2nd (3rd) column, magnitude and phase on 4th and 5th column for B^+ , 6th and 7th for B^- . CP asymmetry on 8th.

7.4.1

Alternatives to Model 2

We also performed a variation of Model 2 in which we use the same components but with the rescattering parameters free to float: the parameter m' that controls where the amplitude ends, and the parameters ϵ_1 and ϵ_2 that are introduced in the inelasticity expression, see Equations 6-19. No significant improvement is noticed here: the value of $-2\log\mathcal{L}$, the fit fractions and magnitudes and phases are all quite the same as in Model 2, the values of ϵ_1 and ϵ_2 go to similar values as those stated in Equation 6-19. The rescattering

³This value was obtained from the fit to the $B^\pm \rightarrow \pi^\pm \pi^+ \pi^-$ data.

amplitudes tested so far are still not good enough to account entirely of this region and better theoretical models are needed.

Another test is performed, in which we add to the Model 2 the $f_0(980)$ resonance. When we do this, the CP asymmetry and the large fit fraction are again attributed to $f_0(980)$. The $-2\log\mathcal{L}$ that we obtain is higher than the obtained for any other model but this is suspicious as was explained before, the contribution for $f_0(980)$ is expected to be very low. This reinforces the need of testing new amplitudes for the rescattering region and for better theoretical models.

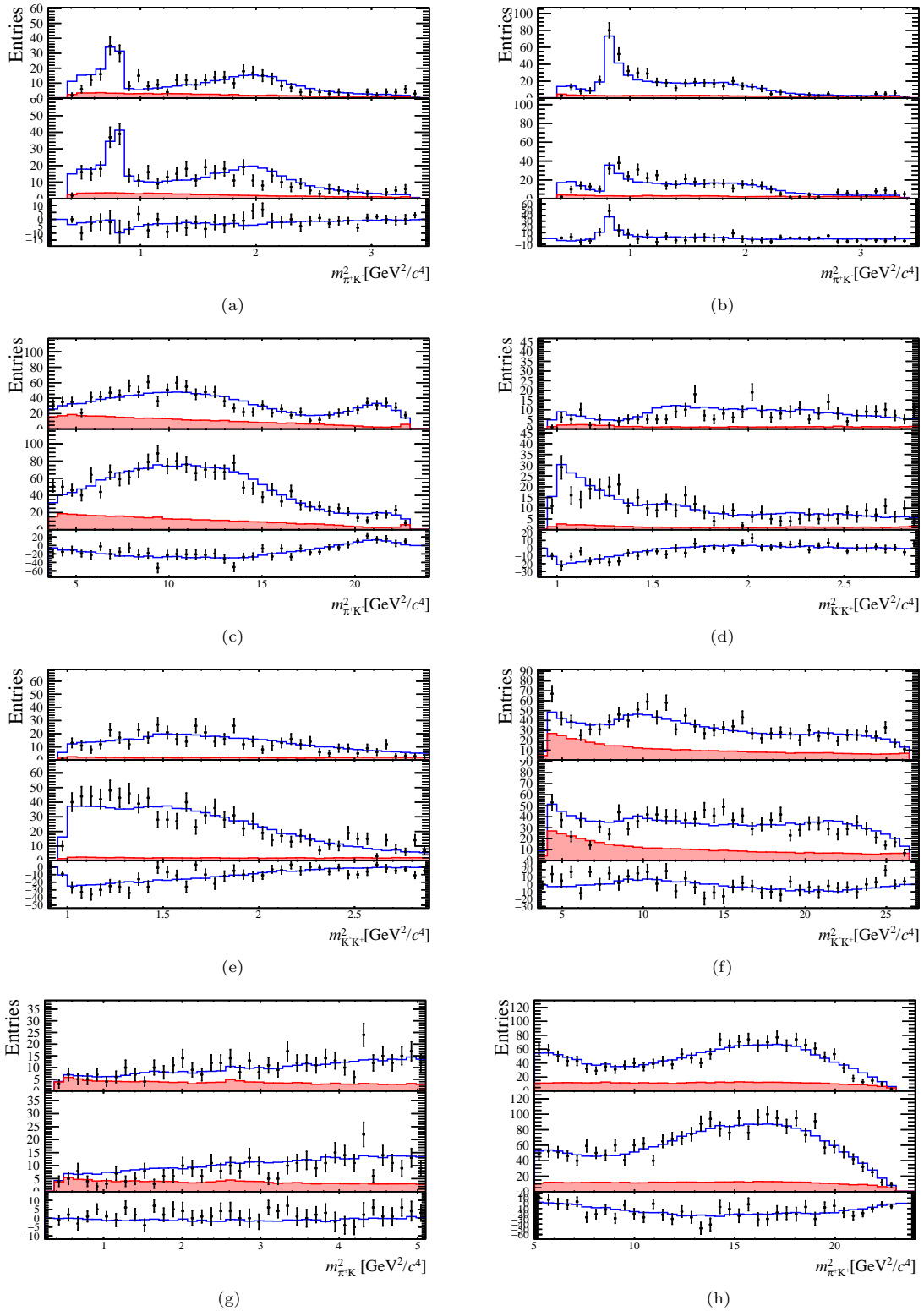


Figure 7.4: Classic model (fit 2011). For each plot B^- (top), B^+ (middle) and the difference ($B^- - B^+$, bottom). a) ($\cos\text{Hel}12 > 0$), b) ($\cos\text{Hel}12 < 0$) and c) show the projections on $m_{\pi^\pm K^\mp}^2$. d) ($\cos\text{Hel}23 > 0$), e) ($\cos\text{Hel}23 < 0$) and f) the projections on $m_{K^- K^+}^2$ and g) and h) the projections on $m_{\pi^\pm K^\mp}^2$. The line in blue represents the model, the black dots the data and the region in red the background estimation

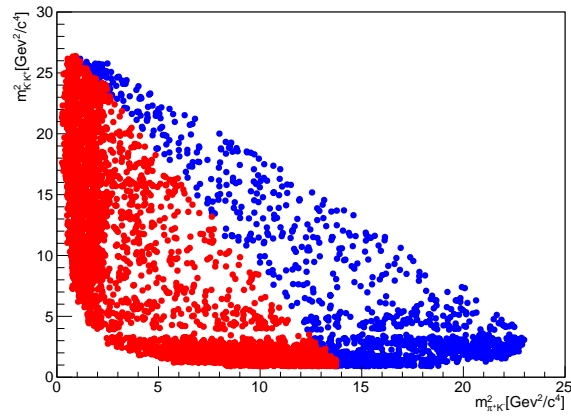


Figure 7.5: Regions of the Dalitz plot that correspond for a $\cos \theta_{23} > 0$ (in blue) and $\cos \theta_{23} < 0$ (in red).

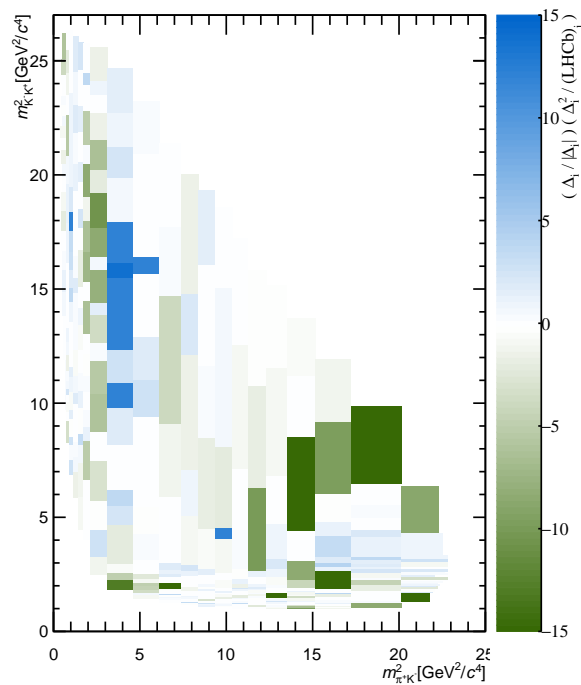


Figure 7.6: Classic model (fit 2011) χ^2 map. The global χ^2 value obtained is of 1.76

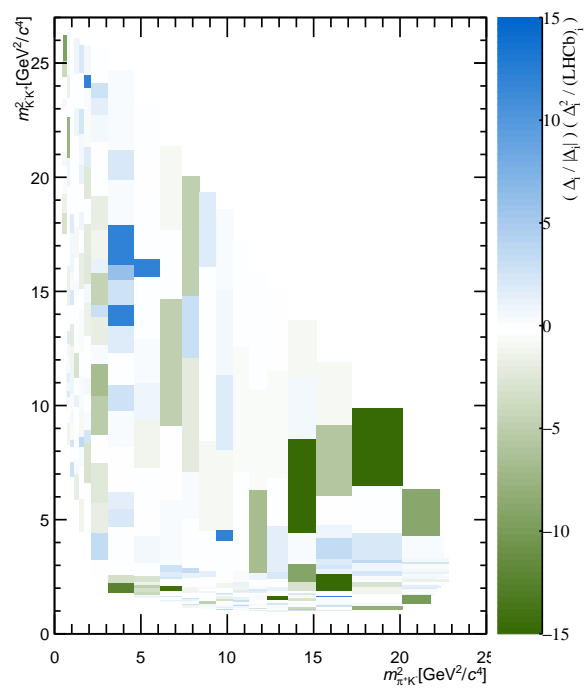


Figure 7.7: Model 1 (fit 2014) χ^2 map. The global χ^2 value obtained is of 1.45

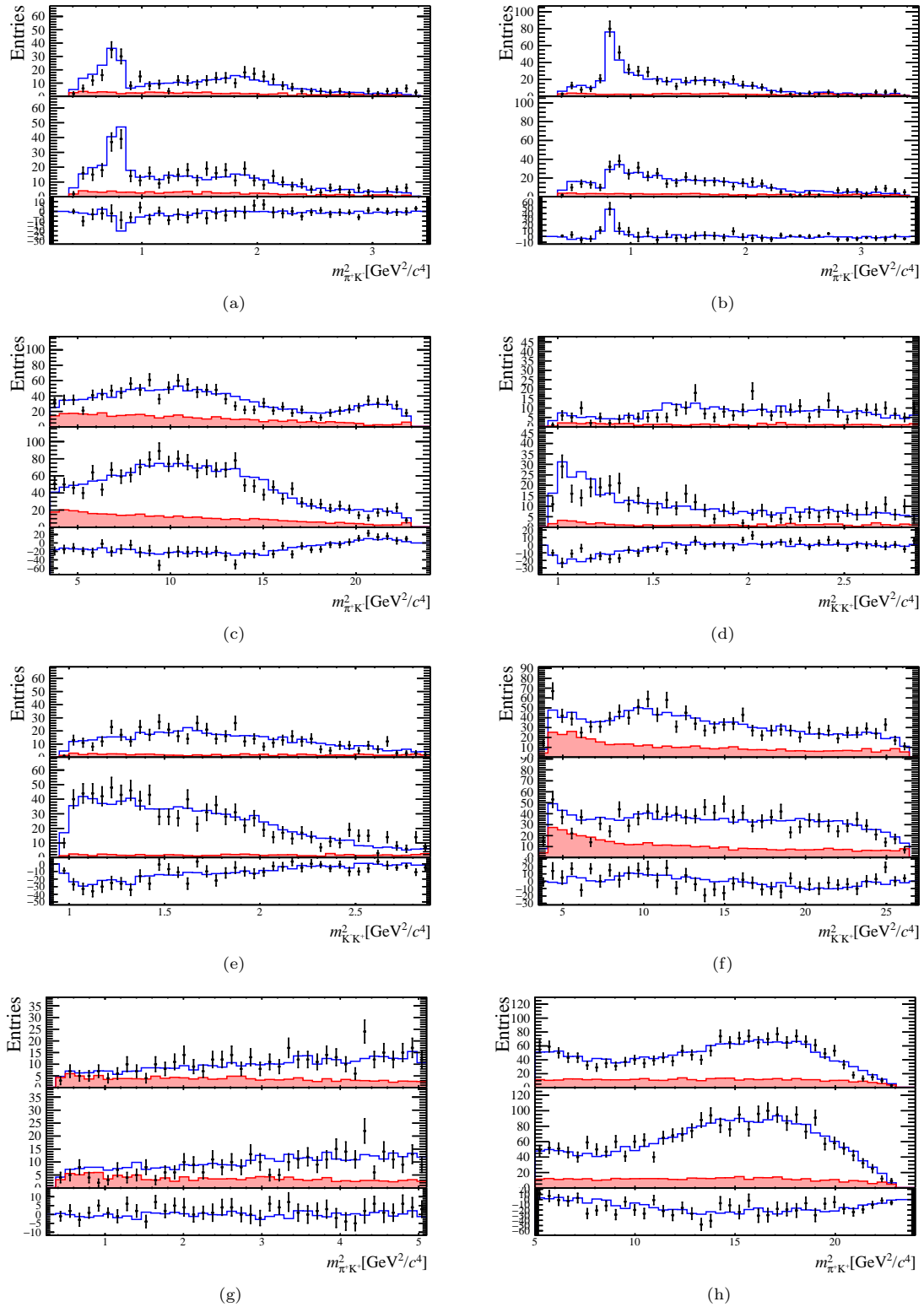


Figure 7.8: Model 1 (fit 2014). For each plot B^- (top), B^+ (middle) and the difference ($B^- - B^+$, bottom). a)($\cos\text{Hel}12 > 0$), b) ($\cos\text{Hel}12 < 0$) and c) show the projections on $m^2_{\pi^\pm K^\mp}$. d)($\cos\text{Hel}23 > 0$), e) ($\cos\text{Hel}23 < 0$) and f) the projections on $m^2_{K^- K^+}$ and g) and h) the projections on $m^2_{\pi^\pm K^\pm}$. The line in blue represents the model, the black dots the data and the region in red the background estimation

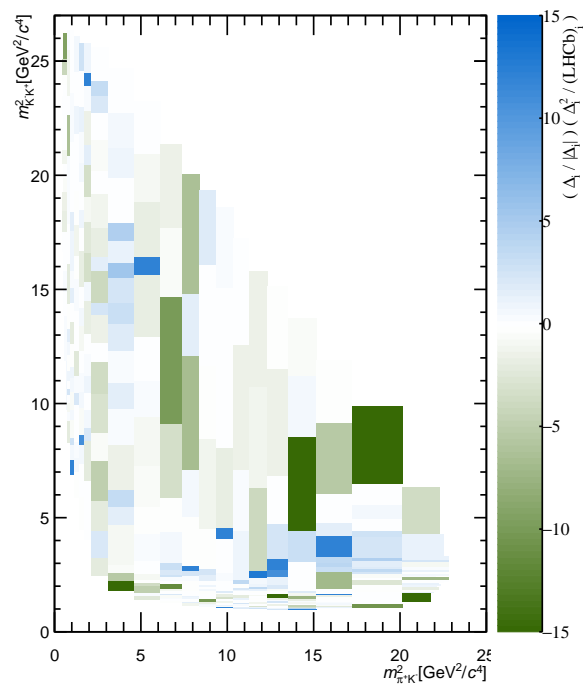


Figure 7.9: Model 2 (fit 1201) χ^2 map. The global χ^2 value obtained is of 1.54

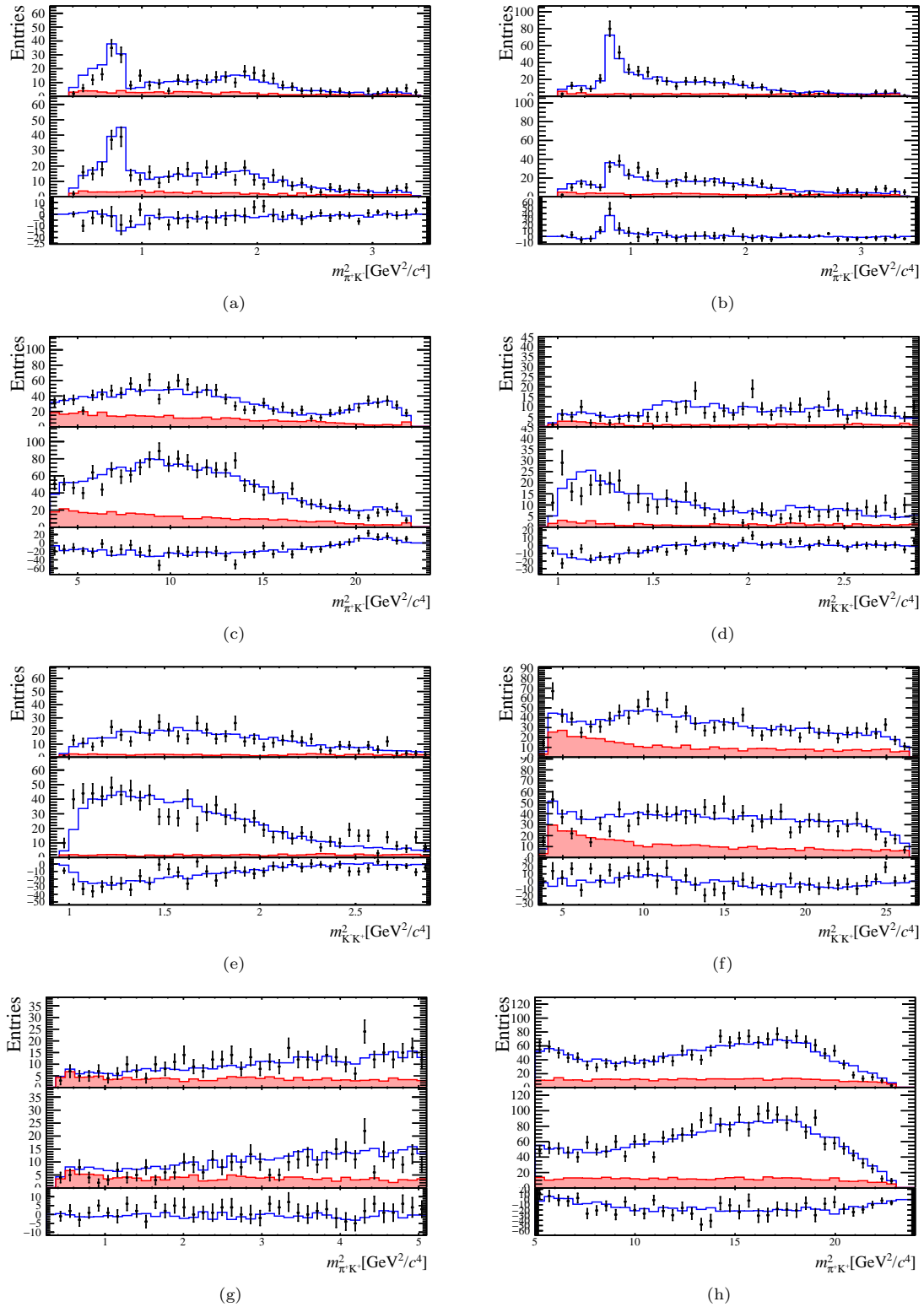


Figure 7.10: Model 2 (fit1201). For each plot B^- (top), B^+ (middle) and the difference ($B^- - B^+$, bottom). a)($\cos\text{Hel}12 > 0$), b) ($\cos\text{Hel}12 < 0$) and c) show the projections on $m_{\pi^\pm K^\mp}^2$. d)($\cos\text{Hel}23 > 0$), e) ($\cos\text{Hel}23 < 0$) and f) the projections on $m_{K^- K^+}^2$ and g) and h) the projections on $m_{\pi^\pm K^\mp}^2$. The line in blue represents the model, the black dots the data and the region in red the background estimation.

8 Conclusions

With the data collected by the LHCb in 2011 and 2012 corresponding to an integrated luminosity of 3.0 fb^{-1} from proton-proton collisions at 7 TeV and 8 TeV, studies in the charmless hadronic three-body $B^\pm \rightarrow \pi^\pm K^- K^+$ decay were performed. This decay mode is of special interest for the study of the CP violation phenomena, which is one of the main ingredients for the matter-antimatter asymmetry observed in the universe. Among the features that make it attractive, is the fact that it is a process dominated by resonant intermediate states, where the interferences between their amplitudes, can be potential sources for the CP violation. Thus, this decay, and in general charmless three-body B decays mediated by both tree level transition as well as loop (penguin) amplitudes, constitute a great laboratory for a better understanding of CP violation.

As a first step for this analysis, event selections applied to the data samples, in several successive stages, were made. A fit to the resulting $B^\pm \rightarrow \pi^\pm K^- K^+$ mass spectrum was performed, in order to determine the number of signal candidates as well as the raw asymmetry. Since this raw asymmetry is not all due to CP violation, corrections for detection and production effects were applied. The total integrated CP asymmetry found for this channel was of [22]:

$$\mathcal{A}_{CP}(B^\pm \rightarrow \pi^\pm K^- K^+) = -0.123 \pm 0.017 \pm 0.012 \pm 0.007,$$

where the first uncertainty is statistical, the second systematic, and the third due to CP asymmetry of the control reference mode. This measurement was obtained with a significance of 5.6σ , thus representing a clear observation of CP violation in this decay mode. Large asymmetries in regions of the phase space were also observed. In particular, for the so-called $\pi\pi \leftrightarrow KK$ rescattering region:

$$\mathcal{A}_{CP} = -0.328 \pm 0.028 \pm 0.029 \pm 0.007, \text{ for } m_{K^- K^+} < 1.5 \text{ GeV}/c^2$$

Several discussions about the possible sources of these charge asymmetries have arisen [76, 75, 77]. For example, for the asymmetry observed in the rescattering region one possibility is that it is due to the rescattering process

$\pi\pi \leftrightarrow KK$. This is reinforced since a large CP asymmetry has been also observed in this region, with opposite sign for $B^\pm \rightarrow \pi^\pm\pi^+\pi^-$. In order to fully understand this an amplitude analysis is needed.

We performed the amplitude analysis for this decay using the Isobar model formalism, in which the total decay amplitude of a process is expressed as a coherent sum of the possible intermediate states. The aim was to determine the resonant sub-structure of this decay mode, their relative contribution and how they were interfering, by performing a fit to the distribution of events in the Dalitz plot. Resonant contributions were expected in the π^+K^- and K^-K^+ systems. Being this the first time that an amplitude analysis is performed for $B^\pm \rightarrow \pi^\pm K^- K^+$, a systematic procedure was adopted for the construction of the Isobar models. The results were presented in terms of the possible resonance components, their relative magnitude and phases associated to their decay amplitudes, their relative contribution in terms of fit fractions for B^+ and B^- , and the CP asymmetry associated to each of them. Three models, the best representative of three families of fits, were presented:

1. A Classic Model, in which we only use known resonance states. Seven components were found: $K^{*0}(892)$, $K_0^{*0}(1430)$ and κ for the π^+K^- system and $\rho(1450)$, $f_2(1270)$, $f_0(980)$ and $f_0(1370)$ in the K^-K^+ system. A good parametrization of data was obtained but still some regions needed better description. We find that for $\pi\pi \leftrightarrow KK$ rescattering region, which shows the larger asymmetry, is parametrized with two pseudoscalars $f_0(980)$ and $f_0(1370)$.
2. The second approach consisted in a family of fits to improve the parametrization in the π^+K^- system. Three components were found for this system: $K^{*0}(892)$, $K_0^{*0}(1430)$ and a third component to account for a NR contribution (instead of the κ component) which is parametrized by an alternative lineshape described in the text as the Tobias non-resonant function. The inclusion of this lineshape improved the fit quality substantially. Still, the main actors of the sources of CP violation remain the same as in the Classic Model.
3. The third approach was focussed in the so-called $\pi\pi \leftrightarrow KK$ rescattering region. For this purpose we used a dedicated rescattering amplitude given by the Pelaez function [2]. The aim was to replace the suspicious components $f_0(980)$ and $f_0(1370)$. The description of the events obtained for this region, using this rescattering amplitude, was not as good as when using the f_0 's components. A model with both rescattering and $f_0(980)$ prefers $f_0(980)$ being the source of CP violation in this region.

This is not expected since $f_0(980)$ is not seem to contribute significantly in $B^\pm \rightarrow \pi^\pm \pi^+ \pi^-$ decays. It is possible that the phenomenological description of the rescattering process is still not good enough.

In summary, a rich resonant substructure was found for the decay mode $B^\pm \rightarrow \pi^\pm K^- K^+$. We obtained three component for the $\pi^\pm K^\mp$ system, namely, $K^{*0}(892)$, $K_0^{*0}(1430)$ and a Tobias non-resonant component. For the $K^- K^+$ system four component were obtained: a vector resonance $\rho(1450)$ and a resonance of spin 2 $f_2(1270)$ which were found to be mainly acting in the region with strong pattern of interferences in the $B^\pm \rightarrow \pi^\pm K^- K^+$ phase space, where a slice with almost not event is observed. For the rescattering region we found two pseudoscalar $f_0(980)$ and $f_0(1370)$, that effectively accounts for this regions but their presence is suspicious. As alternative to these, a rescattering amplitude is tested. This rescattering amplitude provides moderately description of data in this region while keeping some features expected, like the signal of the CP asymmetry. However, the model with rescattering did not show much improvement with respect to the model with resonances, giving a puzzling result. This seems to indicate that the available phenomenological descriptions for the rescattering amplitude must be improved (or some new calculations are needed) in order to explain the significant CP violation measured in this region.

The results presented in this thesis are also present in the full analysis note about to start the scruting within the LHCb collaboration, towards publication. During this internal review, systematic studies will be performed to obtain the final uncertainties in the fit results. This analysis, with less than 5000 events, is in any case limited due to the statistical uncertainties.

With the larger statistics collected by the LHCb in the Run II, a better study of the $B^\pm \rightarrow \pi^\pm K^- K^+$ decays will be possible, with implementation of new strategies of analysis. Together with the studies of the other $B^\pm \rightarrow h^\pm h^- h^+$ decays, and multi-body processes of b-hadrons in general, it will be possible to better understand the CP violation phenomena: as we know, although its origin relies in the weak sector, it is in the rich hadronic enviroment where manifest itself.

Bibliography

- [1] Particle Data Group. 2016 review of particle physics. **Chin. Phys. C**, v. 40, p. 100001, 2016. (document), 2.6, 2.7, 2.4, 2.5, 5.1.2, 6.1.4
- [2] J. Pelaez; Ynduráin. The pion-pion scattering amplitude. **Phys. Rev D**, v. 71, p. 074016, 2005. (document), 6.1.4, 6.1.4, 6.2, 7.1, 7.4, 3
- [3] R. Aaij et al. The LHCb trigger and its performance in 2011. [arXiv:hep-ph/1211.3055v2]. 2012. (document), 3.2.6, C.1, C.1
- [4] A. SAKHAROV. Violation of CP invariance, c asymmetry, and baryon asymmetry of the universe. **Pisma Zh.Eksp. Teor.Fiz**, v. 5, p. 24, 1967. 1
- [5] M. Kobayashi; T. Maskawa. -. **Prog. Theor. Phys.**, v. 49, p. 652–657, 1973. 1, 2.4
- [6] E. Leade; E. Predazzi. **A Introduction to Gauge Theories and the new Physics**. England: Cambridge University Press, 1982. 2.1
- [7] W. Buchmüller; C. Lüdeling. 2.1
- [8] S. L Glashow. Partial symmetries of weak interactions. **Nucl. Phys.**, v. 22, p. 579, 1961. 2.1
- [9] A. Salam; J. C. Ward. Weak and electromagnetic interactions. **Phys. Lett**, v. 13, p. 168, 1964. 2.1
- [10] S. Weinberg. A model of leptons. **Phys. Rev.**, v. 19, p. 1264, 1967. 2.1
- [11] colaboração ATLAS. Observation of a new particle in the search for the standard model higgs with the atlas detector at the lhc. **Phys. Lett. B**, v. 716, p. 1–29, 2012. 2.1
- [12] CMS colaboração. Evidence for a new state decaying into two photons in the search for the standard model higgs boson in pp collisions. CMS PAS HIG-12-015. 2012. 2.1
- [13] F. Englert; R. Brout. Broken symmetry and the mass of the mass of gauge vector mesons. **Phys. Rev. Lett.**, v. 13, p. 321, 1964. 2.1
- [14] P. W. Higgs. Broken symmetries and the masses of gauge bosons. **Phys. Rev. Lett.**, v. 13, p. 508, 1964. 2.1

- [15] Bigi, I.; Sanda A.I. Cp violation. **Camb.Monogr.Part.Phys.Nucl.Phys.Cosmol.**, v. 9, p. 1–382, 2000. 2.2
- [16] G. Branco, L.; J. Silva. **CP Violation**. USA: Oxford University Press Inc., 1999. 2.2
- [17] J. CRONIN, V.; R. Turlay. Evidence for 2π decay of the k_2^0 meson. **Phys. Rev. Lett.**, v. 13, p. 138, 1964. 2.3
- [18] WOLFENSTEIN, L. Final state interactions and CP violation in weak decays. **Phys.Rev.**, D43, p. 151–156, 1991. 2.3, 5.2
- [19] P. W. Higgs. Parametrization of the kobayashi-maskawa matrix. **Phys. Rev. Lett.**, v. 51, p. 1945, 1983. 2.4
- [20] Bander, M.; Silverman, D.; Soni, A. CP noninvariance in the decays of heavy charged quark systems. **Phys.Rev.Lett.**, v. 43, p. 242, 1979. 1, 5.1
- [21] THE BELLE COLLABORATION. **Measurement of branching fraction and direct CP asymmetry in the charmless $B^+ \rightarrow K^+K^-\pi^+$ decays at Belle**. <https://arxiv.org/abs/1704.07566>. 2.7
- [22] LHCb COLLABORATION, R. AAIJ ET AL. Measurement of CP violation in the three-body phase space of charmless B^\pm decays. **Phys. Rev. Lett. D**, v. 90, p. 112004, 2014. 2.7, 5, 5.1.1, 8
- [23] R. Dalitz. On the analysis of tau-meson data and the nature of tu-meson. **Phil. Mag.**, v. 44, p. 1068, 1953. 2.8
- [24] C. Gobél. Estudo da contribuição não ressonante em decaimentos hadrônicos de méson d em três corpos. Tesis de Doutorado, CBPF Rio de Janeiro. 1999. 2.8
- [25] E. Byckling; K. Kajantie. **Particle Kinematics**. New York, NY, USA: John Wiley and Sons, 1973. 2.8
- [26] C. Amsler. Proton antiproton annihilation and meson spectroscopy with the crystal barrel. 2.8
- [27] B. Aubert et al . An amplitude analysis of the decay $B^\pm \rightarrow \pi^\pm\pi^\pm\pi^\mp$. **Phys. Rev D.**, v. 72, p. 052002, 2005. 2.9, 2.9, 6.6, 6.6
- [28] L. Evans; P. Bryant. Lhc machine 3. [S08001]. 2008. 3.1
- [29] K. Aamodt et al. The ALICE experiment at the LHC, JINST 3. [S08002]. 2008. 3.1

- [30] G. Aad et al. The ATLAS experiment at the LHC, *JINST* 3. [S08003]. 2008. 3.1
- [31] G. Aad et al. The CMS experiment at the LHC, *JINST* 3. [S08004]. 2008. 3.1
- [32] A. Alves Jr et al. The LHCb detector at the LHC, *JINST* 3. [S08005]. 2008. 3.1
- [33] Aaij, R. et al. Lhcb detector performance. **Int. J. Mod. Phys. A**, v. 30, p. 1530022. 3.2
- [34] Aaij, R. et al. Performance of the lhcb vertex locator. **JINST**, v. 9, p. 09007. 3.2.1
- [35] Colaboração LHCb. LHCb magnet: Technical design report. CERN-LHCC-2000-007. 2000. 3.2.2
- [36] Aaij, R. et al. Measurement of the track reconstruction efficiency at lhcb. **JINST**, v. 10, p. 02007, 2015. 3.2.3
- [37] Colaboração LHCb. LHCb inner tracker: Technical design report. CERN-LHCC-2002-029. 2002. 3.2.3
- [38] Colaboração LHCb. LHCb outer tracker: Technical design report. CERN-LHCC-2002-029. 2001. 3.2.3
- [39] Arink, R. et al. Performance of the lhcb outer tracker. **JINST**, v. 9, p. 01002, 2014. 3.2.3
- [40] Adinolfi, M. and others. Performance of the LHCb rich detector at the Lhc. **Eur. Phys. J. c**, v. 73, p. 2431, 2013. 3.2.4
- [41] Colaboração LHCb. LHCb RICH: Technical design report. CERN-LHCC-2000-037. 2000. 3.2.4
- [42] Aaij, R. et al. Performance of the lhcb calorimeters. 2014. LHCb-DP-2013-004. 3.2.5
- [43] Colaboração LHCb. LHCb calorimeters: Technical design report. CERN-LHCC-2000-036. 2000. 3.2.5
- [44] Archilli, F. et al. Performance of the muon identification at lhcb. **JINST**, v. 8, p. 10020, 2013. 3.2.6

- [45] Alves Jr. et al. Performance of the LHCb muon system. **JINST**, v. 8, p. 02022, 2013. 3.2.6
- [46] Colaboração LHCb. LHCb muon system: Technical design report. CERN-LHCC-2001-010. 2001. 3.2.6
- [47] Colaboração LHCb. LHCb trigger system: Technical design report. CERN-LHCC-2003-031. 2003. 3.2.6
- [48] J. Albrecht V. V. Gligorov, G.; S. Tolk. The LHCb trigger and its performance in 2011. [arXiv:hep-ex/1310.8544v1]. 2012. 3.2.6
- [49] LHCb Collaboration. Performance of the LHCb detector during the LHC proton runs 2010-2012. LHCb-PROC-2013-030. 2013. 3.3
- [50] LHCb COLLABORATION, R. AAJ ET AL. LHCb detector performance. **Int. J. Mod. Phys A**, v. 30, p. 1530022, 2015. 3.3
- [51] LHCb COLLABORATION. **Performance of the LHCb detector during the LHC proton Runs 2012-2012**. LHCb-PROC-2013-030. 3.3
- [52] GLIGOROV, V. V.; WILLIAMS, M. Efficient, reliable and fast high-level triggering using a bonsai boosted decision tree. **JINST**, v. 8, p. P02013, 2013. 4.3.1
- [53] Aaij, R. and others. The LHCb trigger and its performance in 2011. **JINST**, v. 8, p. 04022, 2013. 4.3.1
- [54] BREIMAN, L. et al. **Classification and regression trees**. Belmont, California, USA: Wadsworth international group, 1984. 4.4
- [55] ROE, B. P. et al. Boosted decision trees as an alternative to artificial neural networks for particle identification. **Nucl.Instrum.Meth.**, A543, p. 577–584, 2005. 4.4
- [56] Hoecker et al. Tmva: Toolkit for multivariate data analysis. 4.4
- [57] POWELL, A. et al. Particle identification at LHCb. **PoS**, ICHEP2010, p. 020, 2010. LHCb-PROC-2011-008. 4.4
- [58] Sjöstrand et al. Pythia 6.4 physics and manual. **JHEP**, v. 05, p. 026. 4.6
- [59] Sjöstrand et al. Pythia 6.4 physics and manual. **Comput. Phys. Commun.**, v. 178, p. 852–867. 4.6

- [60] Agostinelli S. GEANT4 collaboration. Geant4: a simulation toolkit. **Nucl. Instrum. Meth. A**, v. 506, p. 250, 2003. 4.6
- [61] Allison et al. Geant4 developments and applications. **IEEE Trans.Nucl.Sci.**, v. 53, p. 270. 4.6
- [62] W. Verkerke; D. Kirkby. The roofit toolkit for data modeling. ArXiv:physics/0306116v1. 2003. 4.8
- [63] Skwarnicki, T. **A study of the radiative cascade transitions between the Upsilon-prime and Upsilon resonances**. Tese (Doutorado), 1986. [Http://inspirehep.net/record/230779/files/230779.pdf](http://inspirehep.net/record/230779/files/230779.pdf). 4.8.1
- [64] H. Albrecht. Search for $b \rightarrow s\gamma$ in exclusive decays of b mesons. **Phys.Lett. B**, v. 229, p. 304, 1989. 4.8.2
- [65] del Amo Sanchez et al. Study of $b \rightarrow x\gamma$ decays and determination of $|v_{td}/v_{ts}|$. **Phys.Rev. D**, v. 82, p. 051101. 4.8.3
- [66] Aaij et al. Evidence for CP violation in $B^\pm \rightarrow K^\pm\pi^+\pi^-$ and $B^\pm \rightarrow K^\pm K^+K^-$ decays. LHCb-CONF-2012-018. 5.1
- [67] I. Bediaga et al. Search for CP violation in $B^\pm \rightarrow K^\pm\pi^+\pi^-$ and $B^\pm \rightarrow K^\pm K^+K^-$ decays in 2011 data. LHCb-ANA-2012-040. 5.1
- [68] I. Bediaga et al. CP violation measurement in $B^\pm \rightarrow K^\pm\pi^+\pi^-$ and $B^\pm \rightarrow K^\pm K^+K^-$ decays in 2011 data. LHCb-ANA-2012-029. 5.1
- [69] LHCb COLLABORATION, R. AAIJ ET AL. Measurement of CP violation in the phase space of $B^\pm \rightarrow K^\pm\pi^+\pi^-$ and $B^\pm \rightarrow K^\pm K^+K^-$ decays. **Phys. Rev. Lett.**, v. 111, p. 101801, 2013. 5.1, 5.2
- [70] I. Bediaga et al. Search for CP violation in $B^\pm \rightarrow K^+K^-\pi^\pm$ and $B^\pm \rightarrow \pi^\pm\pi^+\pi^-$ decays in 2011 data. LHCb-ANA-2012-077. 5.1
- [71] I. Bediaga et al. Evidence for CP violation in $B^\pm \rightarrow K^+K^-\pi^\pm$ and $B^\pm \rightarrow \pi^\pm\pi^+\pi^-$ decays in 2011 data. LHCb-ANA-2013-052. 5.1
- [72] LHCb COLLABORATION, R. AAIJ ET AL. Measurement of CP violation in the phase space of $B^\pm \rightarrow K^\pm K^+\pi^-$ and $B^\pm \rightarrow \pi^\pm\pi^+\pi^-$ decays. **Phys. Rev. Lett.**, v. 112, p. 011801, 2014. 5.1
- [73] GRONAU, M. U-spin breaking in CP asymmetries in B decays. 2013. 5.1

- [74] Zhang, Z.; Guo, Xin-Heng; Yang, Ya-Dong. CP violation in $B^\pm \rightarrow \pi^- \pi^+ \pi^-$ in the region with low invariant mass of one $\pi^+ \pi^-$ pair. **Phys.Rev. D**, American Physical Society", v. 87, p. 076007, 2013. Disponível em: <<http://link.aps.org/doi/10.1103/PhysRevD.87.076007>>. 5.1
- [75] BHATTACHARYA, B.; GRONAU, M.; ROSNER, J. L. CP asymmetries in three-body B^\pm decays to charged pions and kaons. **Phys.Lett.**, B726, p. 337, 2013. 5.1, 8
- [76] AAIJ, R. et al. Measurement of CP violation in the phase space of $B^\pm \rightarrow K^\pm \pi^+ \pi^-$ and $B^\pm \rightarrow K^\pm K^+ K^-$ decays. **Phys. Rev. Lett.**, v. 111, p. , 101801, 2013. 5.1, 8
- [77] J. H. Alvarenga et al. Cp violation: Dalitz interference, CPT and FSI. **Phys. Rev. D**, v. 92, p. 054010, 2015. 5.1, 6.1.4, 6.1.4, 7.1, 7.3, 8
- [78] Aaij R. et tal. Measurement of j/ψ production in pp collisions at $\sqrt{s} = 2.76$ tev. **JHEP**, v. 2, p. 041. 5.1.1
- [79] Aaij R. et al. Measurement of the $d_s^+ - d_s^-$ production asymmetry in 7 tev pp collisions. **Phys. Lett. B**, v. 713, p. 186–195, 2012. 5.1.2
- [80] MUELLER, D.; VESTERINEN, M. **Measurement of the kaon detection asymmetry using double-tagged partially reconstructed D^0 decays.** LHCb-INT-2013-054. 5.1.2
- [81] CHENG, H.-Y.; CHUA, C.-K.; SONI, A. Final state interactions in hadronic B decays. **Phys.Rev.**, D71, p. 014030, 2005. 5.2
- [82] BEDIAGA, I. et al. On a CP anisotropy measurement in the Dalitz plot. **Phys.Rev.**, D80, p. 096006, 2009. 5.2
- [83] BEDIAGA, I. et al. Second generation of 'Miranda procedure' for CP violation in Dalitz studies of B (and D and τ) decays. **Phys.Rev.**, D86, p. 036005, 2012. 5.2
- [84] D. Herndon , P.; R. Cashmore. Generalized isobar model formalism. **Phys. Rev. D**, v. 11, p. 3165, 1975. 6.1
- [85] Fleming, G. Recoupling effects in the isobar model. i. general formalism for three-pion scattering. **Phys. Rev. B**, v. 135, p. 551–560, 1964. 6.1
- [86] C. Zemach . Three-pion decays of unstable particles. **Phys. Rev. B**, v. 1201, p. 133, 1964. 6.1.1

- [87] C. Zemach . Determination of the spins and parities of resonances. **Phys. Rev. B**, v. 109, p. 140, 1965. 6.1.1
- [88] C. Zemach . Use of angular-momentum tensors. **Phys. Rev. B**, v. 97, p. 140, 1965. 6.1.1
- [89] Blatt John M., W.; Victor F. **Theoretical Nuclear Physics**. New York, NY, USA: John Wiley and Sons, 1952. 6.1.3
- [90] J. D Jackson ; Nuovo Cim. Remarks on the phenomenological analysis of resonances. **Phys. Rev.**, v. 34, p. 1644, 1964. 6.1.4
- [91] LAURA++. -. [Http://laura.hepforge.org/](http://laura.hepforge.org/). 6.2.1
- [92] S. Malde et. al. **PIDCalib packages**. 2017. [Https://twiki.cern.ch/twiki/bin/view/LHCb/PIDCalibPackage](https://twiki.cern.ch/twiki/bin/view/LHCb/PIDCalibPackage). 6.3.1
- [93] D. Craik et al. **Dalitz plot analysis of $B_S^0 \rightarrow \bar{D}^0 K^- \pi^+$** . LHCb-ANA-2013-014. 6.3.3
- [94] A. Martin Sanchez, P.; M. H. Schune. **Performances of the LHCb L0 Calorimeter Trigger**. LHCb-PUB-2011-026. 6.3.3
- [95] BABA COLLABORATION. -. **Phys. Rev. D**, v. 78, p. 012004, 2008. 6.4.2
- [96] COWAN, G. **Statistical Data Analysis**. New York, USA: Oxford University Press Inc., 1998. 6.5.1
- [97] Eric Van Herwijnen. **Bandwidth division**. [Https://twiki.cern.ch/twiki/bin/view/LHCb/BWDivision](https://twiki.cern.ch/twiki/bin/view/LHCb/BWDivision). C.2

A Mass Fit

A.0.2 The signal PDF

The baseline shape of the signal PDF is extracted from the MC sample (built by passing the full event selection criteria and with the L0 Global_TIS or L0 Hadron_TOS trigger configuration). The mass fit to the signal MC samples, for 2011, 2012 and the combined 2011 and 2012 are shown in the Figures A.1, A.2 and A.3 respectively. The plots are divided in trigger lines. The parameter values that were extracted from these fits are listed in Tables A.1, A.2 and A.3 for 2011, 2012 and combined 2011 and 2012 MC samples respectively. These values are used as initial input in the fit to data that is presented in subsection 4.8.3. Parameters with F are those which are left to float when doing the data fit.

Background contributions

As was mentioned in the subsection 4.8.2, the two prominent peaking background contributions comes from the cross-feed of $B^\pm \rightarrow K^\pm \pi^+ \pi^-$ and $B^\pm \rightarrow K^\pm K^+ K^-$. Their respective PDF parameters were extracted from MC studies and fixed in the fit to the data. In Table A.4 are shown their respective values. Notice that the mean of each Crystal-Ball is not listed in the table, this is because it shares the same mean value as the respective Gaussian function. The normalization of each component in their respective PDF is calculated based in the fraction of the Gaussian in the following way:

$$\begin{aligned} B^\pm \rightarrow K^\pm \pi^+ \pi^- : \\ f_G^{K\pi\pi} \rightarrow \text{Gaussian fraction} \\ (1 - f_G^{K\pi\pi})f_{CB1}^{K\pi\pi} \rightarrow \text{CB}_1 \text{ fraction} \\ (1 - f_G^{K\pi\pi})(1 - f_{CB1}^{K\pi\pi}) \rightarrow \text{CB}_2 \text{ fraction.} \end{aligned}$$

$$\begin{aligned} B^\pm \rightarrow K^\pm K^+ K^- : \\ f_G^{3K} \rightarrow \text{Gaussian fraction} \\ (1 - f_G^{3K})f_{CB1}^{3K} \rightarrow \text{CB}_1 \text{ fraction} \\ (1 - f_G^{3K})(1 - f_{CB1}^{3K})f_{CB2}^{3K} \rightarrow \text{CB}_2 \text{ fraction} \\ (1 - f_G^{3K})(1 - f_{CB1}^{3K})(1 - f_{CB2}^{3K}) \rightarrow \text{Exponential fraction.} \end{aligned}$$

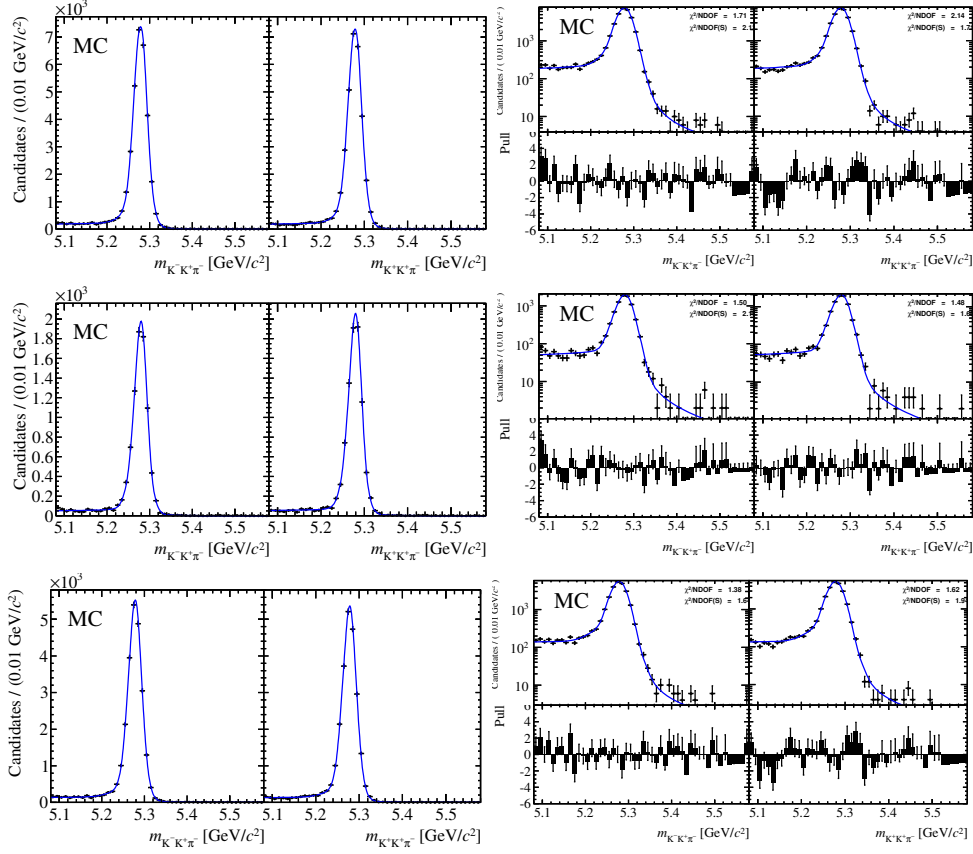


Figure A.1: Fits to the MC invariant mass distributions of the $B^\pm \rightarrow \pi^\pm K^- K^+$ of 2011 MC sample divided in the trigger configuration chosen for this analysis: “Global_TIS or Hadron_TOS” (first row), “Global_TIS and not Hadron_TOS” (second row) and “Hadron_TOS” (last row). The plot on the right side is the same as the left side, but in log scale and with the pull distribution on the bottom pad. In each pair of distributions, the plot on the left is B^- and on the right is B^+ .

In Figure A.4 it is shown the the MC mass distribution, after the selection criteria applied, of the reflections $B^\pm \rightarrow K^\pm K^+ K^-$ (left) and $B^\pm \rightarrow K^\pm \pi^+ \pi^-$ (right). See how the both reflections are located exactly in the B mass peak region, this recall for especial attention when doing the Dalitz plot fit.

For 4-body partially reconstructed decays, the shape for the B_s^0 partially reconstructed background was found from the MC, and was fixed in the fit to data. As mentioned in the subsection 4.8.2, it is parameterized by an Argus function convolved with a Gaussian resolution.

For the components of B (B^0 and B^\pm) there are no MC samples available. Some of these contributions contain charm and have large branching fractions, and for others, only upper limits of the branching ratios are known. We fix the shape of the B partially reconstructed background to that of the B_s^0 one, except for the threshold which is fixed in different values. The fractions of

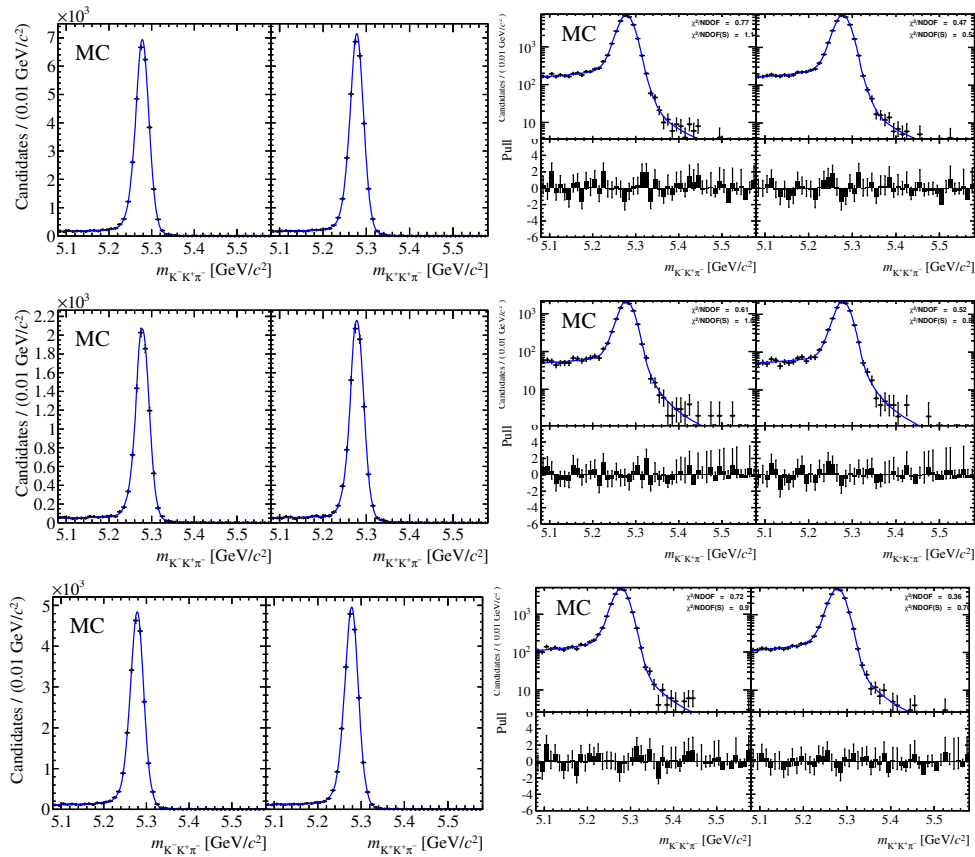


Figure A.2: Fits to the MC invariant mass distributions of the $B^\pm \rightarrow \pi^\pm K^- K^+$ of 2012 MC sample divided in the trigger configuration chosen for this analysis: “Global_TIS or Hadron_TOS” (first row), “Global_TIS and not Hadron_TOS” (second row) and “Hadron_TOS” (last row). The plot on the right side is the same as the left side, but in log scale and with the pull distribution on the bottom pad. In each pair of distributions, the plot on the left is B^- and on the right is B^+ .

both components, B_S^0 and B , are left to float. In Table A.5 are shown the parameters values for both type of components.

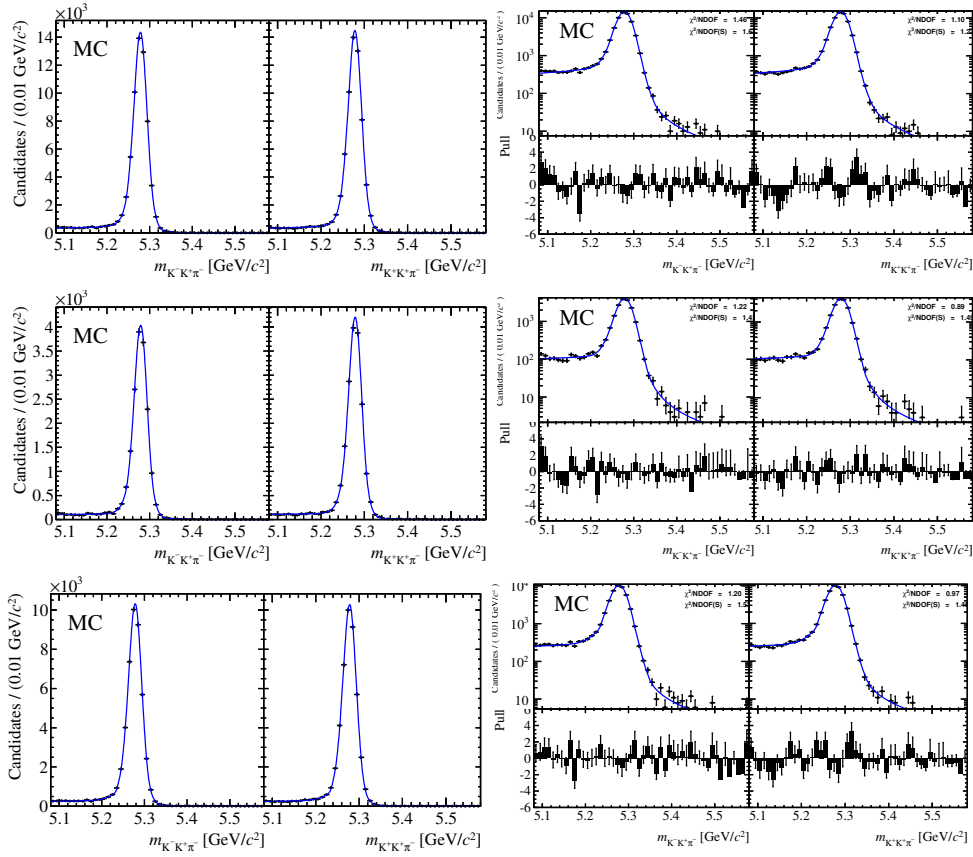


Figure A.3: Fits to the MC invariant mass distributions of the $B^\pm \rightarrow \pi^\pm K^- K^+$ of the combined 2011 and 2012 MC samples, divided in the trigger configuration chosen for this analysis: “Global_TIS or Hadron_TOS” (first row), “Global_TIS and not Hadron_TOS” (second row) and “Hadron_TOS” (last row). The plot on the right side is the same as the left side, but in log scale and with the pull distribution on the bottom pad. In each pair of distributions, the plot on the left is B^- and on the right is B^+ .

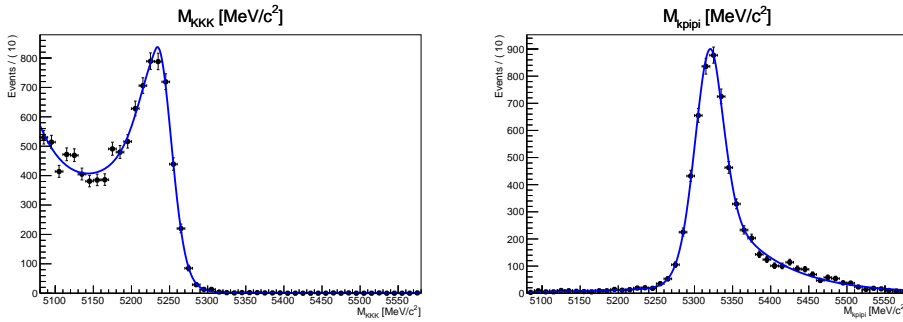


Figure A.4: Peaking background of $B^\pm \rightarrow K^\pm K^+ K^-$ (left) and $B^\pm \rightarrow K^\pm \pi^+ \pi^-$ (right) with the result superimposed.

Table A.1: Parameters of the PDF signal shape extracted from the fit to the 2011 MC sample for the trigger lines “Global_TIS or Hadron_TOS” (second column), “Global_TIS and not Hadron_TOS” (third column)” and “Hadron_TOS” (fourth column). The parameters with F are those which are left to float during the fit to data.

Parameter	TOS or TIS	TIS not TOS	TOS
μ_{MC}^{sig}	5280.4 ± 13.9	5277.5 ± 1.6	5280.3 ± 0.1
σ_{MC}^{sig}	15.35 ± 2.76	18.19 ± 1.45	15.81 ± 0.19
A_{CB1}^{μ}	1.0013 ± 0.0003	1.0015 ± 0.0006	1.0006 ± 0.0002
A_{CB1}^{σ}	0.436 ± 0.137	0.977 ± 0.089	0.593 ± 0.295
α_1^{sig}	0.493 ± 0.234	1.709 ± 0.139	1.485 ± 0.201
n_1^{sig}	0.209 ± 0.088	0.155 ± 0.053	0.049 ± 0.026
A_{CB2}^{μ}	0.9989 ± 0.0004	1.0018 ± 0.0004	0.9975 ± 0.0003
A_{CB2}^{σ}	1.918 ± 0.120	0.633 ± 0.034	2.301 ± 0.058
α_2^{sig}	-2.321 ± 0.099	-2.011 ± 0.141	-2.304 ± 0.037
n_2^{sig}	1.12 ± 0.15	1.63 ± 0.23	1.00 ± 0.08
C^{μ} F	0.999 ± 0.003	0.9990 ± 0.0003	0.99951 ± 0.00002
C^{σ} F	1.00 ± 0.50	1.00 ± 0.32	1.02 ± 0.01
A_{RAW} F	$0.0058 \pm 0.0038 \pm_{0.0000}^{0.0048}$	$-0.0198 \pm_{-0.0075}^{0.0074}$	$0.0150 \pm_{-0.0044}^{0.0045}$
f_G^{sig}	0.711 ± 0.030	0.372 ± 0.051	0.748 ± 0.003
f_{CB}^{sig}	0.532 ± 0.038	0.533 ± 0.065	0.623 ± 0.011
N_S F	68442 ± 262	$18074 \pm 134 \pm_{-135}^{0.00}$	$50369 \pm_{-224.72}^{224.25}$

Table A.2: Parameters of the PDF signal shape extracted from the fit to the 2012 MC sample for the trigger lines “Global_TIS or Hadron_TOS” (second column), “Global_TIS and not Hadron_TOS” (third column)” and “Hadron_TOS” (fourth column). The parameters with F are those which are left to float during the fit to data.

Parameter	TOS or TIS	TIS not TOS	TOS
μ_{MC}^{sig}	5278.5 ± 0.2	5281.8 ± 0.6	5266.0 ± 1.1
σ_{MC}^{sig}	23.99 ± 0.53	12.80 ± 0.26	14.04 ± 0.68
A_{CB1}^{μ}	1.0007 ± 0.0001	0.9977 ± 0.0004	1.0055 ± 0.0002
A_{CB1}^{σ}	0.50 ± 0.03	0.50 ± 0.93	1.26 ± 0.06
α_1^{sig}	1.34 ± 0.04	0.84 ± 0.72	2.08 ± 0.04
n_1^{sig}	0.312 ± 0.02	0.269 ± 0.077	0.283 ± 0.033
A_{CB2}^{μ}	1.0008 ± 0.0001	0.9993 ± 0.0003	1.0059 ± 0.0003
A_{CB2}^{σ}	0.67 ± 0.02	1.57 ± 0.05	0.87 ± 0.06
α_2^{sig}	-2.55 ± 0.04	2.20 ± 0.06	-1.76 ± 0.12
n_2^{sig}	1.43 ± 0.08	1.99 ± 0.18	2.02 ± 0.19
C^{μ} F	0.99918 ± 0.00004	0.9999 ± 0.0001	0.9967 ± 0.0002
C^{σ} F	0.994 ± 0.292	0.990 ± 0.006	0.990 ± 0.056
A_{RAW} F	-0.0147 ± 0.0038	-0.0211 ± 0.0072	-0.0120 ± 0.0047
f_G^{sig}	0.1455 ± 0.0256	0.3925 ± 0.0224	0.0451 ± 0.0075
f_{CB}^{sig}	0.2946 ± 0.0083	0.2620 ± 0.0132	0.7587 ± 0.0374
N_S F	64614 ± 242.49 $^{0.0}_{-253.33}$	$19434 \pm$ $^{139.70}_{-139.11}$	$45182 \pm$ $^{212.22}_{-212.93}$

Table A.3: Parameters of the PDF signal shape extracted from the fit to the combined 2011 and 2012 MC sample for the trigger lines “Global_TIS or Hadron_TOS” (second column), “Global_TIS and not Hadron_TOS” (third column)” and “Hadron_TOS” (fourth column). The parameters with F are those which are left to float during the fit to data.

Parameter	TOS or TIS	TIS not TOS	TOS
μ_{MC}^{sig}	5282.0 ± 2.6	5280.8 ± 1.0	5269.4 ± 0.1
σ_{MC}^{sig}	22.16 ± 3.23	13.76 ± 0.77	27.66 ± 0.48
A_{CB1}^{μ}	1.0023 ± 0.0003	1.0017 ± 0.0005	1.00340 ± 0.00005
A_{CB1}^{σ}	0.560 ± 0.028	0.665 ± 0.121	0.760 ± 0.018
α_1^{sig}	1.687 ± 0.103	0.525 ± 0.016	1.921 ± 0.013
n_1^{sig}	0.296 ± 0.035	0.189 ± 0.065	0.163 ± 0.008
A_{CB2}^{μ}	1.0000 ± 0.0003	0.9995 ± 0.0002	1.00430 ± 0.00003
A_{CB2}^{σ}	0.580 ± 0.025	1.674 ± 0.059	0.504 ± 0.010
α_2^{sig}	-2.234 ± 0.090	-2.335 ± 0.102	-2.515 ± 0.030
n_2^{sig}	1.65 ± 0.14	1.43 ± 0.22	1.38 ± 0.05
C^{μ} F	0.9984 ± 0.0005	0.9996 ± 0.0002	0.99753 ± 0.00002
C^{σ} F	1.05 ± 0.13	1.00 ± 0.11	0.99 ± 0.32
A_{RAW} F	$-0.0043 \pm_{-0.0027}^{0.0027}$	$-0.0205 \pm_{-0.0052}^{0.0052}$	$0.0022 \pm 0.0029 \pm_{0.0000}^{0.0032}$
f_G^{sig}	0.192 ± 0.031	0.548 ± 0.052	0.056 ± 0.004
f_{CB}^{sig}	0.468 ± 0.042	0.354 ± 0.035	0.469 ± 0.010
N_S F	$133057 \pm_{-365}^{365}$	$37508 \pm_{-193}^{194}$	95549 ± 279

Table A.4: Parameters of the $B^\pm \rightarrow K^\pm K^+ K^-$ and $B^\pm \rightarrow K^\pm \pi^+ \pi^-$ reflection extracted from the unbinned extended maximum likelihood fit to the 2011 and 2012 MC samples.

(a) $B^\pm \rightarrow K^\pm K^+ K^-$ combined
2011 and 2012 MC samples

Parameter	Value
μ^{KKK}	5234.2 ± 0.4
σ^{KKK}	23.46 ± 0.96
σ_1^{KKK}	16.94 ± 0.42
α_1^{KKK}	0.15 ± 0.01
n_1^{KKK}	2.20 ± 0.53
σ_2^{KKK}	349.48 ± 24.09
α_2^{KKK}	-0.036 ± 0.019
n_2^{KKK}	0.00 ± 0.44
b^{KKK}	-0.020 ± 0.001
s^{KKK}	5076.6 ± 0.7
f_G^{KKK}	0.79 ± 0.01
f_{CB1}^{KKK}	0.0046 ± 0.0039
f_{CB2}^{KKK}	0.12 ± 0.01

(b) $B^\pm \rightarrow K^\pm \pi^+ \pi^-$ combined
2011 and 2012 MC samples

Parameter	Value
$\mu^{K\pi\pi}$	5320.85 ± 0.01
$\sigma^{K\pi\pi}$	17.77 ± 0.01
$\sigma_1^{K\pi\pi}$	10.65 ± 0.03
$\alpha_1^{K\pi\pi}$	0.090 ± 0.002
$n_1^{K\pi\pi}$	18.42 ± 7.20
$\sigma_2^{K\pi\pi}$	24.64 ± 0.01
$\alpha_2^{K\pi\pi}$	0.348 ± 0.001
$n_2^{K\pi\pi}$	116.14 ± 0.02
$f_G^{K\pi\pi}$	0.337 ± 0.002
$f_{CB}^{K\pi\pi}$	0.090 ± 0.001

Table A.5: Parameters of the partially reconstructed background of $B_s^0 \rightarrow 4$ -body and $B \rightarrow 4$ -body. The C aside the parameters indicates they are fixed during the fit to data but the fraction of its PDF is left to float.

Parameters	$B_s^0 \rightarrow 4$ -body	$B \rightarrow 4$ -body
μ_G C	0.0	0.0
σ_G C	22.1467	21.385
m_t C	5217.74	5130.63
c C	-9.7998	-42.58
p C	0.0	0.0

B Acceptances Maps

B.0.3 PID efficiency from the **PidCalib** package

Since the PID variables are generally not well described in MC simulation samples, a data-driven procedure is used to obtain the PID efficiency for the PID cuts described in Table 4.4.

In MC simulated samples, few factors like variations in the performance of the RICH detectors for different periods of data recording in the year, or non-linear effects like magnetic distortions in the detector and temperature variations, are not considered. This leads to a non reliable simulation of the PID variables and thus to large systematic effects if the PID efficiency were obtained based on them. In this sense, the efficiency associated to the identification of pions and kaons is obtained through the tools from the **PidCalib** package, which is a data-driven technique, that uses a full set of calibration samples of pions, kaons and protons.

The main purpose of this data-driven procedure is to provide a calibration to the particle identification likelihood distributions or NeuraBayes based distributions from a signal sample to then obtain the efficiency associated to a certain PID requirement. To obtain the PID efficiency for any kind of track, K^\pm , π^\pm , p , \bar{p} the package uses *golden decays* that are generously produced in the experiment and that are reconstructed without using the RICH detectors but purely from their kinematics properties. In this analysis we use the distribution of pions and kaons from the $D^* \rightarrow D^0(\pi^+K^-)\pi^+$ decays.

It is important to take into account that the identification of a track has a dependence on its kinematics: also that there is a correlation between the kinematic variables of the tracks in the final-state. The PID efficiency is then obtained in bands of kinematic variables being the most commonly used the momentum (P), pseudorapidity (η) and the number of tracks. For our analysis we use the variables p and η .

In this way, the PID efficiency for a given requirement on pions or kaons in our data sample is obtained by applying this cut on the distribution of pions or kaons in the calibration sample which has been previously weighted to match the kinematics of our sample of analysis. This kinematic weight is performed by doing the comparison of the event population in intervals of (p,η)

on both samples (calibration and the sample of analysis); the ratio of both populations is established as the weight for each interval, which is attributed to the calibration sample.

The PIDCalib implementation

We divide the phase space in bins of p and η (2D-plane) according to an appropriate adaptive binning. It is desirable an uniform PID efficiency distribution as function of the momentum and pseudo rapidity variables, for the cuts applied on pions and kaons, so the binning was chosen taking this as base.

The track convention for $B^\pm \rightarrow \pi^\pm K^- K^+$ is as explained in Section 2.7. The PID cuts applied to each track in our final selection, as described on section 4.4, are:

- ProbNNpi > 0.5 & ProbNNk < 0.05 for the pion, ProbNNk > 0.45 & ProbNNpi < 0.5 for the kaons.

The efficiency associated to these cuts are obtained using the calibration samples for 2011 and 2012 data.

The output ntuple resulting in doing the match between the efficiency tables and the sample of analysis has the overall PID efficiency associated to each event, separated by charge B^+ and B^- . This efficiency is the one used in the generation of the acceptance maps.

Acceptances maps separated by charges and by year.

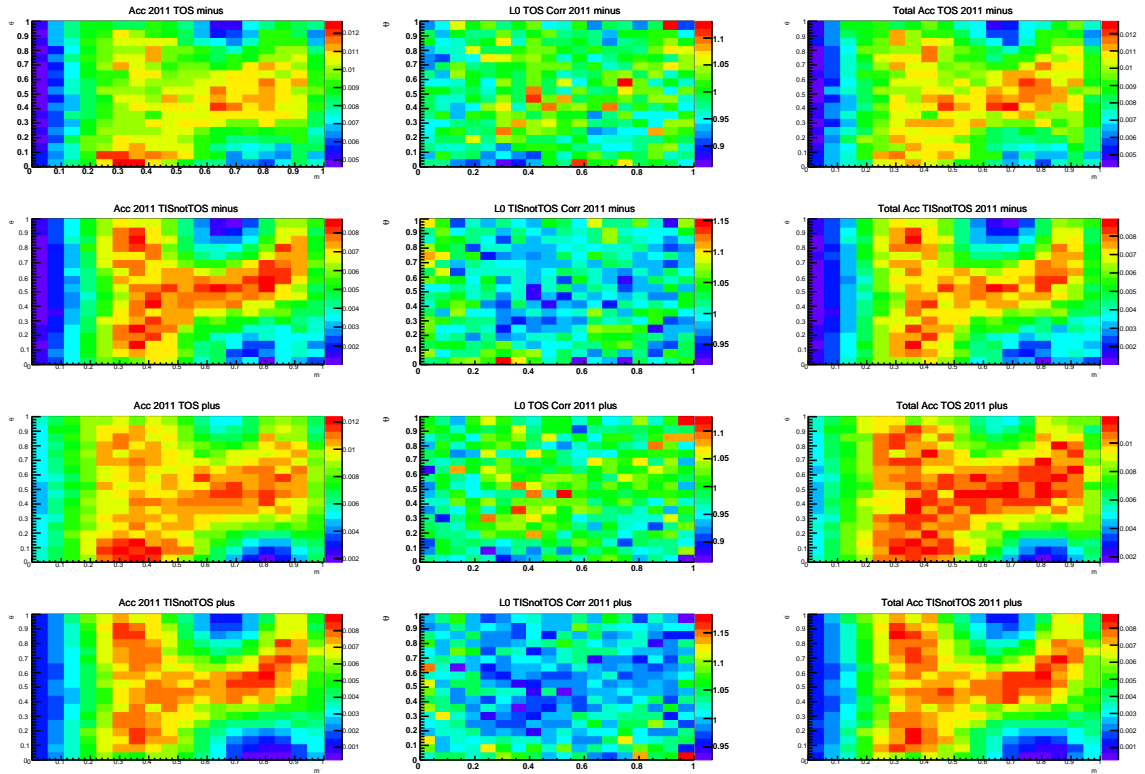


Figure B.1: 2011 Acceptance maps for $B^\pm \rightarrow \pi^\pm K^- K^+$. Acceptance map without correction (first column), L0 Hadron efficiency correction histogram (second column), total acceptance map with correction applied (third column). First row for TOS minus, second row for TISnotTOS minus, third row for TOS plus and fourth row for TISnotTOS plus.

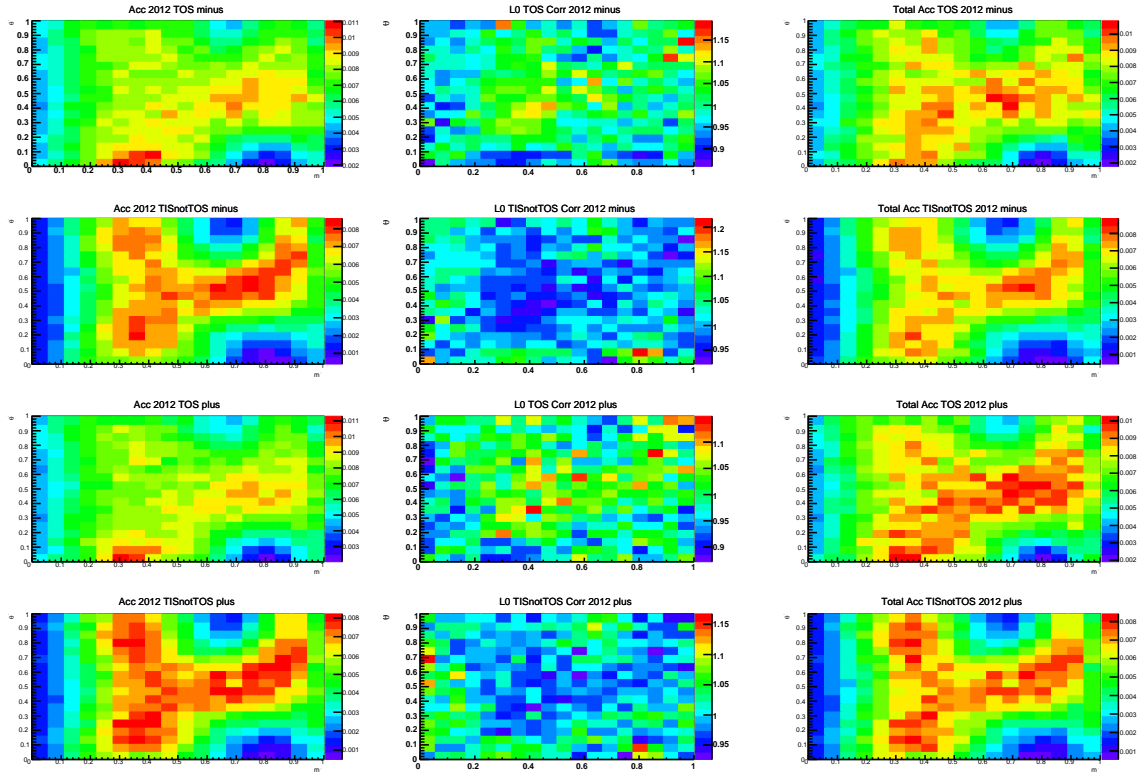


Figure B.2: 2012 Acceptance maps for $B^\pm \rightarrow \pi^\pm K^- K^+$. Acceptance map without correction (first column), L0 Hadron efficiency correction histogram (second column), total acceptance map with correction applied (third column). First row for TOS minus, second row for TISnotTOS minus, third row for TOS plus and fourth row for TISnotTOS plus.

C

Exploring improvements of the L0 hadron trigger for Run II

This analysis was developed as part of the service work required by the LHCb collaboration. It surges as a initiative from the $B \rightarrow hhh$ Rio group and the LHCb based collaborators Diego Tonelli and Patrick Robbe. The team was composed by researches, a postdoctorate and a PhD student (me) from several institutions that includes the INFN, CBPF and PUC-Rio, being the project leader Diego Tonelli. This work has been presented several times to the LHCb collaboration and is now in preparation for an internal note.

The objective of the analysis was to investigate alternative scenarios for the L0 trigger configuration in order to increase the L0 trigger efficiency for multibody decays without degrading the corresponding for two body decays. My main tasks were concentrated in the preparation and implementation of the code of analysis as well as the production of the results for the different samples considered. A description of the work and the results is presented in the following sections.

C.1

Introduction

The Run I LHCb trigger was organized into two decision levels: a hardware level-zero (L0) trigger and a High level trigger (HLT), as explained in section 3.2.6. The L0-trigger is based on the coarse transverse momentum information provided by the muon chambers (muon trigger) and from the transverse energy information given by the calorimeters (hadron, electron, and photon trigger). It has a latency of 4 μ s and aims to reduce the 20 MHz bunch-crossing rate to 1.1 MHz. The second stage consists of a two-staged high-level trigger implemented in software, this is based on C++ and python computer code, running in parallel in a CPU farm. This level has as objective to reduce the accepted rate, output of L0-level, down to 2-5 kHz for storing on permanent memory. In Figure C.1 it is presented the L0-trigger signal efficiency for several decay modes as function of the accepted rate, where the value corresponding to 1.1 MHz is explicitly indicated by a vertical blue line. As can be seen, the L0 hadron triggers suffer of a significant inefficiency due to the 1.1 MHz rate limitation [3]. This impacted most severely in the charm program, with nearly 80% of hadronic two-body charm signal events rejected by the L0 hadron trigger in Run I. It also had significant effects for

all channels with fully hadronic final states, especially those with multibody final states. This manifests thus, the limitations for higher luminosities and collision energies, like those foreseen for Run II.

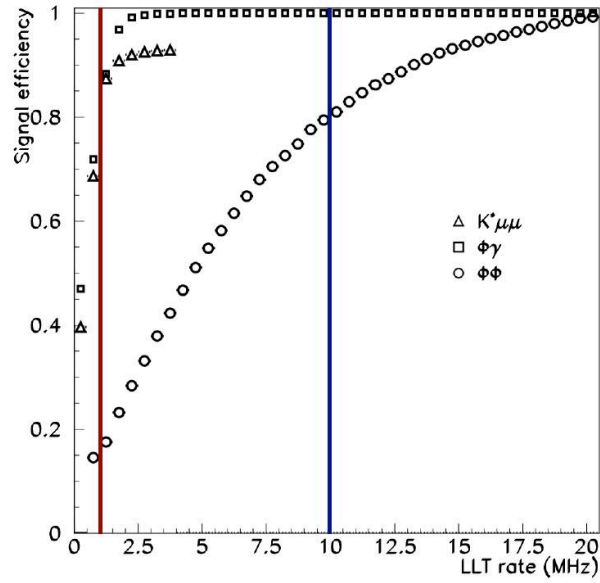


Figure C.1: Efficiency of the LHCb low-level trigger on representative simulated signals as a function of event accept rate at instantaneous luminosity $L = 1 \times 10^{33} \text{ cm}^{-2} \text{ s}^{-1}$. Plot reproduced from Fig. 3.2 in Ref. [3]

In this study, we explore possible alternative trigger strategies that could improve the performance in selecting hadronic decays at L0. The goal is to identify selection variables based on calorimeter information that improve the trigger efficiency on multibody hadronic B and D decays without compromising the performance on two-body decays.

The trigger performance is examined in terms of the efficiency for selecting signal events as a function of the fraction of retained background events. Our baseline study consists in using the first set of real data collected by the LHCb with the Run II conditions, where we test all the possible scenarios only using the available information provided by the actual L0 architecture. As a second approach we also perform studies using simulated samples, where we test new trigger configurations using the information that is stored by the calorimeters but is not available in the current L0. In order to be able to compare the results obtained from data with those using simulated samples, an appropriate correction factor due to the differences between minbias and zerobias rate was applied.

Signal efficiencies are calculated based on the union of events triggered on signal (TOS) and independently of it (TIS). All the performances are quoted relative to that resulting from the baseline L0 hadron Run II trigger (relative

efficiency gain plots). We study numerous alternative trigger requirements based on information available by default to the L0 decision unit or additional information that is available in the calorimeter data banks and could be made available to L0 decision as well.

C.2 Strategy and tools

For this study we use the first set of data collected by the LHCb with the Run II conditions in 2015, that is, bunch crossing every 25 ns and a 13 TeV in the center of mass energy. The signal samples were taken from the validation samples, which have been collected with the trigger key TCK 0x005. This correspond to a configuration of 450 hits on the SPD multiplicity and a threshold on the leading transverse energy of 2496 MeV. The background events are obtained from a zerobias sample. We use approximately 100,000 zero-bias events, 11600 $B^0 \rightarrow \pi^+\pi^-$ events, 35000 $D^+ \rightarrow K^-\pi^+\pi^+$ events, 15000 $D^{*+} \rightarrow (D^0 \rightarrow K^-\pi^+)\pi^+\pi^-$ events, and 180 $B^+ \rightarrow K^+K^-\pi^+$ events.

For the Monte Carlo samples, we use the official simulated data files that were used for the 2015 bandwidth-division studies documented in Ref. [97]. A minbias sample is used for the background. These files contain the L0 information that was emulated¹ by the bandwidth-division group in December 2014. The samples were generated using Pythia 8 and with the nominal 2015 conditions. The signal events were reconstructed using a minimal set of offline requirements that approximate the loosest selections foreseen to be employed in analysis. It is important to remark that a masking of the central-most calorimeter cells², using the official code, was made. This as it was found an abnormally high fraction of events above-threshold, due to this cell, in Run I. We use approximately 100000 minimum-bias events, 7000 $B^0 \rightarrow K^+\pi^-$ events, 8000 $D^+ \rightarrow K^+K^-\pi^+$ events, 15000 $B_s^0 \rightarrow \phi^+\phi^-$ events, and 70000 $B^+ \rightarrow K^+K^-\pi^+$ events.

To establish an order of comparison between data and MC results, it was necessary to match in simulated samples, the online transverse energy threshold used in data: $E_{t1} > 2496$ MeV, and the equivalent threshold of hits on the SPD multiplicity, which correspond to 300 for the MC. Also it was necessary to apply a correction factor to take into account the differences between the min-bias and zerobias rate. The retention obtained from the

¹L0 emulation: a software code that calculates L0-level variables (the ones provided by the hardware during data-taking), starting from the deposits in the calorimeter as well as the responses of all the other detectors.

²Usually referred as the ring of fire.

minbias sample is multiplied by a factor that holds for the bunch crossing with no hard scatter observed in data, this is expressed as:

$$1-e^{-\nu},$$

where ν is the average number of pp interactions per bunch crossing. The value $\nu = 1.5$ was considered in order match the actual μ value observed in data.

As the reliability of the simulation in reproducing the real Run II condition is limited, all performances are quoted relative to that resulting from the baseline L0 hadron Run II trigger. The assumption is that the ratio of performances is less subject to large mismodeling of the environmental conditions than absolute performances.

The strategy

The strategy consisted in the search of alternative trigger scenarios by accessing to the full information stored in the (“FullCallo”) calorimeter bank. This with the aim to obtain a higher efficiency than the one provided by the actual default trigger configuration. The information accessible in the calorimeters comprises the values of energy deposits in each channel and each compartment, along with the associated spatial coordinates. Most of this information is currently not available to the L0 decision unit, but could be made if it is found a scenario with a promising discriminating power.

The actual default trigger configuration consist of a single energy deposit, the highest-energy cluster, to select signal events. This has shown to degrade significantly the trigger efficiency for multibody decays, if compared to that one for two-body decays, especially affecting the charm program.

For all the scenario that are tested, we qualify the trigger performance in terms of signal efficiency versus background retention, in which we assume in the latter, that all the available bandwidth is devoted to the channel under study. We define as *signal efficiency* the fraction of total signal events (from data or MC samples) that meet a test trigger configuration and as *background retention* the fraction of zero-bias (or minimum-bias) events that meet the same requirement.

Some of the variables that can be used from the information provided by the calorimeters are: the highest, second and third-highest hadronic energy deposits, denoted as E_{t1} , E_{t2} and E_{t3} , respectively; their sum, $E_{t1} + E_{t2}, \dots, E_{t1} + E_{t2} + E_{t3}$; their product, $\dots E_{t1} \times E_{t2}$; the sum of the total transverse calorimeter energy denoted as $\sum E_t$; the Cartesian coordinates of these deposits in the calorimeter plane; the tangents of the polar angles of these deposits; the

azimuthal separation between them. Were also used the combination of these variables using the logic gates AND and OR.

In the following are presented the results, which we divide into two part: we first present the possible trigger scenarios that can be constructed using the current trigger architecture, which will not require modifications in the hardware setup, using the data samples; then we present configurations that would need information that is stored but is not available in the current L0 trigger level using the MC samples.

C.2.1

Results using the available information in the L0DU

As mentioned in the previous section, the current L0 hadron trigger decision is based on the presence of at least one transverse energy cluster above a fixed threshold (E_{t1}). However, the L0 decision unit has also access to other variables like the sum of the total transverse calorimeter energy $\sum E_t$, the second leading transverse energy deposit E_{t2} , and the SPD multiplicity. It also supports the logic gates combination AND, OR.

we explored the potential of these variables individually and their allowed combinations by analyzing the relative efficiency gain versus the background retention, as described in the section C.2. In Figures C.2 and C.3 are shown the relative efficiency gain for the 1D configuration E_{t2} and $\sum E_t$, Respectively. In Figures C.4 to C.9 are shown the respective plots using 2D combinations.

In each plot, the horizontal dashed line in one, represents the ratio of the signal efficiency obtained with the standard trigger configuration divided by itself for each retention value. In the same way, every point in the plot represents the ratio of the efficiency obtained with the scenario being tested with respect to the efficiency obtained using the standard configuration for each retention value. Thus, every point above the horizontal dashed line represents configurations which provide a gain in the signal efficiency.

Studying the plots, it is found that there exists improvements in the signal efficiency especially for charm decays. Exploring the 1D trigger configurations, $\sum E_t$ and E_{t2} , it is observed relative efficiency gains in the range of 10%-30%. It is found that all the 1D scenarios tested do better for the two-body decay channel, $B^0 \rightarrow \pi^+\pi^-$, than the default configuration. Nevertheless, on the other hand, these seem not to work well for other decays like $B^+ \rightarrow K^+\pi^+K^-$. From the 2D configurations, which include scenarios of the type $E_{t1} > X \&\& \sum E_t > Y$, $E_{t1} > X || \sum E_t > Y$ or $E_{t1} > X \&\& E_{t2} > Y$, to mention some, it is found that they offer an improvement in the trigger efficiency for all the channels with a relative efficiency gain up to $\sim 15\%$, except for the hadronic

B decay in which is not observed an appreciable improvement but also is not observed a degrade of its efficiency compared with the one obtained in the default configuration.

While significant gains can be obtained for multibody charm decays by replacing a requirement in the highest energy cluster (E_{t1}) with one on the total transverse energy of the event ($\sum E_t$), the degradation of signal efficiencies for other channels is significant and does not make the its simple usage an attractive option. However, simple logical combinations like the logical AND of requirements on E_{t1} and $\sum E_t$ do preserve the baseline performance in hadronic B decays and offer increase in signal efficiency for multibody D decays. In Tables C.2.1 and C.2.1 is shown the corresponding relative efficiency for all the decay considered for two values of background retention, 2.3% and 3.1%, respectively.

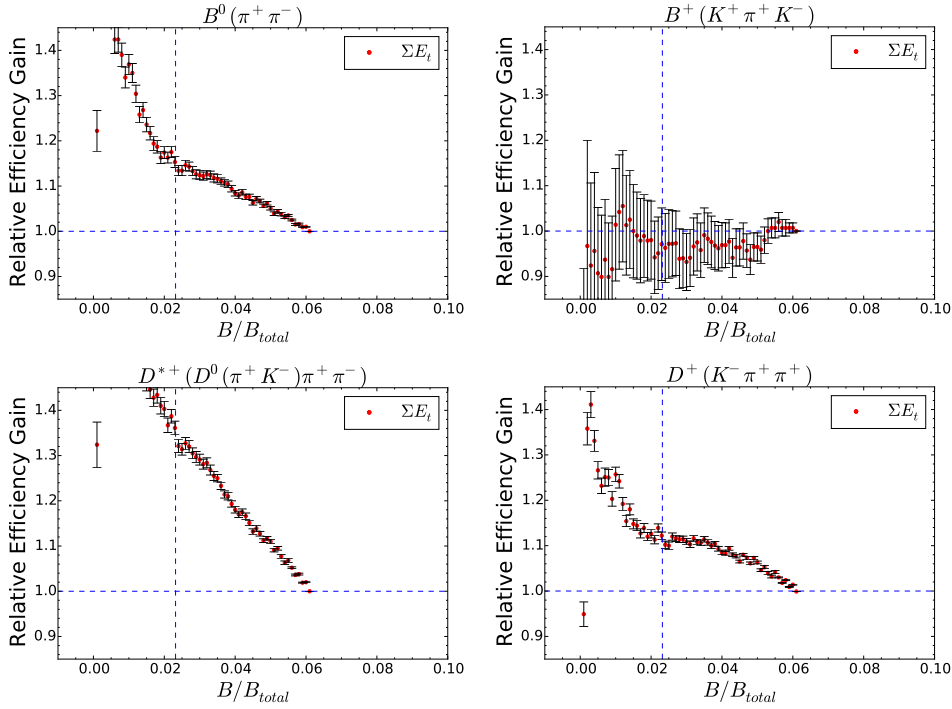


Figure C.2: Distributions of relative gains associated with $\sum E_t$ using real data.

C.2.2 Results from the MC samples

Using the MC samples we tested alternative trigger configurations using decays channels that were not available in real data at the moment. We take the advantage of the high statistic of the simulates samples being this one of the limitations in real data for some channels.

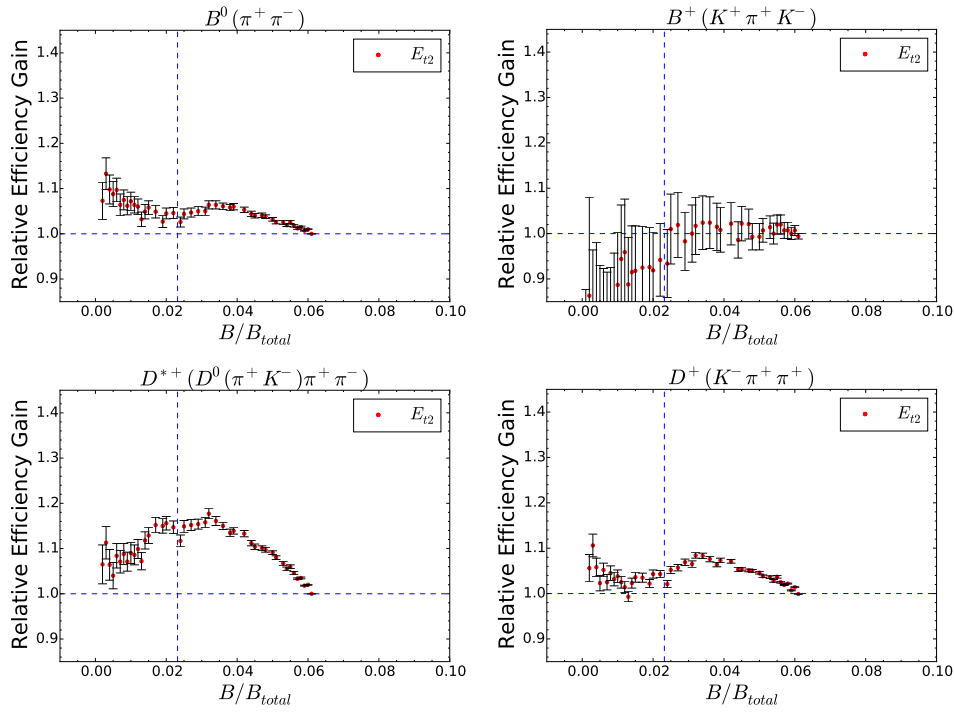


Figure C.3: Distributions of relative gains associated with $\sum E_{t2}$ using real data.

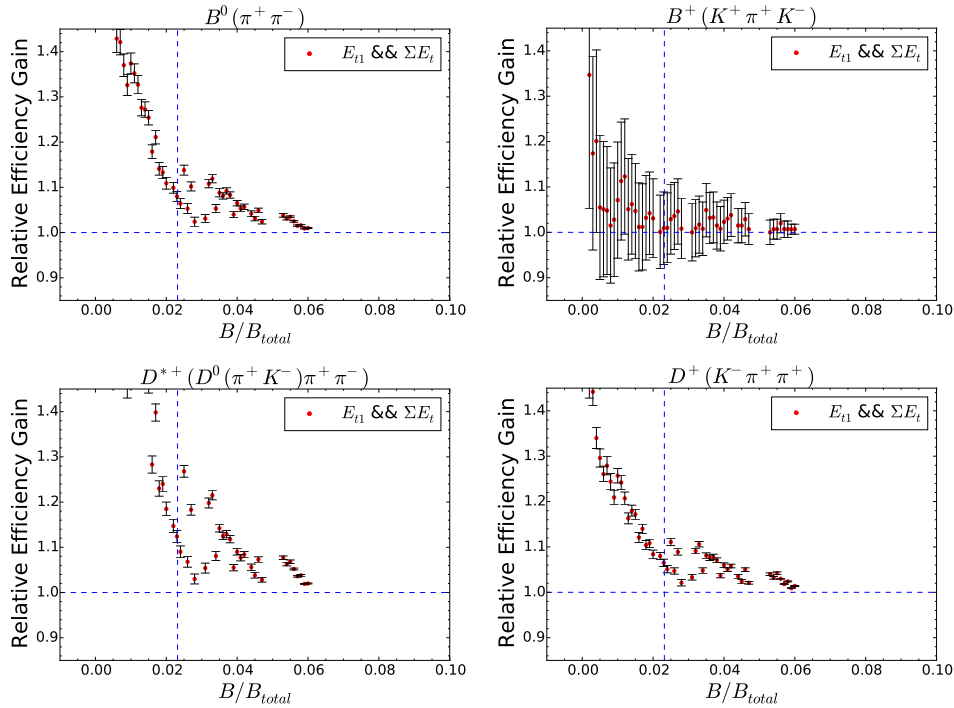


Figure C.4: Distributions of relative gains associated with various requirements on the logical “AND” between the energy of the leading jet and the sum of the energies in all calorimeter towers. Results using real Data

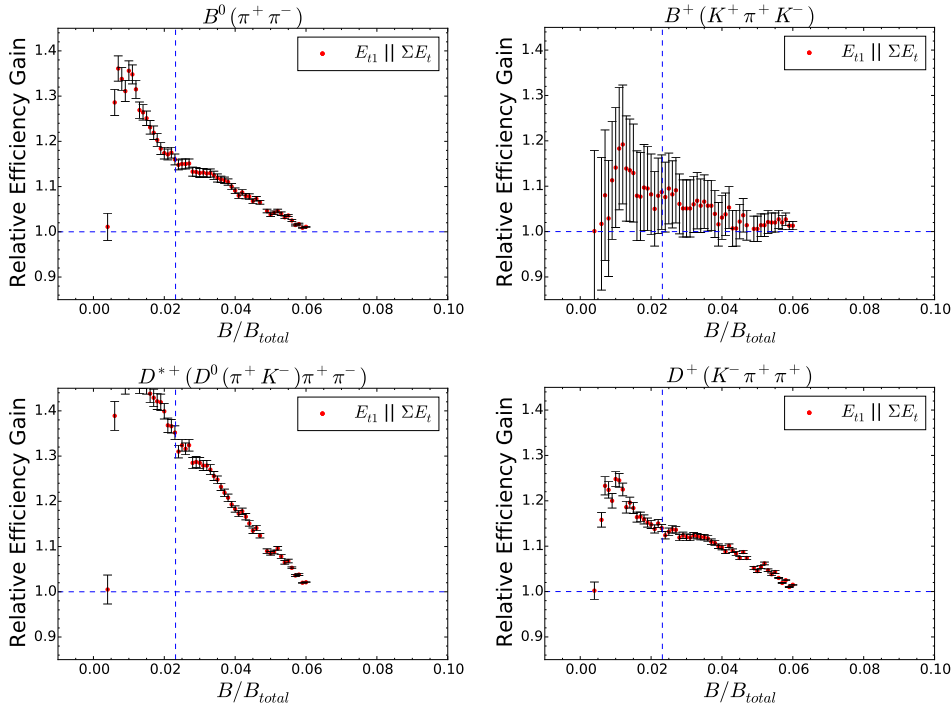


Figure C.5: Distributions of relative gains associated with various requirements on the logical “OR” between the energy of the leading jet and the sum of the energies in all calorimeter towers. Results using real Data.

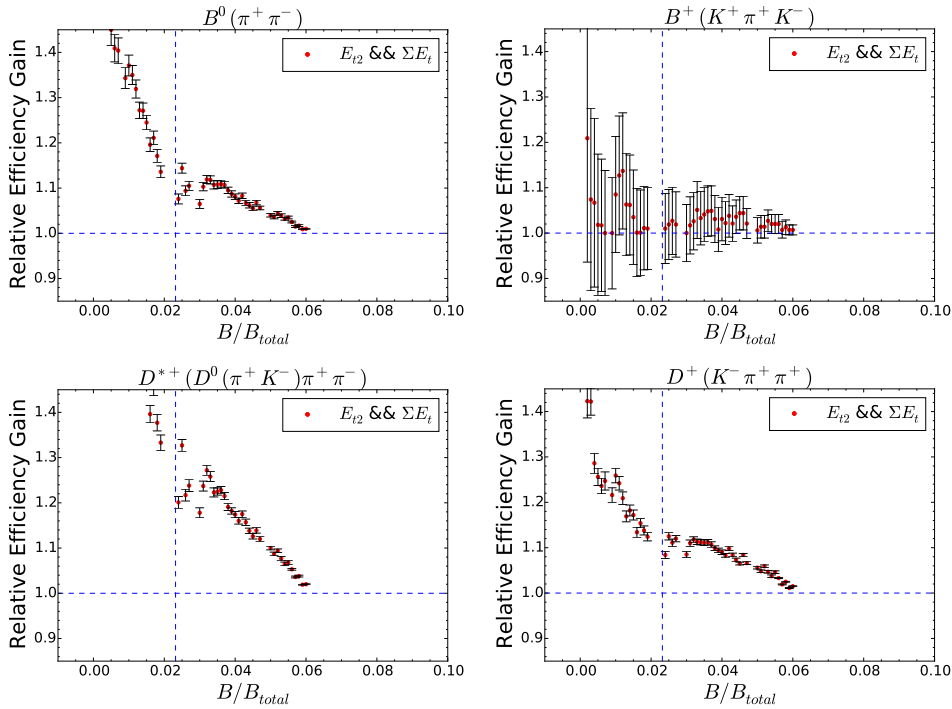


Figure C.6: Distributions of relative gains associated with various requirements on the logical “AND” between the energy of the second leading jet and the sum of the energies in all calorimeter towers. Results using real Data

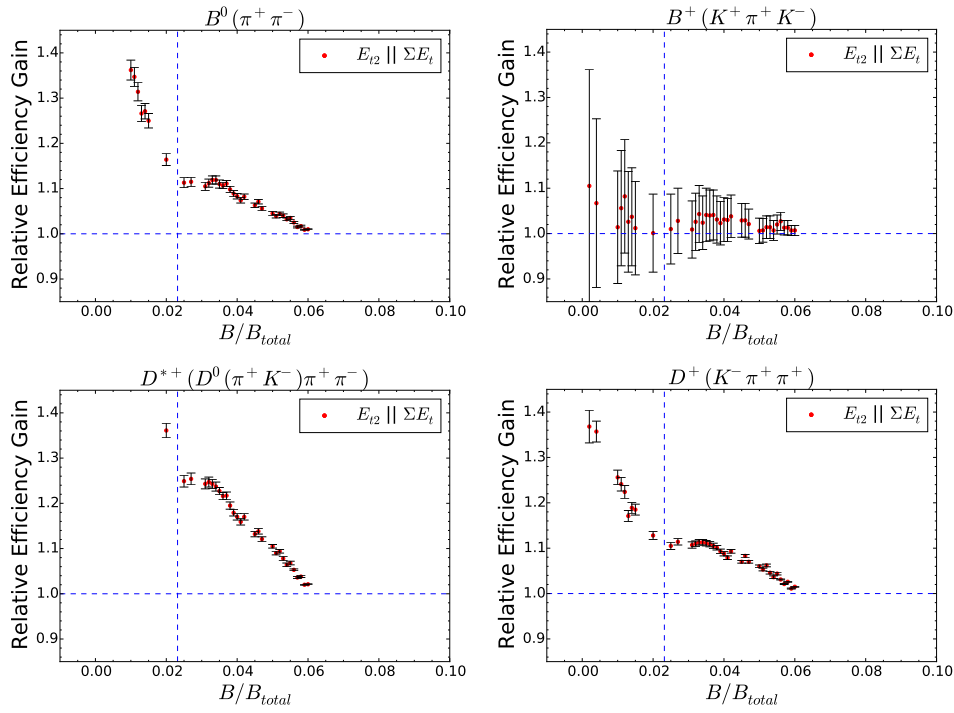


Figure C.7: Distributions of relative gains associated with various requirements on the logical “OR” between the energy of the second leading jet and the sum of the energies in all calorimeter towers. Results using real Data.

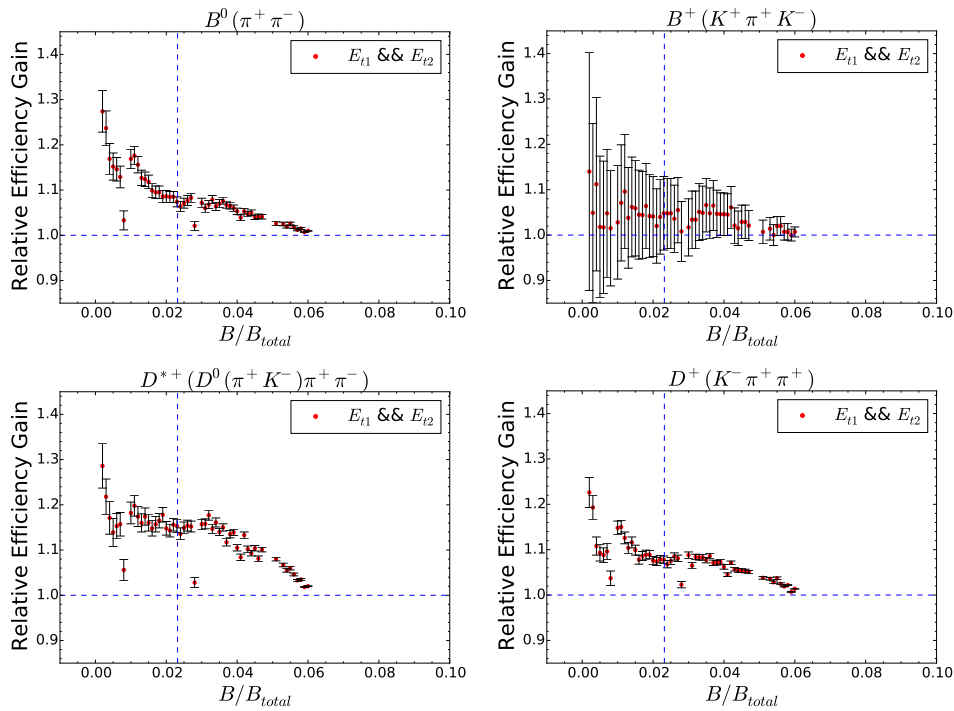


Figure C.8: Distributions of relative gains associated with various requirements on the logical “AND” between the energy of the leading jet and the second leading jet. Results using real Data.

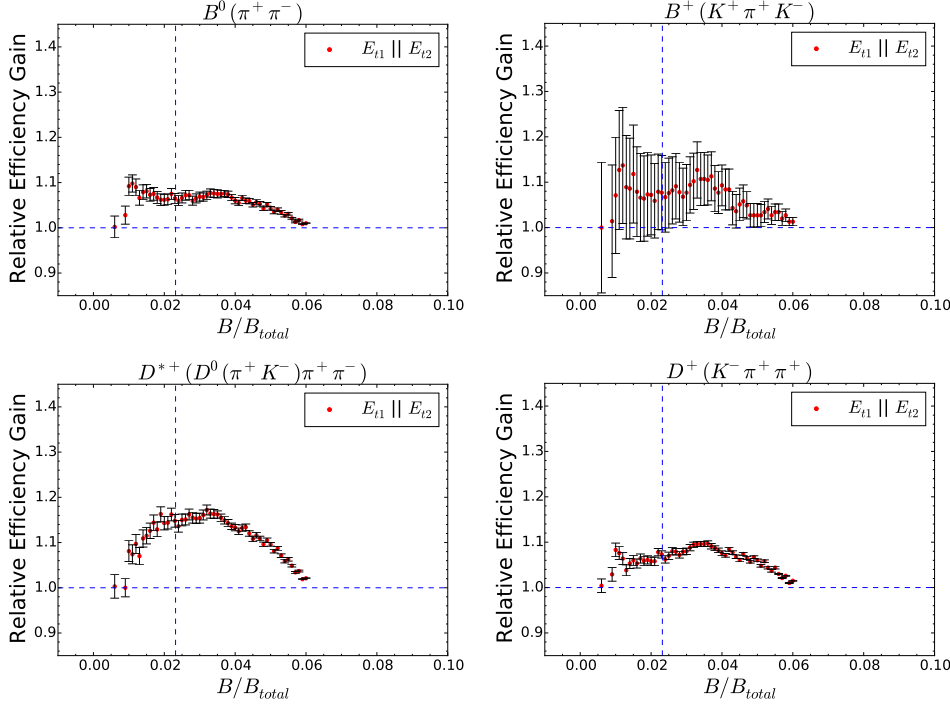


Figure C.9: Distributions of relative gains associated with various requirements on the logical “OR” between the energy of the leading jet and the second leading jet. Results using real Data.

Criterion*	Relative gain			
	$B^0 \rightarrow K^+ \pi^-$	$B^+ \rightarrow K^+ K^- \pi^+$	$D^{*+} \rightarrow D^0 \pi^+ \pi^-$	$D^+ \rightarrow K^- \pi^+ \pi^+$
$\sum E_t > 23.684$	1.153	0.971	1.361	1.122
$E_{t2} > 2.313$	1.026	0.934	1.117	1.021
$E_{t1} > 3.084 \& \sum E_t > 18.468$	1.080	1.009	1.124	1.065
$E_{t1} > 3341 \sum E_t > 30.907$	1.080	1.0019	1.134	1.059
$E_{t2} > 2210 \& \sum E_t > 17.264$	1.076	1.010	1.210	1.084
$E_{t2} > 2262 \sum E_t > 34.318$	1.056	1.010	1.161	1.060
$E_{t1} > 2.724 \& E_{t2} > 2.210$	1.050	1.009	1.138	1.048
$E_{t1} > 33907 E_{t2} > 2.519$	1.053	1.058	1.084	1.055

Table C.1: Trigger scenarios tested only using the available information to the L0DU. In the first column is presented the scenario being tested and in the following columns the relative efficiency gain for the different channels. This values correspond for a retention of 2.3%

In Figures C.10, C.11 and C.12 are shown the results for the configurations $(E_{t1} + E_{t2})$ AND $(E_{t1} + E_{t2} + E_{t3})$, E_{t1} OR $(E_{t1} + E_{t2} + E_{t3})$ and E_{t1} OR $(E_{t1} \times E_{t2})$, respectively. These three scenarios are representative of some of the best scenarios found.

We observed gains in the signal efficiency up to $\sim 15\%$, especially for the charm sector. Even when not larger efficiency gains are observed with the new

Criterion*	Relative gain			
	$B^0 \rightarrow K^+\pi^-$	$B^+ \rightarrow K^+K^-\pi^+$	$D^{*+} \rightarrow D^0\pi^+\pi^-$	$D^+ \rightarrow K^-\pi^+\pi^+$
$\sum E_t > 21.678$	1.122	0.941	1.281	1.103
$E_{t2} > 2.107$	1.050	1.000	1.158	1.065
$E_{t1} > 2.982 \& \sum E_t > 13.853$	1.031	1.000	1.054	1.033
$E_{t1} > 3.084 \sum E_t > 30.105$	1.058	1.026	1.093	1.043
$E_{t2} > 2.005 \& \sum E_t > 16.662$	1.090	1.009	1.216	1.107
$E_{t2} > 2.107 \sum E_t > 28.500$	1.084	1.009	1.209	1.097
$E_{t1} > 2.673 \& E_{t2} > 1.953$	1.060	1.009	1.129	1.061
$E_{t1} > 3.084 E_{t2} > 2.776$	1.012	1.017	1.018	1.010

Table C.2: Trigger scenarios tested only using the available information to the LODU. In the first column is presented the scenario being tested and in the following columns the relative efficiency gain for the different channels. This values correspond for a retention of 3.1%

scenarios tested, they offer an improvement in the signal efficiency favouring the charm decays and without degrading the efficiency for the other modes.

C.3 Summary

We explored possible improvements of the L0 hadron trigger for Run II. Trigger performance is studied in terms of efficiency for selecting signal events as a function of the fraction of retained background events. We use the first set of real data collected by the LHCb with the Run II conditions and simulated samples of representative hadronic B and D decays. We explore alternative trigger requirements based on either information available by default to the L0 decision unit or additional information that could be made available to it. By using information associated with multiple calorimeter clusters in an event, we observe up to 15% improvements in signal efficiency on multibody hadronic channels over the current baseline configuration, without degrading the performance on two-body decays. Requirements based on multiple calorimeter clusters offer the additional benefit of reducing biases in the signal Dalitz-plot with respect to the baseline requirements.

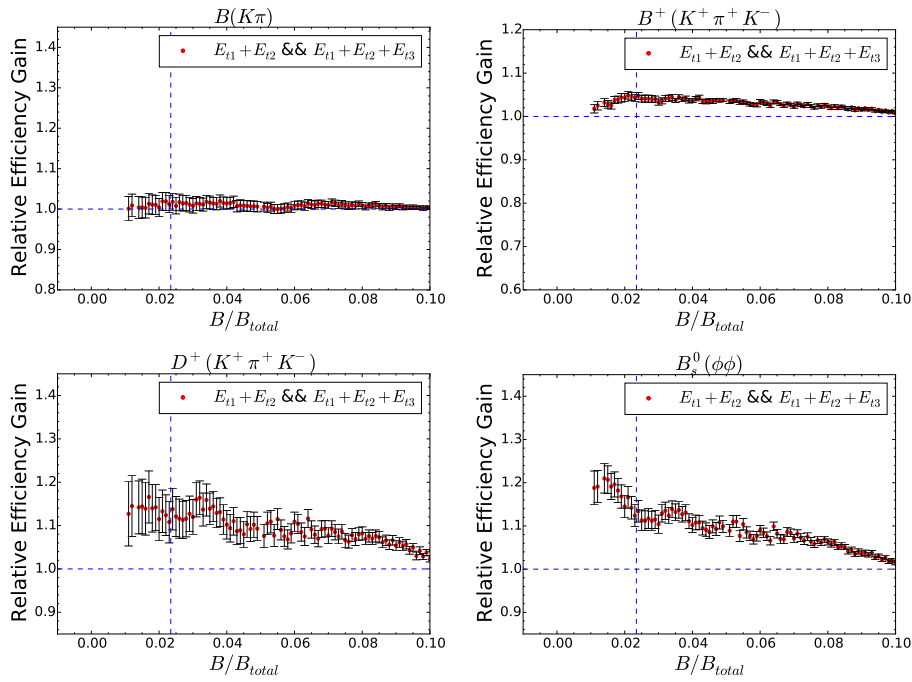


Figure C.10: Distributions of relative gains associated with the $E_{t1} + E_{t2}$ AND $E_{t1} + E_{t2} + E_{t3}$ configuration, using signal MC and min-bias sample.

PUC-Rio - Certificação Digital N° 1313014/CA

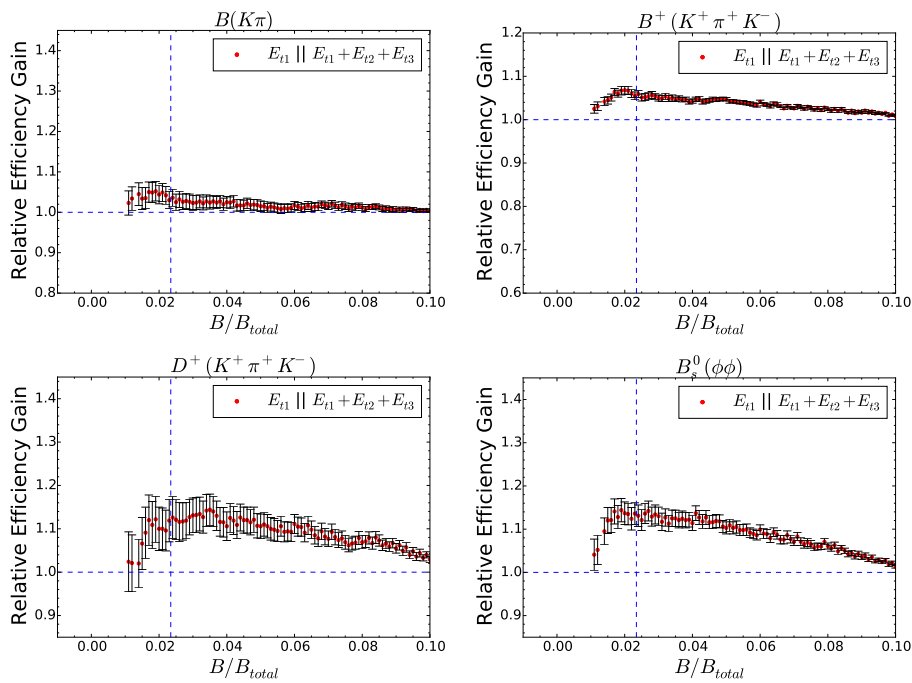


Figure C.11: Distributions of relative gains associated with the E_{t1} OR $E_{t1} + E_{t2} + E_{t3}$ configuration, using signal MC and min-bias sample.

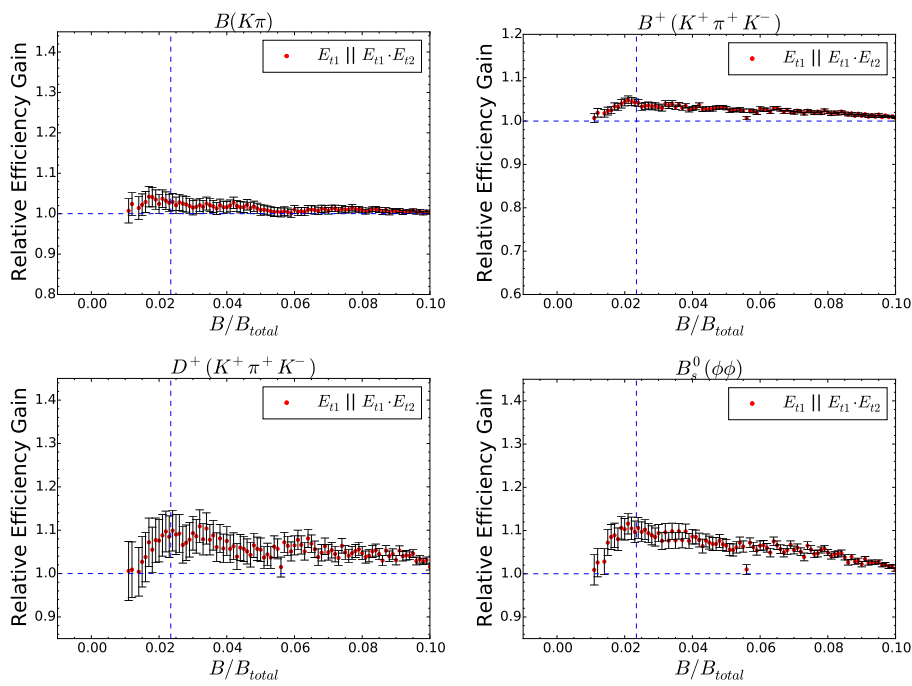


Figure C.12: Distributions of relative gains associated with the E_{t1} OR $E_{t1} \times E_{t2}$ configuration, using signal MC and min-bias sample.